



City Research Online

City, University of London Institutional Repository

Citation: Ghavami, M. (2017). Cycle analysis and optimisation of micro gas turbines for concentrated solar power. (Unpublished Doctoral thesis, City, University of London)

This is the accepted version of the paper.

This version of the publication may differ from the final published version.

Permanent repository link: <https://openaccess.city.ac.uk/id/eprint/19227/>

Link to published version:

Copyright: City Research Online aims to make research outputs of City, University of London available to a wider audience. Copyright and Moral Rights remain with the author(s) and/or copyright holders. URLs from City Research Online may be freely distributed and linked to.

Reuse: Copies of full items can be used for personal research or study, educational, or not-for-profit purposes without prior permission or charge. Provided that the authors, title and full bibliographic details are credited, a hyperlink and/or URL is given for the original metadata page and the content is not changed in any way.



Cycle Analysis And Optimisation Of Micro Gas Turbines For Concentrated Solar Power

by Mohsen Ghavami

Thesis Submitted for the Degree of Doctor of Philosophy in Mechanical
Engineering

City, University of London
Turbomachinery and Energy Systems Research Group

July 2017

ABSTRACT

In recent years there has been an increasing interest in power generation using small-scale concentrated solar power units. Currently, photovoltaics are the main commercialised technology thanks to their low capital cost. However, their relatively low efficiency and power density has motivated research on the application of thermal engines. Dish-Stirling systems achieve reasonable efficiencies, but are relatively expensive and unreliable because of their technical complexity. The reliability of micro gas turbines and their potentially lower costs has motivated the current research, which is part of the EU funded OMSoP project, to study the thermo-economic performance of a micro gas turbine (MGT) engine coupled with dish concentrators in order to achieve suitable efficiency at low cost. To achieve this goal a system design, which takes into account the state of the art technology, is required to achieve an acceptable efficiency with minimised capital cost to promote dish-MGT systems in the market. An important issue to be addressed is to consider the effect of system design parameters on dish-MGT performance under the considerable variations of the solar irradiance.

A computational model for pure solar dish-MGT systems has been developed, which combines the cycle analysis of the MGT with component models to perform design point performance simulation, generate component performance maps and perform off-design performance simulation. The method has been proven to be quick and effective, particularly in terms of using minimal data and providing the component performance maps for off-design simulation. Different strategies which can be applied to pure solar dish-MGT systems are examined and novel concepts have been proposed to increase the generated electricity.

The computational model has been coupled with an up to date economic model which was specifically developed through the OMSoP project for dish-MGT systems. The integrated model is coupled to an optimisation platform to find system designs which lead to optimal thermo-economic performance for a 5kWe system. Then the optimisation has been extended over the rated power of 5-30kWe to find the power rating which results in the minimum cost of generated electricity by the dish-MGT systems.

The proposed concepts for the control and operation of the dish-MGT systems are shown to be advantageous for increasing electricity production and dealing with the variations of power demand. The results demonstrate the potential of pure solar dish-MGT systems to achieve economically competitive electricity when the economy of scale of these systems is taken into account.

ACKNOWLEDGEMENTS

First and foremost I would like to thank my supervisor, Professor Abdalnaser Sayma whom I am very grateful for his support and invaluable advices throughout the progression of my research. I would also like to thank him for giving me the great opportunity to do my PhD in the Turbomachinery and Energy Systems Research Group on a very interesting project, OMSoP. I would also wish to acknowledge my co-supervisor, Professor Keith Pullen for his useful suggestions as well as my thesis examiners, Professor Ian Smith and Professor Alberto Traverso for their thorough review of this thesis and their very useful comments.

I would also like to acknowledge the support from people in the OMSoP project and funding provided by the EU Commission. I am also grateful for working with people from the consortium members in a concerted research which part of it has been reflected within this thesis.

Huge thanks go to my colleague and dear friend Dr Jafar Alzaili who provided me with invaluable comments and pieces of knowledge. I would also like to acknowledge the wide experience and useful comments from Professor Alan Turner, University of Sussex. I am also thankful to my fellow PhD students and colleagues in the thermo-fluid research centre, especially Dr Martin White, Dr Mahmoud Khader, Dr Michael McLorn, Antonio Arroyo and Davide Iaria for both technical and non-technical helpful discussions.

Finally, I would like to thank my dear wife, our wonderful children and my parents for their patience, love and support throughout my work. Without the encouragement I received from them, doing this thesis would have not been a pleasant job.

TABLE OF CONTENTS

ABSTRACT.....	i
LIST OF FIGURES.....	vii
LIST OF TABLES.....	xiii
NOMENCLATURE.....	xv
1 Introduction.....	1
1.1 Solar power generation	1
1.2 Concentrated solar thermal power	2
1.3 The OMSoP project	4
1.4 Solar powered micro gas turbine research.....	7
1.5 Aims and objectives.....	8
1.6 Structure of the thesis and scientific contributions	9
1.7 Publications.....	11
2 Literature review	13
2.1 Introduction.....	13
2.2 Micro gas turbines in power generation.....	13
2.2.1 Classification	13
2.2.2 Power generation	14
2.3 Solar energy	20
2.3.1 Solar radiation concentrators	23
2.3.2 Solar receivers	25
2.4 Solar powered gas turbine systems	27
2.5 Overview of performance models for micro gas turbine cycles	32
2.5.1 Categories of engine models	32
2.6 Economic models for solar powered systems	36
2.7 Conclusion	38
3 Thermodynamic performance modelling	41
3.1 Introduction.....	41
3.1.1 General representation of system components	42
3.2 Governing equations	45
3.2.1 Components equations.....	45
3.2.2 Energy and mass conservation	49
3.3 Design point performance.....	50
3.3.1 Case study.....	51
3.3.2 Cycle analysis.....	52
3.3.3 Evaluation of the rotational speed	54
3.4 Component models for design and off-design simulation	56
3.4.1 Performance maps of the turbomachinery	56
3.4.2 Performance characteristics of the optical system.....	61
3.4.3 The recuperator.....	63
3.4.4 High speed alternator and power electronics.....	65
3.5 Off-design performance	68
3.5.1 System constraints	70
3.5.2 Performance results	70
3.6 Conclusions.....	76

4	Control of the solar micro gas turbines	77
4.1	Introduction.....	77
4.2	Micro-gas turbine operation strategies.....	78
4.2.1	Constant rotational speed operation	79
4.2.2	Constant TIT operation.....	82
4.2.3	Constant TET operation	85
4.2.4	Constant power operation.....	87
4.2.5	Maximum power generation.....	90
4.3	Control systems of the micro gas turbines	91
4.4	Recuperation control.....	97
4.4.1	Dealing with excessive DNI.....	99
4.5	Comparison of the operation strategies.....	102
4.6	Conclusions.....	105
5	Techno-economic optimisation of dish-MGT systems	107
5.1	Introduction.....	107
5.2	Analysis of the optimisation problem	108
5.2.1	System design variables	108
5.2.2	Economic and performance indicators of the system	111
5.2.3	Multi-objective optimisation algorithm.....	113
5.2.4	Optimisation framework.....	114
5.3	Economic model	116
5.3.1	Cost functions for the MGT assembly.....	117
5.3.2	Cost function of the receiver	120
5.3.3	Cost of the dish.....	121
5.3.4	Additional costs of the plant.....	122
5.4	Optimisation of the dish-MGT systems	124
5.4.1	Fixed rated power	125
5.4.2	Variable rated power	133
5.5	Conclusions.....	136
6	Conclusions and recommendations for further work	139
6.1	Conclusions.....	139
6.1.1	Development of the dish-MGT design and analysis tool	139
6.1.2	Control and operation strategies	140
6.1.3	Optimisation of the dish-MGT systems.....	141
6.2	Recommendations for further work	142
6.2.1	Improvements to the system design and analysis	142
6.2.2	Improvements to the control and operation strategies	142
	Bibliography.....	145
	APPENDICES.....	157
	Appendix A Scaling the performance maps	157
	Appendix B Electrical power calculations.....	163

LIST OF FIGURES

Figure 1.1 CST systems: (1) parabolic troughs, (2) parabolic dishes, (3) heliostat fields with central tower and (4) linear Fresnel reflectors (Lemus & Duart, 2012)	2
Figure 1.2 Schematic of piston Stirling engine (or so called ‘kinematic Stirling’) and its components (Schiel & Keck, 2012).....	4
Figure 1.3 Schematic diagram of the system (OMSOP, 2013).....	5
Figure 1.4 Recuperated Brayton cycle (Borgnakke & Sonntag, 2009).....	7
Figure 1.5 hourly variation of the solar irradiance for Cassacia (Italy) for the beginning days of sample months. Solar data from (SoDa, 2016).....	8
Figure 2.1 Ideal (1-2 _s -3-4 _s) and actual (1-2a-3-4a) Brayton cycles (Çengel & Michael, 2015) .	14
Figure 2.2 Ideal recuperated Brayton cycle. Input heat reduced because of the heat recovery (Çengel & Michael, 2015).....	15
Figure 2.3 effects of TIT and pressure ratio on the efficiency of micro gas turbine	16
Figure 2.4 turbine and recuperator material requirements map for common range of TIT and compressor pressure ratio (R _c) in the micro gas turbines. Extracted from (McDonald, 2003)	17
Figure 2.5 diabatic processes in compressor (left) and turbine (right). Adapted from (Van den Braembussche, 2005)	19
Figure 2.6 beam and diffuse solar radiations	21
Figure 2.7 cosine effect in direct radiation.....	21
Figure 2.8 pattern of variations of DNI for Casaccia, Italy.....	22
Figure 2.9 reference: (SCHOTT, 2016)	23
Figure 2.10 McDonnell Douglas (currently Boeing) Dish Concentrator; Daggett, California; USA (courtesy NREL). The Solar One Tower which is powered by a heliostat field is in the background.	23
Figure 2.11 Concentration ratio	24
Figure 2.12 Ideal system efficiency as a function of receiver temperature. The dotted lines include the effect of convective heat losses (Lovegrove & Wes, 2012)	25

Figure 2.13 Solar-only (left) and Solar-hybrid (right) system configurations	27
Figure 2.14 typical performance of a hybrid system in an ideal (left) and cloudy (right) day (Spelling, 2013).....	28
Figure 2.15 representative of the performance curve generated from empirical equation used to evaluate the engine efficiency in off-design conditions (Gallup & Kesseli, 1994).....	31
Figure 2.16 Microturbine cost (Purchased Equipment Cost) given by Park et al. model.	37
Figure 3.1 General structure of the computational model.....	42
Figure 3.2 single shaft recuperated micro-gas turbine cycle.....	45
Figure 3.3 centrifugal compressor stage, Mollier diagram (left) and schematic (right) (Dixon & Hall, 2010).....	46
Figure 3.4 radial turbine, Mollier diagram (left) and schematic (right) from (Dixon & Hall, 2010)	47
Figure 3.5 schematic of the recuperator	49
Figure 3.6 average annual solar irradiance in Italy between 2004 to 2010 (SolarGIS, 2011)	51
Figure 3.7 parametric study for the dish-MGT system for variation of cycle parameters	53
Figure 3.8 variation of TET in the same parametric study as Figure 3.7	54
Figure 3.9 contours of dish area between the allowable limits of rotational speed and TET.....	55
Figure 3.10 centrifugal compressor map.....	57
Figure 3.11 β -lines on the compressor map	59
Figure 3.12 turbine performance maps, non-dimensional mass flow rate (left) and efficiency (right) against the pressure ratio	60
Figure 3.13 schematic of the CSP system components (parabolic dish and the receiver)	61
Figure 3.14 correlation for the pressure loss in a cavity receiver with $\pm 10\%$ deviation bounds. 63	
Figure 3.15 thermodynamic characteristics of the recuperator	64
Figure 3.16 pressure losses in the recuperator	65
Figure 3.17 system arrangement schematic in power generation mode.....	66
Figure 3.18 variation of net output power of the electrical system with electric current for different speeds. Current in electrical machines is proportional to the torque exerted by the load... 67	
Figure 3.19 overall efficiency of the electrical system	68
Figure 3.20 system performance for the variations of DNI. Dish-MGT system cannot deliver any positive power below a certain DNI.....	71
Figure 3.21 mass flow rate and speed of the MGT	72
Figure 3.22 variation of turbine's inlet and exit temperature with DNI.....	72
Figure 3.23 running line of the MGT for the full range of the variation of DNI	73

Figure 3.24 variations of DNI and corresponding system performance during a summer day, Casaccia.....	73
Figure 3.25 variations of DNI and corresponding system performance during a winter day, Casaccia.....	74
Figure 3.26 Annual solar irradiance and generated electricity for Casaccia and Seville	75
Figure 3.27 solar to electric efficiency of the dish-MGT system in Casaccia and Seville.....	75
Figure 4.1 variations of turbine inlet temperature when MGT operates at different constant speeds	80
Figure 4.2 variations of turbine exit temperature for different constant speeds.....	80
Figure 4.3 the net electric power output of the dish-MGT system when MGT operates in different speeds	81
Figure 4.4 overall efficiency of the dish-MGT system for operation of MGT in different constant speeds	81
Figure 4.5 variations of rotational speed for operation with different turbine inlet temperatures	82
Figure 4.6 turbine exit temperature for operation with different TITs.....	83
Figure 4.7 net electric power of the dish-MGT system when operated with different TITs.....	83
Figure 4.8 overall efficiency of the dish-MGT system for different turbine inlet temperatures .	84
Figure 4.9 DNI duration curve for Casaccia and Seville based on average annual insolation data. Data from (SoDa, 2016)	84
Figure 4.10 variations of the rotational speed for operation in different turbine exit temperatures	85
Figure 4.11 variation of turbine inlet temperature for constant TET operation strategy.....	86
Figure 4.12 variations of the net output power when MGT operates in different turbine exit temperatures	86
Figure 4.13 variations of the dish-MGT efficiency versus DNI for operation with different TETs	87
Figure 4.14 performance of the dish-MGT system when operated on fixed output power (a) PWe=3kWe, (b) PWe=4kWe and (c) PWe=5kWe.....	88
Figure 4.15 Comparison of annual generated electricity of the dish-MGT system when operated in different constant output powers in Casaccia, Rome, Italy	89
Figure 4.16 variation of mass flow rate for constant power operation.....	89
Figure 4.17 rotational speed and turbine temperature in MPP operation strategy for variations of DNI.....	90
Figure 4.18 system performance with MPP operation strategy for variations of DNI.....	91
Figure 4.19 control loops for MGT to run on the MPP strategy	92

Figure 4.20 single dish-MGT unit connected to a large power grid	93
Figure 4.21 modular arrangement of several dish-MGT units which can be to a large or local grid	93
Figure 4.22 schematic of EPCS. Generation mode is activated	93
Figure 4.23 control loops of the micro gas turbine	95
Figure 4.24 variations of proposed controlling parameters with DNI for MPP operation strategy	96
Figure 4.25 schematic of recuperation control for a recuperated cycle. Part of the flow is by-passed via port “B” of the three way diverting valves.....	98
Figure 4.26 performance of the dish-MGT system with the recuperation control strategy applied for DNIs above 900W/m ²	100
Figure 4.27 variations of speed, mass flow rate and inlet temperature of the receiver recuperation control applied for DNIs above 900W/m ²	100
Figure 4.28 reduction of the receiver inlet temperature when recuperation control strategy is applied	101
Figure 4.29 effect of recuperation control strategy on the efficiency of the system	101
Figure 4.30 rotational speed of the MGT. Constant speed is achievable as soon as the recuperation control is applied	102
Figure 4.31 generated power vs DNI. Recuperation control strategy allows for keeping a constant power output by fixing the TIT and speed through the control loops	102
Figure 4.32 annual generated electricity for different operation strategies (RC: Recuperation Control)	103
Figure 4.33 overall solar efficiency for different operation strategies	105
Figure 5.1 position of the system design point on a sample compressor map generated by scaling. Maximum efficiency point (X) appears in the middle of the line.	110
Figure 5.2 Pareto optimality.....	113
Figure 5.3 diagram of the optimisation framework.....	115
Figure 5.4 shares of the components costs in the total cost of the system designed for case study.	124
Figure 5.5 evolution of the optimisation results towards Pareto front	126
Figure 5.6 LCOE for the Pareto solutions.....	127
Figure 5.7 shares of the components in the total cost of the optimised system	128
Figure 5.8 Turbine inlet and exit temperatures for Pareto line designs.....	129
Figure 5.9 size of the components for the optimal design points	130
Figure 5.10 Pareto solutions for 5kWe dish-MGT in Seville.....	130

Figure 5.11 comparison of the performance indicators of the optimised designs for Casaccia and Seville.....	131
Figure 5.12 variation of LCOE with the total DNI income.....	131
Figure 5.13 cost of electricity for larger production volumes of a 5kWe dish-MGT system ...	132
Figure 5.14 components shares in the purchase cost of the optimal design for Casaccia	134
Figure 5.15 economic indicators (LCOE and C_{inv}) for optimised dish-MGT systems with different rated power from 5kWe to 30kWe	135
Figure 5.16 solar to electric efficiency and the size of the dish for the optimised designs	135
Figure 5.17 variations of LCOE with production volume for the optimised dish-MGT system	136

LIST OF TABLES

Table 2-1 specifications of the micro gas turbines in the market. All engines use single shaft recuperated configuration with radial turbomachinery.....	15
Table 2-2 reference: (Steinhagen & Trieb, 2004)	25
Table 2-3 main characteristics of different solar receiver technologies (Avila-Marin, 2011)	26
Table 2-4 constants in the modified forms of equations 2.6 and 2.7.....	37
Table 3-1 components parameters.....	52
Table 3-2 design point data for the case study of section 3.3.1 (DNI, 800W/m ²).....	56
Table 4-1 absolute accuracy of the electrical parameters for a typical inverter rated at 5kWe... 95	
Table 4-2 values of the proposed controlling parameters at the minimum and maximum DNI . 96	
Table 4-3 gain factor (rate) of the controlling parameters	96
Table 5-1 dish-MGT performance results for sample design points with different pressure ratios. Initial design point is shaded.	109
Table 5-2 dish-MGT performance results when the position of the design point changes on the compressor map.....	111
Table 5-3 coefficients of the economic model for the micro gas turbine.....	118
Table 5-4 specific cost of the micro gas turbine for two set of design data (Sánchez, 2015) ...	118
Table 5-5 cost of stainless steel recuperator and the corresponding multiplier	119
Table 5-6 maximum working temperature of the recuperator for different materials and the corresponding multiplier in respect to stainless steel (S/S)	119
Table 5-7 coefficients of the economic model for equation 5.19.....	121
Table 5-8 manufacturing cost of the solar dish as for different aperture sizes (Sánchez, 2015)121	
Table 5-9 manufacturing cost of the solar dish as for different aperture sizes (Sánchez, 2015)122	
Table 5-10 cost of the components for the case study system with net power output of 5kWe (design point).....	123
Table 5-11 problem setup to find optimal compressor design parameters.....	126

Table 5-12 specifications of minimum LCOE point on the Pareto front	127
Table 5-13 performance data for the selected points on Pareto front.....	128
Table 5-14 real interest rates for Italy and Spain for three consecutive years (World Bank, 2016)	131
Table 5-15 specifications of the optimal design of the MGT for Casaccia and Seville	132
Table 5-16 problem setup to find optimal compressor design parameters.....	133
Table 5-17 performance specifications of the optimal design for Casaccia.....	134

NOMENCLATURE

Greek Symbols

α	Capital recovery factor
α_{recv}	Absorptivity of the receiver
β	Auxiliary coordinate for compressor map
γ	Specific heat ratio
ε	Effectiveness
ϵ_{recv}	Emissivity of the receiver
η	Efficiency
η^*	Non-dimensional efficiency
η_{cycle}	Micro gas turbine's cycle efficiency
η_e	Electrical efficiency
η_{solar}	Solar to electric efficiency
μ	Viscosity
π	Pressure ratio
ρ	Density
σ	Speed ratio for the compressor map
$\varphi_1, \varphi_2, \dots, \varphi_n$	Weight factors for objective functions
Ω, ω	Rotational speed (rad/s)

Roman Symbols

A	Area
A_r	Aperture area of the receiver
A_{conc}	Aperture area of the concentrator
$a_{Dish}, \dots, c_{Dish}$	Coefficients of production volume for dish
$a_{Dish,A}, \dots, c_{Dish,A}$	Coefficients of cost function for dish

a_{MGT}, \dots, c_{MGT}	Coefficients of production volume for MGT
$a_{MGT,m}, \dots, c_{MGT,m}$	Coefficients of cost function for MGT
$a_{recv}, \dots, c_{recv}$	Coefficients of production volume for receiver
$a_{recv,q}, \dots, c_{recv,q}$	Coefficients of cost function for receiver
a_w	Cost of water per cubic meter
C	Total cost
c	Specific cost, coefficients in cost functions
C_{eq}	Cost of equipment
C_{inv}	Cost of investment
C_{min}	Minimum heat capacity rate in recuperator
C_p	Specific heat
C_r	Ratio of the minimum and maximum heat capacity rates
CR_g	Geometrical concentration ratio
CR_{opt}	optical concentration ratio
D	Characteristics diameter of turbomachinery
DNI_{an}	Annual solar irradiance
ΔDNI	Minimum variations of DNI for power regulation control
dp/p	relative pressure loss
E_{an}	Annual generated electricity
Err	Absolute accuracy of electrical parameters for inverter
F	Matrix form of system equations
f	Components' characteristics functions, scaling factors
f_{aux}	Production volume factor for auxiliary equipment
f_{Dish}	Production volume factor for dish
f_{MGT}	Production volume factor for MGT
f_{recv}	Production volume factor for receiver
h	enthalpy
Δh_{0s}	Isentropic change of enthalpy
I	Electric Current, radiation
i	real interest rate
I_b	Beam or Direct Radiation
I_d	Diffuse Radiation
I_{sc}	Solar constant
J	Jacobian matrix of system equations
j	Imaginary number

k_{HSA}	Loss factor of the high speed alternator
k	Gain factor for controlling parameters
k_{recp}	Coefficient of the cost of recuperator
L	Production volume rate (units/year)
L_{12}	aerodynamic losses in turbine or compressor
\dot{m}	mass flow rate
\dot{m}_l	Leakage mass flow rate
N	Rotational speed (rpm)
N^*	Normalised speed
N_s	Specific speed
N_X	rotational speed of maximum efficiency point (X)
NTU	Number of transfer units
p	pressure
PM	Profit margin
PW	power
PW_l	Electrical power losses of the high speed alternator
PWe	Electric power output
PWe^*	Normalised electric power output
q	Solar heat
Q	Volume flow rate
Q_{12}	transferred heat in turbine or compressor
q_H	Input heat to the MGT
q_{recv}	Input heat to the receiver
R	Universal gas constant
Re	Reynolds number
RH	Relative humidity
R_{HSA}	Winding resistance of the high speed alternator
R_{rec}	Resistance in rectifier
R_{recp}	Correction factor for advanced recuperator
SM	Surge margin
T	Temperature
t	number of years of operation
T_{sky}	Sky temperature
TET^*	Normalised turbine exit temperature
TIT^*	Normalised turbine inlet temperature

U	Heat transfer coefficient
V	Voltage
$W_{net}, PWSD$	Net power delivered by the shaft
\mathbf{X}	Matrix form of unknowns in system equations
x	By-pass ratio in recuperation control
X_{HSA}	Reactance losses in high speed alternator

Subscripts

01-06	Cycle stations (total thermodynamic properties)
a	Adiabatic process
amb	Ambient
an	Annual
aux	Auxiliary equipment
aux, m	Manufacturing costs, auxiliary equipment
$c, cold$	Recuperator cold side
$c, comp$	Compressor
$civil$	Civil work expenses
$comm$	Commissioning expenses
cnt	Control system
$conc$	Concentrator (dish)
d	Non-adiabatic process
$dish$	Parabolic dish concentrator
$dish, m$	Manufacturing costs, dish
dp	Design point
dp, map	Design point properties for scaling
$entry$	Compressor's inlet
eq, m	Manufacturing costs, equipment
h, hot	Recuperator hot side
I	Parameters in electric current regulation control
i	Inlet
$inst$	Installation expenses
inv	Inverter
$maint$	Maintenance expenses
map	Performance map parameter
max	Maximum allowable limit

<i>mech</i>	Mechanical
<i>MGT, m</i>	Manufacturing costs, MGT
<i>o</i>	Outlet
<i>op</i>	Operation expenses
<i>opt</i>	Optical
<i>PW</i>	Parameters in power regulation control
<i>R, map</i>	Reference map properties for scaling
<i>rec</i>	Rectifier
<i>ref</i>	Reference (map or data)
<i>recp</i>	Recuperator
<i>recp, m</i>	Manufacturing costs, recuperator
<i>recv</i>	Solar receiver
<i>recv, m</i>	Manufacturing costs, receiver
<i>s</i>	Isentropic process
<i>surge</i>	Surge line parameters
<i>t, tur</i>	Turbine
<i>ts</i>	Total to static
<i>V</i>	Parameters in voltage regulation control
<i>w</i>	Water cost

Abbreviations

CHP	Combined heat and power
CPV	concentrated photovoltaic
CSP	Concentrated solar power
CST	Concentrated solar thermal
DNI	Direct normal irradiance
DOF	Degree of freedom
GA	Genetic algorithm
HSA	High speed alternator
HSG	High speed generator
HTF	Heat transfer fluid
IDP	Initial design point
INV	Inverter
ISA	International standard atmosphere
ISO	International organisation for standardisation

LCOE	Levelised cost of electricity
LFR	Linear Fresnel reflector
MGT	Micro gas turbine
OMSoP	Optimised Microturbine Solar Power
PV	photovoltaic
PWSD	Deliverable shaft power
REC	Rectifier
RECP	Recuperator
RECV	Solar receiver
RC	Recuperation control
SOFC	Solid oxide fuel cell
TET	Turbine exit temperature
TIT	Turbine inlet temperature

1 Introduction

1.1 Solar power generation

The energy from one hour of solar irradiance received on Earth is enough to cover global energy demand for one year (Fiedermann, et al., 2012). This interesting potential has motivated numerous research and global development plans for the deployment of solar energy systems as one solution to growing energy demands and environmental concerns. In the energy perspective plan of the European Commission (Hewicker, et al., 2011), it has been recommended to elevate solar electricity production to 12TWh in 2030 and to 42TWh in 2050. Compared to 1990, this is expected to result in the reduction of CO₂ production in the power sector in Europe by 60% in 2030 and 95% in 2050. The two main technologies predicted to dominate solar power production are photovoltaic (PV) panels and solar thermal systems. PV systems entered the market earlier and are successfully used in individual domestic units and larger scale distributed generation systems thanks to their low cost. However, except for concentrated photovoltaic (CPV) cells which are still in the laboratory stage, they have low solar to electric efficiencies and also low power density (area required per unit power). Concentrated solar thermal (CST) systems coupled with efficient thermodynamic cycle engines provide reasonably higher power density and efficiency. As such, they have the potential to be used in distributed power generation applications. The need for exploitation of these systems has opened a wide field of research and development to improve the techno-economic performance of such systems. The solar power production by such systems is predicted to contribute between 7% and 25% of the global electricity production by 2030 and 2050 respectively (Richter & Teske, 2009). It is worth noting that a wider term, concentrated solar power (CSP) includes not only the CST systems, but also the concentrated PV (CPV). Because the main focus of the current thesis is not on the PV systems and CSP is often used synonymously as CST systems, both terms have been used equally in this work.

1.2 Concentrated solar thermal power

The main CST technologies are shown in Figure 1.1. Parabolic troughs use reflective surfaces with a parabolic shaped cross section which produces a linear concentration on a receiver tube where a heat transfer fluid (HTF) can be heated up to 390°C. Because of their low concentration ratio (the ratio of trough's aperture area to projected area of the tube) which is typically below 80, they normally work even in lower temperatures. The HTF is used to convey the thermal power to the point of use which can be a power production, chemical process or direct heating application. Parabolic troughs and heliostat fields have been used in combination with Rankine, Brayton or combined thermodynamic cycles between 100kWe and 80MWe (Lovegrove & Wes, 2012).

Central receiver tower systems receive the concentrated solar radiation from an array of heliostats which are large mirrors. They have much higher concentration ratios than parabolic troughs; typically between 300-1000, and may achieve temperatures as high as 900°C in a fixed solar receiver mounted at the top of the tower. Central tower systems become economically advantageous above 10MWe installation. However, installations exist from 250kWe to 110MWe (Steinhagen & Trieb, 2004).

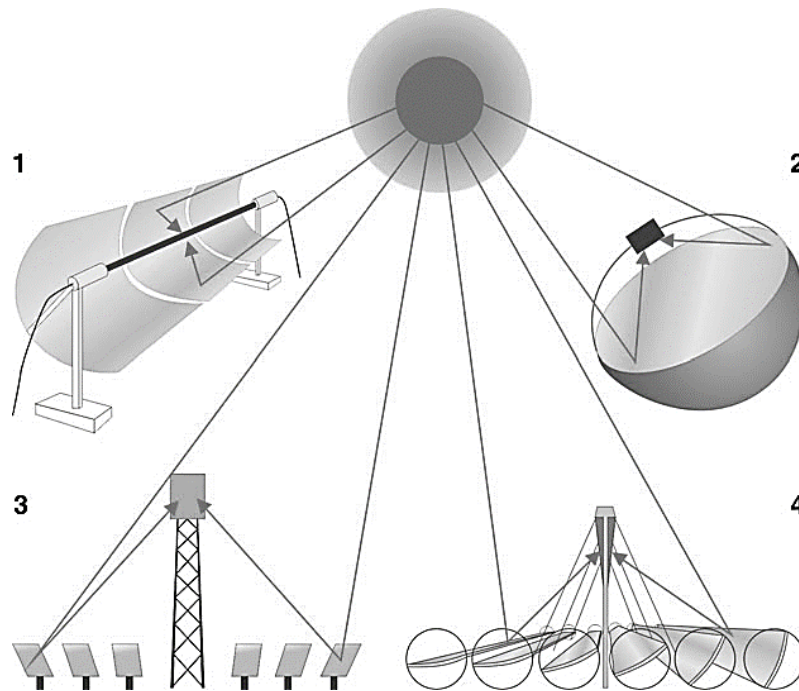


Figure 1.1 CST systems: (1) parabolic troughs, (2) parabolic dishes, (3) heliostat fields with central tower and (4) linear Fresnel reflectors (Lemus & Duart, 2012)

Similar to parabolic troughs, linear Fresnel reflector (LFR) systems focus on a line where a downward facing receiver is mounted. Compared to troughs, the receiver in LFR systems is a

cavity facing the ground which helps to prevent the convection losses. Linear Fresnel reflectors can achieve up to 450°C and are commonly used in plants of a few megawatts.

Parabolic dish systems reflect direct beam radiation to a focal point where a solar receiver is mounted, and can reach temperatures of over 1000°C. Parabolic dish systems have very high concentration ratios; typically between 1000-3000, and with two axis tracking are able to face the sun with their full aperture and avoid the so called ‘cosine loss effect’ which is a common problem in other CSP technologies. As a result, they currently offer the highest potential optical efficiency in converting solar to thermal energy among the CSP technologies. Each dish system is able to work as a self-contained power generation system which allows these systems to be used either as a single unit with a few kilowatts power rating or as modular units assembled together to generate larger powers. For such assembly of modular units, it is suggested that systems with maximum total power rating of 10MWe can be economic (Schiel & Keck, 2012).

An early application of concentrated solar power for the electricity generation was proposed using an individual turbine to generate 2 to 10kW power with low temperature mono-chloro-benzene as the working fluid (Tabor & Bronicki, 1963). However, the initial surge in research on CST technologies took place in the mid-eighties in the hope of developing alternative energy resources, but slowed down in 1995 because of low oil prices. However, after climate change became a decisive factor in the global energy agenda for the future, and the international acceptance that despite the fluctuations, the fossil fuels prices generally follow an increasing trend, concentrated solar thermal technologies have experienced a resurgence of research and development. It is acknowledged that CST is a technology which can quickly cut a large amount of the greenhouse gas emissions and has the potential to increase dispatchability via the integration with thermal storage systems. For parabolic dish systems there is particularly a hope to reduce the cost of the technology through recent technical improvements and also by mass production of the modular units. The combination of such systems with Stirling engines has been studied before. A schematic of these engines is shown in Figure 1.2.

Stirling engines are externally fired engines; similar to Brayton engines, which makes them suitable to work with solar heat. The system works on a closed thermodynamic cycle which uses a gaseous working fluid, usually Hydrogen or Helium, at 600°C to 800°C. The Stirling cycle includes two isothermal compression and expansion processes which are completed by two constant volume heat transfer processes from the cold (ambient) and hot (solar receiver) sources. Stirling engines can achieve reasonably high efficiencies close to 40%, but suffer from complexity and relatively expensive maintenance. Besides, their specific costs are higher than Brayton

engines which can be similarly coupled with parabolic dishes and have proved to be unreliable for distant installations (Schiel & Keck, 2012).

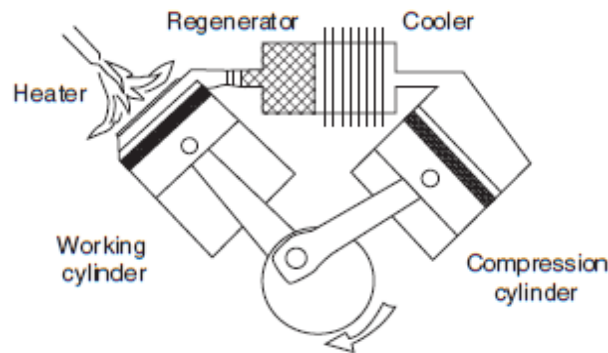


Figure 1.2 Schematic of piston Stirling engine (or so called 'kinematic Stirling') and its components (Schiel & Keck, 2012)

A suitable alternative is a micro gas turbine (MGT) which utilises the Brayton cycle. Reliability, good power density, lower cost and ease of maintenance are considered as the important advantages of micro gas turbines compared to Stirling engines (Neber & Lee, 2012). These engines also have the advantage that the hot exhaust gas can be used in combined cycles and Combined Heat and Power (CHP) systems. However, in their roadmap to enter the renewable energy market, dish-MGT systems require further research and development, particularly to reduce the ultimate cost of the system while at the same time ensuring that a higher overall solar to electric efficiency is achieved.

1.3 The OMSoP project

Optimised Microturbine Solar Power (OMSoP) is an EU funded project under the seventh framework programme (FP7) which started in 2013. The main goal of OMSoP is to provide and demonstrate technical solutions for the use of state-of-the-art dish-MGT systems to produce electricity in the range of 3-10kWe. This power range covers the electric power demand of domestic and small commercial applications. A schematic diagram of OMSoP system and the final system assembly are shown in Figure 1.3 and Figure 1.4 respectively. The main focus in OMSoP project is on the so-called pure solar (or solar-only) dish-MGT systems which are only powered by the solar energy.

The main vision of this project is to develop innovative concepts that can improve the solar to electric efficiency and improve operability in relation to solar energy short time fluctuations. The optimised solar dish-MGT system will then have the potential to replace Photovoltaic and solar dish-Stirling engine systems in the target power range. OMSoP is structured as a consortium of seven contributors including City, University of London as the scientific coordinator of the whole

project who also lead the design, development and testing of the micro gas turbine. Two other major components in the whole system, the solar receiver and dish concentrator, are designed and developed by the Royal Institute of Technology (KTH) in Stockholm and Innova in Rome respectively. Ultimately, system assembly and test is done by ENEA in Casaccia, near Rome. Three other contributors of the project, University of Roma3, University of Seville and Compower in Stockholm, collaborate in the analytical investigation on the concepts related to the visions of the project including integration of thermal storage, cost analysis and marketing study.

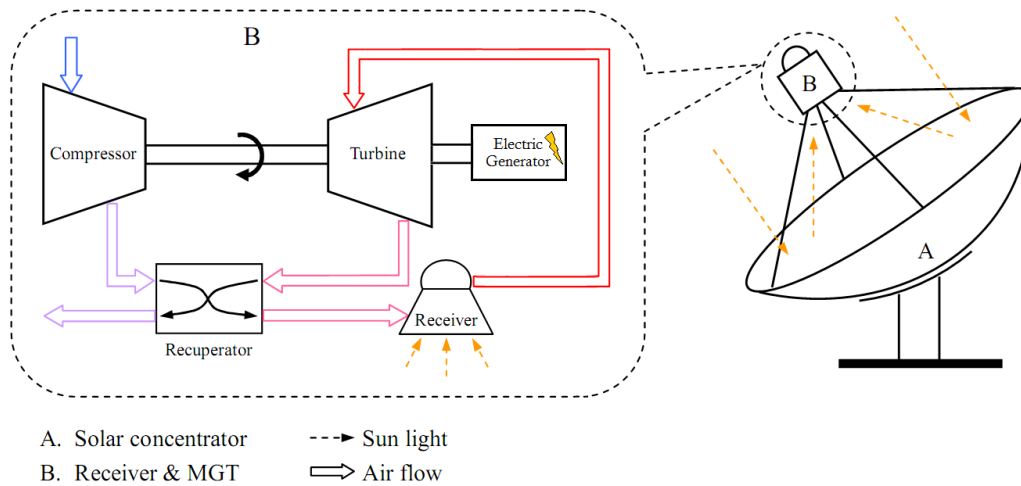


Figure 1.3 Schematic diagram of the system (OMSoP, 2013)



Figure 1.4 dish-MGT system installation of OMSoP project in Casaccia

The present thesis is part of the design and development of the micro gas turbine in City. Cycle analysis of the micro gas turbine is done to allow for the determination of component design parameters which are then designed by other colleagues within the City team. Further analysis on the optimisation of the dish-MGT systems to investigate their potential in achieving competitive thermo-economic performance is accomplished afterwards. For this purpose, control strategies to deal with the fluctuations of solar irradiance are also suggested and applied in the performance simulation of the system. Figure 1.5 shows the developed micro gas turbine in City on the test rig for a cold test.

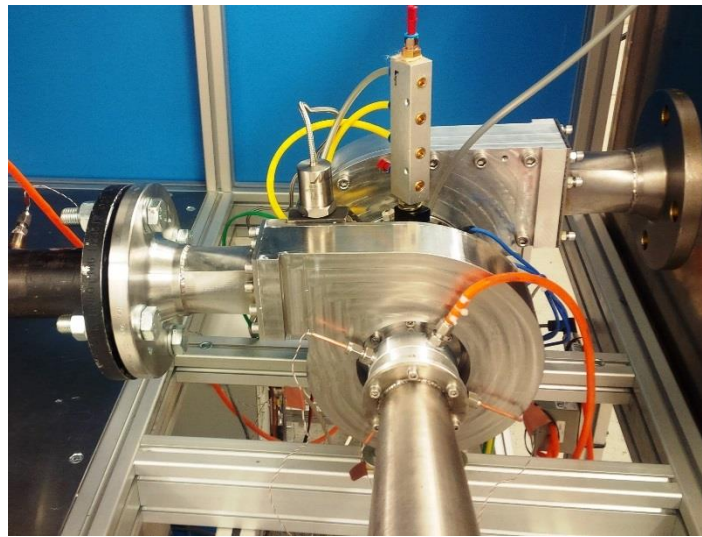


Figure 1.5 The micro gas turbine which was designed and developed in City University for OMSoP

To achieve a small-scale, cost effective, efficient and reliable dish-MGT system, some technical issues must be addressed during the project. Micro gas turbine and optical components, including the parabolic dish and the solar receiver must be developed. Development of the MGT is the responsibility of the technical and research team at City. Although gas turbines are well known for their reliability and power density, downsizing these machines brings about some technical challenges in terms of cost and performance. While in large turbines blade cooling allows inlet temperatures as high as 1600K, this is not a feasible option in small MGTs limiting the maximum temperature to between 1200K and 1300K which directly affects the thermodynamic efficiency. Besides, to attain pressure ratios higher than about 3.5, more sophisticated architectures than single shaft recuperated engines are required which increases the complexity, cost and introduces maintenance issues. The aerodynamic efficiencies of the small compressor and turbine are also affected by the relative dimensions of the applicable gaps and clearances to the size of these machines. On the other hand, more advanced materials and manufacturing technology which result in more efficient and more expensive MGT can become more cost effective because it results in smaller dish. This is also true for the optical components of the system including the

dish which can be slightly more expensive and efficient, but with smaller size. Clearly, a trade-off can be made between the main important design parameters of the system to achieve competitive cost and thermodynamic performance.

1.4 Solar powered micro gas turbine research

A micro gas turbine is usually designed to work in a regenerated (recuperated) Brayton cycle which is shown schematically in Figure 1.6. Air enters the compressor where its pressure and temperature increase in a compression process. The temperature increases further by recovered heat from the turbine exhaust flow using a recuperator. This reduces the amount of heat which the solar receiver should provide to the cycle to achieve a certain temperature before the turbine. Power is generated by the expansion process in the turbine which drives the compressor and a high speed generator (HSG).

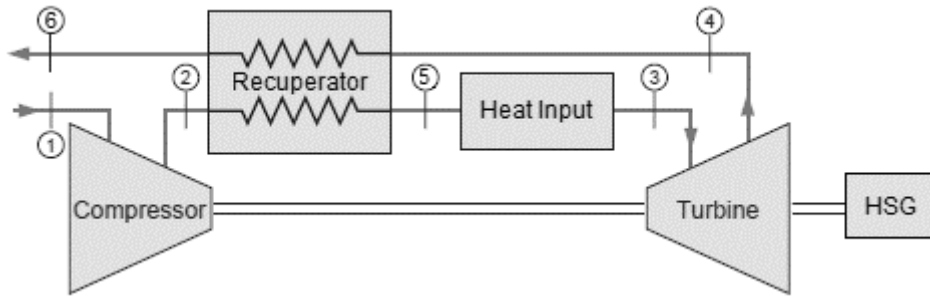


Figure 1.6 Recuperated Brayton cycle (Borgnakke & Sonntag, 2009)

The overall efficiency of the cycle is defined as the ratio of the net generated electric power, W_{net} to the total input heat, q_H as shown in eq. 1.1.

$$\eta_{cycle} = \frac{W_{net}}{q_H} \quad 1.1$$

Several conflicting technical and economic parameters contribute in the design of the system which determine this efficiency and are studied in detail in the next chapters. Generally, it can be said that the efficiency increases with the turbine inlet temperature and components efficiencies, which are corresponding to higher costs. For large power generation gas turbine engines which provide the base load, the design conditions which lead to maximum efficiency for a nominal output power, are chosen for the design point of the system because such systems work almost always at this point. The fuel flow is generally constant and the system generates maximum electricity by operating at the maximum efficiency point. For solar powered gas turbines, the heat input into the system is provided by solar irradiance received at the concentrator and its nominal value is determined by the design point which is then used for the design of the optical

components. However, solar powered systems face some challenge as the actual input energy that reaches the solar concentrator is directly affected by the climate conditions, and in the majority of the operation time, is different from the nominal value. Figure 1.7 shows that the insolation value varies significantly during four sample dates of a year. These variations will affect not only the thermodynamic performance of the system and the annual generated electricity, but also the cost of the electricity which is generated by the system.

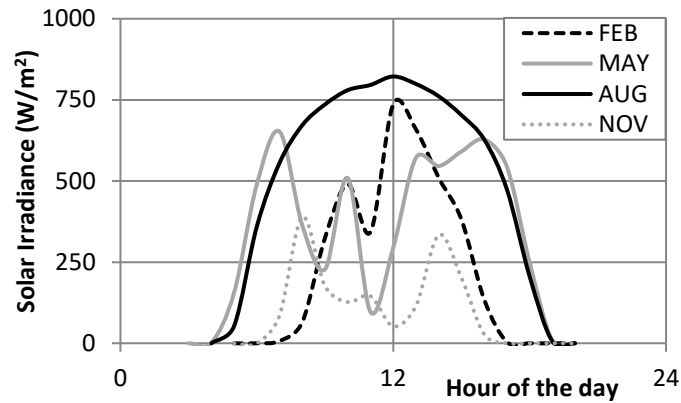


Figure 1.7 hourly variation of the solar irradiance for Cassacia (Italy) for the beginning days of sample months. Solar data from (SoDa, 2016)

To bring the solar-only dish-MGT systems to their maximum potential and make them a thermo-economic competitive option for harnessing solar energy in small-scales, two issues must be addressed. The first problem is that variations of solar irradiance inevitably moves the MGT to off-design conditions. Having considered that the maximum achievable efficiencies of the components in the system is limited by the state of the art technology, an idea which is focused on in this work is to alter the design point of the system so that the overall performance of the system over a wide range of insolation improves. This may result in lower efficiency at the design point, but solar powered MGTs mostly work in off-design conditions. The second issue which must be considered is that the operation strategy of the microturbine also affects its performance. An operation and control strategy which is practical and allows for maximum power production must be found. The main point here is the possibility of controlling the electrical load by a sophisticated control system rather than conventional control strategies which are based on following the variations of the load. Nevertheless, this requires studying the system performance under different system control schemes.

1.5 Aims and objectives

The aim of this work is to investigate and develop modelling methods which can be used for thermodynamic and economic analysis of the performance of solar-only small scale dish-MGT

systems in order to find an optimised design of the system. Fluctuations of solar irradiance have significant effects on the performance of solar-only systems. Dealing with these effects, and achieving an optimised design, requires specific modelling and analysis tools to be developed and used. The specific objectives of this project are set as follows:

- To design and implement a dish-MGT design tool that builds on component performance map generation models with minimum required information and analyse the system performance over the course of variations of solar irradiance more realistically
- To investigate control strategies for micro gas turbines and develop a control strategy to achieve maximum power generation and avoid technical damage in extreme working conditions
- To design a method to analyse and evaluate optimal values of key parameters in solar powered micro gas turbines which result in optimised techno-economic performance by combining optimisation techniques and realistic performance calculation

Ultimately, it is expected that a number of contributions to the engineering science community will be made through the completion of this work and meeting the above objectives in terms of the design and analysis methods for the pure solar powered micro gas turbines.

1.6 Structure of the thesis and scientific contributions

This thesis consists of six chapters which represent the progression of this research project. Followed by the present introduction, a comprehensive literature review on the key concepts and previous research which are related to this work is presented in Chapter 2. In the beginning, the application of micro gas turbines in the power generation sector, concentrated solar thermal systems and the previous research on the combination of micro gas turbines and CST systems including the technical and economic key points are thoroughly reviewed. The next sections in chapter 2 cover thermodynamic and economic modelling of micro gas turbines and the concept of optimisation methods applied for such systems. The outcomes of chapter 2 are the key conclusions that reinforce the project objectives and provide the required technical and scientific knowledge in the next chapters.

Chapter 3 is dedicated to the thermodynamic modelling of the dish-MGT systems. A component based system simulation tool is developed for this purpose during the progression of the present thesis which can perform both design point and off-design performance calculations. To conform to the objectives of the present thesis, the tool is designed with a separate module which can generate the performance maps of the system components with minimum required information and apply any operation strategy for the dish-MGT system which is chosen by the user. This is

an interesting feature brought to the dish-MGT research community which allows for more realistic system performance calculation before the detailed design of components is even attempted. A case study based on the specifications of the dish-MGT system, designed for the OMSoP project, is used to demonstrate the methods implemented in the simulation tool.

Having established the system performance model, control and operation strategies which can be applied on the micro gas turbine have been studied in Chapter 4 to propose suitable strategies which result in maximum power generation by the system. The control strategy of the system is suggested based on the important point that the input heat to the system cannot be controlled like the fuelled micro gas turbines. Therefore, a control strategy which is based on the load control is proposed and used in the system performance modelling. This is an interesting contribution to the research community as it introduces a means of control where the main controlling parameter in the micro gas turbine (i.e. fuel mass flow rate) is absent. The operation strategy for the system is also studied in this chapter based on two distinct applications. A novel concept has been developed here which allows the dish-MGT system to generate constant power with a constant rotational speed while the solar irradiance varies. This developed concept presents a significant contribution to the solar powered MGT community and a paper is published based on this work. The comparison of system performance under the suggested operation strategies is accomplished at the end of this chapter.

For the dish-MGT system, low cost and high performance are not achievable at the same time. To realise the optimal key design parameters of the dish-MGT system which provide a reasonable trade-off between thermodynamic and economic performance of the system, optimisation techniques, an economic model and thermodynamic performance simulation tool which is developed in chapter 3 are brought together in chapter 5. With the method developed in chapter 3 to generate components performance maps with the minimum information and by the application of the operation strategy, a more realistic off-design performance is applied to the optimisation procedure which is a considerable contribution to the research community as the similar work in the past mostly used constant performance at the design point or used off-design performance correlations. The optimisation is done for two separate scenarios. The first scenario is focused on the base design case of the OMSoP project and comprises a multi-objective optimisation problem with the investment cost of the system and annual electricity generation as the objective functions. The second scenario extends the optimisation of the dish-MGT systems to the entire feasible range of dish-MGT installations. The outcome of the second scenario shows at which size the pure solar dish-MGT unit delivers electricity with minimum cost of electricity.

The interesting finding is that despite expectations, it is not the largest system size that delivers the minimum cost.

Final conclusions of this research are summarised in chapter 6. The outcomes of each chapter, especially chapters 4 and 5, are evaluated against the project objectives. Recommendations for further work in future research are provided afterwards.

1.7 Publications

Conference paper

Ghavami, M., Alzaili, J. & Sayma, A.I., 2017, June. *A Comparative Study of the Control Strategy for Pure Concentrated Solar Power Micro Gas Turbines*. In ASME Turbo Expo 2017: Turbomachinery Technical Conference and Exposition. Charlotte, American Society of Mechanical Engineers.

Conference poster presentation

Ghavami, M., Alzaili, J. & Sayma, A.I., 2016, October. *Optimisation of Pure Solar Small-Scale Micro-Gas Turbines*. In SolarPaces 2016. Abu Dhabi

2 Literature review

2.1 Introduction

The present review is aimed to develop an understanding of the subject of the thesis. The main attention is on the critical analysis of previous work, key parameters in the performance and design of the solar powered micro gas turbines and thermo-economic modelling of dish-MGT systems. Focus will be on the solar-only small scale systems although research on the hybrid systems is also reviewed for comparison and developing the concepts for this research. In the first part, research on the micro gas turbines is studied to examine their main design issues and review the work done to address these issues. In the second part, concentrated solar power systems and their coupling to micro gas turbines have been studied. Modelling of gas turbines is reviewed and capabilities of different engine models are discussed to find a proper modelling approach for the current work. A conclusion on the findings of this review is presented at the end where some decisions are also explained.

2.2 Micro gas turbines in power generation

2.2.1 Classification

It is about two decades since micro gas turbines have been introduced in the distributed generation market (Ferrari & Pascenti, 2011). Despite this relatively long period, there is no consensus on the classification for micro gas turbines. An almost widely used norm is based on the output power so that engines in the range of 2-200kWe are regarded as micro gas turbines (Leyes & Fleming, 1999). A rotor speed of about 100krpm and above has been also suggested (Rodgers, 2003) as a criterion, which originated from the fact that small gas turbines work at higher speeds compared to large engines. Nevertheless; as it will be seen later in this section, most of the built and tested engines reported are above 30kWe with rotational speeds as low as 70krpm.

2.2.2 Power generation

Micro gas turbines use the Brayton cycle with air commonly used as the working fluid. Ideal cycles includes isentropic compression and expansion processes (Figure 2.1). However, actual processes in the compressor and expander (turbine) involve aerodynamic losses and increase the entropy during compression and expansion processes. Assuming that the heat loss to the surroundings is negligible because of the high velocity of the flow, these processes can be considered to be adiabatic. Pressure loss along the other components of the gas turbine and the flow lines also affect the overall performance of the cycle. Figure 2.1 also shows a simplified representation of the actual cycle and its deviation from the ideal Brayton cycle. Nevertheless, it is still not a real representation of all the existing differences between real and ideal cycles as, for example, it doesn't include the effects of heat and flow leakages in the engine.

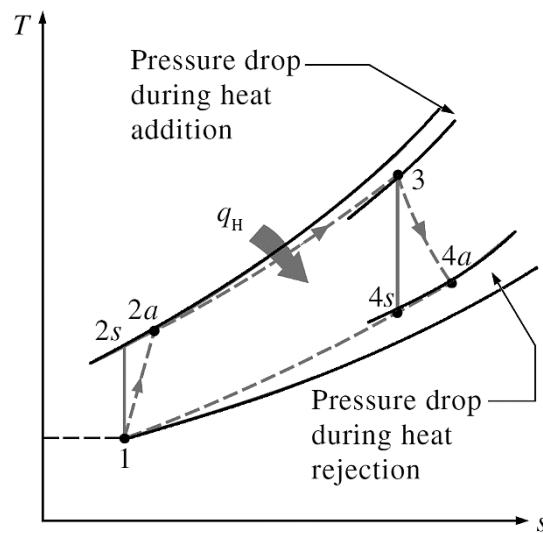


Figure 2.1 Ideal (1-2_s-3-4_s) and actual (1-2_a-3-4_a) Brayton cycles (Çengel & Michael, 2015)

The thermal efficiency of a gas turbine is defined as the ratio of the power delivered by the shaft, P_{WSD} , to the input heat, q_H , as shown by Eq. 2.1. To achieve higher efficiencies, most of the micro gas turbines are designed on a recuperated Brayton cycle configuration to recover part of the thermal energy in the turbine exhaust gases by a recuperator and reduce the required input heat. In Figure 2.2 the temperature rise from state point 2 to 5 shows the influence of the recuperator. For an ideal Brayton cycle the thermal efficiency only depends on the pressure ratio of the compressor (Saravanamuttoo, et al., 2009). In real gas turbines, efficiency depends on more and often conflicting factors like cycle arrangement, performance of all components and also compressor and turbine inlet temperatures.

$$\eta_{cycle} = \frac{W_{net}}{q_H} = \frac{(h_3 - h_4) - (h_2 - h_1)}{q_H} \quad 2.1$$

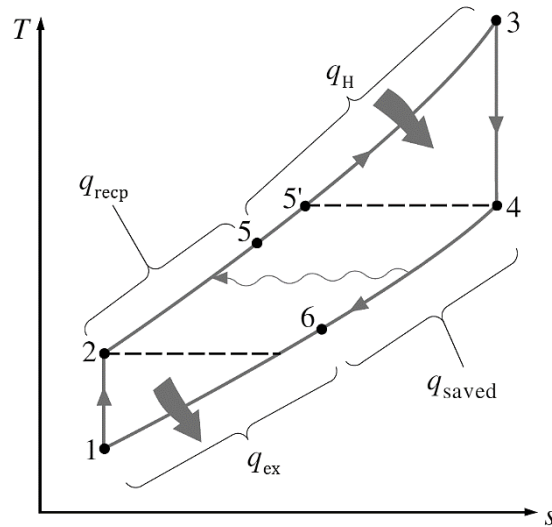


Figure 2.2 Ideal recuperated Brayton cycle. Input heat reduced because of the heat recovery (Çengel & Michael, 2015)

Development of micro gas turbines in power scales above 30kWe has been attempted several times with some engines successfully entered the energy market. Table 2-1 shows a number of micro gas turbines which have been introduced to the energy market. Smaller MGTs have been also attempted, but with less success.

Table 2-1 specifications of the micro gas turbines in the market. All engines use single shaft recuperated configuration with radial turbomachinery (do Nascimento, et al., 2013)

Model	Manufacturer	Output Power (kW)	η_{cycle} (%)	TIT (°C)	Speed (krpm)
C30	Capstone	30	28	870	96
TA 45	Elliot Energy	45	30	870	116
C65	Capstone	65	29	870	85
Parallon 75	Honeywell (AlliedSignal)	75	30	870	85
TA 80	Elliot Energy	80	30	870	68
T100-NG	Ansaldo (Turbec)	100	30 ± 2	950	70
TA 200	Elliot Energy	200	30	870	43
C200	Capstone	200	33	870	45
MT 250	Ingersoll-Rand	250	30 ± 2	900	45

A small MGT with power rating of 2.6kWe was introduced by NISSAN (later IHI) Company to the market which was not successful because of very low efficiency (Nakajima, 1995). Currently, there is no MGTs below 30kWe available in the market as a commercial product. The reason is mainly the specific cost of the machine (cost per unit output power) for smaller machines which

results in high cost of electricity. This high cost is because of many factors including higher cost of manufacturing per kW for smaller machines, and other system parameters which affect either the cost or performance (or both) such as maximum allowable temperatures in the components, aerodynamic losses in the small size turbomachinery, pressure loss (Rodgers, 2003) and flow or heat leakage (McDonald & Rodgers, 2008).

It is known that thermal efficiency increases with TIT as shown in Figure 2.3. However because blade cooling is presently not feasible in small microturbines, maximum inlet temperature in the turbine is limited by the material concerns (McDonald & Rodgers, 2008). Ceramic turbines have been studied and attempted in the past years, but there is still a long way to consider them as a practical solution (Vick, et al., 2010) and (Richerson, 2006). Pulsation induced to the flow by the combustion chamber, centrifugal forces, alternating forces due to rotor stator interaction and other factors such as hydrothermal degradation of ceramics may result in breakdown of the ceramic parts. Such circumstances have been observed several times during experimental research on small scale ceramic turbines (Iki, et al., 2007). A higher TIT also results in higher turbine exit temperature (TET) and consequently requires a recuperator which is made from more temperature resistant materials.

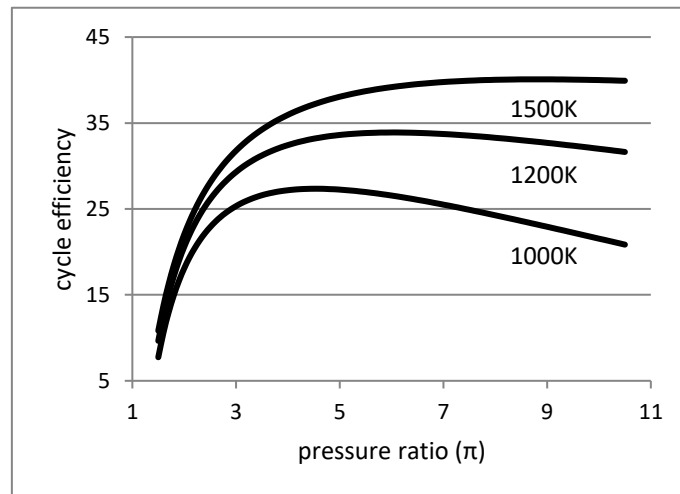


Figure 2.3 effects of TIT and pressure ratio on the efficiency of recuperated micro gas turbine (real cycle)

Figure 2.4 shows the interconnection between TIT, TET and pressure ratio in micro gas turbines and how the recuperator material determines maximum allowable TET. Higher TIT would be feasible with ceramic turbines, but it then requires more advanced materials for the recuperator to resist against the higher temperatures.

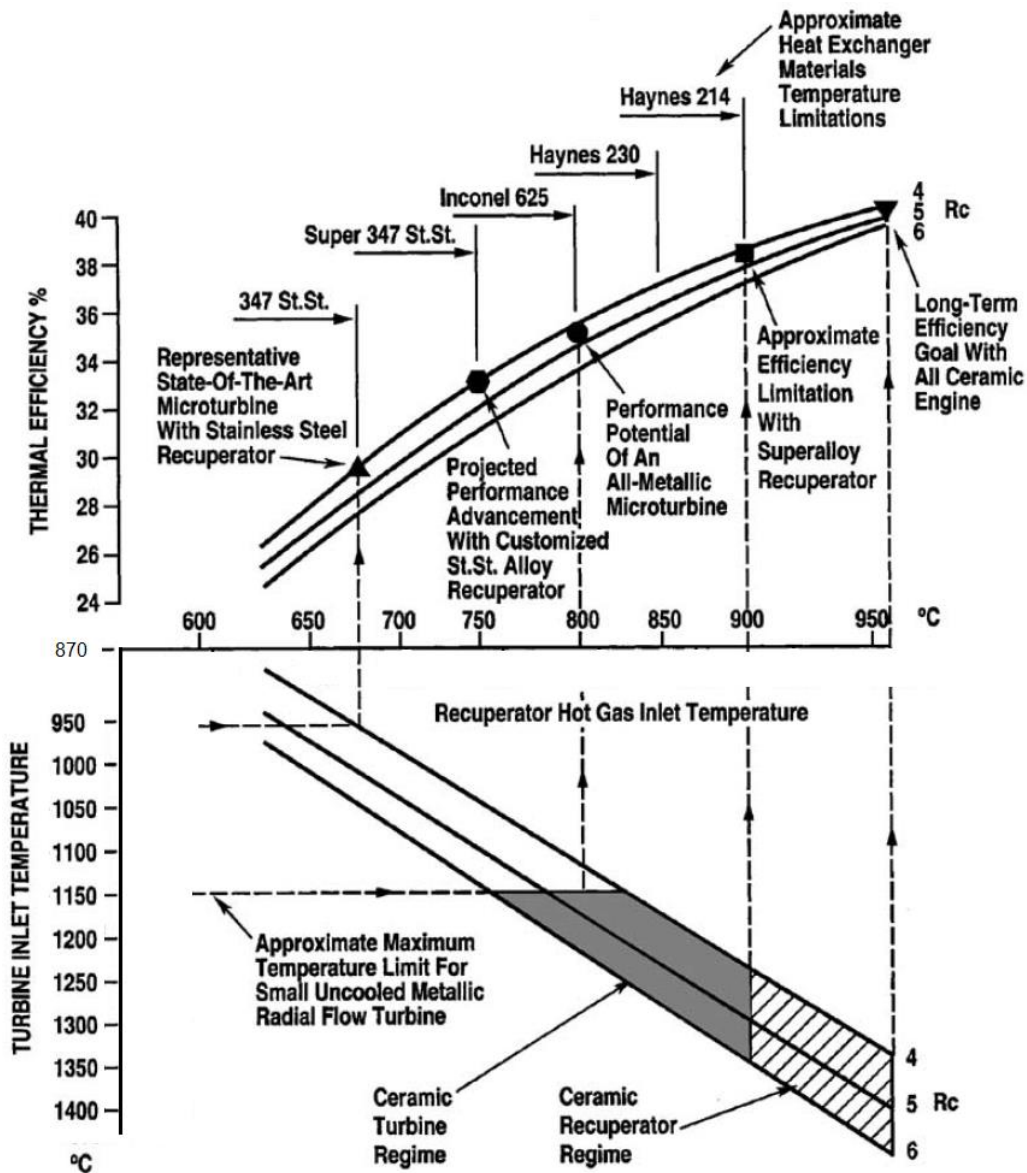


Figure 2.4 turbine and recuperator material requirements map for common range of TIT and compressor pressure ratio (R_c) in the micro gas turbines. Extracted from (McDonald, 2003)

The recuperator performance is defined by its effectiveness which is the ratio of recovered heat to the maximum possible heat recovery from the turbine's exhaust. Higher effectiveness increases the thermal efficiency of the MGT, but requires larger heat exchange area and as a consequence larger size and weight (Saravanamuttoo, et al., 2009).

High pressure ratio also requires higher rotational speed and cause the rotor dynamics, mechanical stresses and creep to become more critical. Multistage compression and expansion i.e. application of more than one compressor and turbine leads to lower pressure ratio of each component. The advantage would be lower design speed and consequently lower mechanical stresses. Intercooling between compressors and reheating between turbines can be introduced for such arrangements to

improve the efficiency. This will in turn increase the size, cost, complexity of the shaft arrangement and considerable pressure loss and there is still ongoing research in this direction. (Saravanamuttoo, et al., 2009). Nevertheless, advanced cycle configurations are continually studied and several theoretical and experimental studies have been done in this field. These conceptual designs are still far from being a feasible techno-economic solution for exploitation of small-scale micro gas turbines (Sadeghi, et al., 2006), (Poullikkas, 2005) and (Bianchi, et al., 2005). Currently, the single shaft recuperated Brayton cycle is the most common cycle configuration used for the micro gas turbines, as mentioned before.

There has been much research work on the application of turbochargers or turbocharger components in the development of small scale micro gas turbines. Such components are easily available at reasonable costs. However, they do not provide a suitable basis for micro gas turbine turbomachinery. To improve the efficiency of an MGT, a higher ratio of turbine to compressor tip diameter is needed compared to turbochargers (Rodgers, 2011). Visser et al. reported design and experimental test of a 3 kWe micro gas turbine system, which has been considered for combined heat and power (CHP) applications (Visser, et al., 2011). They used off-the-shelf turbocharger components to develop a recuperated cycle. However, they couldn't obtain efficiencies of more than 12.2% even for a turbine inlet temperature (TIT) as high as 1333K. Improvement in the efficiency of turbomachinery is possible by redesigning these components rather than using turbocharger parts. The efficiency of the mentioned 3kWe MGT was improved to 17.2% by redesigning the compressor and increasing its pressure ratio from 2.8 to 3 (Visser, et al., 2012).

Internal heat transfer is also among the issues which have a significant impact on the performance of small micro gas turbines. The heat transfer from the turbine to the compressor results in two unwanted effects which deteriorate the overall efficiency of an MGT. The temperature will rise at the compressor while it decreases at the turbine (Van den Braembussche, 2005). As a result, the compression and expansion processes will no longer be adiabatic. In the compressor, more work is required to reach the same exit pressure (i.e. equal pressure ratio) while the turbine will generate less power in a non-adiabatic expansion with the same pressure ratio. This is depicted in Figure 2.5. In this figure, L_{12} and Q_{12} are the aerodynamic losses and the transferred heat and points 2s, 2a and 2d represent the isentropic, adiabatic and non-adiabatic processes respectively. The area pertaining to L_{12} shows the required work by compressor or work done by the turbine in the case of adiabatic flow which only experiences aerodynamic losses. The additional area Q_{12} represents the added work required by the compressor or, on the right figure, the deducted energy from the turbine. The surface to volume ratio is also larger in small engines and the effects of heat

transfer on steady state and also transient performance become more significant (Visser & Dountchev, 2015). Gong et al. studied the impact of internal heat transfer on micro gas turbine performance by dividing the real compression into an isobaric heating and an adiabatic compression (Gong, et al., 2004). A different method approximates the diabatic compression and expansion to polytropic processes and finds the value of the corresponding polytropic power from the losses of the adiabatic processes and the heat transfer value (Van den Braembussche, 2005). The method of Gong et al. (Gong, et al., 2004) was adopted for a study to find out the reasons for the very low efficiency of NISSAN's 2.6kWe engine and it appeared that internal heat transfer effects contributed to over 21% of the power reduction (Monroe, et al., 2005). Rautenberg and Kammer have also proposed procedures to include the heat transfer in MGTs (Rautenberg & Kammer, 1984) in the simulation models.

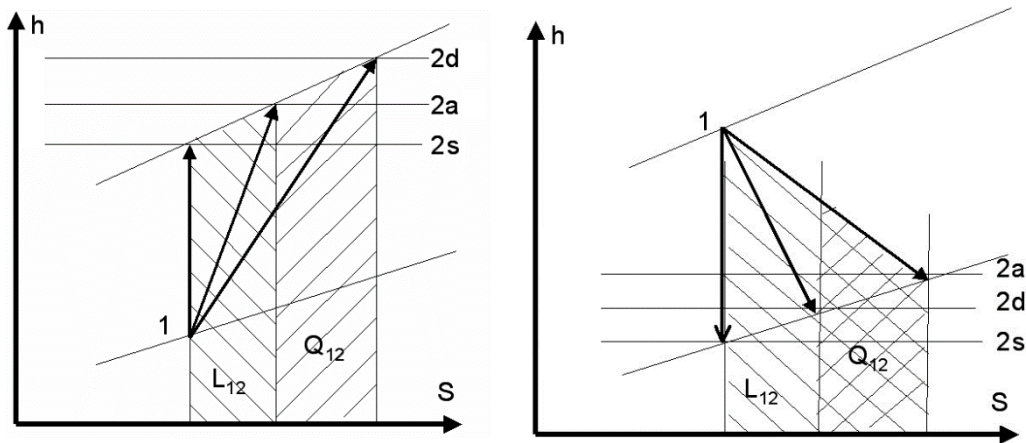


Figure 2.5 diabatic processes in compressor (left) and turbine (right). Adapted from (Van den Braembussche, 2005)

The aerodynamic, thermal and mechanical difficulties in the development of small MGTs limit the maximum efficiency. To increase the overall efficiency of the system, microturbines have been also used in combination with other cycles for co-generation. The main concept is to use the thermal energy in the hot exhaust gases of the microturbine. Costamagna et al. discussed a 50kWe MGT coupled with 240kWe solid oxide fuel cell (SOFC) hybrid system with the individual MGT having an electrical efficiency of 30% (Costamagna P, 2001). Simulations show that the electrical efficiency of the hybrid system could reach 60% at the design point and using an appropriate control strategy it would not fall below 50% at off-design conditions. Micro gas turbines have also been coupled with a bottoming lower temperature cycle, commonly a Rankine or organic Rankine cycle. Rosfjord et al. realised that using an organic Rankine cycle as the bottoming cycle for a 200kWe MGT, the electrical efficiency could be increased from 30% to 40% (Rosfjord, T., et al., 2008). A good potential for application of micro gas turbines which has been under

considerable attention is to use the thermal energy of the exhaust gases for heating in combined heat and power (CHP) systems. Overall system efficiencies of 47% and 59% have been achieved with 30kW and 65kW MGTs used as the prime movers for CHP units while their electrical efficiencies were only about 23% and 25% respectively (Energy Nexus Group, 2008).

It is important to notice that the performance data given in the literature such as the above-mentioned values are calculated at the design point. Commonly, the maximum efficiency of the engine is achievable at its design point. For most applications, the predominant operation condition of the engine during its life is considered for design point calculation (Walsh & Fletcher, 2004). Cycle parameters at the design point such as pressure ratio, TIT and component efficiencies are used for the initial design of the engine components. However, as soon as the working conditions deviate from the design point, off-design performance could be of very high importance. As such, in the design procedure of gas turbine engines, iterations must be done during the design process in which, the off-design performance of the engine is also considered (Saravanamuttoo, et al., 2009). A point which should be emphasised here is that in addition to the effects of working conditions, the performance of the gas turbine is also a function of the way that it is being controlled. A number of control strategies with different controlling parameters are used in gas turbines including constant TIT and speed (Traverso, 2004). For some applications with small micro gas turbines, low mechanical inertia of the rotor assembly and the possibility to control the load provide more controllability of the system. It has been found that with variable MGT speed, reasonable efficiencies even at very low part-load conditions can be achieved (Li, et al., 2013). Li et al. also reported improvement in part load efficiency by the application of speed control in addition to the fuel flow management.

2.3 Solar energy

Solar energy is the source of most renewable energy forms that are available on Earth. In addition to solar thermal, the hydropower, ocean, wind, biomass and biofuels energies are all generated from solar energy. Only tidal energy initiated from gravitational forces and geothermal energy are regarded as non-solar renewable resources with a total potential of 33 terawatts compared to 120×10^3 terawatts from solar radiation resources (Twidell & Weir, 2015). This huge amount of energy is provided from the radiation of the photosphere, the uppermost layer of the sun which is regarded as a blackbody radiating at a surface temperature of about 5777K. The extra-terrestrial solar flux which reaches just outside the Earth's atmosphere is about 1367W/m^2 and is called the solar constant (I_{sc}). Passing through the atmosphere, this value reduces because of the absorption and reflection by the air molecules, dust particles and also the clouds coverage, generally called climate conditions. The radiation angle has a significant effect on scattering and reduction of the

solar flux because it determines the distance that solar radiation must pass the atmosphere to reach the Earth's surface.

It is important to define the specific terms used in solar energy science, Irradiation, Irradiance and Insolation. **Irradiation** is the amount of solar energy received on a surface per unit area (J/m^2), while **irradiance** is the rate of irradiation and is given in W/m^2 . Irradiation can be calculated by integration of irradiance over a specified time, usually an hour or a day. The terms **insolation** and irradiation are interchangeably used in solar energy applications although irradiation is a more general concept that applies to any form of radiant energy. The solar irradiance arriving on Earth is a composed of two components as shown in Figure 2.6 and are defined below:

- Beam or Direct Radiation which is received without being scattered (I_b)
- Diffuse Radiation which is scattered by the atmosphere (I_d)

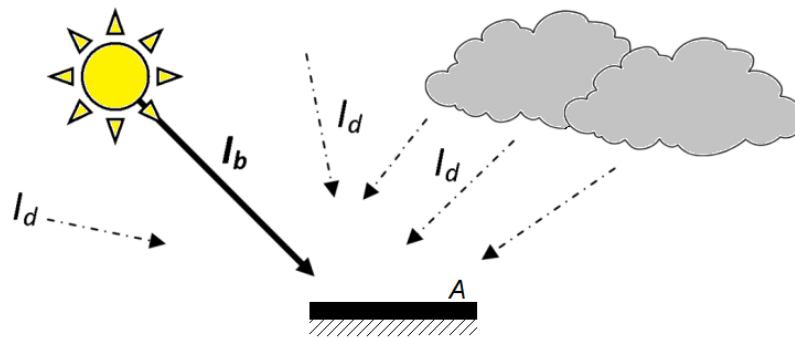


Figure 2.6 beam and diffuse solar radiations

The beam component of irradiance received per unit area of a surface perpendicular to the direction of radiation is known as direct normal irradiance (DNI) given in W/m^2 . For a surface which is not perpendicular to the radiation, the effective value will be reduced according to the cosine of the incident angle effect as explained by Figure 2.7. The diffuse radiation; on the other hand, does not depend on the angle of the surface.

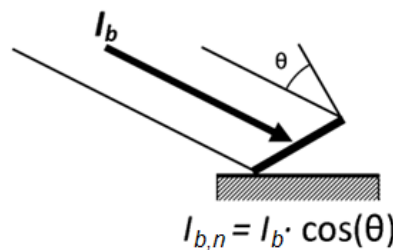


Figure 2.7 cosine effect in direct radiation

Photovoltaic systems and solar panels can collect the solar radiation in all directions and therefore can make use of both radiation components. Solar concentration systems are required to precisely

redirect the sun rays to a receiver and consequently cannot use the diffuse radiation as it reaches the concentrator in various direction. Therefore, only regions with high DNI are attractive for CSP systems.

Not only DNI is a function of latitude and position of the Sun with respect to the location of study on Earth, it is also highly dependent on cloud coverage and atmospheric conditions. As a result, DNI value at any specific point on Earth is a considerably variable quantity. Figure 2.8 shows the variations of DNI during a whole year from January to December for Casaccia in Italy where the OMSoP dish-MGT is installed and will be tested. Because the performance of solar power systems is directly related to DNI, variations of this value bring about an important challenge to these systems.

Data for DNI are provided by several meteorological centres and stations along with other climate parameters such as humidity and temperature in hourly basis and high resolutions. Two main references which are used in the present thesis are SolarGIS databank (SolarGIS, 2016) and SoDa services (SoDa, 2016). Data that were used to generate Figure 1.7 and Figure 2.8 were taken from SoDa service.

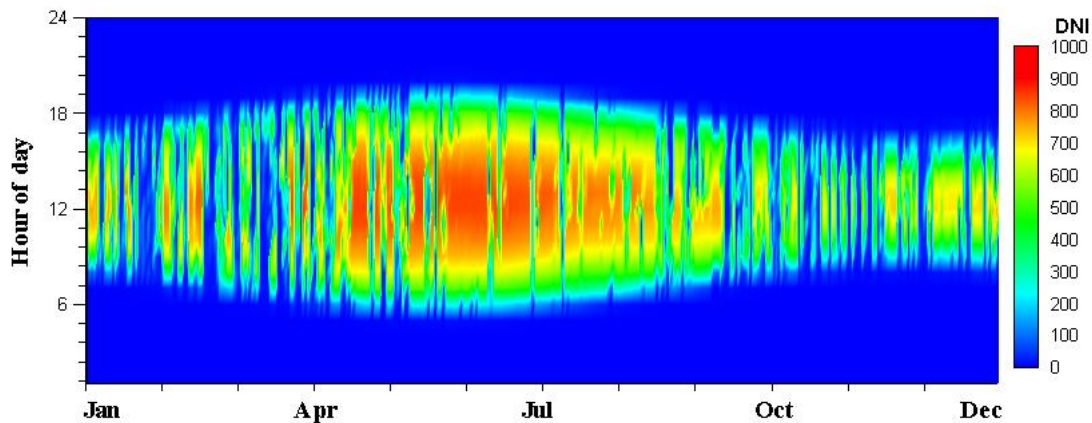


Figure 2.8 pattern of variations of DNI for Casaccia, Italy

Figure 2.9 shows the areas with different potential for concentrated solar power taking into account not only the average insolation, but also the land usability criteria such as flatness of the land, climate conditions, seas and forests. It can be seen that deserts in Africa, Middle East, Australia and also regions in north and South America are the most suitable areas for installation of concentrated solar power systems. Southern Europe particularly Spain, Italy and Greece have also good potentials to use CSP.

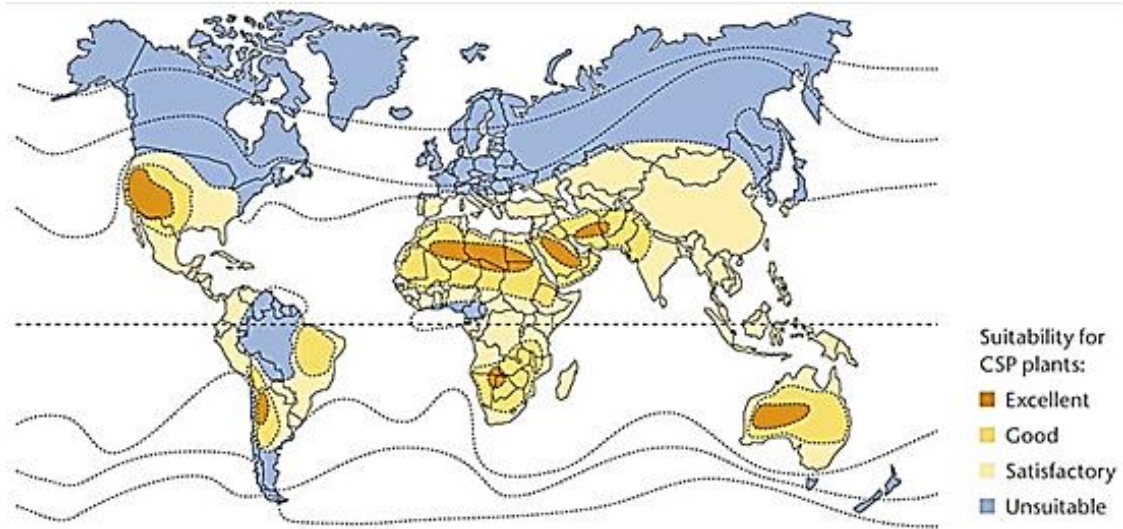


Figure 2.9 reference: (SCHOTT, 2016)

2.3.1 Solar radiation concentrators

The irradiance initially received by the concentrator, is reflected towards the solar receiver to convert it to thermal energy. Along this path, there are some losses caused either by the concentrator or the receiver. The effects of these losses are defined in the form of concentrator and receiver efficiencies. Figure 2.10 shows a parabolic dish which is made from several glass-metal facets and an engine sitting at its focal point. As explained below, the parabolic dish is the most efficient concentrator among currently available CSP technologies due to its high concentration ratios.



Figure 2.10 McDonnell Douglas (currently Boeing) Dish Concentrator; Daggett, California; USA (courtesy NREL). The Solar One Tower which is powered by a heliostat field is in the background.

The performance of the concentrator is determined by its optical efficiency. The optical efficiency of the concentrator is defined as the ratio of the total irradiance reflected by the dish (or received by the receiver) over the total irradiance received by it as shown in Equation 2.2. Indices ‘recv’ and ‘conc’ indicate the receiver and concentrator respectively.

$$\eta_{conc} = \frac{A_{recv} I_{recv}}{A_{conc} I_b} = \frac{(I_{recv}/I_b)}{(A_{conc}/A_{recv})} \quad 2.2$$

Ideally, all the incident radiation must be reflected by the dish towards the receiver. However, part of the radiation would either be absorbed by the dish or redirected outside of the receiver’s aperture because of the quality of the reflective surface. For a particular irradiance, the effective reflected radiation depends on the optical efficiency of the concentrator and the geometrical concentration ratio, where the geometrical concentration ratio is the ratio of the effective areas of the concentrator and receiver as shown in Figure 2.11 and equation 2.3.

$$CR_g = \frac{A_{conc}}{A_{recv}} \quad 2.3$$

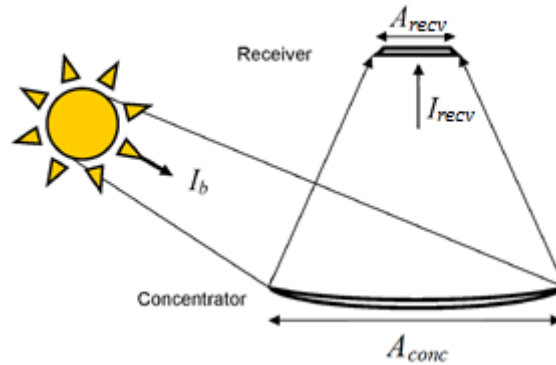


Figure 2.11 Concentration ratio

The relations between irradiance received by the dish and the effective reflected part shown by Eq. 2.4 which also introduces the optical concentration ratio of the concentrator.

$$CR_{opt} = \frac{I_{recv}}{I_b} = \eta_{conc} CR_g \quad 2.4$$

Typical range of concentration ratios expected from different CSP systems are shown in Table 2-2. Although high CR_g is beneficial for better performance of the optical system, it is limited by the fact that the spread angle of the concentrator cannot increase more than 90° because otherwise, part of the solar radiation will be reflected back to the concentrator. Additionally, sunrays do not reach the earth exactly in parallel. Because the diameters of Sun and Earth are very different, the

solar disc angle at which the radiation arrives on the earth is not zero, but a tiny angle of about 9.13 milliradians. For 3D concentrators like parabolic dish, CR_g would be limited to 11600, but for 2D concentrators such as parabolic troughs the uppermost value is 108 (Lovegrove & Wes, 2012).

Table 2-2 reference: (Steinhagen & Trieb, 2004)

Concentrator Technology	Type of focus	Typical Concentration Ratio
Linear Fresnel	Linear	25-100
Parabolic Trough	Linear	70-80
Central Tower	Point	300-1000
Parabolic Dish	Point	1000-3000

2.3.2 Solar receivers

Efficiency of the receiver is defined based on the solar energy it receives by the concentrated radiation and the thermal energy it provides to the engine. The losses from the receiver are in the form of radiation and convection (Spelling, 2013). As the temperature increases, losses from the receiver increase with radiation becoming the predominant loss mechanism and the losses will increase rapidly with the temperature. Absorption of the concentrated solar radiation by the receiver also directly depends on the absorptivity of its surface. Ultimately, the maximum achievable temperature in a receiver is limited by the material properties.

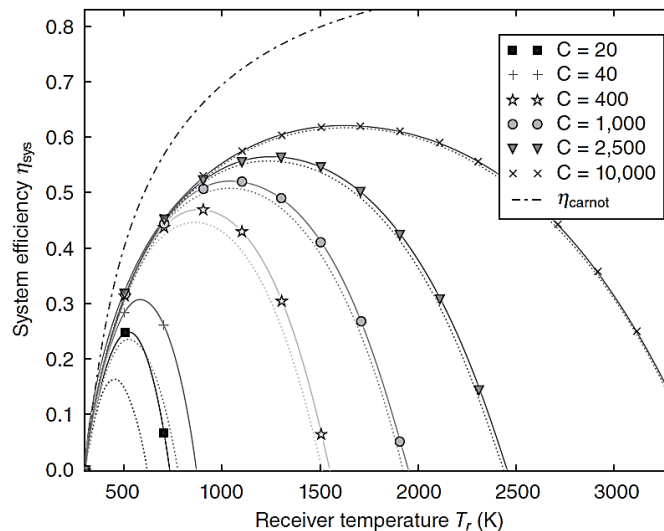


Figure 2.12 Ideal system efficiency as a function of receiver temperature. The dotted lines include the effect of convective heat losses (Lovegrove & Wes, 2012)

Since the losses in the receiver increase with its temperature, high efficiency is achievable at low temperatures while for a Brayton cycle engine thermal efficiency increases with the temperature.

Consequently, there is an optimal temperature for the receiver to be found. Lovegrove and Wes calculated overall system efficiency for different geometric concentration ratios and temperature of the receiver (Lovegrove & Wes, 2012). The results are shown in Figure 2.12 and demonstrate such optimal points for different concentration ratios. It can be seen that as CR_g increases, efficient operation takes place at higher receiver temperatures. The effect of the convective losses on the performance of the receiver can be seen for different concentration ratios by comparing the full lines for system efficiency with the corresponding dotted lines which include the convective losses. It can be seen that the significance of convective losses dramatically reduces in high concentration ratios.

Table 2-3 main characteristics of different solar receiver technologies (Avila-Marin, 2011)

Technology	Type	Heat transfer medium	Operating Temperature
Volumetric Receiver	Open Volumetric Receiver	Ambient air, pressure less	up to 800°C
	Closed Volumetric Receiver	Compressed air (common operating pressures 4 to 10 bar)	up to 1000°C
Tube receiver		Ambient air	up to 800°C
		Water/steam	up to 600°C
		Molten metal	up to 890°C
		Molten salt	min. 280°C, max. 565°C (solar salt)
Direct absorbing receiver	Falling Particle Receiver	Particles	up to 1000°C
	Centrifugal Receiver (CentRec)	Particles	up to 1000°C
Ceramic receiver	Flat Receiver	Compressed air (common operating pressures 4 to 10 bar)	up to 1000°C

Solar receivers which are used in point focus CSP systems are categorised based on the heat exchange media as gas, liquid or solid particle receivers (Ho & Iverson, 2014). Gas receivers mostly are used for the systems with an air cycle as the prime mover while the liquid receivers are used with a heat transfer fluid like molten salt or metal to use the absorbed thermal energy in a Rankine cycle or other processes. The idea of solid particle receivers has been developed theoretically since the 1980s to achieve temperatures above 1000°C, but only one simple falling film particles receiver was tested with poor efficiency and maximum temperature not better than 800°C (Siegel, et al., 2010). The most common gas receivers are open and pressurised volumetric

receivers which can achieve temperatures as high as 800°C and 1200°C respectively. A comprehensive review of volumetric receivers is given by (Avila-Marin, 2011). Table 2-3 summarises the existing solar receiver technologies. Recently, a special type of open volumetric receiver called MetRec was made and tested by DLR. It replaces the ceramic porous media with razor-thin and corrugated, high temperature steel foils capable of operating permanently at 900°C or intermittently at 1100°C (Fend, 2015).

2.4 Solar powered gas turbine systems

Coupling of gas turbines with concentrated solar power systems to generate electricity is not a new concept by itself. NASA pioneered research on the application of solar powered micro gas turbines to provide electricity for their space facilities. They studied closed Brayton cycle engines powered by a parabolic dish (Cameron, et al., 1972). A few years later, they made a pure solar closed cycle MGT of 10kWe equipped with a melting salt short term storage system for shadow periods and achieved an overall efficiency of 29% (English, 1986). The system was tested based on periods of constant solar radiation similar to a low Earth orbit and successfully passed continuous operation for 38000hrs as an endurance test. No input heat transients were considered as the system was supposed to work outside the atmosphere of the earth.

Unlike NASA’s project, solar powered systems on Earth face an important problem which is the variations of DNI. Such variations directly affect the input heat supplied to the MGT through the components of the CSP system. Deviation of the input heat from its nominal value moves the MGT to off-design conditions and affects the system performance. As such, most of the solar powered CSP-MGT systems are designed using the so called solar-hybrid (or simply hybrid hereafter) configuration that uses an auxiliary combustion to assist the thermal input from the solar receiver and maintains stable working conditions for the MGT despite the variations of DNI (Figure 2.13). Thus, it will be more appropriate to consider such systems as ‘solar assisted’ systems and use the term solar powered for the pure solar (i.e. solar-only) systems which only use solar energy.

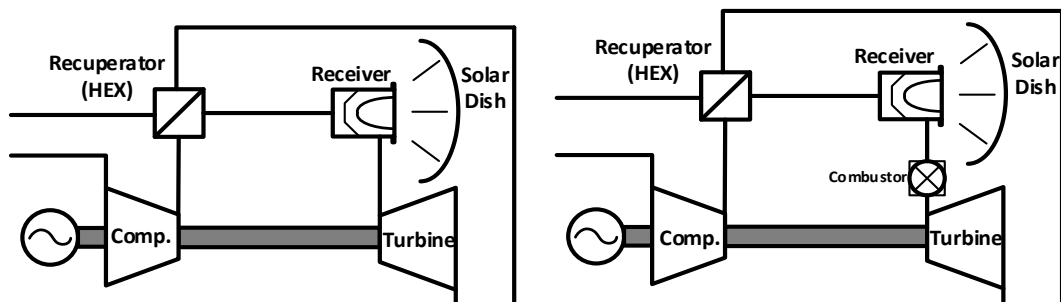


Figure 2.13 Solar-only (left) and Solar-hybrid (right) system configurations

In hybrid systems, the combustor is always in operation. When the receiver adds solar heat to the system, fuel flow decreases to keep the MGT working point at the design conditions. This is explained in Figure 2.14 for two different regime of DNI. Ideally, the combustion system will be able to accommodate the variations of fuel flow and as a result, the off-design conditions will not force any fluctuations in the generated electricity.

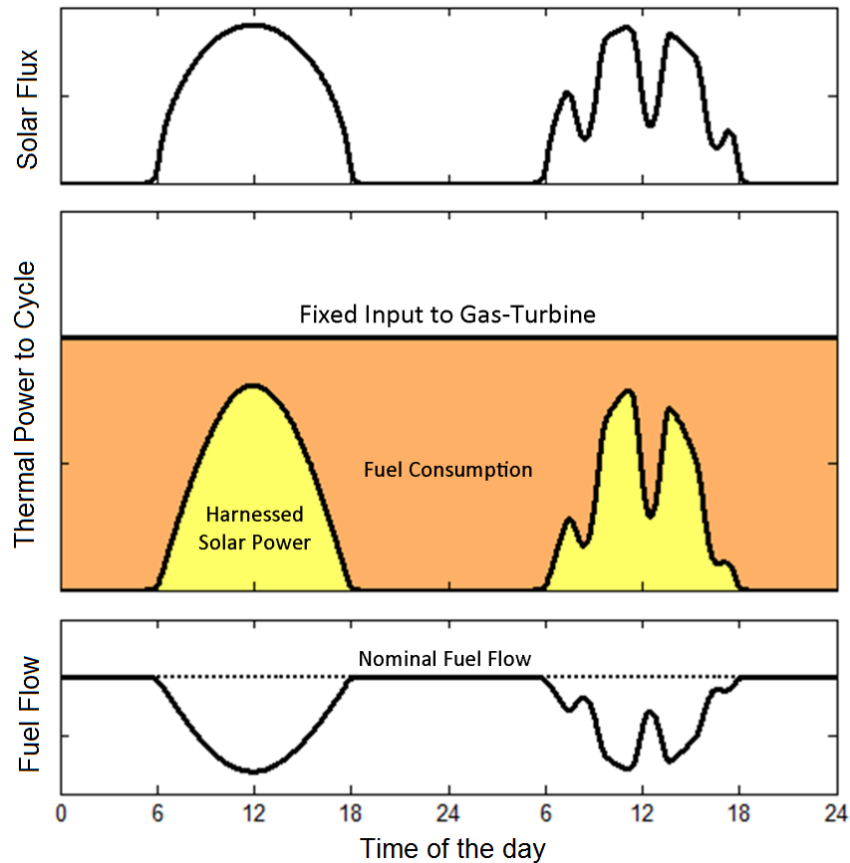


Figure 2.14 typical performance of a hybrid system in an ideal (left) and cloudy (right) day (Spelling, 2013)

Research on the hybrid CSP-MGT systems are abundant in the literature with some projects including build and installation of systems, mostly in the US and Spain. Barigozzi et al. gave a comprehensive list of recent research on the solar gas turbine systems, most of which are hybrid-solar (Barigozzi, et al., 2012). An early study on hybrid solar powered systems was conducted by the US Department of Energy (DOE) from 1976 to 1985, where different hybrid-solar dish-engine systems in the power range of 20-25kWe including Brayton, organic Rankine, steam and Stirling heat engines were studied (Jet Propulsion Laboratory, 1981). An engine efficiency of 32% was estimated for turbine inlet temperature of 870°C which was less than the Stirling engine (39%) but considerably higher than other engines. Larger scale systems have been under more focus with most of these installations in combined Brayton and Rankine cycles. In SOLGATE, an EU

funded project, an aero-derivative MGT with nominal output power of 240kWe was modified to be used in a hybrid solar system powered by a heliostat field CESA-1 tower in Spain (SOLGATE, 2005). Three low, medium and high temperature pressurised receivers were used in series to achieve temperatures as high as 960°C before the combustor.

Thermo-economic optimisation of the systems has been the subject of several research studies to find an optimal design for a particular CSP-MGT system. A key objective is to reach an acceptable levelised cost of electricity (LCOE) compared to the direct competitor, PV systems. LCOE is defined based on the initial cost and the production expenses for an assumed duration of duty life of the system. A very important parameter here is the amount of electricity that the system generates from solar radiation. Because of the variations of insolation even during a single day, the performance of the system is considered over a period of at least one year. During this period, a micro gas turbine would work at its design point conditions for a tiny amount of time and the rest of its operation would be under lower or higher insolation values which run the MGT to off-design conditions. Off-design performance of the gas turbine depends on its design and components performance, load variations and its control strategy. Because several parameters take part in the off-design performance, a proper system model is required to evaluate its performance value as realistically as possible. However, as explained in the next paragraphs, in the calculation of the annual performance, two approaches dominate the existing literature. Either the performance of the MGT is considered to be fixed at the design point, without any variations, or very simple models with poor levels of detail have been formulated in the calculation of the engine's performance. Most of the available papers have focused on the optical components of the system.

When a hybrid system is used, it is normally assumed that the auxiliary combustion completely compensates the variations of DNI. As a result, the system would always work at the design point. The annual performance of the system can be easily calculated based on its design point performance and the total working hour. Therefore, variation of DNI is only used in the calculation of fuel consumption and the related cost (Spelling, et al., 2012). Such an assumption has been used in some thermo-economic studies on hybrid systems. Schwarzbözl et al. considered three different hybrid systems using gas turbine engines in the power ranges from 1.4 to 16.1MWe with different technologies from a simple cycle combined with a bottoming cycle to an intercooled, recuperated reheat cycle (Schwarzbözl, et al., 2006). Two installation points in USA and Spain were assumed to make seven individual case studies. Despite the difference of system architecture, it was simply assumed that the hybrid configuration will always be able to keep the TIT constant and did a thermo-economic optimisation to achieve the lowest LCOE with

200€/MWh for 1.4MWe units and only 63€/MWh for 16.1MWe units installed in Seville, Spain. Price has used this assumption to perform a thermo-economic study on the installation of a 10MWe hybrid system in solar two site in Daggett, California, USA and use the Nitride salt thermal storage central tower powered by a heliostat field (Price, 1997). LCOE was found to be 54€/MWh when life expectancy is 20 years.

However, assuming that the hybrid system would be able to work constantly on the design point regardless of variations of the DNI, is very optimistic because this assumption requires the combustor to work over a very wide range of fuel flow. When DNI reduces from a high value at the design point of the system to zero, the fuel flow rate changes in the opposite direction increasing from a very low value at the design point to a maximum in which only combustion runs the engine. For DNI values above the design point, the combustor must be able to work with even lower mass flow rates of the fuel. Such a wide range of variations of the fuel flow would impose serious flame out and instability problems in the combustor according to intensive research done by the ORMAT Company through their work on a number of hybrid solar research projects (Sinai, et al., 2005) and (Fisher, et al., 2004). In fact, hybridisation of the gas turbines adds more complexity to the working conditions which require modifications of the engine (Fisher, et al., 2004). The first point is that the combustor in hybrid-solar receives substantially higher inlet temperature and consequently much higher volumetric flow rates. Another important point is more pressure losses because of the added combustor. The effect of increased pressure losses can be critical in the small micro gas turbines as explained in section 2.2. The large engines can compensate this effect by changing the Nozzle Guide Vanes (NGV) but at the expense of lower airflow and lower power output.

To calculate the performance of the system under variations of DNI in a more realistic way, off-design performance must be calculated using an appropriate thermodynamic model of the system. This is especially important for solar-only systems where fluctuations of DNI directly affect the system performance. Solar-only systems are of considerable interest as they are not dependent on fuel combustion and are completely emission free. There is only a limited number of work focusing on solar only micro gas turbines. Among these few efforts, most of the focus have been on the optical part of the system and an optimised design taking the off-design performance of the MGT under variable conditions of solar irradiance is difficult to find. Le Roux et al. tried to model a small-scale pure solar recuperated micro gas turbine and optimise it so that the system produces maximum net power output with the main focus on reducing the losses in the recuperator and solar receiver (Le Roux, et al., 2011) and (Le Roux, et al., 2012). Although, optimisation of the system was performed for a number of different design point conditions, off-design

performance of the system was not considered. In the work done by Sandia Laboratories for a feasibility study of relatively small hybrid and solar only micro gas turbines, the annual performance of the system was calculated by taking the off-design performance into account. To calculate the off-design performance, a simple empirical equation is used to determine a correction factor which is applied to the efficiency of the MGT if the thermal input power from the receiver is below the design point. Figure 2.15 represents this simple model. Such general correlations are easy to implement in the system performance model and reduce the number of variables and also calculation time when overall system optimisation requires thousands of iterations. However, these models are very general and consequently comprise two essential problems. The first is that such simplified models are built based on some fixed assumptions for primary parameters of the MGT. For example this model assumes a free power turbine after the first turbine with a TIT of 850°C. As a result, application of this model will associate errors when other TIT values are used. The second problem is that such models do not include the design parameters of the engine and consequently achieving an optimised MGT will not be feasible when such models are used. Using this performance model and purchase costs of the equipment for low system production rate, an LCOE of 129€/MWh was predicted for a 30kWe solar-only system (Gallup & Kesseli, 1994).

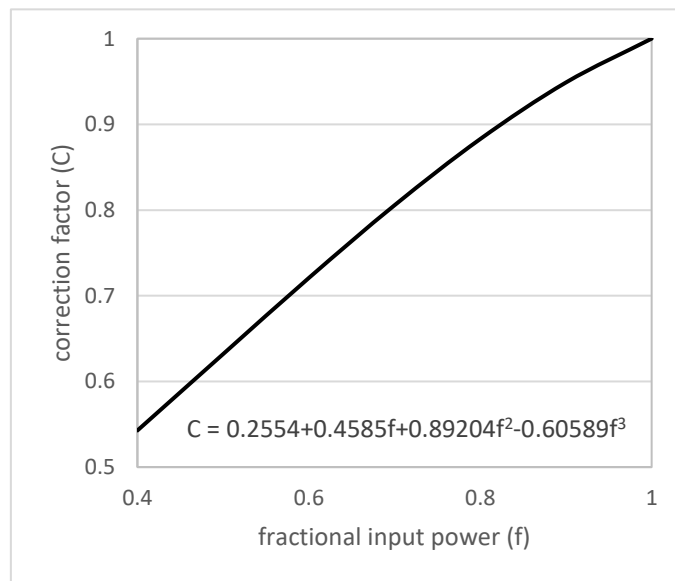


Figure 2.15 representative of the performance curve generated from empirical equation used to evaluate the engine efficiency in off-design conditions (Gallup & Kesseli, 1994)

Spelling et al. used efficiency correlations for gas and steam turbines to estimate the off-design performance of the engine in a solar only combined cycle that is also equipped with a thermal storage system (Spelling, et al., 2012). They concluded that for pure solar combined Brayton and Rankine cycles below 20MWe, efficiencies in the region of 18-24% can be achieved with an

LCOE around 92€/MWh to 185€/MWh. These correlations use more details of the engine parameters such as the pressure ratio and mass flow rate of the engine. More importantly, the allowable limits of the engine operation are also considered in this work. Although their work takes more details of the engine design parameters into account, there are still key points in the performance calculation of a pure solar dish-MGT system which must be considered. Because of the considerable variations of DNI during a year, the performance model must be able to predict as much as possible of the details pertaining to these variations. As an instance, the minimum DNI where power production starts, i.e. self-sustaining point, must be calculated for a particular system design. This is a point which depends on the system design parameters. Additionally, constraints which determine the safe operation limits of the system such as the maximum allowable temperatures at the turbine inlet and exit, will be applicable to the calculations only if the model takes the related parameters into account. Similarly, controlling parameters used by the control strategy should be part of the parameters that the model uses because the performance of the system is highly affected by the strategy that it is operated. Such detailed models to calculate the annual performance as a key objective for solar powered micro gas turbines are very difficult to find in the literature while a realistic evaluation of CSP-MGT systems really depends on it especially when optimised design of the system and MGT components are targeted.

2.5 Overview of performance models for micro gas turbine cycles

From start-up to shut down of any gas turbine engine, there are numerous complicated issues interacting and being mixed which affect the performance of the machine. Probably Otto and Taylor were the first who attempted to show that an engine's response to change in fuel flow can be approximated by a mathematical model (Otto & Taylor, 1950). Engine models have been developed continuously along the time as the capabilities of computational platforms increased. Some general criteria for an engine simulation code are defined as very good repeatability and reliability, accurate representation of engine's behaviour and at the same time, user friendliness characteristics (Sanghi, et al., 2000).

2.5.1 Categories of engine models

Along the gas-path of the engine, characteristics of the flow may be calculated at any point by solving the three dimensional governing equations that may also include time dependent terms when transient phenomena are to be precisely modelled. Depending on the level of information available from the engine, especially its geometric design and also type of the analysis to be made, engine models may use different levels of space discretisation. Categorisation of the models are based on their time dependency and level of geometrical details.

Space discretisation level

Zero dimensional (0-D) models consider the engine as a set of black boxes (components) and only deal with performance data at the interface points between the components. The thermodynamic and other governing equations of the engines would use these data. To acquire the performance data of each component, these models are dependent on the characteristics maps or analytical representations of the components. The validity of the model is directly related to the accuracy of components' maps. GasTurb (Kurzke, 1995) and GSP (Visser & Broomhead, 2000) are two well-known 0-D codes which are developed based on an object-oriented programming approach and are able to run steady state and transient simulations of the gas turbines. GSP gas turbine simulation code has been frequently used for performance analysis and development of small scale MGTs (Visser, et al., 2011). More general simulation codes like TRNSYS (Klein, et al., 2004) have also been used as a platform for component based modelling of gas turbines. Examples are work done by (Spelling, et al., 2004) and (Garcia, et al., 2008). Solar thermal electric libraries, STEC have been developed to use for performance modelling of solar powered gas turbines in TRNSYS (Schwarzbözl, 2006). However, commercial software like the codes mentioned here does not allow complete control on every detail and do not have the flexibility to couple the program with other codes for additional tasks. For example hybrid modelling as explained later in this section or coupling the performance simulation with an optimisation code would not be a straightforward task when commercial software is used.

One dimensional (1-D) and higher order engine models use information inside the components of the engine. Depending on these data, it would be possible to discretise the governing equations either just along the gas path (1-D) or in more directions (2-D and 3-D). Such models can provide more detailed phenomena such as the internal heat transfer effects and provide closer insight into the component design. As a result, such models would be beneficial when improving the design of the components for better performance of the engine. However, the amount of component details increases for higher order models. Consequently, such models may not be used in the early stage of engine design when this information normally is not available. Higher order models especially 3-D models are mostly used for the prediction of high frequency phenomena such as surge and combustion instabilities in an individual component rather than for performance analysis.

Rather than modelling the entire engine with one unique mathematical approach and the same level of accuracy, it is possible to perform more detailed simulation in complicated turbomachinery flows and treat the remainder of the engine with lower level models. This approach is called hybrid modelling. Successful hybrid modelling methods have been reported in

the past. One setback related to this approach is that more execution time is needed for complete simulation as some matching procedures may need to be repeated several times. 1-D models show a proper choice as the platform for hosting the characteristics or data obtained for complicated components from detailed codes (NATO, 2007).

Steady state and transient models

The gas turbine steady state performance simulation models assume that all flow characteristics in the engine have reached a steady condition. As soon as the working point changes to a new state because of any reason (ex. Change in DNI), it will take a transition time for the engine to reach the new working point. Depending on the application of the engine, its transient response can be critical. For example gas turbines used in emergency electricity generation units require a start-up time of about 10 seconds to let the unit feed the synchronised electricity to the grid very quickly (Saravanamuttoo, et al., 2009). Such quick start-up applies aggressive changes in the temperatures of the engine components resulting in extreme thermal stresses. Transient models take the variations of the engine conditions into account when the working point changes from one steady state to another. These models calculate time dependent values of the same working parameters as steady state models. Besides, they can at least provide rotor dynamics related information (Walsh & Fletcher, 2004). Transient models in 1-D level deal with low frequency phenomena including rotor accelerations, heat transfer and geometry changes (variable stators, change of tip clearance or exhaust nozzle area with temperature). More sophisticated modelling is required when it is needed to address higher frequency dynamic events such as stall (axial compressors), surge or combustion instability. TRANSEO (Traverso, 2004) is a MATLAB based 1-D approach for transient modelling of micro gas turbines. Like almost all other 1-D level codes, it uses the Euler equations in a finite difference scheme and calculates heat transfer in the engine. Modelling of an 80kW externally fired MGT cycle which is accomplished using this code has been reported (Traverso, et al., 2006).

Iteration methods

A well-known approach (Saravanamuttoo, et al., 2009) in 0-D level modelling is to presume a single point on the compressor map for a particular speed. All conditions for the compressor then will be derived from the characteristics map expressed as above and calculation will continue up to engine's exhaust point where a matching evaluation can be done to see if the delivered power at the selected speed meets the required power by the load at the same rotational speed. Several iterative computations are normally needed before the procedure reaches a satisfactory convergence. Depending on the type of the engine and components, the matching criteria and the presumed variable may be different. This type of the calculation which includes a number of

iterative nested loops is known as local iteration (NATO, 2002). Algorithms for a variety of engine arrangements are available in the literature (Walsh & Fletcher, 2004). Local iterations method is very similar to the normal calculation procedure which one may do manually. Because of its simple structure, it is very easy to be implemented in a computer code. However, this method has a number of disadvantages especially when it is supposed to perform the simulation calculations for more complicated engines. The main reasons are presented here:

- Because too many loops are implemented in this method, it will be needed that the internal loops meet high precision convergence criteria. This results in some complexities especially when there are parameters which are cross referenced in different loops for example in recuperated cycles temperatures in the initial stages of the gas path (cold side of the recuperator) are related to the turbine's exhaust.
- To involve additional parameters in the output of calculations such as surge margin, there will be more sophisticated calculations. Therefore, a nested loop structure is deemed to be impractical.
- Because the design of iteration loops is strongly depended to the configuration of the engine, any small change in its configuration or the components, will have significant effects on this algorithm. As a consequence, considerable programming will be needed.

A very suitable replacement; the global method, is based on an iterative resolution of the whole set of equations. In this method, any of the compatibility criteria will be considered as a constraint equation which includes a number of characteristic parameters of the corresponding components. Altogether, there will be a matrix (vector) form of the equations like $\mathbf{F}(\mathbf{X}) = \mathbf{0}$. These sets of equations represent the compatibility conditions which are defined based on mass conservation, power balance and mechanical integrity between the engine's components. All equations can then be solved simultaneously using different methods. A multidimensional Newton-Raphson algorithm is the usual approach to solve this system of equations and consists of linearising the function $\mathbf{F}(\mathbf{X})$ around the point \mathbf{X}_0 , such that (Woodford & Phillips, 2012):

$$\mathbf{F}(\mathbf{X}) = \mathbf{F}(\mathbf{X}_0) + \mathbf{J}(\mathbf{X} - \mathbf{X}_0) \quad 2.5$$

\mathbf{J} is the Jacobian matrix of \mathbf{F} . There are some important remarks:

- The initial values are very important to achieve convergence quickly. The initial point is preferred to be chosen close enough to the real operating point within the operating envelope. Some methods include an initialisation procedure which provides an appropriate guess for the initial point.

- It is often needed to set upper and lower limits for the unknowns during the iterations. Because the problem is non-linear, it is very likely that large variations of the unknown parameters result in the solution to diverge.

The main advantage of the global iteration method is that the component related calculations and mathematical resolution are two individual sections of the computation procedure. Thanks to this modular structure, the mathematical algorithm is not dependent on the engine arrangement and can be easily adjusted when the configuration of the cycle is changed.

2.6 Economic models for solar powered systems

An economic model normally consists of a number of cost functions which allow for the calculation of the purchase costs of system components as well as the other costs associated with raising and operating of a solar powered system such as the cost of the installation and the operating costs. A model which has been widely used for the calculation of the cost of gas turbines consists of individual cost functions for the components of the gas turbine. The model was first introduced by El-Sayed and Tribus and uses existing cost and design data of a reference engine to predict the cost of a new engine with different design values (El-Sayed & Tribus, 1983). The original model has been then modified by several researchers to the specific problem of their interest particularly based on the size and layout of the engine. Equations 2.6 and 2.7 show the cost functions for the compressor and turbine in later models based on El-Sayed and Tribus model in a general form. The main design parameters for each component which are used in these equations are mass flow rate \dot{m} , compressor or turbine efficiency (η_c or η_t) and the pressure ratio π . Subscript “ref” is used to indicate the values pertaining to the reference machine.

$$C_{comp} = \frac{c_1 \dot{m}_{ref} \left(\frac{\dot{m}}{\dot{m}_{ref}} \right)^{n_1} \pi_{ref} \ln(\pi)}{c_2 - \eta_c} \quad 2.6$$

$$C_{tur} = \frac{c_3 \dot{m}_{ref} \left(\frac{\dot{m}}{\dot{m}_{ref}} \right)^{n_2} (\pi_{t,ref}) \ln(\pi_t)}{c_4 - \eta_t} \left(1 + \exp(c_5(TIT - c_6)) \right) \quad 2.7$$

In the above functions, the pressure ratio appears as a multiplier with an increasing trend and therefore, directly affects the cost. Because this model is proposed for large engines with multistage turbine and compressor, the pressure ratio has an important role in the final cost. However, for a recuperated micro gas turbine the architecture of the compressor and turbine are different and the pressure ratio of the compressor is not considered as an influential factor on the final cost of the engine. When design parameters of small scale microturbine are used in any of

these formulae, the costs of the components are higher than expected. Table 2-4 shows constant factors for a number of modified versions of the model. Except for the last model which provides the cost value of the components in Euro, the rest of models in Table 2-4 are in US\$.

Table 2-4 constants in the modified forms of equations 2.6 and 2.7

	c ₁	c ₂	c ₃	c ₄	c ₅	c ₆	n ₁	n ₂	π _{ref}	ṁ _{ref}	π _{t,ref}	ṁ _{t,ref}
(Frangopoulos & von Spakovsky, 1993)	39.5	0.9	266.3	0.92	0.036	1511	1.0	1.0	π	N/A	1.0	N/A
(Agazzani & Massardo, 1996)	41.5	0.9	279.9	0.92	0.036	1824	1.0	1.0	π	N/A	1.0	N/A
(Pelster, 1998)	27.7	0.96	12.4	0.94	0.025	1600	0.7	0.7	15	515	15	460
(Galanti & Massardo, 2011)	55.8	0.942	376.1	0.903	-∞	0.0	1.0	1.0	π	N/A	1.0	N/A

Individual cost functions have been also suggested for other components of the gas turbine system including the electrical generator and auxiliary mechanical and electrical components. Cost functions for these components are generally given in form of a power relation based on a reference value as shown in equation 2.8 where PWe is the rated electric output power, PWe_{ref} is the reference rated power and C_{aux} is the cost of equipment. The value for n has been suggested to be 0.7 to 0.9 (Spelling, 2013).

$$C_{aux} = C_{aux,ref} \left(\frac{PWe}{PWe_{ref}} \right)^n \quad 2.8$$

For micro gas turbines more recent models have provided just a single cost function rather than separated costs of the components. Park et al. have generated a simple cost model for microturbines from 500 to 3000kW (Park, et al., 2014) as shown in Figure 2.16.

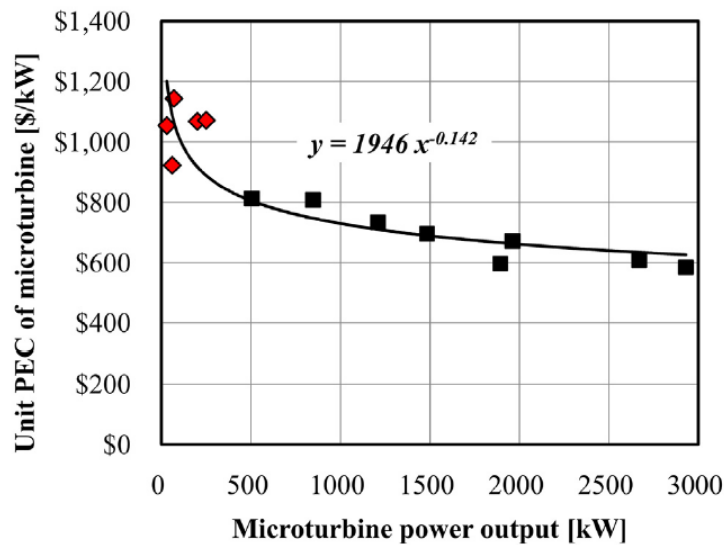


Figure 2.16 Microturbine cost (Purchased Equipment Cost) given by Park et al. model.

This model is based on available data for the purchase cost of microturbines in the literature. It doesn't include the cost of the recuperator and additional costs pertaining to the installation of the system. It also excludes any other components like a high speed generator (HSG), control and power electronics. The model is based on available cost data in the literature. The red points on the graph represent modified data for small engines which originally included the cost of the recuperator.

These simple models are not able to provide any relation between the engine's key parameters and its cost. For example two 5kWe micro gas turbines with different maximum TIT levels would have the same cost, while more expensive materials and higher manufacturing technology are required to achieve higher TIT. Although it is not the target of the present thesis to provide an economic model for dish-MGT systems, a clear gap in the knowledge is realised on the economic models for the small scale micro gas turbines. A more updated model which has been developed during the OMSoP project by the consortium members is introduced and applied to the calculations in chapter 5.

2.7 Conclusion

The majority of the research work available in the literature have focused on the hybrid-solar gas turbines. The unstable conditions of DNI can be covered by an auxiliary combustor in hybrid systems. However, these systems have to deal with technical and economic issues because of high temperature unsteady combustion and environmental and economic expenses that ultimately affect the cost of the generated electricity. Pure solar systems do not face such problems and have a number of advantages regarding environmental concerns and more simplicity. Only a few research projects have attempted to study and test these systems. Two main concerns for the deployment of the pure solar dish-MGT systems are the economic figures (investment cost and cost of electricity) and the variation of the generated power imposed by the solar irradiance. Throughout the literature review, it was realised that the efforts done on the pure solar dish-MGT systems to achieve an optimised design for minimum cost of electricity have mainly used simple empirical equations for the evaluation of the off-design performance which doesn't appropriately take the effects of system design parameters and component design into account. The effects of system control and operation strategy on the system performance have also been neglected in the past work. This must be properly addressed considering the variable regime of DNI. Further points from the literature review are summarised below:

- Variable load control has proved to be useful in controlling micro gas turbines and is deemed to have potential to be applied to the pure solar dish-MGT systems to deal with variations of input solar heat
- Pure solar MGT systems have lower investment and operating costs than the hybrid-solar, but the ultimate cost of electricity is higher because of their lower performance which indicates their potential to reduce the cost of electricity by increasing the annual system performance
- Existing economic models for gas turbine systems are not appropriate for small micro gas turbines either because they are based on data from larger power range or they don't take the effect of system design parameters into account

3 Thermodynamic performance modelling

3.1 Introduction

One of the challenges in the design of gas turbine systems is that an accurate performance map for any component cannot be generated until its design is finalised which requires the design point to be fixed as the first instance. However, finalising the design point is an outcome of an optimisation study which requires off-design performance calculation and therefore requires the components performance maps. Clearly, this is an iterative procedure which begins by approximating the components' maps based on an initial design point and then improving the components design after an optimised design is achieved. In this chapter a method is developed and adapted to the pure solar dish-MGT systems which allows the performance simulation of such systems over the full course of DNI variation. The method is developed by the combination of existing techniques for gas turbine system modelling and component map generation with minimum design parameters required. Compared to existing empirical (or analytical) off-design performance correlations, the developed model requires a few more design data, but is able to provide much more details about the system performance as well as the component design and performance maps.

A dish-MGT performance simulation code is developed during the progress of the current thesis, based on the above mentioned method. Figure 3.1 shows the general structure of the computational model. Thermodynamic model of the dish-MGT system is included in the core of this code where it communicates with the components' models and the input sections. The input data are introduced to the computational model through a number of individual sections. The climate conditions include the DNI value as the solar parameter and also the ambient conditions that determine the properties of the inlet air to the MGT. These conditions are ambient temperature and pressure and the relative humidity (RH) of the air at the inlet of the compressor. The boundary conditions define the load applied to the dish-MGT system. This is the electric power that the control system adjusts to be able to control the operation of the micro gas turbine.

It is different from a conventional gas turbine system which is controlled by the fuel flow. Therefore, the electrical load on the MGT is an input condition which is determined by its operation strategy and enforced through the action of control system over the high-speed alternator (HSA). The system constraints section provides input data to restrict the operation of the dish-MGT system beyond certain limits to ensure safe and stable operation. The main limiting parameters are Maximum TIT, TET, rotational speed and maximum current allowed in the high-speed alternator. Performance of the system which is calculated within the core will be considered valid only if the working point of the system appears inside the operating window defined by the system constraints. For a set of design data given to the computational model, design point performance is calculated by the core. The results are input to the components' models section to generate the performance maps and provide them to the core for off-design performance simulation. The thermodynamic properties of the fluid are corrected using the pressure and temperature values provided by the performance simulation algorithm in the core in an iterative procedure

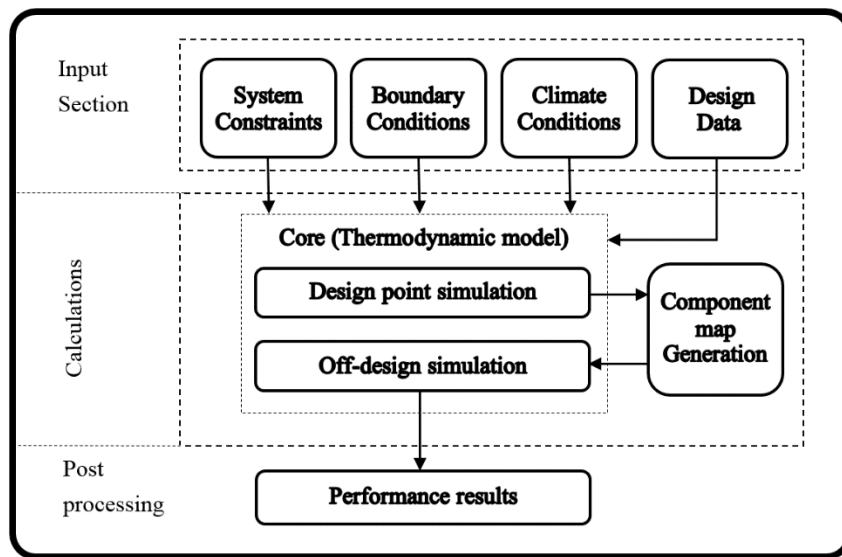


Figure 3.1 General structure of the computational model

3.1.1 General representation of system components

The core of the computational model requires the component models. The component model determines the relations between the components' performance characteristics. The general form of the components' models are given by equations 3.1 to 3.143.13. More details of these models are given in section 3.3.

The compressor characteristics are pressure ratio, π , rotational speed, N , mass flow rate, \dot{m} , and the efficiency, η and their relations are shown in equations 3.1 and 3.2. It should be noted that

these characteristics also depend on the ratio of the specific heats of the fluid, γ and the inlet conditions i.e. ambient temperature, T_{01} and pressure, p_{01} . The same type of equations would represent the characteristics of the turbine.

$$\dot{m}_c = f_{\dot{m},comp}(N, \pi_c, T_{01}, p_{01}, \gamma) \quad 3.1$$

$$\eta_c = f_{\eta,comp}(N, \pi_c, T_1, p_1, \gamma) \quad 3.2$$

The recuperator accommodates two individual streams known as cold and hot flows. Its two main characteristics are the pressure loss across each side and the effectiveness. The relative pressure loss, dp/p for each side of a recuperator, with a given geometry, must be represented in form of equations 3.3 and 3.4. Also, the effectiveness, ε depends on all the flow parameters of the cold and hot side except the pressure assuming that the gas properties don't change too much with the pressure.

$$(dp/p)_{recp,cold} = f_{dp,recp,cold}(\dot{m}_{cold}, T_{i,cold}) \quad 3.3$$

$$(dp/p)_{recp,hot} = f_{dp,recp,hot}(\dot{m}_{hot}, T_{i,hot}) \quad 3.4$$

$$\varepsilon = f_{\varepsilon}(\dot{m}_c, \dot{m}_h, T_{i,c}, T_{i,h}) \quad 3.5$$

Where indices 'cold' and 'hot' indicate the flow properties for the cold and hot sides respectively and T_i is the inlet temperature to each side. In practice, the sensitivity of the pressure loss to the inlet temperatures is negligible (Shah & Sekulic, 2003) and in the case of equal mass flow rate in both sides, the above equations can be simplified to:

$$(dp/p)_{recp,c} = f_{dp,recp,c}(\dot{m}) \quad 3.6$$

$$(dp/p)_{recp,h} = f_{dp,recp,h}(\dot{m}) \quad 3.7$$

$$\varepsilon = f_{\varepsilon}(\dot{m}) \quad 3.8$$

The main performance characteristics of optical components (i.e. concentrator and the receiver) are the pressure loss in the receiver, $(dp/p)_{recv}$, and optical efficiency, η_{opt} . The latter is the ratio of the total thermal power given to the MGT by the receiver and the solar thermal power received at the surface of the dish. For any particular CSP system with given design parameters (i.e. concentration ratio, CR_g , absorptivity of the receiver, α_{recv} , and geometrical design of the receiver and the dish), performance characteristics can be represented by equations 3.9 and 3.10.

$$(dp/p)_{recv} = f_{dp,recv}(DNI, \dot{m}, T_{i,recv}) \quad 3.9$$

$$\eta_{opt} = f_{\eta,opt}(DNI, \dot{m}, T_{i,recv}) \quad 3.10$$

Where index ‘recv’ represents properties pertaining to the receiver. To generate electrical power, a high speed alternator (HSA) is coupled to the MGT. Although during the normal operation, the HSA works as a generator and must be called a HSG (high speed generator), there are circumstances during the start-up and shut down periods that this machine must work as a motor. This is discussed when the control and operation strategies of the system are analysed in chapter 4. Therefore, there will be two different characteristics for the HSA during generation and motoring. The main characteristics are power, PW_{HSA} , efficiency, η_{HSA} and speed and can be related to each other by the equations 3.11 and 3.12.

$$PW_{HSA} = f_{PW,HSA}(N) \quad 3.11$$

$$\eta_{HSA} = f_{\eta,HSA}(N) \quad 3.12$$

Control and auxiliary components are used in the system and consume a certain amount of power. The power electronics components are required to convert and synchronise the generated electricity with the main grid and run the control system. The Sun tracking and lubrication oil systems are the main auxiliary components. Accurate calculation of the power consumed by the control and auxiliary systems requires detailed information of their components and ultimately is not a strongly variable parameter. Therefore, a constant value is assumed for power consumption of control and auxiliary components combined, PW_{aux} as given by equation 3.13.

$$PW_{aux} = const. \quad 3.13$$

The pressure loss in the connections between each two consecutive components is commonly treated as an individual component with only one characteristic equation which relates pressure drop to the mass flow rate and Reynolds number similar to equation 3.14. However, this approach is more suitable in the models of higher order of detail which include geometrical input. Here, the pressure losses are considered as part of the characteristics of the recuperator and the receiver.

$$(dp/p)_n = f_{dp,n}(\dot{m}, Re) \quad 3.14$$

It is important here to distinguish between performance characteristics of the components and their design parameters. Although the performance of a component is determined by its design parameters, these parameters do not necessarily appear in the performance map. As an example, the performance characteristics of the compressor are represented by equations 3.1 and 3.2. However, its design parameters include important geometrical values such as the tip diameter and blade angles. Such parameters in fact determine the f functions used in equations 3.1 to 3.13.

The thermodynamic simulation code introduced in this chapter uses a component-based 0-D approach and requires the f functions to be known in mathematical form, either as a performance map or a set of equations.

3.2 Governing equations

Thermodynamic and other governing equations are used in the core of the simulation code similar to a thermodynamic cycle analysis. Component performance maps or their representatives in the form of equations 3.1 to 3.13 can be used to find the flow properties along the gas-path at the interface points of the components numbered in Figure 3.2.

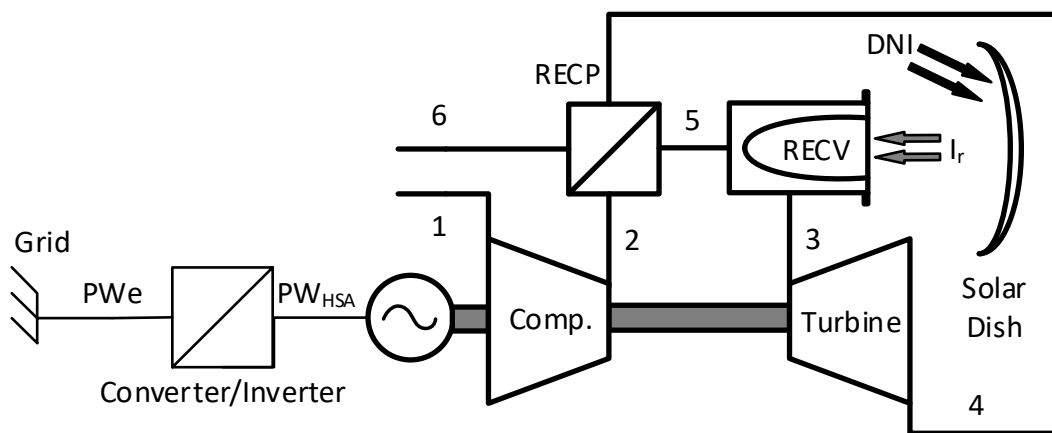


Figure 3.2 single shaft recuperated micro-gas turbine cycle

The governing equations of the dish-MGT system can be divided in three groups. The first group of equations is derived from the thermodynamic processes that take place in the individual components. The second group is the conservation equations and the last group pertains to the mechanical integrity of the system.

3.2.1 Components equations

Compressor

Assuming an adiabatic compression process, the isentropic efficiency of the process is defined as the ratio of work required by an isentropic process to the work that an adiabatic process actually needs to achieve the same pressure ratio. This efficiency also called adiabatic efficiency by some references. Figure 3.3 shows the state points and their positions in the compressor. The work required for the adiabatic compression process by the compressor wheel is simply calculated using equation 3.15.

$$W_c = h_{02} - h_{01} \quad 3.15$$

Because the compressor is regarded as a single component with a performance map which uses flow characteristics at the inlet and outlet points, it is more appropriate to modify equation 3.15 to use the properties at these points. Since no work is done after the compressor wheel and the flow is adiabatic:

$$h_{02} = h_{03} \quad 3.16$$

Isentropic efficiency will be represented by considering the compression process from 1 to 3.

$$\eta_c = \frac{h_{03s} - h_{01}}{h_{03} - h_{01}} \quad 3.17$$

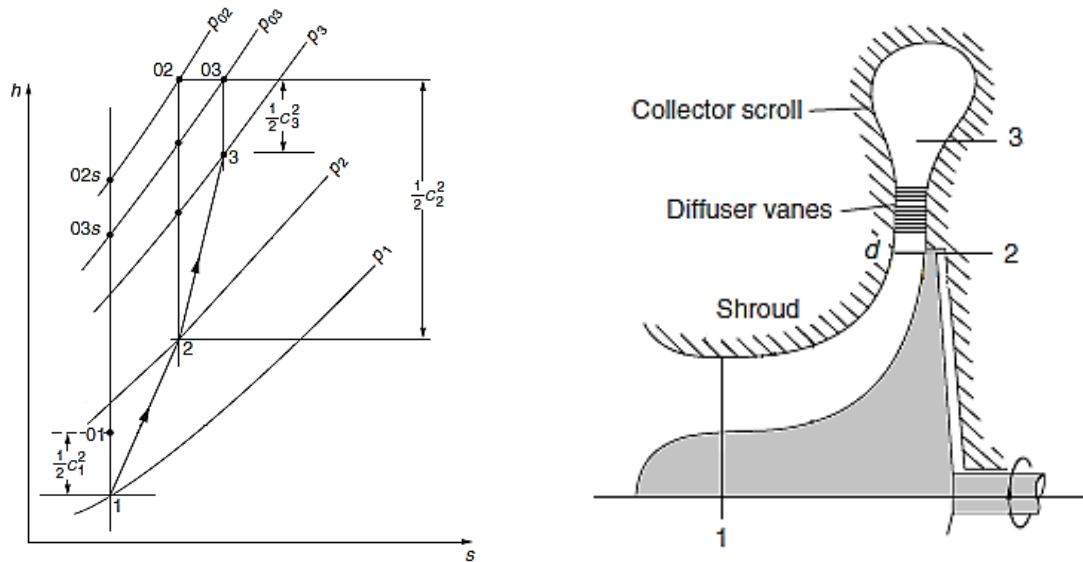


Figure 3.3 centrifugal compressor stage, Mollier diagram (left) and schematic (right) (Dixon & Hall, 2010)

Replacing the enthalpy terms with temperature and using the isentropic relations, the essential equation for the compressor is:

$$T_{03} = T_{01} \left[1 + \frac{\left(\left(\frac{p_{03}}{p_{01}} \right)^{(\gamma-1)/\gamma} - 1 \right)}{\eta_c} \right] \quad 3.18$$

Where the term $\left(\frac{p_{03}}{p_{01}} \right)$ is the compressor pressure ratio (π). Equation 3.18 can easily be used in combination with the compressor performance map when efficiency and pressure ratio are known from the other characteristics (equations 3.1 and 3.2).

The total pressure at the inlet is equal to the ambient pressure (p_{amb}) assuming no intake losses. For a compressor with a filter in the inlet, the pressure loss caused by the filter reduces the inlet pressure. Pressure loss is usually given in form of a percentage relative to the inlet value as is used for the calculation of the pressure loss in equation 3.19.

$$p_{01} = p_{amb} - \left(p_{amb} \left(\frac{dp}{p} \right)_{entry} \right) \quad 3.19$$

Turbine

The expansion process in the turbine and the main points are depicted in Figure 3.4. Here, the isentropic efficiency of the turbine is defined as the ratio of the work done by the turbine in the actual adiabatic process to the ideal isentropic expansion.

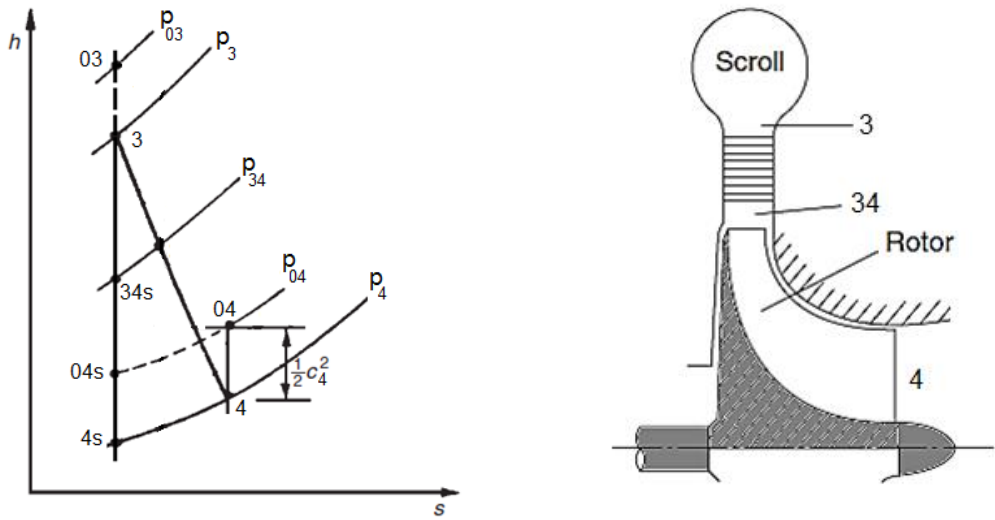


Figure 3.4 radial turbine, Mollier diagram (left) and schematic (right) from (Dixon & Hall, 2010)

When the turbine exhausts to the atmosphere, the kinetic energy of the flow is wasted and it is more appropriate to define its efficiency based on the expansion from the total pressure at the inlet to the static outlet pressure. This total-to-static efficiency is defined by the equation 3.20.

$$\eta_{ts} = \frac{h_{03} - h_{01}}{h_{3s} - h_{01}} \quad 3.20$$

The principal equation used for the turbine will be in the form of equation 3.21. The term $\left(\frac{p_{01}}{p_3} \right)$ is the total-to-static pressure ratio. For a simple un-recuperated cycle, p_3 is equal to the ambient pressure. Even if a diffuser is used to recover the kinetic energy of the turbine exhaust, it is possible to use the static pressure at the diffuser's outlet (ambient pressure) assuming the turbine and diffuser as a single component.

$$T_{03} = T_{01} \left[1 - \eta_{ts} \left(1 - \frac{1}{\left(\frac{p_{01}}{p_3} \right)^{(\gamma-1)/\gamma}} \right) \right] \quad 3.21$$

Recuperator

The governing equations of the recuperator are used in order to calculate the exit temperatures of the cold and hot streams. In general, the effectiveness of the recuperator shown in Figure 3.5 is given by equation 3.22.

$$\varepsilon = \frac{h_{c,o} - h_{c,i}}{h_{h,i} - h_{c,i}} \quad 3.22$$

Where 'h' is the enthalpy of the flow and the indices are as shown in Figure 3.5. Using the temperatures, the essential equation to calculate the recuperator exit temperature on the cold side, $T_{c,o}$ is calculated by equation 3.23.

$$T_{c,o} = T_{c,i} + \varepsilon(T_{h,i} - T_{c,i}) \quad 3.23$$

Assuming that no heat and flow leakage takes place in the recuperator and referring to Figure 3.5 for the definition of indices, it is possible to find a relation between the hot and cold sides like equation 3.24.

$$q = \dot{m}_c(h_{c,o} - h_{c,i}) = \dot{m}_h(h_{h,i} - h_{h,o}) \quad 3.24$$

$$\varepsilon = \left(\frac{\dot{m}_h}{\dot{m}_c} \right) \frac{h_{h,i} - h_{h,o}}{h_{h,i} - h_{c,i}} \quad 3.25$$

Where \dot{m}_h and \dot{m}_c are the mass flow rates in the hot and cold sides respectively. For given values of \dot{m}_h and \dot{m}_c , it will be possible to use equation 3.25 in combination with equation 3.23 and a characteristics map or mathematical representation of the recuperator.

Having pressures at the inlets of the cold and hot sides, the pressure loss in each side gives the outlet pressure value. However, for the hot side, if it directly outputs the flow to the ambient, then the static pressure at the exit will be equal to the ambient pressure. This will be used to calculate the static pressure at the turbine exit (equation 3.27).

$$p_{05} = p_{02} - \left(p_{02} \left(\frac{dp}{p} \right)_{recp,c} \right) \quad 3.26$$

$$p_4 = \frac{p_{amb}}{\left(1 - \left(\frac{dp}{p}\right)_{recp,h}\right)} \quad 3.27$$

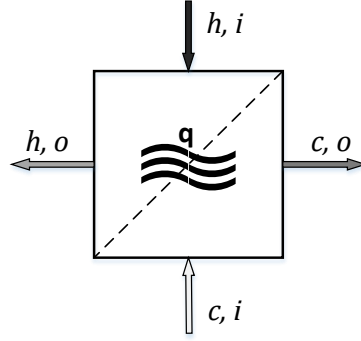


Figure 3.5 schematic of the recuperator

Optical components (CSP)

Having the optical efficiency of the CSP system from its characteristics map in the form of equation 3.10, it is possible to calculate the size of the dish (equation) 3.28.

$$A_{dish} = \frac{q_H}{DNI \eta_{opt}} \quad 3.28$$

The pressure at the inlet of the receiver is known from the recuperator cold side exit conditions. The receiver exit pressure is calculated by accounting for the pressure loss which is given by its characteristics map.

$$p_{03} = p_{05} - \left(p_{05} \left(\frac{dp}{p}\right)_{recv}\right) \quad 3.29$$

3.2.2 Energy and mass conservation

In the case of no flow leakage, the mass flow rate along the gas-path in a solar only MGT is constant as there is no added fuel. The conservation of mass is written in form of equation 3.30.

$$\dot{m}_c = \dot{m}_t \quad 3.30$$

Where \dot{m}_c and \dot{m}_t are the mass flow rates in the compressor and turbine respectively. A more complete form in the presence of leakage flows in the recuperator $\dot{m}_{l,recp}$ and the receiver $\dot{m}_{l,recv}$ is shown by equation 3.31.

$$\dot{m}_c = \dot{m}_t + \dot{m}_{l,recp} + \dot{m}_{l,recv} \quad 3.31$$

Conservation of energy leads to the calculation of the net shaft power, $PWSD$ assuming a mechanical efficiency, η_{mech} which includes the bearing losses and windage. The concept of mechanical efficiency may be defined as a percentage of the total work required by the compressor (Saravanamuttoo, et al., 2009). Therefore, the total consumed power can be represented based on the required power by the compressor and the mechanical losses as applied in equation 3.32. Electrical losses pertaining to the HSA are applied by multiplying its efficiency, η_{HSA} by its input mechanical power to determine the net electric power generated, PW_{HSA} . To calculate the net electric power output of the system, PW_e , an efficiency for the control equipment, η_{cnt} can be considered which accounts for their electrical losses. As such, PW_e can be determined using equation 3.34 provided that this efficiency is known. It will be shown in section 3.4.4 that this efficiency can be broken down further before it is calculated, using the design data of the pertaining equipment. The input heat to the gas-path from the receiver is given by the change in the total enthalpy of the flow when it passes through the solar receiver as shown in equation 3.35.

$$PWSD = \dot{m}_t(h_{03} - h_{04}) - \dot{m}_c(h_{02} - h_{01})/\eta_{mech} \quad 3.32$$

$$PW_{HSA} = \eta_{HSA}PWSD \quad 3.33$$

$$PW_e = \eta_{cnt}PW_{HSA} \quad 3.34$$

$$q_H = \dot{m}_t h_{03} - \dot{m}_c h_{05} = \dot{m}_t C_p TIT - \dot{m}_c T_{05} \quad 3.35$$

It should be emphasised that there are additional equations required to include losses in the MGT such as heat transfer, flow leakage and mechanical losses. However, such loss mechanisms require geometrical data which are normally not available at this stage.

3.3 Design point performance

Design point studies are discussed in this section as the initial step to do the performance simulation and analysis. Typically, the design of the components and their characteristics maps are not known when a new machine is to be designed. Therefore, there is no information to help build these maps or 'f' functions introduced in equations 3.1 to 3.14. The purpose of this section is to demonstrate the initial selection of the design point parameters, calculation of other performance parameters of the system at the design point and the application of operating limits, which will be used to derive a suitable initial value for the rotational speed at the design point.

However, such a design point will be just an 'initial' choice. The method which is proposed in the current thesis is based on the consideration of the annual performance to ultimately determine the system design point. This is done by the combination of an optimisation algorithm and

procedures which are demonstrated in this section. Throughout the calculations, component maps will be generated as they are required by the off-design performance model. The generation of the component maps and calculation of the off-design parameters will be discussed in the next two sections respectively.

To demonstrate the method used in this section and also in the next chapters, a case study is considered based on a dish-MGT system in the target power range of the OMSoP project. The design point calculation starts with the net output (nominal) power of the dish-MGT system.

3.3.1 Case study

A dish-MGT solar-only system with the nominal output power of 5kWe at the connection point to the grid is considered for demonstration of the methods used in this section. Having done the design point calculations, the results can be used in the consecutive sections. The presumed geographical point of installation is Casaccia, Rome, Italy, where the Italian national agency for new technologies (ENEA) is located. The annual DNI received in this area is about 1600-1700 kWh/m² (SolarGIS, 2011). Figure 3.6 shows the annual solar irradiance in the neighbourhood regions in Italy for comparison.

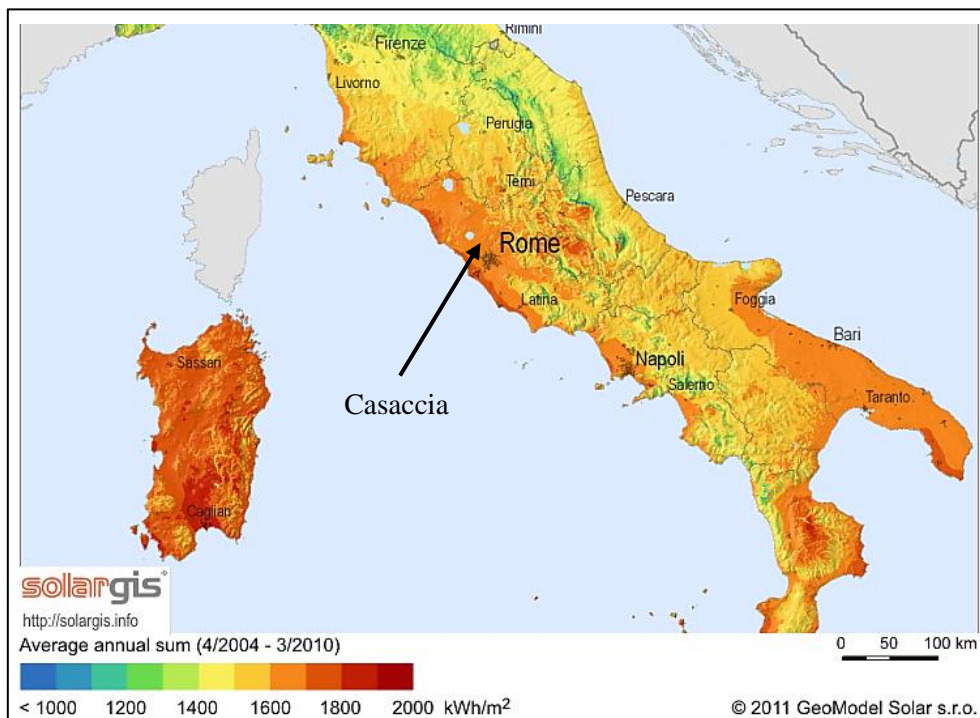


Figure 3.6 average annual solar irradiance in Italy between 2004 to 2010 (SolarGIS, 2011)

The climate conditions for the design point are assumed to be equal to the international standard atmosphere (ISA) at sea level as specified by the International Organisation for Standardisation (ISO):

$$T_{amb} = 288K \quad 3.36$$

$$p_{amb} = 1.01325bar \quad 3.37$$

$$\text{Relative Humidity (RH)} = 60\% \quad 3.38$$

3.3.2 Cycle analysis

For the design point calculations, characteristics of the components are not required to be in the form of functions or characteristics maps. For example the efficiency of the compressor is assumed as a fixed value shown in Table 3-1. Variation of this efficiency with speed or pressure ratio will be required only for the off-design calculations.

Table 3-1 components parameters

Component parameter	suggested in the literature	Reference	Selected value
η_c	73% - 76%	(Lee, et al., 2007)	74%
η_t	80% - 84%	(Lee, et al., 2007)	80%
ε	85%	(Rodgers, 2011) & (Visser, et al., 2011)	85%
$(dp/p)_{recp}$	4% (total)	(Vick, et al., 2010) & (Visser, et al., 2011)	2% cold side 2% hot side
η_{opt}	80%-85%	(Wu, et al., 2010)	85%
$(dp/p)_{recv}$	1% and 3%	(Vick, et al., 2010) & (Visser, et al., 2011)	2%
η_{mech}	95%	(Visser, et al., 2011)	95%
η_{HSA}	87% - 92%	(Vick, et al., 2010)	90%

Since none of the components parameters are known at the beginning, these values for each component are initially chosen from state of the art data available in the literature. Table 3-1 shows the values suggested by a number of references. The selected values for design point study are shown in the last column. To perform cycle analysis and determine the design point performance, the computational model developed in this work uses the governing equations introduced in section 3.2 and the values in Table 3-1. Although the rotational speed is related to the design parameters of the turbine and compressor, it is not directly included in the thermodynamic cycle analysis of the design point. This will be studied in more detail later in this section.

A parametric study to realise the performance is performed with the fixed values given in Table 3-1 and the variations of the main cycle parameters; TIT and pressure ratio. Results will help to

choose the initial design point based on a figure of merit which is the overall efficiency of the system. More efficient systems will be able to generate the same power with lower input heat which can be interpreted as smaller dish area. The variation range of TIT and pressure ratio is based on the achievable values in the micro gas turbine technology. For a dish-MGT system the maximum value of achievable TIT is determined by the solar receiver. The data matrix for the parametric study here is constructed using pressure ratio and TIT in the following ranges:

$$700^{\circ}\text{C} \leq T \leq 900^{\circ}\text{C}$$

$$2 \leq \pi \leq 4.5$$

Figure 3.7 shows the results of the parametric study for the variation of cycle parameters mentioned before. The results are shown in the form of overall efficiency against required mass flow rate in the MGT to generate 5kWe net power output. Mass flow rate is the main factor to determine the engine size and also rotational speed for a given pressure ratio. Lines of constant pressure ratio and TIT show how the efficiency and engine size change with pressure ratio for a specific turbine inlet temperature. A clear trend in the figure is that as the TIT increases, the maximum efficiency of the system takes place at a higher pressure ratio. While for a TIT of 700°C the maximum efficiency is achieved at pressure ratio of about 2.5, a pressure ratio of about 3.5 is required to achieve maximum efficiency for 900°C. For each constant TIT, the smallest size is achieved at pressure ratios higher than the maximum efficiency point.

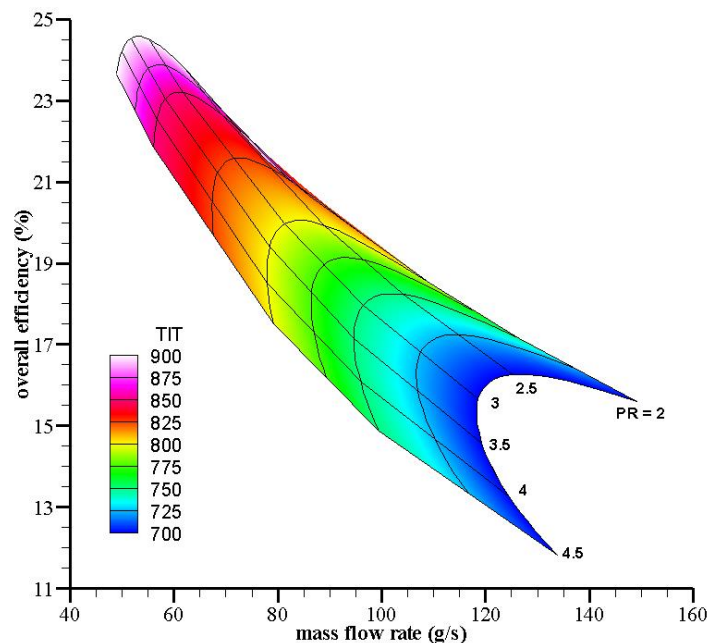


Figure 3.7 parametric study for the dish-MGT system for variation of cycle parameters

An important parameter calculated in this analysis is the turbine exit temperature which is critical for the recuperator because it determines the maximum temperature. This temperature increases with TIT while it reduces with the pressure ratio because a higher expansion ratio in the turbine results in a lower exit temperature. Figure 3.8 shows the contours of TET for the same cycle analysis of Figure 3.7. Maximum limit of the TET is determined by the recuperator material. For a recuperator with common austenitic stainless steels, the maximum continuous operation temperature is about 650°C (McDonald, 2003).

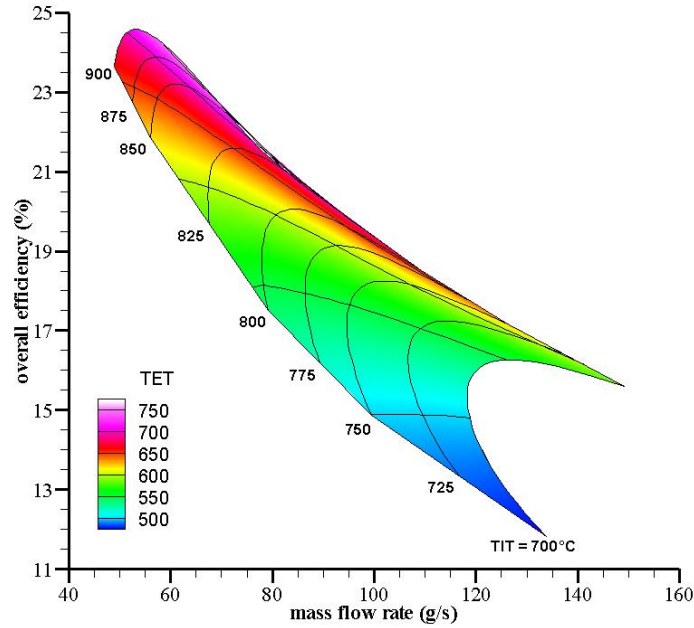


Figure 3.8 variation of TET in the same parametric study as Figure 3.7

3.3.3 Evaluation of the rotational speed

The above parametric study should also include the rotational speed of the MGT. This parameter affects the rotor dynamics and also the bearing system design and arrangement. Although speed doesn't directly appear in the above thermodynamic analysis, its value at the design point is related to the pressure ratio and mass flow rate of the engine. Such a relation can be realised by the definition of specific speed (equation 3.39). In this equation, Ω is the rotational speed in (rad/s), Δh_{0s} is the isentropic change of enthalpy across the wheel in (J/kg K) and Q is the volume flow rate (m^3/s) which is calculated based upon the density at the inlet conditions for the compressor and the outlet conditions for the turbine (Whitfield & Baines, 1990).

$$N_s = \frac{\Omega \sqrt{Q}}{\Delta h_{0s}^{0.75}} \quad 3.39$$

Compared to axial turbomachines, centrifugal compressors and radial turbines provide better performance for low specific speeds. It has been found that the suitable specific speeds for the compressor and turbine to achieve optimal efficiency in the micro-gas turbines, are about 0.6 and 0.5 respectively (Rodgers, 2013). Having used these general figures, the approximate design speed of the MGT can be derived from the mass flow rate and pressure ratio values. Figure 3.9 shows the contours of the dish area and constant TIT lines for the same case explained before. The size of the dish can be calculated by combining equations 3.35 and 3.51 and is considered as an important parameter in the initial cost of the system and its overall power density. The Two dashed lines limit the results to a region where the rotational speed and TET are within the system constraints. The maximum permissible value for TET is assumed to be 650°C for a stainless steel recuperator. Maximum limit for the speed of 150krpm is roughly considered as a limit for the simplicity of bearing system design, rotor dynamics and availability of a high speed alternator.

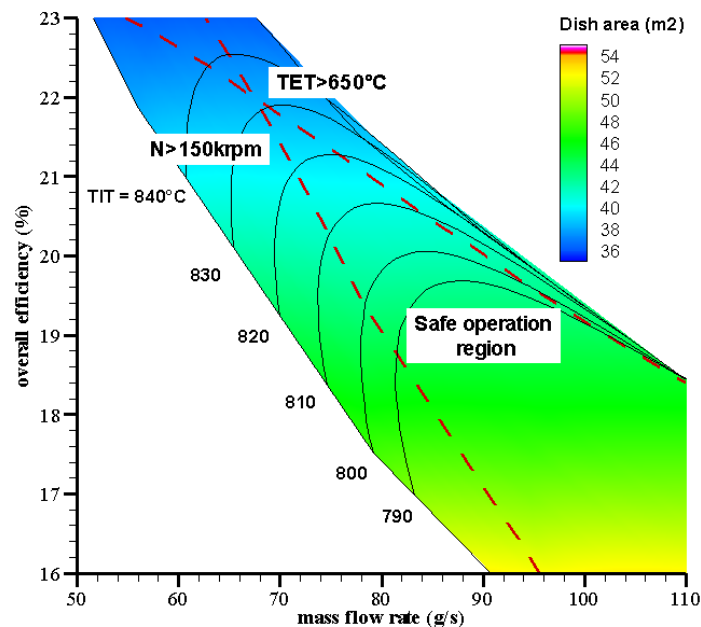


Figure 3.9 contours of dish area between the allowable limits of rotational speed and TET

Assuming the above mentioned values for TET and speed as the actual limits for the current case study, two dashed lines of constant TET and N are shown in Figure 3.9. Each of the lines separates the entire solution area into two parts to distinguish the safe operating region. The maximum system efficiency and minimum dish size within the safe operating limits are achievable with a TIT of about 840°C. However, this point is very close to the limiting boundaries. Selecting this point as the design point, the system would have problems at off-design conditions when lower expansion ratio or higher speed may force the system beyond its operating limits. A safer point can be picked on the TIT line of 800°C where the maximum efficiency is achieved which is also far enough from both limiting lines.

Having decided on the design point TIT value, the compressor pressure ratio which corresponds to the maximum engine efficiency and minimum dish size is chosen from Figure 3.9. Data for the selected design point are summarised in Table 3-2.

Table 3-2 design point data for the case study of section 3.3.1 (DNI, 800W/m²)

TIT (°C)	800	T ₀₁ (compressor inlet, °C)	15
Pressure ratio, π_c	3.0	p ₀₁ (compressor inlet, kPa)	101.3
N (krpm)	130	A _{dish}	42.07
q _H (kWth)	27.4	p ₀₃ (turbine inlet, kPa)	291.9
\dot{m} (g/s)	88	Overall efficiency (%)	20.7

3.4 Component models for design and off-design simulation

The characteristics of the components of the dish-MGT system were reviewed in section 3.1.1. The component models can be used in combination with the governing equations of section 3.2 to calculate the system performance. To achieve this goal, it is required that the mathematical representations of the f functions in 3.1.1 or alternatively, the performance maps for the components are known. In this section, it will be demonstrated how these performance maps or mathematical representations are built, based on minimum data, from the system design point. It should be clarified here that two design points are pointed out and used in this chapter especially for the scaling techniques. The component design point on its performance map is usually located where the efficiency of that particular component is at its maximum, while the system design point is determined by a number of cycle parameters similar to the data sets shown by Table 3-2. This is accomplished for most of the components including the compressor and the turbine by starting from a known component design (performance map) and then scaled to match the design point of the dish-MGT system. The scaling technique is chosen to minimise the required data and computation resource and time. This is considered as an important advantage because a large number of design and off-design calculations will be required when the optimisation algorithm is applied (chapter 5) to find system designs for optimal thermo-economic performance.

3.4.1 Performance maps of the turbomachinery

The characteristics of the turbine and compressor are indicated in equations 3.1 and 3.2. In addition to these parameters, a characteristic diameter, D (typically, tip diameter of the wheel), and viscosity of the fluid, μ are the main parameters that determine performance of a compressor or turbine. Using the similitude theory, these parameters are arranged in form of the following non-dimensional groups to represent similar machines.

$$\left\{ \left(\frac{p_{02}}{p_{01}} \right), \eta, \left(\frac{\dot{m} \sqrt{RT_{01}}}{D^2 p_{01}} \right), \left(\frac{ND}{\sqrt{RT_{01}}} \right), \left(\frac{p_{01} D}{\mu \sqrt{RT_{01}}} \right) \right\} \quad 3.40$$

R is the universal gas constant. The last two non-dimensional groups represent Mach and Reynolds numbers. Reynolds number is usually dropped since it is very high and its changes don't significantly affect the flow. However, it will be considered later in section 3.6 for the scaling of the turbomachines. For a particular compressor or turbine, it is also possible to drop the characteristic diameter and universal gas constant. The characteristics of the compressor and turbine then can be represented by equations 3.41 and 3.42.

$$\eta = f_{\eta} \left\{ \pi, \left(\frac{N}{\sqrt{T_{01}}} \right) \right\} \quad 3.41$$

$$\left(\frac{\dot{m} \sqrt{T_{01}}}{p_{01}} \right) = f_{\dot{m}} \left\{ \pi, \left(\frac{N}{\sqrt{T_{01}}} \right) \right\} \quad 3.42$$

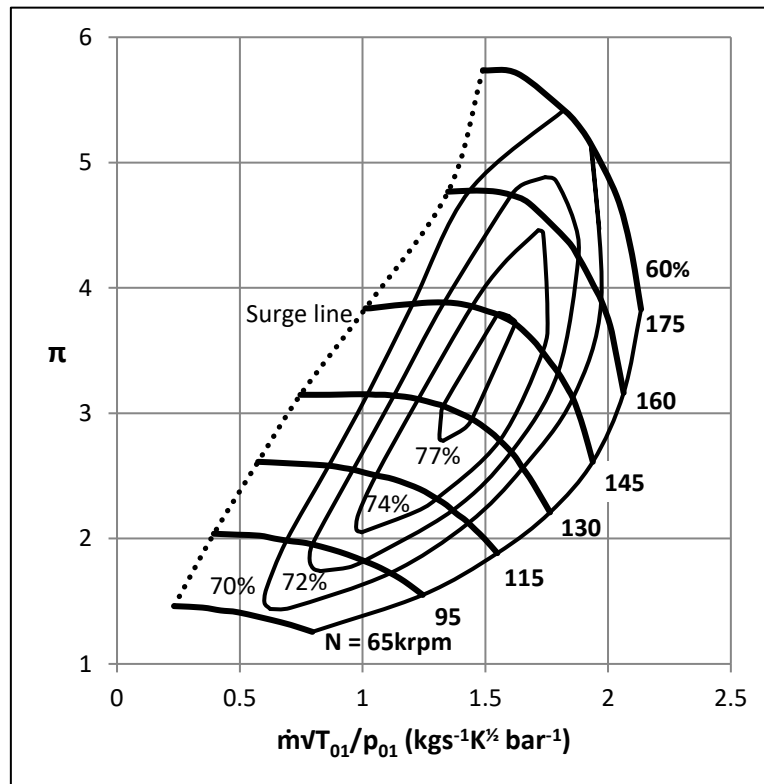


Figure 3.10 centrifugal compressor map

Functions f_{η} and $f_{\dot{m}}$ determine the variations of efficiency of the machine and mass flow rate with pressure ratio and the speed and are depending to its design. Ultimately, these functional are represented as compressor or turbine performance maps. Figure 3.10 shows a centrifugal

compressor map with constant speed lines and efficiency contours. The performance maps are generally given in non-dimensional (or quasi non-dimensional) format. If fully dimensional, the reference conditions of the map must be known. Using the non-dimensional groups of variables introduced in equation 3.40, the performance data which are taken from the map can be corrected for any particular inlet conditions.

$$\left(\frac{\dot{m}\sqrt{T_{01}}}{p_{01}}\right)_{corrected} = \left(\frac{\dot{m}\sqrt{T_{01}}}{p_{01}}\right)_{ref} \quad 3.43$$

$$\left(\frac{N}{\sqrt{T_{01}}}\right)_{corrected} = \left(\frac{N}{\sqrt{T_{01}}}\right)_{ref} \quad 3.44$$

In the method which is developed in the current thesis, two known performance maps for the compressor and turbine will be used as the basis to generate new performance maps using the scaling techniques. Consequently, it will be repeatedly required to read and process the digitised data of the compressor and turbine maps. However, the following problems appear when reading a typical compressor performance map, which must be addressed in the performance simulation code.

- The pressure variation for a given speed is not necessarily monotonic. Therefore, there can be more than one point corresponding to a particular pressure ratio for any constant speed-line
- The same problem occurs for non-dimensional mass flow rate when the compressor is in the choking region (right side of the speed lines)
- The range of variations of the pressure ratio and mass flow rate are different for each speed line which makes it difficult to represent a digitised performance map in a uniform table

To resolve these issues, an auxiliary coordinate, β is used (Mirandola & Macor, 1986) and (Kurzke, 1996). Equally spaced parabolic lines are generated on the compressor performance map so that they cover the performance characteristics area. The β number assigned to each β -line is just for indexing and doesn't have any physical meaning. Figure 3.11 shows the β -lines generated for a compressor map.

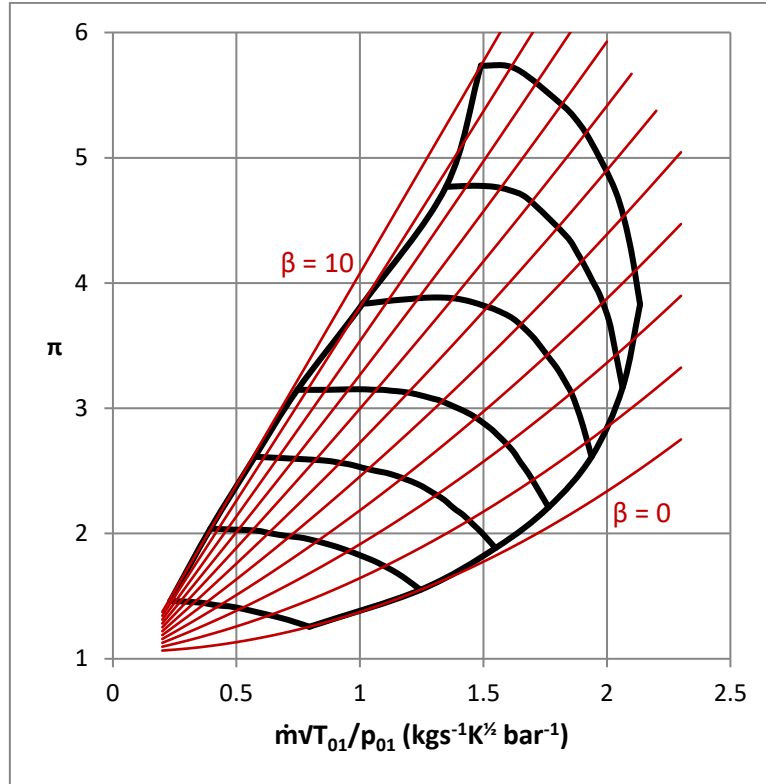


Figure 3.11 β -lines on the compressor map

The points that β -lines cross the speed lines can be used to generate a uniform table of data for all performance characteristics $\left(\frac{\dot{m}\sqrt{T_{01}}}{p_{01}}, \pi, \eta\right)$ without the problems mentioned before. Therefore, the compressor map can be ultimately represented by the following equations:

$$\pi = f_{\pi,comp} \left\{ \beta, \left(\frac{N}{\sqrt{T_{01}}} \right) \right\} \quad 3.45$$

$$\left(\frac{\dot{m}\sqrt{T_{01}}}{p_{01}} \right) = f_{\dot{m},comp} \left\{ \beta, \left(\frac{N}{\sqrt{T_{01}}} \right) \right\} \quad 3.46$$

$$\eta = f_{\eta,comp} \left\{ \beta, \left(\frac{N}{\sqrt{T_{01}}} \right) \right\} \quad 3.47$$

Performance maps of the turbine will be used in the form of equations 3.41 and 3.42 and do not require the introduction of β -lines. As it can be seen in Figure 3.12, using turbine pressure ratio and the speed lines, two other characteristics (i.e. mass flow rate and efficiency) can be easily represented and problems mentioned in reading the compressor map do not exist here.

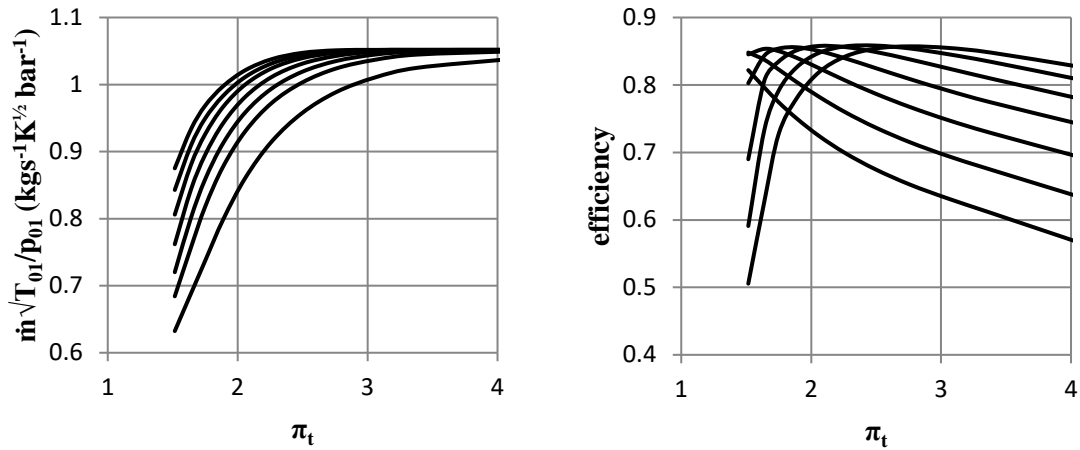


Figure 3.12 turbine performance maps, non-dimensional mass flow rate (left) and efficiency (right) against the pressure ratio

Choosing an existing compressor and turbine, their performance maps can be read and used by the computational model for scaling. For any set of system design point parameters similar to the data sets shown by Table 3-2, the performance maps should be scaled to match their new design point with the system design point data. This can be done by scaling techniques available in the literature. Two scaling methods, the so called ‘linear scaling’ and ‘constant speed scaling’ have been introduced and examined in the current thesis and are presented in details in Appendix A. The former is based on the similitude theory (Dixon & Hall, 2010) and has the advantage of providing the geometrical design in addition to the scaled performance map. However, it was shown that this method is not able to provide a complete match between the scaled map and the system design point. The constant speed scaling method is chosen in the current thesis because a full match between the scaled map and the system design point parameters is achievable using this method. Kurzke has applied this method for the development of the widely used gas turbine performance simulation code, GasTurb (Kurzke, 2012).

The method is based on the calculation of three factors to convert mass flow rate, pressure ratio and efficiency values of the design point of the original performance map, $((\dot{m}\sqrt{T}/p)_{R,map}, \pi_{R,map}, \eta_{R,map})$, to the system design point values at the same speed, $((\dot{m}\sqrt{T}/p)_{dp,map}, \pi_{dp}, \eta_{dp})$.

$$f_{mass} = \frac{(\dot{m}\sqrt{T}/p)_{dp}}{(\dot{m}\sqrt{T}/p)_{R,map}} f_{mass,RNI} \quad 3.48$$

$$f_{eff} = \frac{\eta_{dp}}{\eta_{R,map} f_{\eta,RNI}} \quad 3.49$$

$$f_{\pi} = \frac{\pi_{dp} - 1}{\pi_{R,map} - 1} \quad 3.50$$

Two Reynolds number correction factors, $f_{mass,RNI}$ and $f_{\eta,RNI}$, are applied to account for the viscous effects in low Reynolds conditions. Details of the calculation of these factors are given in 6.2.2 Appendix A.

3.4.2 Performance characteristics of the optical system

Characteristics of the optical components in the CSP system were introduced by equations 3.9 and 3.10. The relation between these characteristics is a function of the components' design.

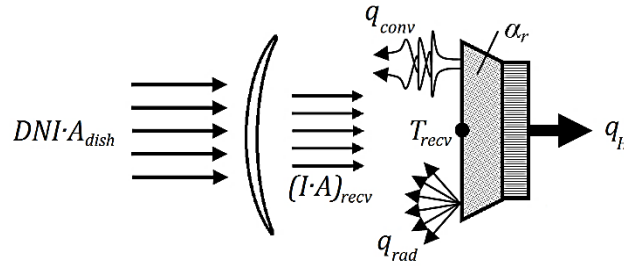


Figure 3.13 schematic of the CSP system components (parabolic dish and the receiver)

Figure 3.13 shows the losses in optical components from insolation received by the dish to conversion to the thermal power given to the MGT by the receiver. The optical efficiency of the CSP system is defined as the ratio of the thermal power generated by the receiver to the total solar power received at the surface of the dish:

$$\eta_{opt} = \frac{q_H}{A_{dish} DNI} \quad 3.51$$

Having considered the convection and radiation losses in the receiver and the optical losses in the dish, the energy conservation law for the receiver leads to equation 3.52 (Spelling, 2013).

$$q_H = I_{recv} A_{recv} \alpha_{recv} - \epsilon_{recv} \sigma A_{recv} (T_{recv}^4 - T_{amb}^4) - U A_{recv} (T_{recv} - T_{amb}) \quad 3.52$$

In this equation I_{recv} is the irradiance at the receiver's aperture which has an area of A_{recv} . The absorptivity and emissivity of the receiver's material α_{recv} and ϵ_{recv} are used to determine the amount of radiation absorbed by the receiver and the thermal radiation emitted to the surroundings. Temperature of the receiver, T_{recv} , can be approximated as the flow temperature at the receiver's exit (Lovegrove & Wes, 2012). This assumption results in the evaluation of the lowermost value for the heat losses in the receiver. Assuming that the receiver body is properly

insulated, the convection losses are only through its aperture window with an overall heat transfer coefficient U . Substituting q_H in the equation 3.51 and using the definition of concentration ratio, CR_g and optical efficiency of the dish (equations 2.3 and 2.4), the efficiency of the optical system can be arranged as:

$$\eta_{opt} = \eta_{dish} \alpha_{recv} - \frac{\epsilon_{recv} \sigma (T_{recv}^4 - T_{sky}^4) + U(T_{recv} - T_{amb})}{CR_g DNI} \quad 3.53$$

T_{sky} is the effective sky temperature and changes from about 230K for a cold and clear sky to approximately 285K for warm and cloudy conditions. An average value for moderate temperature with transient clouds can be assumed to be about 275K (Bergman & Incropera, 2011).

Equation 3.53 shows that the efficiency of the optical system is a function of the receiver's temperature and DNI. It also depends on the receiver's material properties, concentration ratio CR_g and dish efficiency. However, for a given system with these parameters fixed, performance of the system only changes with the DNI and receiver temperature.

Pressure loss in the receiver is a function of its geometry, mass flow rate and temperature. Since the designs of receivers are very different, a unique mathematical representation cannot be applied for the pressure loss. However, for turbulent flow which is normally the dominant flow regime in the receiver, it has been shown by Shah that the pressure loss can be calculated from equation 3.54 (Shah & Sekulic, 2003).

$$\Delta p_{recv} = 0.023 \frac{\mu^{0.2} 4L}{\rho D_h A_o^{1.8} D_h^{0.2}} \dot{m}^{1.8} \quad 3.54$$

Equation 3.54 shows that the pressure loss in the receiver is proportional to the power of 1.8 of the mass flow rate. It is also related to the viscosity μ and density ρ which are related to the gas temperature. Other parameters in equation 3.54 are related to the geometrical design and it is reasonable to assume they are fixed for a particular receiver. The viscosity of air is given with Sutherland's equation as a function of its temperature (Walsh & Fletcher, 2004):

$$\mu = 1.5105 \times 10^{-6} \frac{T^{1.5}}{T + 120} \quad 3.55$$

The density of the air is proportional to T^{-1} for a similar pressure. Therefore, if the pressure loss of the receiver is known for specific mass flow rate, inlet pressure and temperature (normally at the design point), the pressure loss of the same receiver in the off-design conditions can be calculated.

Figure 3.14 shows results of the CFD analysis for the pressure drop across a receiver provided by OMSoP project partners from KTH, Sweden. The receiver is of the cavity type and is designed for the 5kWe dish-MGT system of the OMSoP project (Aichmayer, 2015). CFD results were generated for five different mass flow rates equally divided into a range of 0.03kg/s to 0.12kg/s and five different temperatures. Individual points represent the CFD results for different temperature and mass flow rates. Two curves are fitted to the lowest and highest temperatures and are given in the form of $\Delta p = k\dot{m}^{1.8}$ with coefficient k representing the geometrical and temperature dependent factors appeared in equations 3.54 and 3.55. It can be seen that the correlated function with a power of 1.8 properly fits the simulation results. The ratio of the coefficients (k) of the fitted curves well matches the temperature analogy mentioned before. Therefore, variation of pressure loss for the receiver in terms of mass flow rate and temperature can be calculated by equation 3.56.

$$\Delta p_{recv} = 41160 \left(\frac{T_{recv}}{723} \right)^{1.3} \left(\frac{723 + 120}{T_{recv} + 120} \right)^{0.2} \dot{m}^{1.8} \quad 3.56$$

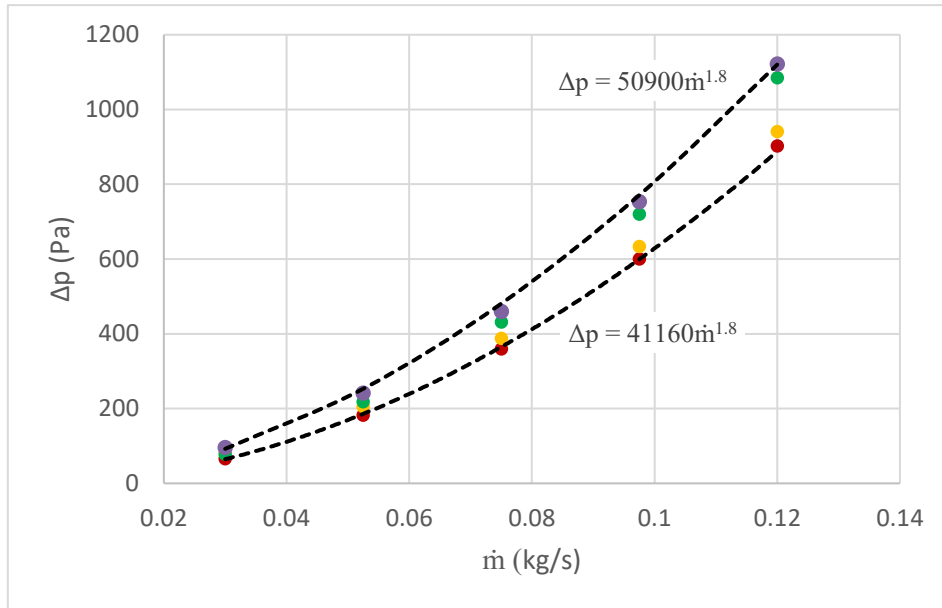


Figure 3.14 correlation for the pressure loss in a cavity receiver with $\pm 10\%$ deviation bounds

Equations 3.53 and 3.56 provide a simple model for the optical components independent from the geometrical design data to calculate the off-design performance of the optical system and are used in the present thesis for the performance analysis of the system.

3.4.3 The recuperator

To formulate a performance model for the recuperator, normally its detailed design and architecture of the core matrix must be known. However, before achieving an optimal design

point for the system, such a detailed design cannot be done. To provide a suitable model that can quickly generate performance maps of the recuperator with the minimum information during the iterative process of system optimisation, an approach similar to the method used for the scaling of the compressor and turbine is applied here. The base design for this purpose is a counter flow primary surface recuperator which was designed for the OMSoP project by one of the project partners, ENEA in Italy (Lanchi, 2015). This design is done according to the initial design point data which was introduced in section 3.3 (Table 3-2). For any other design point generated during the iterations, the performance maps of the recuperator will be scaled to match the new design point. Performance maps of the recuperator are shown in Figure 3.15 and Figure 3.16. It is a primary surface type which uses corrugated surface plates of type CC4-60 (Utriainen & Sundén, 2002) with an overall core size of 19x19x12 cm³.

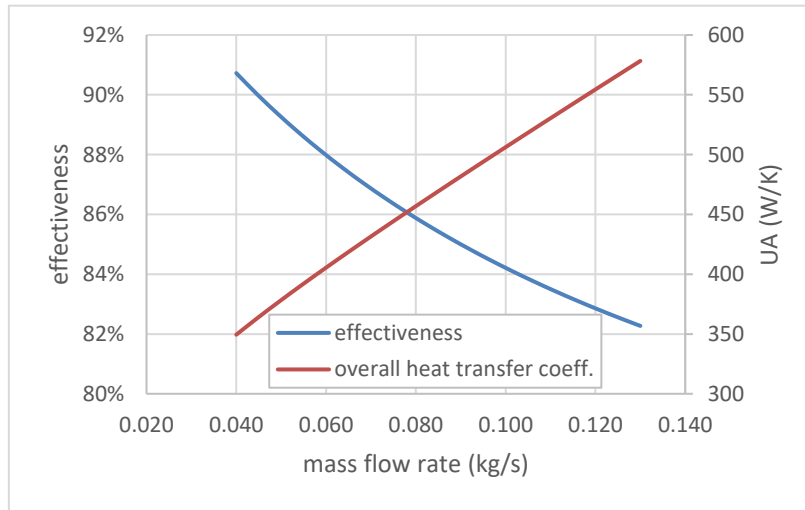


Figure 3.15 thermodynamic characteristics of the recuperator

To scale the recuperator performance maps for any design point of the system, the mass flow rate and recuperator effectiveness at the new design point are considered. Scaling of the performance maps will be done to match these parameters in the scaled maps with the new design point values. The effectiveness ε of a counter flow heat exchanger is given as a function of its number of transfer units NTU as shown by equations 3.57 and 3.58.

$$\varepsilon = \frac{1 - \exp(-NTU(1 - C_r))}{1 - C_r \exp(-NTU(1 - C_r))} \quad 3.57$$

$$NTU = \frac{UA}{C_{min}} \quad 3.58$$

Where C_{min} is the minimum heat capacity rate between the cold and hot sides and C_r is the ratio of this value to the maximum heat capacity rate. The overall heat transfer coefficient, UA depends

on the architecture of the recuperator core matrix and the mass flow rate passing through the matrix. For a fixed matrix design, it can be said that the variations of heat transfer coefficient, U will remain the same. Therefore, change in the effectiveness will be achievable by changing the size of the recuperator, A for a given mass flow rate. Knowing the design point data of the recuperator and its performance characteristics map, this concept can be used to scale the map for a different design point (mass flow rate and effectiveness) when a similar matrix structure is used.

The pressure drop in the cold and hot sides of the recuperator are shown in Figure 3.16. These losses are mainly functions of the recuperator geometry and mass flow rate. However, as far as the geometrical design of the matrix and distribution sections (i.e. aspect ratio of the flow passages) are kept unchanged, variation of the size doesn't significantly affect the pressure loss characteristics of the recuperator.

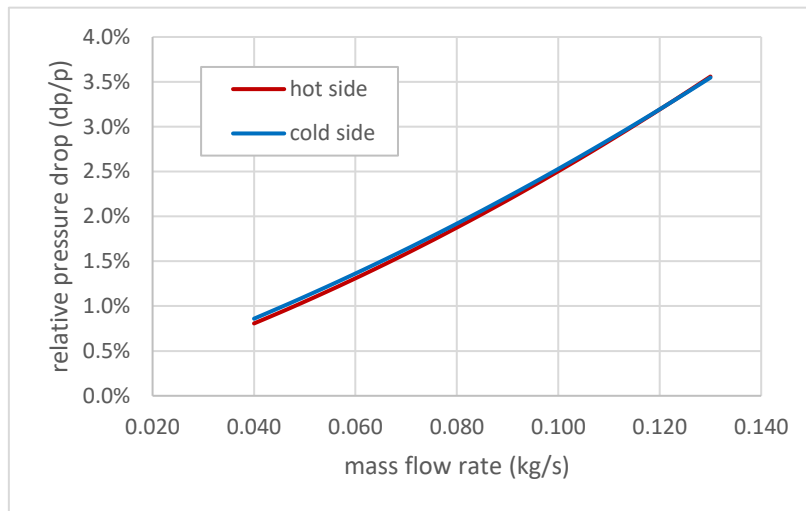


Figure 3.16 pressure losses in the recuperator

3.4.4 High speed alternator and power electronics

The high speed alternator is an AC, 3-phase high frequency voltage permanent magnet machine. Figure 3.17 shows the arrangement of the system in the power generation mode. Whenever required; such as start-up and shut down periods, the system will switch to motoring mode. The arrangement for motoring mode will be discussed in the next chapter. Performance of the HSA and power electronics is modelled as a single component and characterised by its overall efficiency that ultimately is a function of the rotational speed and power. The overall electrical efficiency, η_e is defined as the ratio of the output electric power to the shaft mechanical power, $PWSD$ which is supplied to the generator.

$$\eta_e = \frac{PW_e}{PWSD} \quad 3.59$$

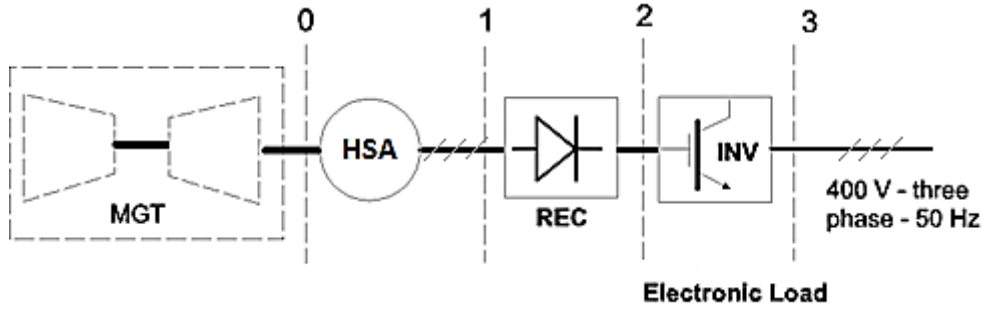


Figure 3.17 system arrangement schematic in power generation mode

Concerning the numbered stations introduced in Figure 3.17, $PWSD$ is given at point '0' and PW_e is taken at point '3'. A rectifier which is placed after HSA converts hi-frequency AC to DC where it can be regulated by a frequency inverter to be synchronised and fed to the grid. For the simulation and also laboratory tests, the inverter is used as a controllable load bank (rheostat). This function provides a means of system control and is described in chapter 4. The total electrical losses in the system consist of winding (inductive and resistive) losses in the HSA and the losses of the rectifier and inverter. Equations 3.60 to 3.62 represent the relation between these losses and the corresponding component efficiencies.

$$\eta_{HSA} = \frac{PW_{HSA}}{PWSD} = \frac{PW_1}{PWSD} \quad 3.60$$

$$\eta_{rec} = \frac{PW_2}{PW_1} \quad 3.61$$

$$\eta_{inv} = \frac{PW_e}{PW_2} \quad 3.62$$

Equation 3.63 is the energy balance for the high speed alternator and shows that the output voltage of the HSA, V_1 is equal to the no load voltage $V_{no\ load}$ minus the voltage losses because of the winding resistance, R_{HSA} and the reactance (inductive) losses, X_{HSA} in the stator when electric current, I passes through the HSA. The equation is presented in phasor (vector) form and the values of voltage and current are the RMS (Root Mean Square) values. In the equation the inductive losses are separated from other terms by multiplying them with the imaginary number j to emphasis that there is 90° phase difference between the resistance and inductive losses. Details of the derivation of equation 3.63 are given in Appendix B. The no load voltage and reactance losses are proportional to the rotational speed while the resistance of the winding is assumed constant since it is only a function of the temperature which doesn't significantly change during operation.

$$\vec{V}_1 = \vec{V}_{no\ load} - R_{HSA}\vec{I} - jX_{HSA}\vec{I} \quad 3.63$$

For any given speed and current, I , the voltage V_1 can be found from the solution of the equation 3.63 to allow for the calculation of HSA's output power, PW_1 . The input power to the HSA can be then calculated from equation 3.64. The losses (PW_l) can be modelled as a function of the rotational speed as shown in equation 3.65. Coefficients, resistances and winding reactance are normally given by the manufacturer.

$$PW_0 = PW_1 + 3R_{HSA}I^2 + PW_l \quad 3.64$$

$$PW_l = k_{HSA}N \quad 3.65$$

The main losses in the rectifier are ohmic because of the resistances inside its circuits (equation 3.66). For the inverter, a constant efficiency is normally provided by the manufacturer.

$$PW_1 = PW_2 + 3R_{rec}I^2 \quad 3.66$$

As it is explained in Appendix B, the equations governing the electrical system are solved for a high speed alternator which is specifically designed for the OMSoP project to provide its performance map. In generating the performance map, the maximum current limitation is also taken into account. Figure 3.18 and Figure 3.19 show the performance maps for selected rotational speeds from 70krpm to 150krpm with the rated speed at 130krpm that match the design point value of the dish-MGT system. Further details on the contributions of each of the electrical components in the output power have been given in Appendix B.

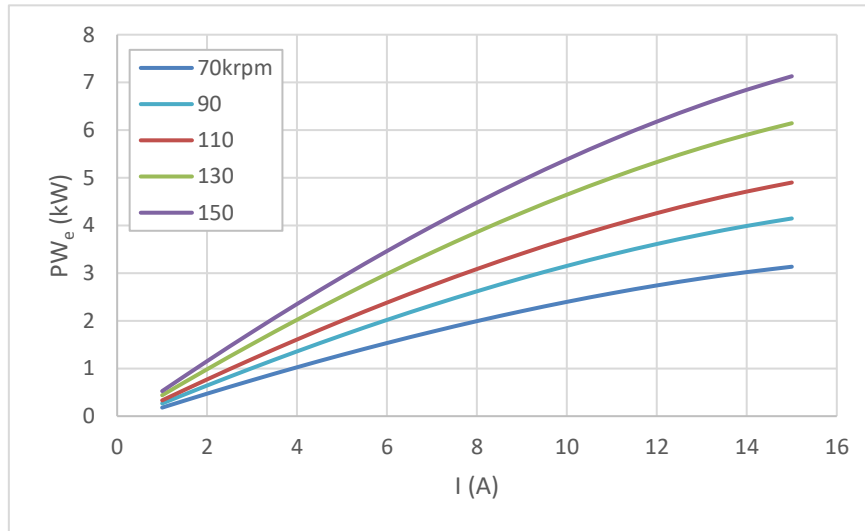


Figure 3.18 variation of net output power of the electrical system with electric current for different speeds. Current in electrical machines is proportional to the torque exerted by the load.

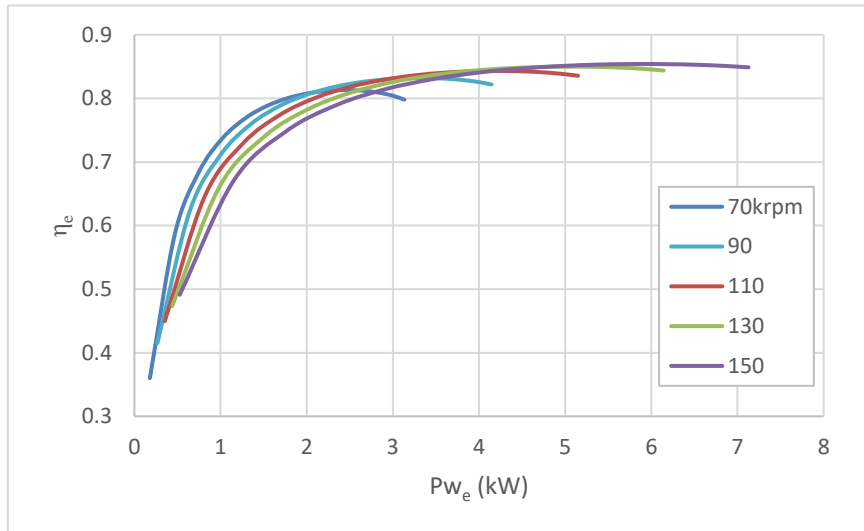


Figure 3.19 overall efficiency of the electrical system

Because the system study for finding the optimal design point of the dish-MGT system is done for a fixed net output power, performance of the high speed alternator will not change. However, when the power rating of the HSA changes, the performance maps will change and can be calculated by solving equation 3.63 that is introduced here using the new design point data as the rated data of the HSA. However the performance curves of the electrical system have been scaled by the ratio of the rated power assuming the same behaviour of the systems.

3.5 Off-design performance

The dish-MGT system runs at the design point as long as all conditions remain fixed at this point. For a purely solar powered system, changes in the climate conditions (DNI, inlet temperature and pressure) or electrical load will run the system to off-design performance. To calculate the off-design performance, such changes in the climate or boundary conditions are given to the computational model as the input data. The general structure of the model, which is schematically represented in Figure 3.1, shows how these data modules are related to the core of the computational model.

The general procedure of the off-design calculation in the core of the computational model is similar to that of the design point. However, rather than using fixed performance parameters for the components, their models which were introduced in section 3.4 are used. As explained in section 2.5, the calculation procedure of the engine performance can be done by either local or global iteration methods. Because of the advantages of the global iteration method and its potential for modelling different cycle architectures, this method is used for the development of

the performance simulation code in the current thesis. In accordance with this method, the governing equations of the section 0 are defined in form of a set of equations:

$$\mathbf{F}(\mathbf{X}) = \mathbf{0} \quad 3.67$$

Where $[\mathbf{F}]$ represents the functions derived from the governing equations discussed in section 3.2 and $[\mathbf{X}]$ includes the unknown parameters in the system. The unknown parameters for a single shaft recuperated cycle, which are defined in the computational model, are shown in equation 3.68. Eight equations based on the governing equations introduced in section 3.2 and eight unknown parameters make a consistent system of equations for the dish-MGT system.

$$X = \begin{bmatrix} \beta \\ T_{02} \\ T_{03} \\ T_{04} \\ T_{05} \\ p_{03} \\ \pi_t \\ (N/\sqrt{T})_t \end{bmatrix} \quad 3.68$$

Index t corresponds to the turbine. β is the auxiliary coordinate in compressor map and T_{02} to T_{05} are the temperatures at the stations numbered in Figure 3.2 (N/\sqrt{T}) and is the non-dimensional speed. The global iteration approach has the advantage that any changes in the architecture of the system can be applied with minimum effort and alterations in the computational model. If a component is added to the system for example in the case of replacing a simple cycle with a reheat cycle, the model can be easily adapted by applying the added governing equations and unknown parameters to the set of system performance equations (equation 3.67). For any given DNI, the computational model solves the system performance equations which provide all the data required to calculate the generated power. Alternatively, it is possible to modify the energy conversion equation to use generated power as the input data and calculate the required solar heat to the system. It is also possible to set other variables like the turbine inlet temperature (T_{03}) or the rotational speed as the input by changing the corresponding equations in the set of system performance equations 3.67.

An important point which must be taken into account is that the working point of the system for any given set of input data (DNI and ambient conditions) will be unique. However, when one of the component models or boundary conditions (electrical load) are not fully defined or fixed, equation 3.67 will have a degree of freedom (DOF) greater than zero which means that for a given DNI, the system performance result is also dependent on an additional parameter pertaining to the under defined component model or the boundary condition. For example if the electrical load

on the system is not defined, the generated power by the dish-MGT system at a particular DNI is not constrained by the electrical load and can be changed by varying any of the variables of the system such as the rotational speed, TIT or TET as the additional input parameter. This is an interesting case which can be applied to the pure solar dish-MGT systems because these systems cannot follow load variations like the fuelled gas turbines. Such application and the options for the operation of pure solar dish-MGT systems is discussed in detail in chapter 4.

The solver of the equations is developed for the performance simulation tool based on an improved globally convergent Newton-Raphson algorithm which has been introduced for a non-linear set of equations (Press, et al., 2002). Generally, the Newton-Raphson method requires the derivatives of $[F]$ for the calculation of the Jacobian matrix. However, the algorithm which has been introduced by Press et al. is based on a finite difference routine and doesn't require the analytical form of the $[F]$ functions.

3.5.1 System constraints

The performance of any dish-MGT system is limited by some operational constraints which must be taken into account while simulating the system's behaviour at off-design conditions. The main limitations that apply to dish-MGT units have been already introduced as the maximum receiver and recuperator temperatures and maximum rotational speed. These boundaries are mainly based on the functions of the materials used in the construction of the components and rotor assembly dynamic characteristics. A further constraint is the maximum current which the high speed alternator is able to tolerate during operation. For the sample case study here, these boundaries are defined as:

$$TIT_{max} = 800^{\circ}C \quad 3.69$$

$$TET_{max} = 650^{\circ}C \quad 3.70$$

$$N_{max} = 150krpm \quad 3.71$$

$$I_{max} = 13A \quad 3.72$$

The computational model uses these conditions to ensure that the performance of the system is confined within the safety limits.

3.5.2 Performance results

The system performance results are presented and discussed in this section. The system is considered to be the pure solar dish-MGT system with the recuperated Brayton cycle which was

introduced as the case study in section 3.3.1. To avoid free power generation, which is left for the next chapter, it is assumed that the high speed generator operates at its maximum current. Without variation of the electric current, the performance of the high speed alternator will be only a function of the rotational speed which is similar to the case when an electrical load is actually applied to the system. Figure 3.20 shows the generated power due to variation of the DNI. As the DNI changes, the input heat to the receiver change and affects the system performance. The graph shows that power generation will not start until the DNI reaches a certain value. This point is of special interest because it specifies the conditions at which the MGT may generate power. Any drive which is supposed to run the system from the stationary state, must be capable to speed up the MGT at least to this particular point. As the DNI increases, the system will generate more power with the maximum efficiency at the design point. For DNIs higher than the design point value, generated power still increases, but at a lower rate.

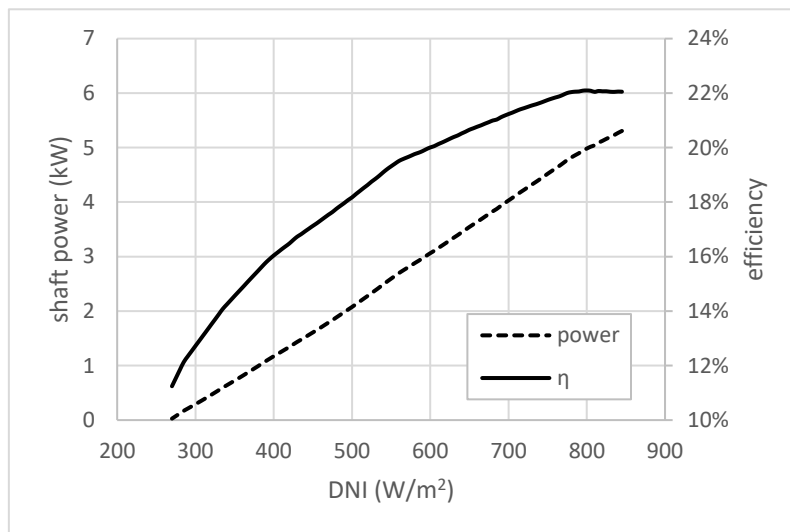


Figure 3.20 system performance for the variations of DNI. Dish-MGT system cannot deliver any positive power below a certain DNI

The effects of variation of the rotational speed, mass flow rate and turbine inlet and exit temperatures are shown in Figure 3.21 and Figure 3.22. It can be seen that the TIT exceeds the maximum allowable value for the receiver. At lower speeds; on the other hand, the TET moves beyond the safety limits. Such variations are inevitable when the performance of the HSA is fixed by its characteristic curve, as shown in Figure 3.19. However, in most cases, the high speed generator can be controlled to work at any other point in the region below its nominal performance curve. As such, a control system will be required to change the working point of the HSA and keep the working conditions of the dish-MGT system within the safety limits defined in equations 3.69 to 3.71.

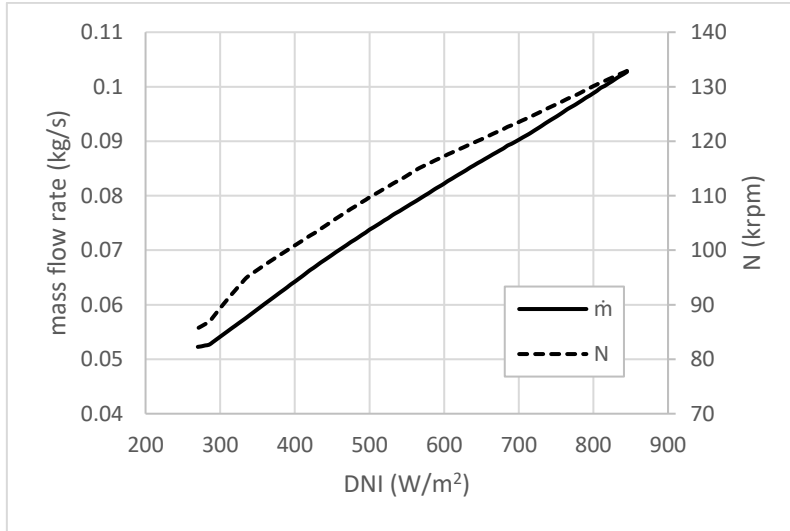


Figure 3.21 mass flow rate and speed of the MGT

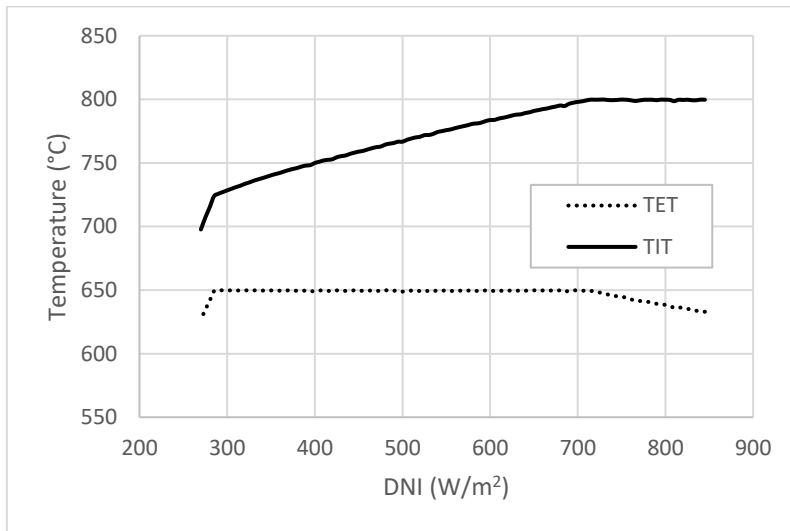


Figure 3.22 variation of turbine's inlet and exit temperature with DNI

Variation of the DNI changes the working point of the MGT; consequently, the position of the working point on the compressor map will also change as shown in Figure 3.23. The working point moves towards a higher speed, pressure ratio and mass flow rate when the DNI increases. Such behaviour has been already seen in Figure 3.21 and Figure 3.22. Knowing the position of the working point, it is possible to determine its corresponding surge margin. The surge margin is defined by the mass flow rate, pressure ratio or both of these parameters at the working point. A definition which is used here is shown by equation 3.73. The critical value for the safe operation of the compressor based upon this definition is 15-30% (GSP, 2014).

$$SM = 100 \left(\frac{\dot{m}\pi_{surge}}{\dot{m}_{surge}\pi} - 1 \right) \quad 3.73$$

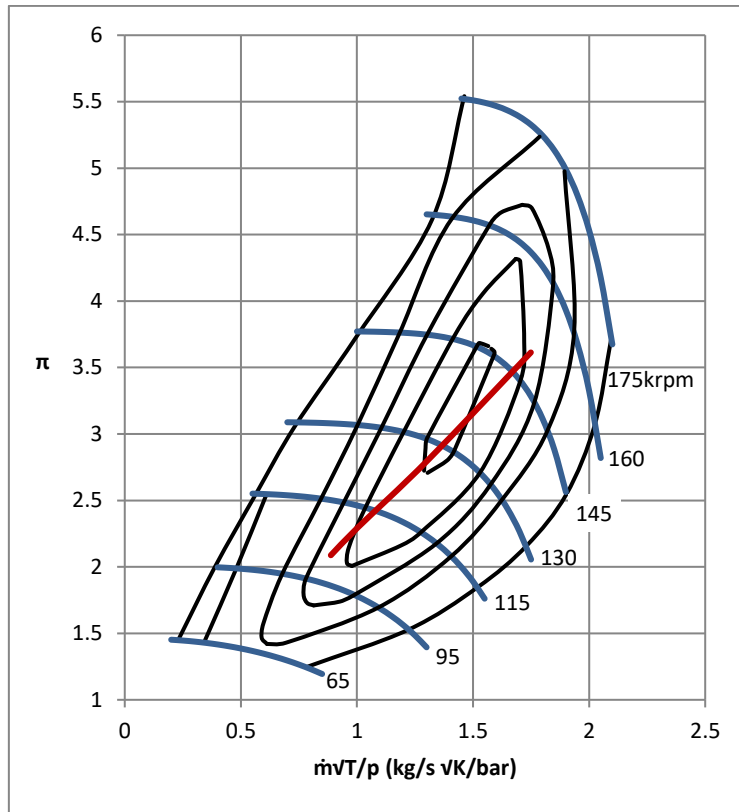


Figure 3.23 running line of the MGT for the full range of the variation of DNI

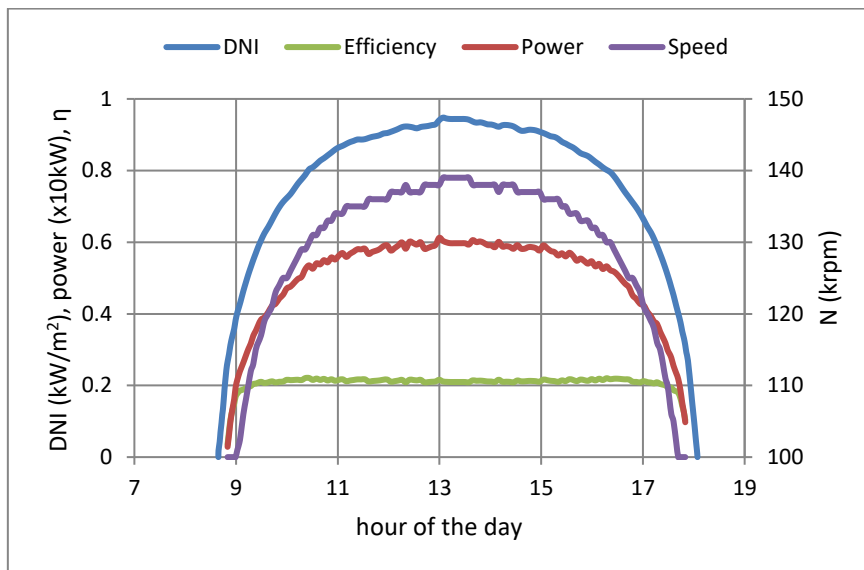


Figure 3.24 variation of DNI and corresponding system performance during a summer day, Casaccia

The performance of the system at any particular place depends on the variation of DNI and ambient conditions. It can be calculated in a similar way to that of the performance calculation for the whole range of DNI variation as above. However, the DNI value or ambient conditions can be very different even for the same place during a year. This difference can be clearly seen in Figure 3.24 and Figure 3.25 which show the performance of the system on two different days.

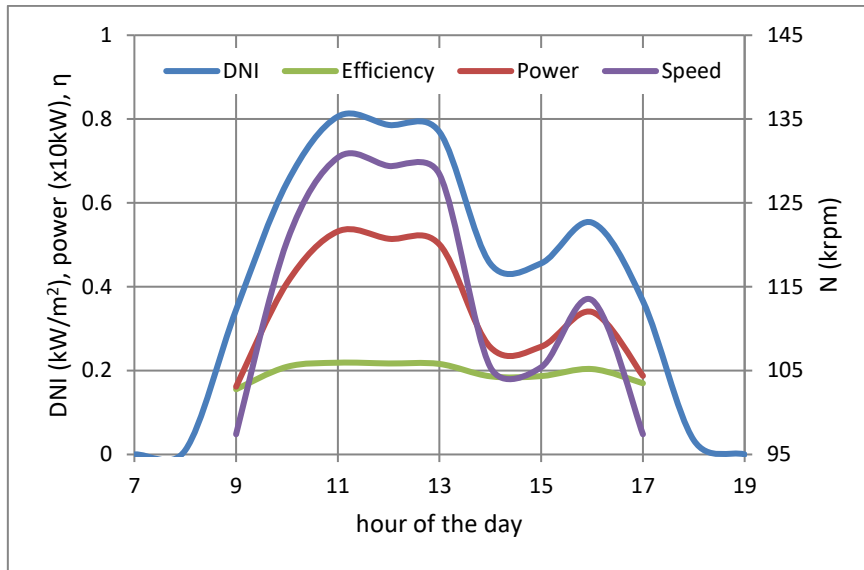


Figure 3.25 variations of DNI and corresponding system performance during a winter day, Casaccia

The calculation of the system performance must be done for a long period of time, at least for a full year, to provide a more reliable estimate of the overall system performance. To demonstrate the method described in this chapter, two different locations have been considered; namely Casaccia in Italy, where the dish-MGT of the OMSoP will be installed, and Seville in Spain where a number of solar powered installations have been already made and which has a good potential for solar power generation in Europe.

Comparison of the overall performance of the system has been done for these locations by the calculation of the annual generated electricity by the solar-only dish-MGT system. DNI data for these two areas are taken from SoDa services, which provides solar radiation data for a wide area on the Earth (SoDa, 2016). The annual solar irradiance is calculated per unit area of a plane which is always perpendicular to the direction of radiation. It is determined as the sum of the average DNI value received over a short time interval multiplied by the time interval's length. Therefore, it is calculated in terms of energy and is normally represented in MWh/m². The annual generated electricity is the cumulative result of the net generated electricity in each time interval. The generated electricity for each time interval is calculated based on the average DNI during that period. Figure 3.26 shows the annual solar income and the generated electricity for the installation of a dish-MGT in Casaccia and Seville. It can be seen that the system is able to generate more electricity in Seville because of its higher solar irradiance received during one year. It should be noted, however, that these results are achieved for the dish-MGT system of the case study and may be improved by improving the system design which will be discussed in chapter 5. Besides, the system is assumed to use the HSA with a constant electrical current. In practice, better

operation strategies can be applied to the pure solar micro gas turbines which result in better performance and is discussed in the next chapter.

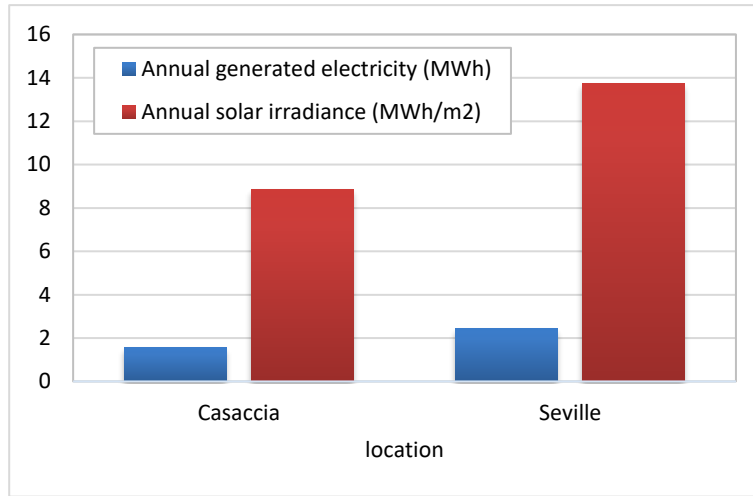


Figure 3.26 Annual solar irradiance and generated electricity for Casaccia and Seville

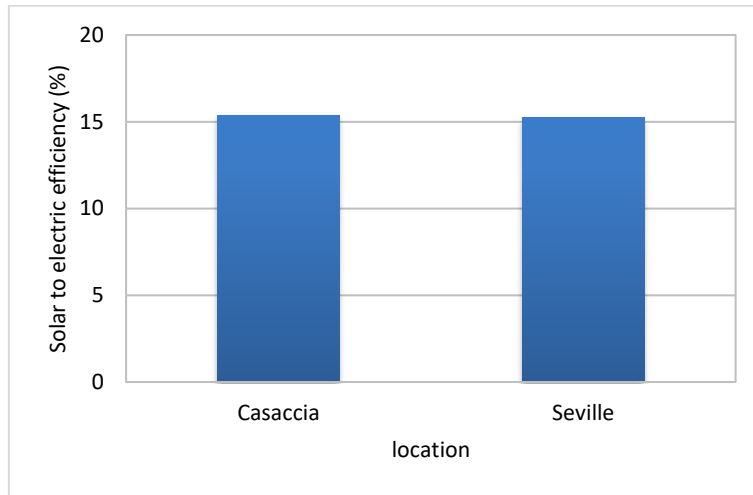


Figure 3.27 solar to electric efficiency of the dish-MGT system in Casaccia and Seville

An important parameter in the evaluation of the overall performance of the dish-MGT system is the solar to electric efficiency which is calculated as the ratio of the annual generated electricity, E_{an} , to the total solar irradiance received at the dish aperture area during a year as shown by equation 3.74.

$$\eta_{solar} = \frac{E_{an}}{DNI_{an}A_{Dish}} \quad 3.74$$

Where DNI_{an} and A_{Dish} are the annual DNI and aperture area of the dish respectively. The solar to electric efficiency or simply solar efficiency of the dish-MGT for the chosen locations is shown in Figure 3.27. It can be seen that the effect of the higher solar irradiance in Seville on the solar

efficiency is not very significant because the solar to electric efficiency is strongly depended on the efficiency of the MGT which is determined by the design point.

3.6 Conclusions

It has been shown that the computational model developed in the current thesis is capable of calculating the design and off-design performance of the system. Component maps are required when using this model and it was shown that these maps can be generated using a scaling method. It was demonstrated that this method is relatively quick and simple. In the method which is developed in this chapter, the performance maps of the components or their mathematical representations are generated using the design point data and, therefore, depend on the system design point. However, it was shown that simple empirical off-design models, which are mainly based on the design point performance, are not adequate and reliable to realise details of the off-design performance such as the minimum DNI required for the self-sustaining point or the surge margin and a component based model is required to approximate these details more accurately.

Furthermore the following points can be concluded from the results presented in this chapter.

- To evaluate the performance of a solar powered system, it is required that the system performance is calculated for a long period of time, preferably one year or several years to address the seasonal variations of the DNI.
- The performance of the dish-MGT system is affected not only by its design, but also by the way that it is connected to the electrical load.
- Free power generation provides more options to operate the system which result in different system performance
- Off-design performance correlations do not take the effects of system operation into account and therefore are reliable enough only for the particular case that they have been developed for.
- One of the outcomes of the developed method is the component design and associated performance maps, which compared to an empirical correlations, is a step forward allowing the ultimate components design to be easier

4 Control strategies for the solar micro gas turbines

4.1 Introduction

This chapter is dedicated to the control of a solar-only dish-MGT system. The performance of the system is directly related to the way that it is operated. Several operation strategies, used for micro gas turbines, have been studied and compared at the beginning of this chapter. An important fact which has been taken into account is the safe operation limits of the MGT and their effects on the applicability of each strategy. Based on the study of these strategies, an operation strategy which allows for maximising the power generation has been proposed. The structure of a control system to operate the dish-MGT is briefly explained. The control system requires to change the rotational speed of the high speed alternator and a sensitivity analysis has been done to compare three power regulation strategies based on voltage, current and output power. The key point which makes a big difference between the control of solar-only micro gas turbines and fuelled MGTs has been also discussed in this chapter. While the input heat to a solar-only MGT is dictated by the solar irradiance, fuelled MGTs are easily controlled by changing the input heat via the variation of fuel flow. Additionally, even if the solar heat, received at the aperture of the solar receiver, is controllable, its characteristics are far different from fuel flow to the combustor particularly in terms of rate of change which can be applied to each of them. It is shown in this chapter that when the proposed strategy is applied by power regulation, the system can only be used where it is connected to a large or flexible power grid. For the cases where the electric load on the system varies independently, a new concept has been introduced, which allows the system to operate in the safe envelope and generate electricity, to meet instantaneous power demand while the DNI is changing. A comparison of the system performance, when each of the operation strategies are applied, is given in the last section before the conclusions on this chapter are provided.

It is important to emphasise here that this thesis focuses on the control strategies and hence, applies to off-design steady-state simulation rather than the development of the actual controller.

Obviously, development of the controller requires dynamic simulation of the system. The implementation of a control strategy into the actual system may require re-consideration of the proposed loops based upon possible system stability issues.

4.2 Micro-gas turbine operation strategies

The main operation strategies that are applied to the conventional (fuelled) micro gas turbines are devoted to keep one of the MGT parameters constant, namely Speed, TET or TIT (Traverso, 2004). These strategies are applied by variation of the fuel flow as the controlling parameter. The first one has the advantage of operating in a fixed rotational speed which in turn results in a constant output frequency. Therefore, to adapt the generated power to the main power grid, the control system would require relatively simpler power electronics in comparison to other operation strategies, hence, lower cost. The key advantage of the second strategy is to avoid thermal cycling which is not desirable in particular for the recuperator as its temperature at the hot side inlet (TET) is kept constant in this method. This strategy will also allow the MGT to work on one of its ultimate operation limits if TET is set to its maximum allowable value. The generated power is then expected to be higher than the constant speed strategy, but at the cost of variable speed. The TIT constant control allows to achieve maximum power generation. Similarly, this will result in variable speed. In this operation strategy TET will not be constant, but compared to constant speed control there will be much smaller variations in TET. Additionally, this method requires reliable measurement of TIT to use it in the control system. Measurement of TIT requires carefully designed temperature probes to avoid all potential sources of reading errors such as radiation and conduction effects (Wilson, et al., 2012) and (Massini, et al., 2011).

In a fuelled micro gas turbine, variation of the fuel flow changes the input heat given to the engine and controls its performance. However, in a solar powered MGT, the input heat is provided by the solar radiation received at the dish and therefore it is directly determined by DNI. As such, to compare the system performance of a solar powered MGT under any of the above mentioned strategies, variations of DNI is considered. Clearly, the system would work at its design point only when the DNI and environmental conditions are equal to the rated values as specified in Table 3-2.

The system performance under the above mentioned strategies is presented in the following subsections. The system constraints for safe operation limits which were introduced in section 3.5.1 by equations 3.69 to 3.72 determine the practical range of DNI variations in which the dish-MGT system would be able to operate. These limits are determined by maximum allowable

temperatures in the solar receiver and recuperator, maximum rotational speed and maximum electrical current allowed in the high speed alternator. The system performance within these limits is shaded in the graphs which are presented in this section to indicate the operating boundaries. However, the performance simulations were carried out beyond these limits to provide a wider picture of each corresponding operation strategy. Unless otherwise specified, results in this chapter are calculated using the data and the performance maps that were generated for the case study introduced in section 3.3.1. To compare the operation strategies introduced here, the generated electricity is considered as the main performance parameter while the efficiency of the MGT is also studied. The computational model which is developed in the current thesis performs steady-state performance simulation. Although a transient simulation is typically essential for the design of the control system, it is not required here because the purpose of the simulations and analysis done in this chapter is about devising a control strategy and not designing a control system.

4.2.1 Constant rotational speed operation

Simulation results when constant speed strategy is applied are shown in this section. Simulations were done based on the model presented in chapter 3 and for the variations of DNI from zero to 1200W/m² with ambient conditions set to be equal to ISA conditions given by equations 3.36 to 3.38. The results are represented in normalised form for easier comparison. Normalisation is done using the design point data, (TIT_{dp} , TET_{dp} , PWe_{dp} , η_{dp} , N_{dp}) in Table 3-2 and equations 4.1 to 4.5. The normalised parameters are shown with an asterisk (*).

$$TIT^* = \frac{TIT}{TIT_{dp}} \quad 4.1$$

$$TET^* = \frac{TET}{TET_{dp}} \quad 4.2$$

$$PWe^* = \frac{PWe}{PWe_{dp}} \quad 4.3$$

$$\eta^* = \frac{\eta}{\eta_{dp}} \quad 4.4$$

$$N^* = \frac{N}{N_{DP}} \quad 4.5$$

Figure 4.1 and Figure 4.2 show the variations of the turbine's inlet and exit temperatures when MGT is controlled to operate at constant speed. As it can be seen, for any particular speed, the

MGT would be able to operate only in a very limited range of DNI. As an example, working constantly at the design speed (DNI* equal to one), the system would be able to work only when DNI* is changing from 0.68 to 1.0 which is equal to the variation of DNI from 550W/m² to 800W/m². The figures, however, show that the operation in a wider range of DNI is possible if different speeds are chosen (i.e. lower the speed with DNI).

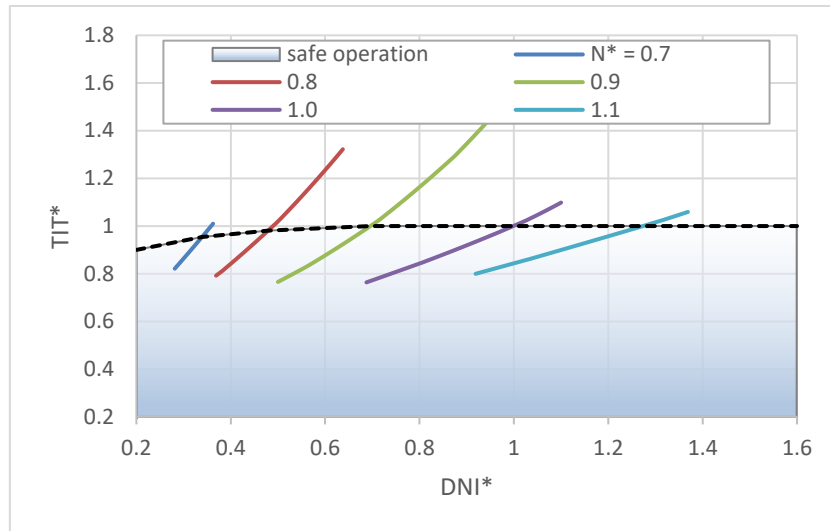


Figure 4.1 variations of turbine inlet temperature when MGT operates at different constant speeds

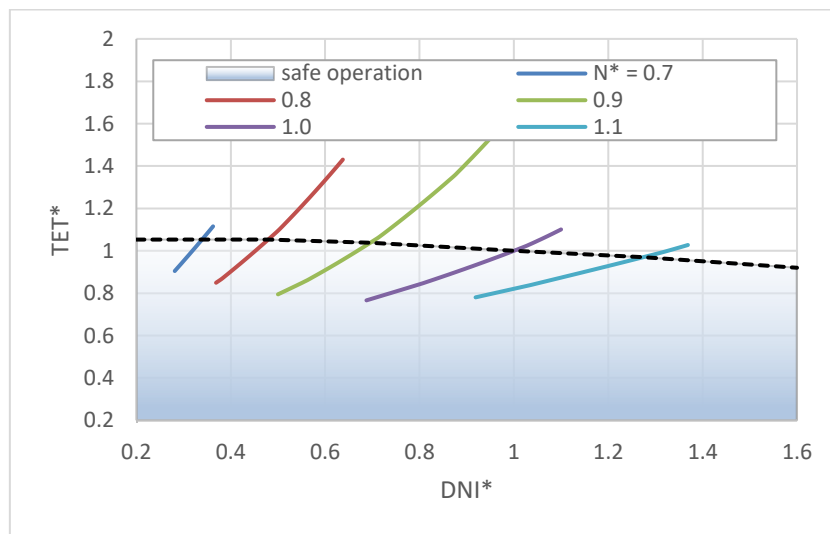


Figure 4.2 variations of turbine exit temperature for different constant speeds

It is also clear from the figures that a wide range of operation of the MGT would fall beyond the safety window if constant speed operation is chosen. Figure 4.2 also indicates that for low DNI values, the turbine exit temperature exceeds the design point (TET* greater than one) while it is still in the safe region. This is possible because unlike TIT, the maximum limit of TET in Table 3-2 is higher than the design point value.

Figure 4.3 shows that the generated power steeply changes with DNI when the speed is kept constant. For rotational speed set on the design value, the generated power by the dish-MGT system would decrease from 5kWe to less than 0.5kWe when the DNI drops from the design value (800W/m²) to about 550W/m² and it will not be able to cope with any higher DNI values because both TIT and TET would exceed their maximum limits (see Figure 4.1 and Figure 4.2). Consequently; as it can be seen in Figure 4.4, η^* drops from 1.0 to 0.14 for the same change of DNI which means the MGT efficiency at 550W/m² would be less than 3% compared to nearly 21% at 800W/m².

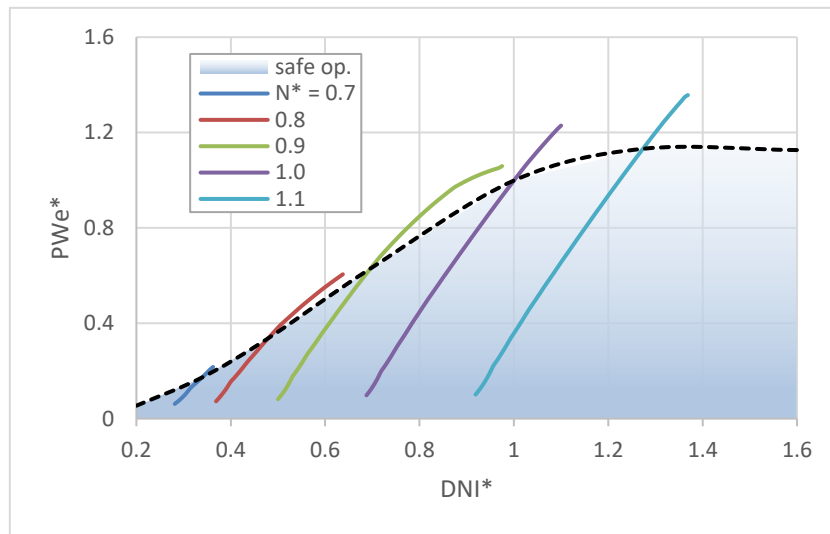


Figure 4.3 the net electric power output of the dish-MGT system when MGT operates at different speeds

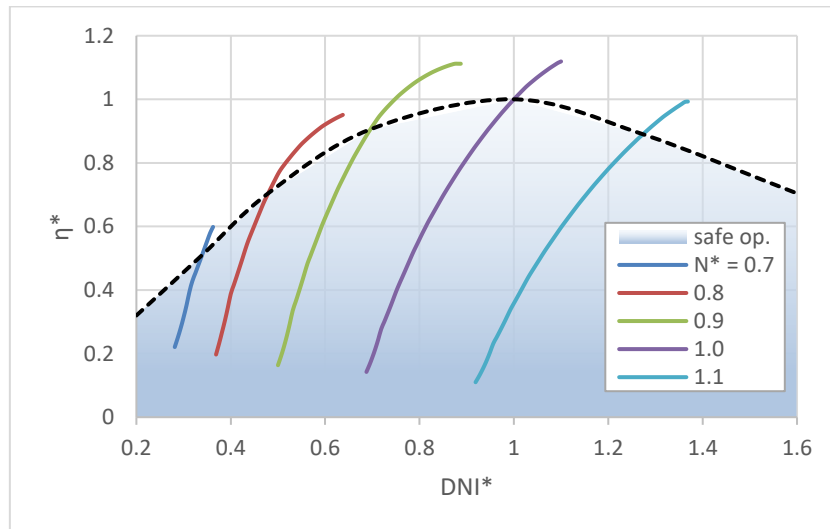


Figure 4.4 overall efficiency of the dish-MGT system for operation of MGT in different constant speeds

Figure 4.4 also shows efficiencies which are higher than the design point efficiency. This can be justified by considering the fact that these points are located beyond the safety limit which is not considered valid in the design procedure of the system in chapter 3. As it can be seen from Figure

4.1, the turbine inlet temperature for these points is higher than the design point value which results in higher overall efficiency.

Operation of the micro gas turbine in a constant speed has advantages in terms of minimisation of the cyclic mechanical stresses on the compressor and turbine wheels. It also allows operating the MGT in a safe speed which is far from the vibrational modes of the rotor assembly. Compared to other operation strategies that require relatively wide bands of speed variation, the constant speed operation causes reasonably less rotor dynamics problems when the solar MGT has to operate under variation of DNI. However, the narrow operation range and dramatic reduction in system performance make the constant speed operation strategy unsuitable for solar-only MGTs.

4.2.2 Constant TIT operation

The performance of the MGT when operated with different constant TIT values is presented in the following figures. Constant lines of the normalised TIT which are presented here cover its variation from 640°C to about 900°C. To ensure constant turbine inlet temperature, the mass flow rate must be changed proportional to the variations of input heat received at the solar receiver. Therefore, as shown in Figure 4.5 the rotational speed increases with DNI when the system is operated with a constant TIT strategy. An immediate advantage of this operation strategy over constant speed which can be seen in Figure 4.5 to Figure 4.8 is that it is applicable for a much wider range of variations of DNI.

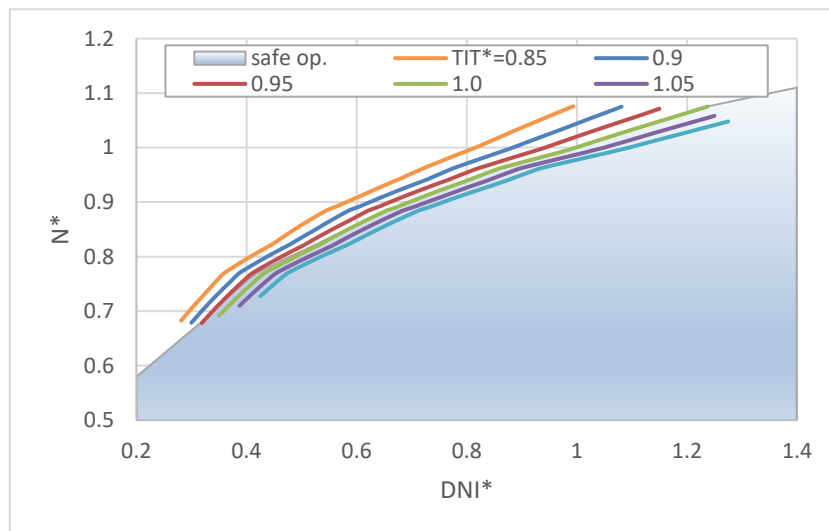


Figure 4.5 variations of rotational speed for operation with different turbine inlet temperatures

As the rotational speed increases, the pressure ratio of the compressor and consequently the expansion ratio of the turbine increase. Figure 4.6 shows that the increased expansion ratio results in the reduction of the turbine exit temperature for any constant TIT. Similarly, reduced rotational

speed at low DNI values results in higher TET values where it may exceed its maximum allowable limit. Below a certain TIT value the entire operation range of the MGT would be in the safe region. For the case study here, this safe value is about 745°C or TIT* equal to 0.95.

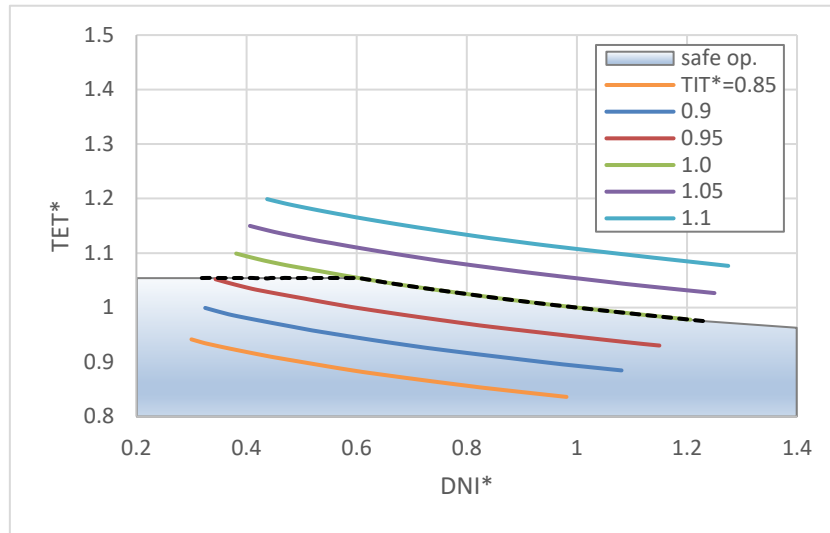


Figure 4.6 turbine exit temperature for operation with different TITs

Figure 4.7 shows that if the MGT operates in lower DNIs, the generated power will decrease and as a result, the MGT efficiency will also be lower as shown by Figure 4.8. It can be also seen that with the previously mentioned TIT value, the power generation can be started from DNI* values as low as 0.3 which is equal to 250W/m². If the system is to operate at TIT* equal to one (800°C), then the operation may not begin below DNI* of 0.6 which means the solar irradiance must be higher than 420W/m². As a consequence, the operation range of the system will be substantially decreased considering the daily variations of the solar irradiance.

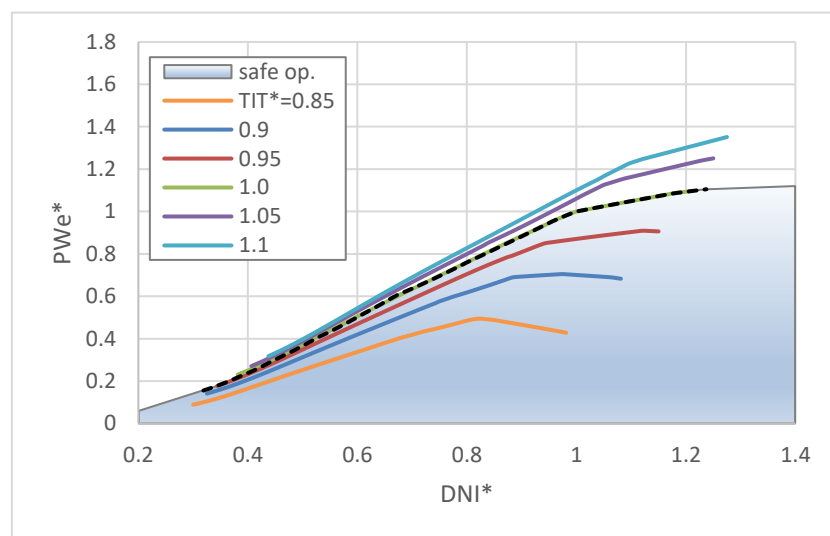


Figure 4.7 net electric power of the dish-MGT system when operated with different TITs

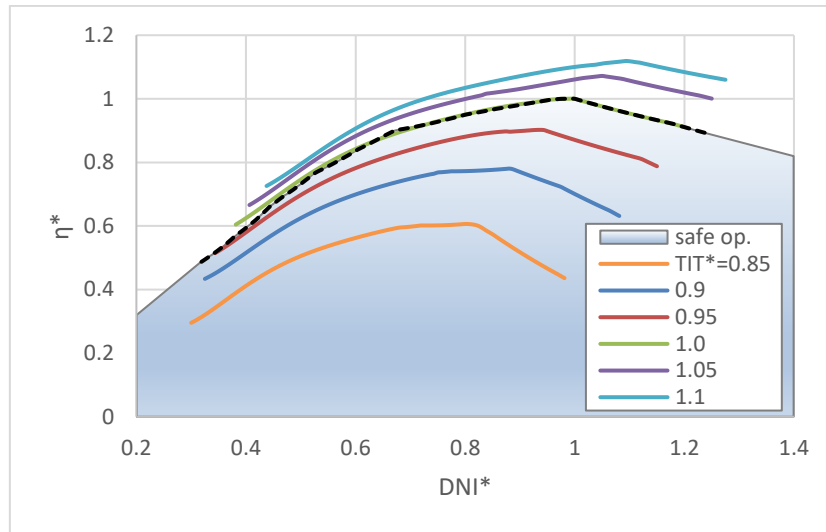


Figure 4.8 overall efficiency of the dish-MGT system for different turbine inlet temperatures

Figure 4.9 represents average annual data for the total duration hours of the solar irradiance in Casaccia, Italy and Seville in Spain. It can be seen that for Casaccia, the duration time that the direct normal irradiance is above $400\text{W}/\text{m}^2$, will be 500 hours less than the total time that it is above $250\text{W}/\text{m}^2$. This results in losing 500 hours of operation and power generation for a solar-only micro gas turbine.

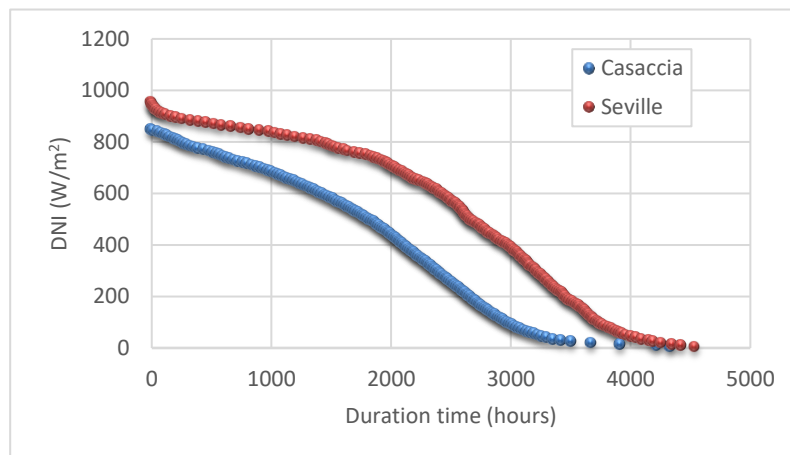


Figure 4.9 DNI duration curve for Casaccia and Seville based on average annual insolation data. Data from (SoDa, 2016)

Unlike constant speed strategy, the operation of the system can be continued even above the design point. The upper limit for the maximum DNI is generally determined by the solar receiver. Depending on the material which is used in the construction of the receiver, its design and thermal stresses in the body of the receiver, maximum allowable temperature in the receiver is determined. Although TIT is constant, the air flow and temperature distribution inside the solar receiver may

result in some hot spots when the system is exposed to extreme DNI values. This issue will be discussed later in section 4.4.1.

It can be seen from Figure 4.7 and Figure 4.8 that the performance of the dish-MGT system covers a wider range of DNI compared to the constant speed operation strategy. Additionally, as shown by Figure 4.7 and Figure 4.8, the generated power and efficiency is much higher compared to constant speed strategy during the course of DNI variations. The constant TIT operation is much more promising than the constant speed in terms of overall performance especially for solar-only systems because of two reasons: it increases the generated power for a given DNI and also it allows to operate the system for a wider range of DNI which increases the total electricity generation. However, operating the MGT with a constant TIT strategy requires sophisticated power electronics for the control system and results in a relatively wider band of speed variation. The latter requires that the rotor dynamics issues of the MGT are properly addressed.

4.2.3 Constant TET operation

Figure 4.10 to Figure 4.13 show the system performance when it is controlled to operate with constant turbine exit temperature. The results are presented for normalised values (TET*) from 0.85 to 1.1 which are corresponding to TET values from 470°C to 740°C. The safe operation limits have been already presented in the previous graphs and will not be shown in the next figures.

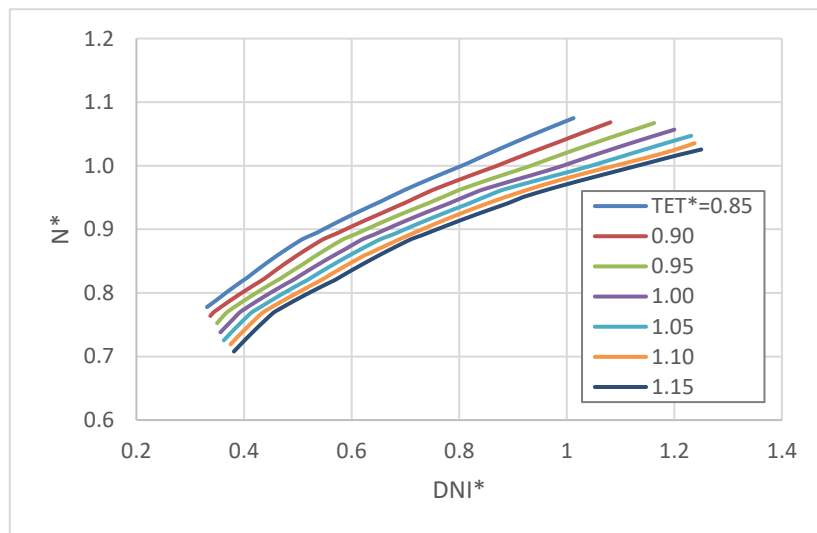


Figure 4.10 variations of the rotational speed for operation in different turbine exit temperatures

The system performance under constant TET strategy is very similar to the constant TIT strategy particularly in terms of the variations of speed, generated power and efficiency. The rotational

speed of the MGT continuously increases with DNI when the turbine exit temperature is kept constant as shown in Figure 4.10.

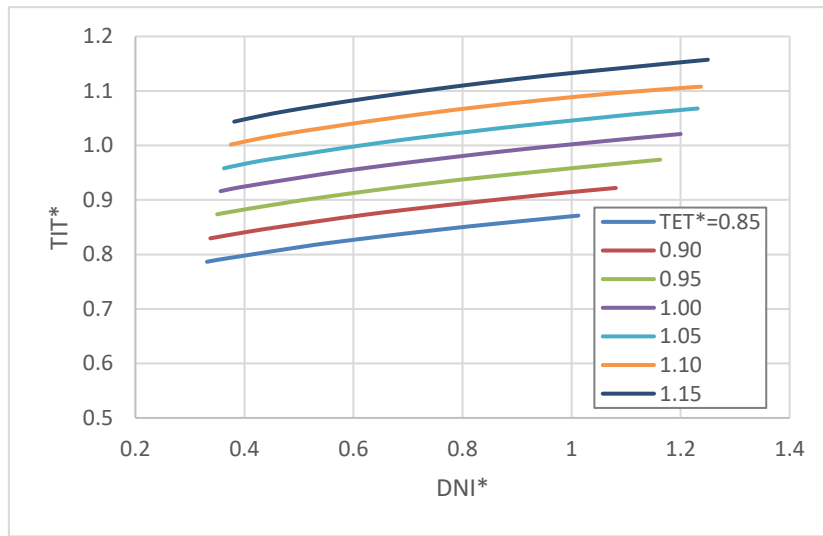


Figure 4.11 variation of turbine inlet temperature for constant TET operation strategy

Figure 4.11 shows that for the TET* equal to one (design point), the operation cannot be continued when the DNI is higher than the design point because the turbine inlet temperature exceeds its upper limit. It can also be seen that for any given DNI the rotational speed decreases as the system operates at a higher TET. Because the DNI determines the achievable turbine inlet temperature, operation at a higher TET requires a lower turbine expansion ratio, hence lower rotational speed.

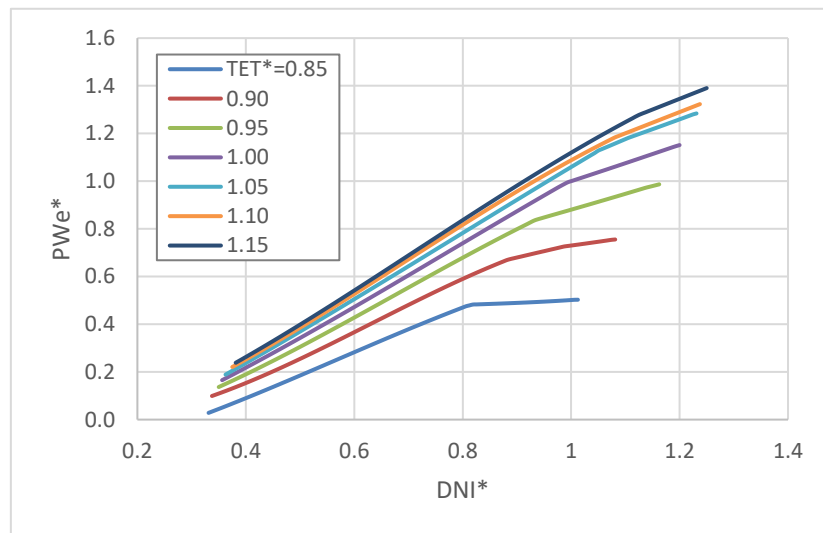


Figure 4.12 variations of the net output power when MGT operates in different turbine exit temperatures

Figure 4.12 and Figure 4.13 show that the generated power and overall efficiency of the MGT are lower than with constant TIT operation. The reason is that, unlike a constant TIT strategy, the

turbine inlet temperature decreases with DNI (Figure 4.11) which results in the reduction of the generated power by the turbine, hence lower net generated power and efficiency.

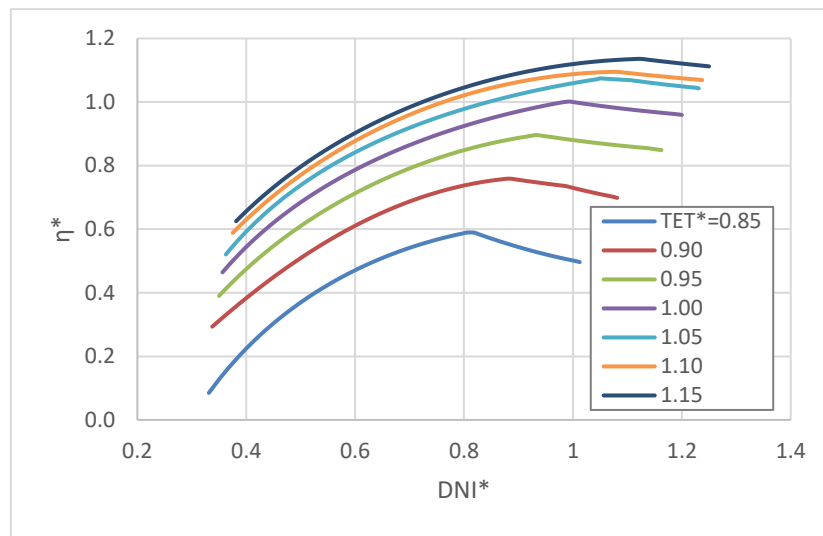
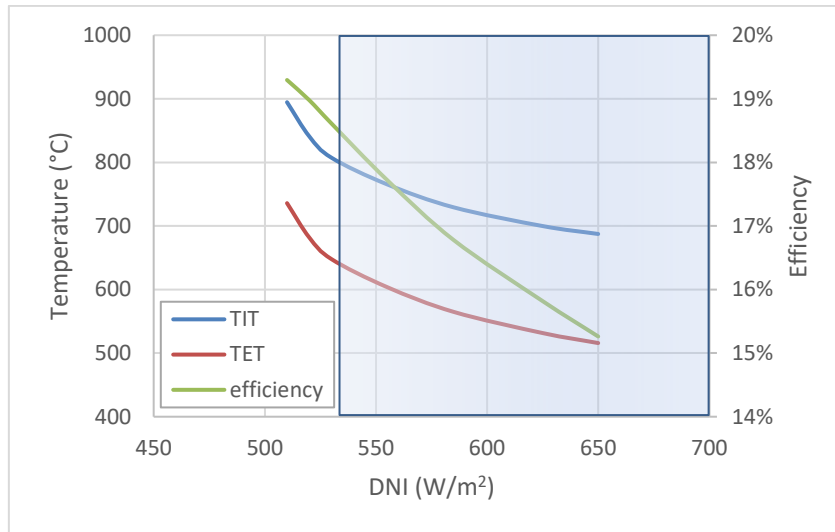


Figure 4.13 variations of the dish-MGT efficiency versus DNI for operation with different TETs

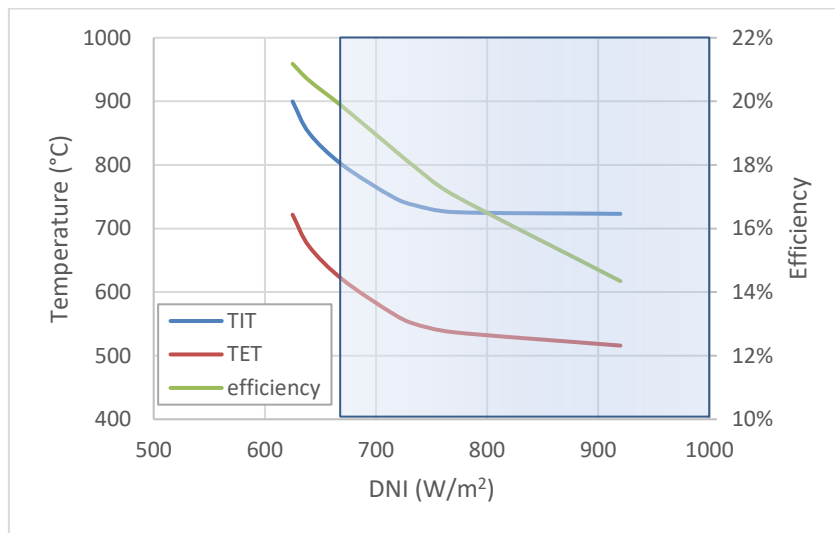
As for constant TIT operation, the constant TET operation strategy demonstrates similar advantages over the constant speed operation strategy. These are mainly about wider operation range and higher power and efficiency. However, in comparison with TIT constant operation, it results in slightly less power generation and limited operation range in the course of DNI variation. On the positive side, TET constant operation requires measurement of turbine exit temperature which is considerably lower than TIT and can be measured more reliably. TET is used to be the main system health control signal even when other performance control strategies have been used because it ensures healthy operation of the solar receiver and the expander at the same time.

4.2.4 Constant power operation

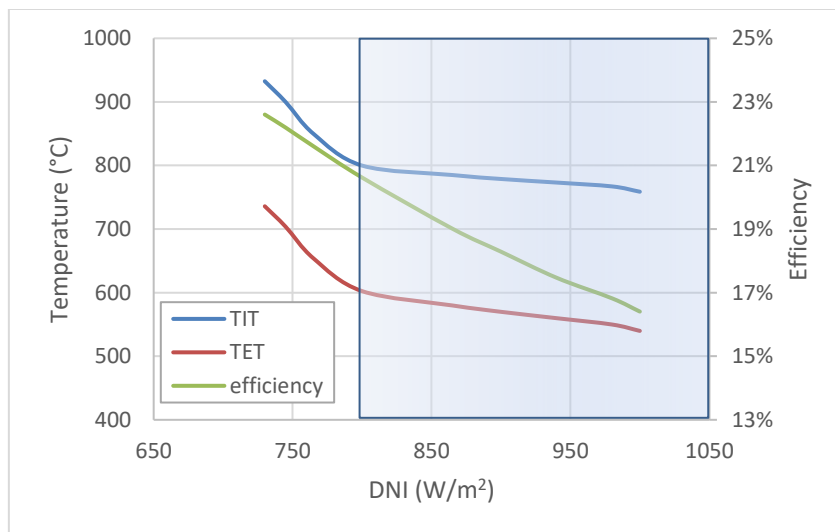
Studying the power graphs for the mentioned operation strategies above, it can be seen that in all of them the generated power varies with the DNI. Theoretically, the system performance can be controlled to generate constant output power. Such a case of constant power generation does not apply to typical consumers. However, this is just studied for the sake of understanding the system performance when a particular output power output is required. The system design and dish area are kept the same as the case study and it is assumed that the MGT is controlled to generate a constant power under variations of DNI.



a)



b)



c)

Figure 4.14 performance of the dish-MGT system when operated on fixed output power (a) $P_{We}=3kWe$, (b) $P_{We}=4kWe$ and (c) $P_{We}=5kWe$. The shaded area shows the safe operation region.

The system performance is studied when the control system runs the dish-MGT for three different output power values as shown in the three graphs of Figure 4.14. The shaded area represents the safe operation region. It can be seen from Figure 4.14 that the minimum DNI, where the safe operation of the system can be started, dramatically increases with the output power setting. This ultimately reduces the allowable operation range of the system for higher constant power settings. For operation of the system with constant output power equal to the design point, (Figure 4.14c), the operation is only allowed when the DNI is higher than 800W/m^2 . This limited range of operation affects the annual generated electricity by the dish-MGT as shown in Figure 4.15. It can be seen that the overall performance of the system dramatically decreases when the generated power is constantly equal to the nominal value.

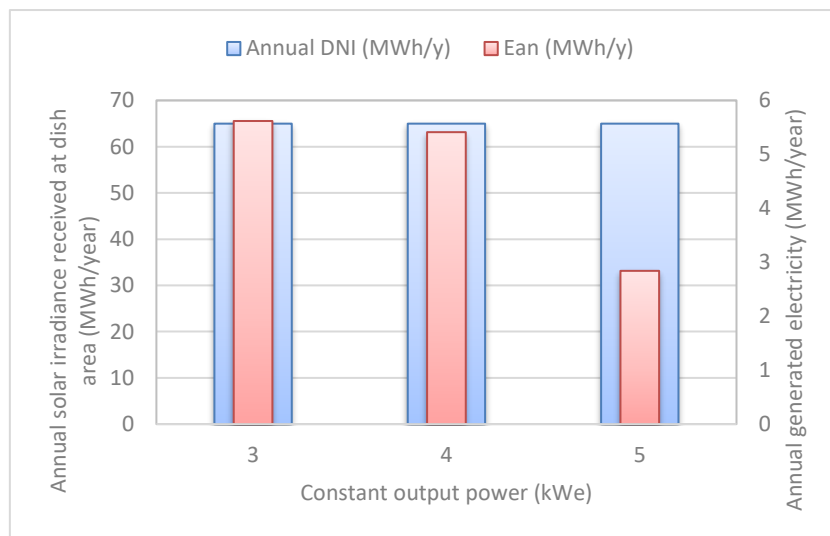


Figure 4.15 Comparison of annual generated electricity of the dish-MGT system when operated in different constant output powers in Casaccia, Rome, Italy

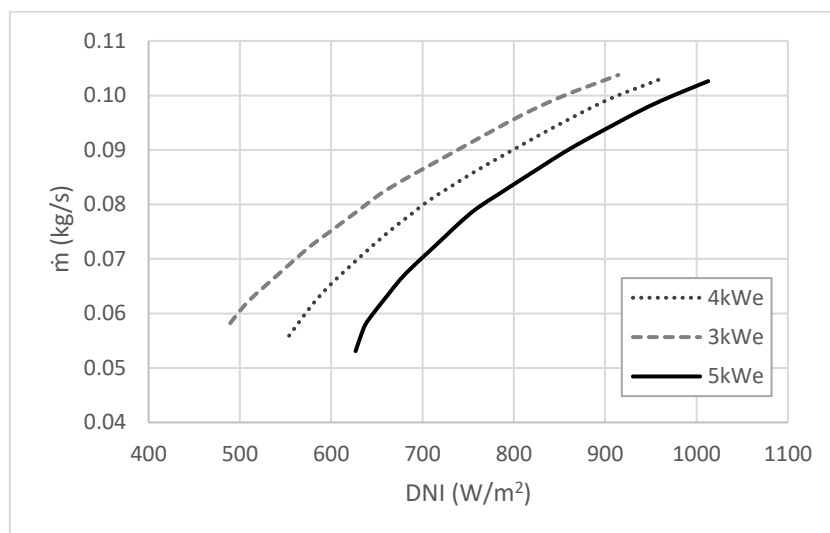


Figure 4.16 variation of mass flow rate for constant power operation

In addition to the reduction of the generated electricity by the system when it is operated with fixed output power, this type of operation results in several starts and stops of the system because the minimum required DNI to safely generate power is relatively high. As can be seen from Figure 4.14, the minimum DNI is changed from 530W/m^2 to 800W/m^2 for operation with power output of 3kWe to 5kWe . Operation with constant output power also requires the receiver to work at its highest temperature when the mass flow rate is at its lowest values (see Figure 4.14 and Figure 4.16).

4.2.5 Maximum power generation

Performance results of the previously mentioned operation strategies show that all of them would lead the MGT to work beyond the safe operation limits at least in part of the DNI variations. Therefore, a different operation strategy must be applied to achieve the maximum generated power at any particular DNI while the system performance parameters do not exceed the allowed limits. Therefore, the performance simulation was done to find the key system parameters (TIT and speed) for any particular DNI which result in maximum generated power within the safe operation limits. The calculation was done for the entire range of DNI variations. The performance results of this operation strategy are shown in Figure 4.17 and Figure 4.18.

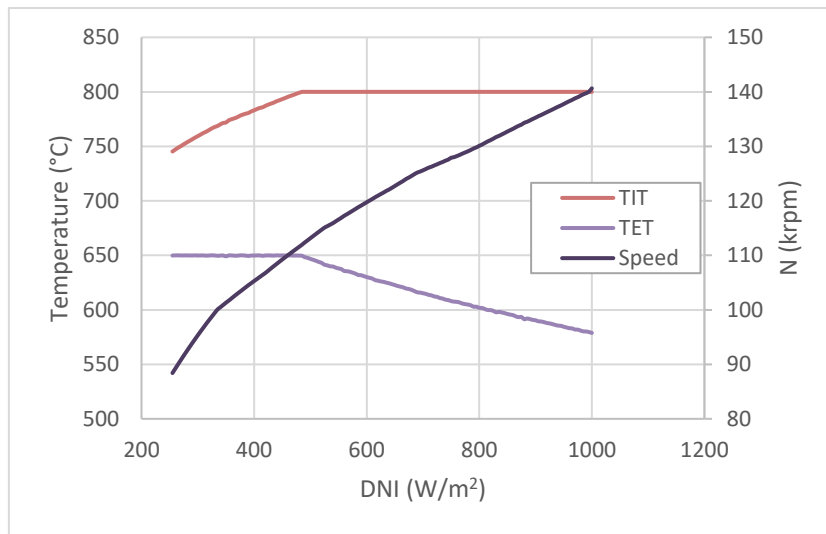


Figure 4.17 rotational speed and turbine temperature in MPP operation strategy for variations of DNI

Comparison of these results with the other operation strategies studied in the previous sections, shows that the outcome of this strategy is a combination of the constant TIT and constant TET operation strategies when they are set to their maximum allowable limits. From Figure 4.17 it can be seen that for lower DNI values the turbine exit temperature is the critical parameter until the DNI values gets close to 500W/m^2 where the turbine inlet temperature reaches its ultimate limit. Principally, it can be said that the proposed operation strategy is to keep the TIT at its highest

value allowed by all the safe operation limits. The proposed operation strategy in this work will be termed ‘*maximum permissible power (MPP)*’.

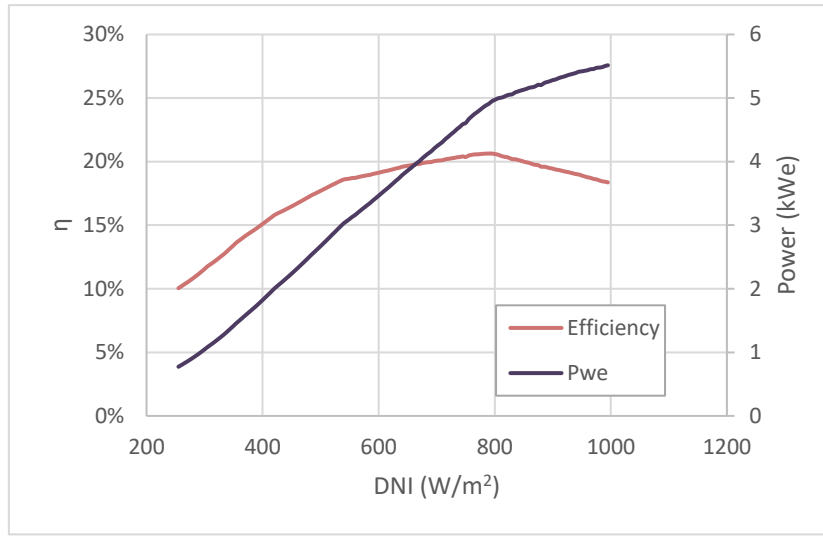


Figure 4.18 system performance with MPP operation strategy for variations of DNI

MPP strategy allows power generation for the widest range of variations of DNI. As a result, it leads to higher generated electricity compared to other operation strategies when the long-term performance of the system such as annual electricity generation is considered. System performance with different operation strategies is compared in section 4.5.

4.3 Control systems of the micro gas turbines

It can be seen that in all of the operation strategies discussed here, the rotational speed continuously changes during the variation of DNI. Therefore, the operation of the system in any of these strategies requires that the control system change the rotational speed of the MGT. Clearly, the variation of the speed is not the objective of the control system, but it will be done to achieve the ultimate objective for control which, depending on the selected operation strategy, can be different. Variation of the rotational speed can be done by the application of sophisticated power electronics between the high-speed alternator and the output power connection point. These power electronics are used by the control system to regulate the electrical parameters (voltage, current and power) and will be called here “power regulation”.

To operate the system in MPP strategy, it is proposed that the control system is comprised of three feedback loops as shown in Figure 4.19. The main loop is to control TIT, the objective of the control, and keeping it at its maximum allowable value. As such this loop determines the net output power. The second and third loops are to control TET and speed respectively. These two loops apply the safety limits and at the same time interact with the TIT loop. In case of excessive

TET or over speed, the first loop would change the TIT set point to keep the MGT in the safe operation window.

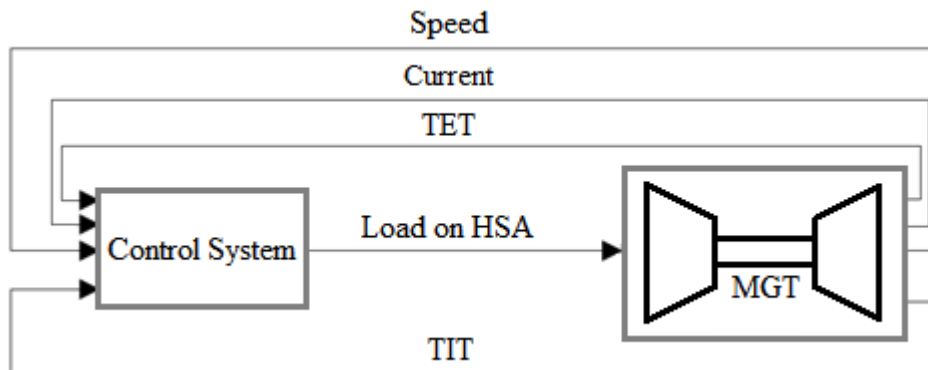


Figure 4.19 control loops for MGT to run on the MPP strategy

It is important at this point to explain the differences between controlling a purely solar powered and a fuelled micro gas turbine and how this should be addressed by the control system in order to operate the MGT with a MPP operation strategy. In a solar powered MGT, once the design is fixed, there is no control on the amount of DNI received at the surface of the dish. As a result, the amount of the input heat to a solar-only MGT varies independently of the MGT parameters or control system settings. In contrast, the fuel flow rate in a fuelled MGT is not only controllable, but also it is usually used as the main controlling parameter to operate the MGT. Therefore, controlling the operation of a solar-only micro gas turbine must rely on other system parameters. Additionally, it is possible in fuelled MGTs to change the fuel flow rate very quickly in response to any sudden change in the working conditions of the system such as rapid load change. With the solar irradiance, such a quick actions is not achievable because of the large inertia of the dish and practical considerations. As such, if the system ought to follow the load and provide the electric power demand, the performance of the fuelled and solar MGTs will be different. When the load on the system changes, a fuelled MGT control system can simply change the fuel flow and keep the system stable and match the new working point, whereas in a solar MGT, changing the load results in either acceleration or deceleration which may run the system to either overspeed and break the rotor or shut down. Therefore, for a solar-only system it is more practical to give the priority to maximise the generated power and to operate the system with MPP strategy. Instead of following electric power demand (load-oriented control) the strategy of the control system would be to generate the maximum achievable power for the available DNI at any time. The main applications of the dish-MGT units which have been considered here are that they would be connected to a large capacity power grid either as a single unit (Figure 4.20) or in the form of a modular array system (Figure 4.21). Therefore, the variation of the power demand on the main grid would not directly affect the system.

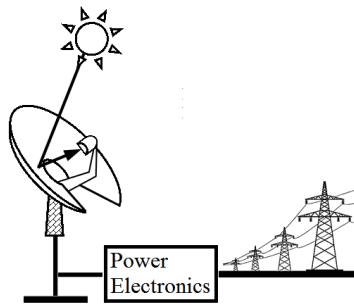


Figure 4.20 single dish-MGT unit connected to a large power grid

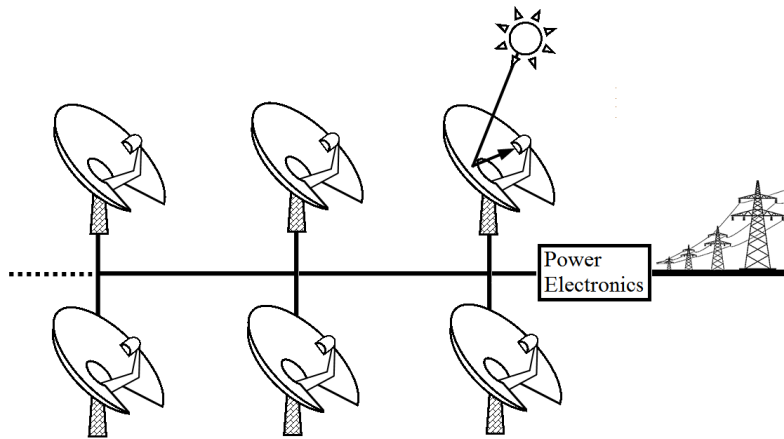


Figure 4.21 modular arrangement of several dish-MGT units which can be to a large or local grid

The general layout of an MGT control system, when it is not load-oriented and the power grid can consume whatever the dish-MGT generates, is briefly discussed here. The MGT is connected to the power grid by means of a bi-directional Electronic Power Conversion System (EPCS) as shown in Figure 4.22.

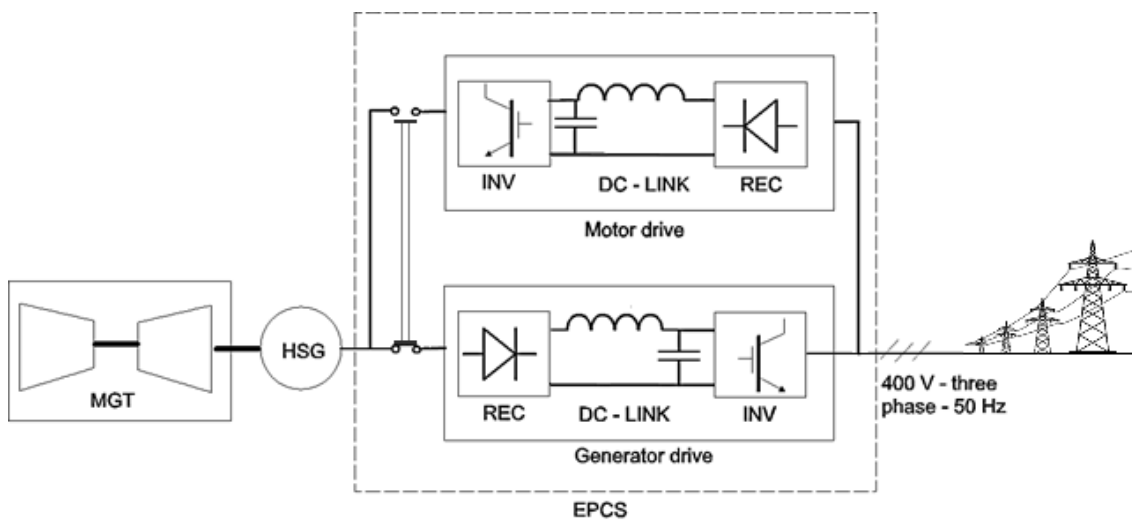


Figure 4.22 schematic of EPCS. Generation mode is activated (Ghavami, et al., 2017)

The bi-directional architecture of the EPCS enables the HSA to work either as a high speed generator or a high speed motor. It consists of two separate drives for the generation and motoring modes. Switching between the two modes is done by a commutator implemented in EPCS controlled by the dish-MGT control system.

When the control system is set to the generation mode as in Figure 4.22, the HSA converts the mechanical power input from the MGT to hi-frequency AC electric power. The rectifier then converts it to DC by a rectifier (REC). The frequency inverter (INV) converts the DC input to a 3-phase AC power synchronised with the grid. The rectifier works as a passive component and its output voltage is directly proportional to the input voltage which in turn is a direct function of the rotational speed (Rashid, 2014). The inverter in the generator drive is of the active type which allows regulation of either of the following electrical variables. All three methods are known as ‘Power Regulation’.

- a) Input voltage to the inverter. It is related non-linearly to the rotational speed and therefore regulating of voltage results in speed regulation.
- b) Electric current which corresponds to the torque that is exerted on the shaft.
- c) The input electric power to the inverter. This is a result of the voltage and current of the high speed alternator and is proportional to the product of its rotational speed and torque.

Figure 4.23 shows how the control strategy is performed by the main three loops as mentioned in the beginning of this section. The set point for each of the parameters which are being controlled is defined as the reference (REF) value. Each time that the sensors measure the real value of the controlled parameters, an error signal is created which is sent to the controller for the corresponding loop. However, only one of these signals will be used by the control system to change the controlling parameter in the inverter. The TIT loop uses a PID (Proportional–Integral–Derivative) controller because it is the main control loop while the other loops use PI (Proportional–Integral) controllers. The fourth loop is used to protect the HSA from excessive electric current.

It is important to distinguish between the controlling and controlled parameters here. Any of the above mentioned electrical characteristics could be chosen as the controlling parameter. The control system regulates the controlling parameter in order to keep the controlled parameters at the desired values and within the specified range. For the dish-MGT system the controlled parameters are TIT, TET and rotational speed which are controlled through three control loops as shown before in Figure 4.19.

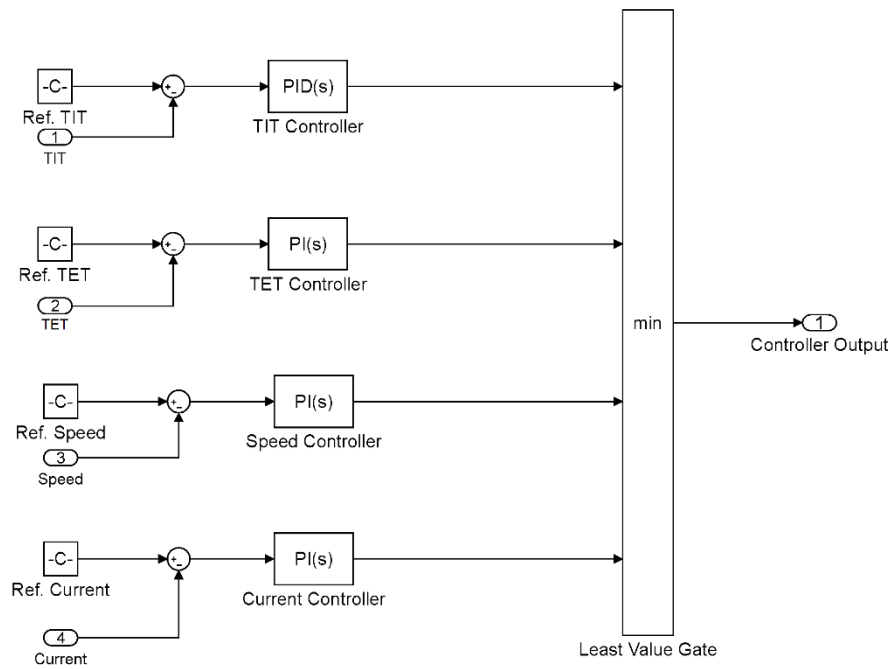


Figure 4.23 control loops of the micro gas turbine

Sensitivity analysis of the controlling parameters

Because the MPP operation strategy is based on the variation of system performance with the DNI, selection of one of the above mentioned parameters (current, voltage and power) as a controlling parameter directly depends on their sensitivity to the DNI. The sensitivity determination is based on the variation of the controlling parameter with the DNI and the accuracy of the inverter as the controller when regulating that parameter. The rate of the variation and the accuracy allows the calculation of the minimum change in DNI for accurate regulation of each of the proposed controlling parameters. Typical data for an active inverter are given in Table 4-1 as well as the rated values and the resultant value of the minimum readable value (elektroautomatik, 2015). The absolute accuracy (error) is the product of accuracy percentage and the rated value.

Table 4-1 absolute accuracy of the electrical parameters for a typical inverter rated at 5kWe

Parameter	Percentage error (err)	Rated value	Absolute error (Err)
Current	0.4	13 (A)	0.052 (A)
Voltage	0.3	400 (V)	1.2 (V)
Power	1.5	5 (kW)	0.075 (kW)

The variation of the electric current, voltage and power with DNI are given in Figure 4.24 when the MGT is operated under MPP strategy. The graphs for current and voltage are generated from

the performance model of the electrical system which was explained briefly in section 3.4.4 and in more details in Appendix B.

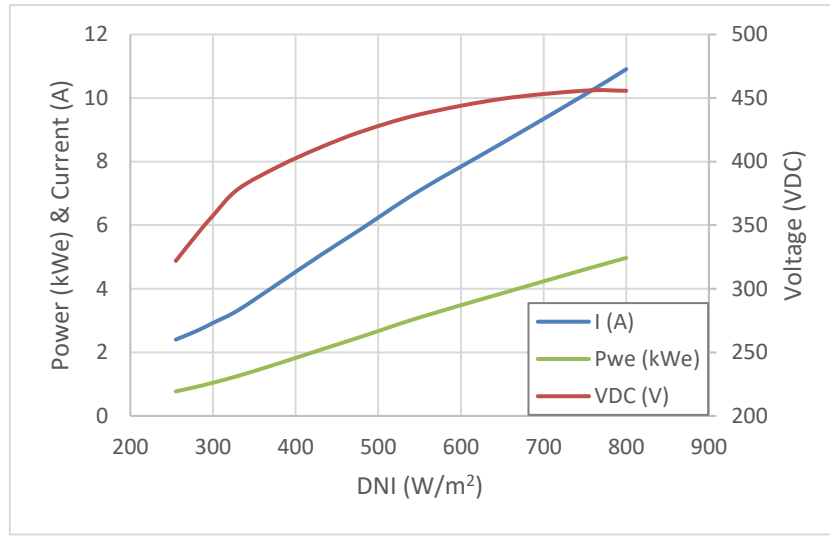


Figure 4.24 variations of proposed controlling parameters with DNI for MPP operation strategy

To calculate the rate of variations of each of these parameters with the DNI, the numerical data for minimum and maximum DNI within the operation range are also given in Table 4-2. An average rate of variation is calculated for each parameter and is given in Table 4-3.

Table 4-2 values of the proposed controlling parameters at the minimum and maximum DNI

DNI (W/m²)	Current (A)	Voltage (V)	Power (kWe)
255	2.40	322	0.773
800	10.91	455	4.971

Table 4-3 gain factor (rate) of the controlling parameters

k_I [A/(W/m²)]	K_V [V/(W/m²)]	K_{PW} [kW/(W/m²)]
0.0156	0.244	7.703×10^{-3}

Having the absolute accuracy of the controller and the variation rate for the controlling parameters, it is possible to calculate the minimum change of DNI which allows the inverter to perform a reliable regulation. For each parameter, the minimum value is given as below:

$$\Delta DNI_I = \frac{Err_I}{k_I} = 3.33 \text{ W/m}^2 \quad 4.6$$

$$\Delta DNI_V = \frac{Err_V}{k_V} = 4.93 \text{ W/m}^2 \quad 4.7$$

$$\Delta DNI_{PW} = \frac{Err_{PW}}{k_{PW}} = 9.74 \text{ W/m}^2 \quad 4.8$$

Where indices I, V and PW represent the corresponding parameters to electric current, voltage and power regulation respectively and *Err* is the absolute error expectable from typical inverters as shown in Table 4-1. The results of the sensitivity analysis show that if the generator drive controls the MGT by regulating the electrical current, it will be able to operate with minimum variations of DNI. This implies that the electrical current would make a suitable controlling parameter. However, as it can be seen in Figure 4.24, the electrical current dramatically reduces for low DNIs. In comparison, the reduction in voltage is much less than the current. The low electric current makes it unsuitable for controlling purposes compared to voltage because of the following points:

- Low current can be affected by the electrical noise
- The output voltage is mainly proportional to the rotational speed for an electric machine and it is always available regardless of the electric current value, but the opposite statement is not valid.

Therefore, it can be concluded that the suitable controlling parameter to operate the solar powered MGT is the input voltage to the rectifier.

4.4 Recuperation control

The power regulation control strategy provides the possibility to run the dish-MGT system using one of the operation strategies mentioned before. However, because the recuperated MGT has only one degree of freedom, only one of the performance parameters of the system (TIT, TET, speed or power) can be used for the control procedure. Inevitably, the remaining parameters would change during operation. An immediate consequence of such a system; as was discussed in section 4.3, is that the control system cannot operate the MGT in a load-oriented application. A novel concept to address this issue and provide flexibility to the solar-only micro gas turbine has been proposed and developed in this work. The proposed concept termed here as “Recuperation Control” is depicted schematically in Figure 4.25.

The three-way valve V1 is a proportional diverting valve which allows part of the compressed air to bypass the recuperator and flow from port “B” directly to the solar receiver inlet line (point M) where it is mixed with compressed hot air from the recuperator. The temperature of the inlet flow to the receiver is therefore controlled by the by-pass ratio of the diverted flow (*x*) which is applied

by the proportional valve V1. The second valve V2 is used to divert the same amount of flow to the recuperator exit to ensure equal mass flow rates in the hot and cold sides of the recuperator.

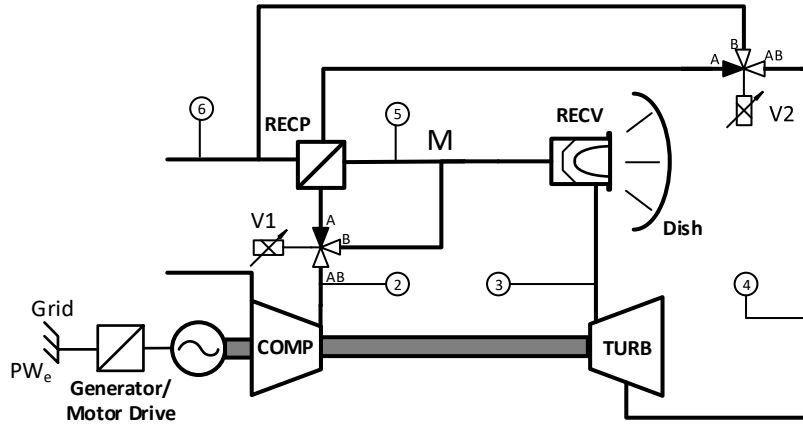


Figure 4.25 schematic of recuperation control for a recuperated cycle. Part of the flow is by-passed via port “B” of the three way diverting valves

Equal mass flow rates in both sides of the recuperator is not necessary for the recuperation control. However, it allows to simplify the calculations here for easier demonstration of the concept. As such, the bypass ratio will be the same on both sides assuming no flow leakage in the system.

$$x = \frac{\dot{m}_B}{\dot{m}_{AB}} \quad 4.9$$

Where \dot{m}_B is the mass flow rate in the by-pass lines and \dot{m}_{AB} is the mass flow rate entering the three way valves. Neglecting the heat and flow leakages, the conservation laws of mass and energy can be used to find the total temperature at the receiver’s inlet, $T_{recv,i}$ in terms of the by-pass ratio, specific heat, C_p and temperatures of the recuperator and compressor exit (T_2 and T_5). Obviously, all temperatures are total temperature values.

$$T_{recv,i} = \frac{(1-x)(C_p T)_5 + x(C_p T)_2}{(C_p)_{recv,i}} \quad 4.10$$

With the diverting valves V1 and V2 and their bypass ratio added to the system, it would be possible to control one more performance parameter in the system. For example, while in MPP operation increase in DNI requires to increase the speed to keep the temperatures of the turbine within the safe window, it is possible in recuperation control to keep the speed constant and change the bypass ratio to prevent overheating of the receiver. Similarly, it would be possible to operate the system for constant power generation without the overheating problems shown in Figure 4.14.

To apply the recuperation control strategy, an additional feedback loop must be added to the control loops of MPP. The parameter to be controlled by this loop is determined by the objective of the control. If the system is to be operated for a load-oriented application, the additional loop must control the generated power. The controlling parameter always will be the bypass ratio. Therefore, for a solar-only MGT to be able to meet variable power demand, there will be two controlling parameters; bypass ratio and voltage, which will be used to ultimately control the generated power and match it with the power demand (load) while the system operates within the safety limits. An example of system performance when the recuperation control is applied is shown in the following subsection.

4.4.1 Dealing with excessive DNI

Recuperation control was originally considered in the current research to resolve the problem of an overheated receiver when the dish-MGT system is exposed to excessive solar irradiance. For a solar receiver of a given design, the exit temperature is mainly determined by the inlet temperature, input heat to the receiver from concentrated solar irradiance and the mass flow rate. Assuming that the heat loss in the flow line between the receiver and the turbine is negligible, the receiver's exit temperature is equal to the TIT. Under extreme DNI, the solar receiver will be overheated particularly if the air mass flow rate is not enough to keep the receiver's temperature within the safe limit. It is normally expected that the increase of speed with DNI, as shown in Figure 4.17, prevents overheating. However, this is limited by the maximum allowable speed of the MGT. To deal with this problem, recuperation control can be applied whenever the DNI reaches a certain value. Below that DNI value, the system would be controlled to operate in MPP strategy. When the DNI exceeds the set point value, the recuperation control is activated. At the set point, the by-pass ratio is zero and as the DNI continues increasing, the control system opens the valves V1 and V2 to keep the TIT constant. As mentioned before, any other objective may be defined when using recuperation control. Performance results of the dish-MGT system are shown in Figure 4.26 and Figure 4.27 for the case that recuperation control loop keeps TIT constant and the power regulation control loop assures constant rotational speed. It can be seen that as soon as the combined control starts, the generated power remains at a constant value. The reason is that the TIT, compressor ratio and mass flow rate (because of the speed) have been already kept constant and therefore, increase in DNI will not change the working point of the system. However, the effect of bypassing the recuperator can be seen in the reduction of system efficiency because the MGT generates the same power while it receives more heat. The additional heat received by the system results in the increase of the recuperator's exhaust line temperature, T_6 .

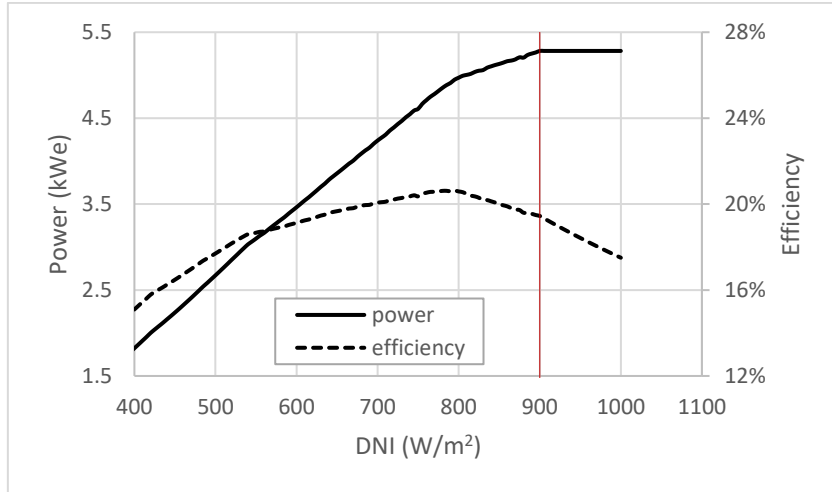


Figure 4.26 performance of the dish-MGT system with the recuperation control strategy applied for DNIs above 900W/m^2

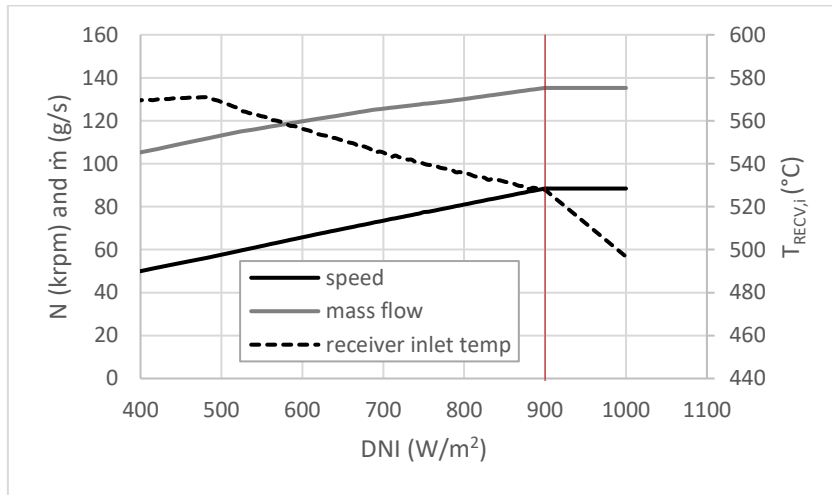


Figure 4.27 variation of speed, mass flow rate and inlet temperature of the receiver recuperation control applied for DNIs above 900W/m^2

The performance of the dish-MGT under recuperation control strategy for excessive DNIs shows a very important advantage which is the possibility to keep the rotational speed and the generated power constant while the DNI fluctuates. The elevated exhaust temperature may be used in a bottoming cycle which in this case will recover part of the heat lost because of the recuperator bypass and resultant reduction in the overall efficiency. Nevertheless, cycles including heat recovery are not the subject of this study. The dish-MGT performance has been studied when the recuperation control strategy is applied above certain DNI values to keep the rotational speed and generated power fixed at the values pertaining to that particular DNI.

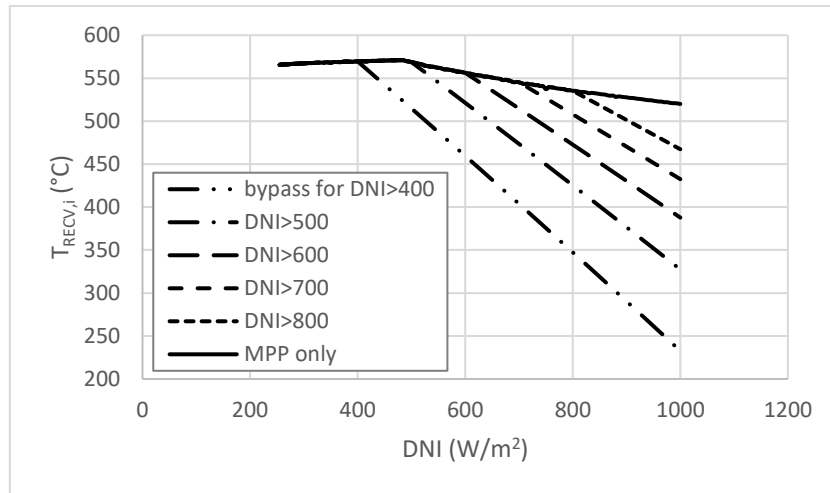


Figure 4.28 reduction of the receiver inlet temperature when recuperation control strategy is applied

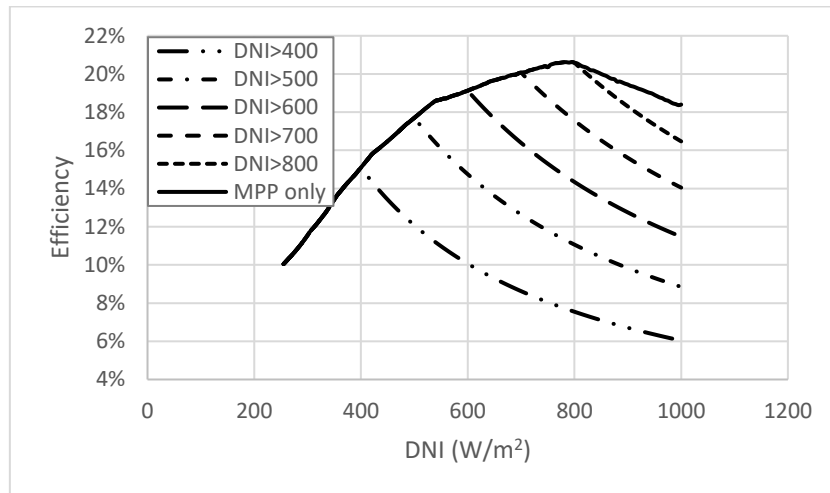


Figure 4.29 effect of recuperation control strategy on the efficiency of the system

Figure 4.28 to Figure 4.31 show the performance of the dish-MGT system when the recuperation control is activated at different DNI values. These figures demonstrate that the performance of the system can be flexibly controlled through the recuperation control strategy. The flexibility that the recuperation control provides to the control system can be also beneficial when the dish-MGT system has to deal with some particular circumstances such as start up or re-starting after a passing cloud. Depending on the DNI value at which the dish-MGT is starting, overheating of the receiver may occur. The start-up period always begins with motoring to circulate the air through the system to not only warm up the system components but also provide enough cooling for the receiver. If the mass flow rate provided by the motorised MGT is not enough for the existing DNI, it is very likely that the receiver is damaged because of overheating. This is especially important when the system has to start or re-start under DNI values greater than 450W/m^2 because at such DNI values the rotational speed must be higher than 110krpm to prevent the TIT exceeding the

maximum allowable limit (see Figure 4.17). Because the high speed alternator cannot reach higher speeds when working as a motor, overheating of the receiver may take place in such circumstances. The recuperation control allows enough cooling of the receiver inlet temperature to keep it in safe operation until rest of the system warms up and the MGT is able to generate power and the control system may switch to generation mode.

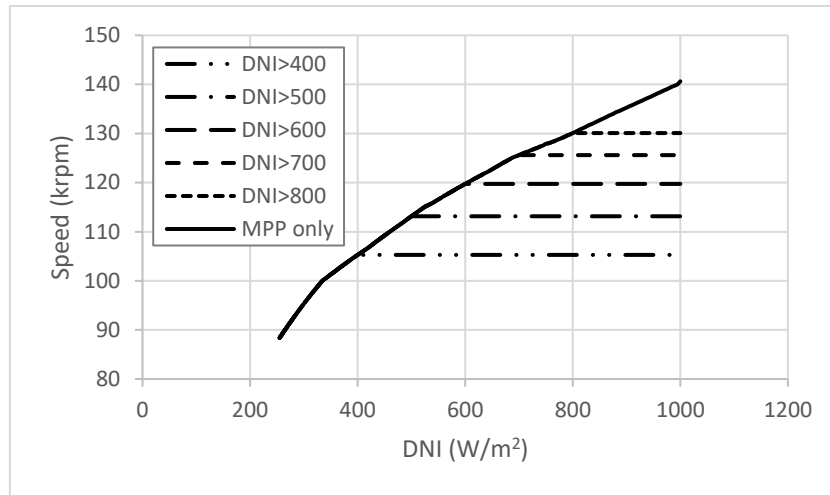


Figure 4.30 rotational speed of the MGT. Constant speed is achievable as soon as the recuperation control is applied

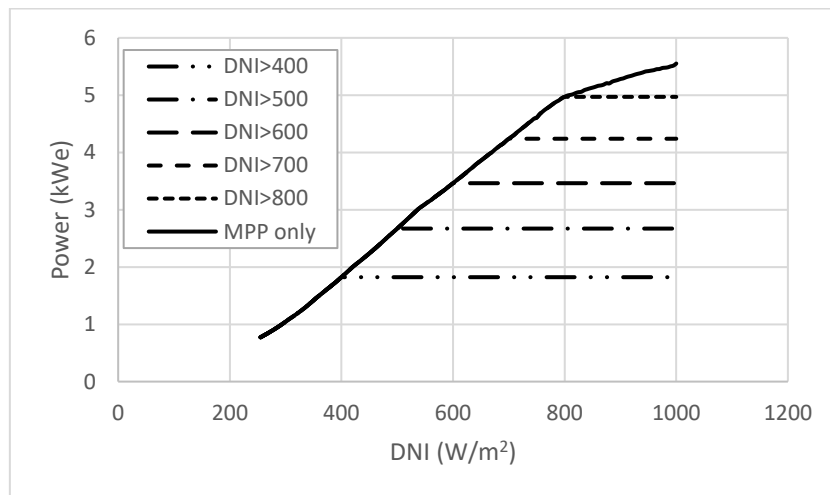


Figure 4.31 generated power vs DNI. Recuperation control strategy allows for keeping a constant power output by fixing the TIT and speed through the control loops

4.5 Comparison of the operation strategies

The performance of the dish-MGT system is now compared for the operation strategies studied here. The simulation has been done for conditions in Casaccia, Italy and Seville, Spain. These areas are among the sunniest regions in Europe. Casaccia is the position where the dish-MGT system of the OMSoP project is currently being installed as the first small scale solar-only dish-

MGT system. The overall performance of the system is calculated in the same way as presented in section 3.5. Results for annual generated electricity are shown in Figure 4.32. Three different recuperation control power levels (abbreviated in the graphs as RC) are also examined in the simulation. The operation of the system for these three cases is actually a combination of MPP strategy and recuperation control. For the low DNIs when the output power is below a particular value, the system operates using the MPP strategy and no by-pass is required. For higher DNI values, recuperation control is activated. The results shown here are for the case when the control system keeps the generated power and TIT constant which is similar to the performance of the system shown in Figure 4.28 to Figure 4.31. The only difference is that the recuperation control is activated at a particular power rather than at a DNI value. The results are shown for three cases when the recuperation control begins at output power equal to 3kWe, 4kWe and 5kWe. The latter is the expected power at the design point and therefore it means that for this particular case, the recuperation control is applied when the DNI exceeds the nominal value of 800W/m².

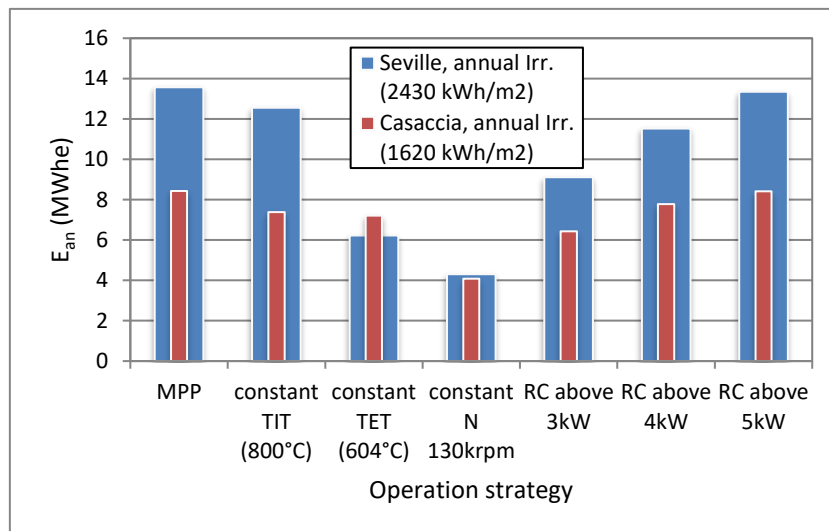


Figure 4.32 annual generated electricity for different operation strategies (RC: Recuperation Control)

For each of the constant TIT, TET and speed operation strategies, the corresponding constant value of the design point is considered for a suitable comparison. Therefore; as it was discussed in section 4.2, the range of DNI values for which the dish-MGT can generate power, will be different for each of these operation strategies. The results show some interesting points. Generally, the generated electricity in Seville is higher than Casaccia because it receives a higher annual solar irradiance. However, it can be seen that for constant TET operation, the annual generated electricity of the system in Casaccia is higher than that in Seville. It shows that the total duration time for the range of DNI that the MGT can be safely operated with constant TET is larger in Casaccia than in Seville. In other words, the majority of the annual solar irradiance in Casaccia takes place in low DNI values where TET constant performance of the system takes

place within safe limits, while for Seville this is not the case. For Seville, the duration time of high DNI values, above 700W/m^2 , where TET constant operation leads the system beyond the safe limits, is almost twice the time for Casaccia (see Figure 4.9). Nevertheless, the MPP operation strategy shows maximum generated electricity in both geographical positions and will be the first choice for a solar-only dish-MGT system when its generated power is fed to a large grid similar to the applications shown in Figure 4.20 and Figure 4.21. However, when the system is required to be load-oriented, recuperation control can be considered for the power generation. The system performance when recuperation control is applied above the design point shows almost no difference with MPP strategy either for Casaccia or Seville. However, using the recuperation control just above the design point also restricts the flexibility of the system to a narrow band of DNI above 800W/m^2 . It is interesting that because the duration of low DNI values is relatively higher for Casaccia than Seville, the degradation of system performance is less significant for Casaccia than Seville when recuperation control starts from lower output power (hence lower DNIs). It is therefore more advisable to apply recuperation control strategy when the dish-MGT system is in regions with lower duration of excessive DNI values. In other words, the potential for a dish-MGT system to be used in a load oriented application is higher in such regions whilst in high DNI areas it is better to use the pure solar dish-MGT units with an MPP operation strategy in a power network to achieve the highest allowable efficiency. The following paragraph summarises the above discussion.

Except for TET constant operation strategy, the generated electricity in Seville is higher than Casaccia because of the higher solar income. MPP strategy results in the highest electricity generation by the dish-MGT system. Application of the recuperation control strategy above the DNI value of the design point can only be considered as an effective method to protect the receiver against excessive DNI. Recuperation control can be more effectively used in regions with low DNIs.

Figure 4.33 shows the overall solar to electric efficiency of the dish-MGT system which was given by equation 3.74 in chapter 3 and is defined as the ratio of the annual generated electricity by a particular system over the annual solar heat received at the dish area. The concept of solar efficiency helps to envisage the points mentioned before regarding the comparison of the annual generated electricity for different operation strategies. It can be seen that the solar efficiencies when the dish-MGT system is operated at constant TET or speed are higher for Casaccia than Seville because the distribution of solar irradiance in Casaccia is much more in favour of these two operation strategies than that in Seville. For the same reason, the solar efficiency is also higher in Casaccia when recuperation is applied from relatively higher DNI values.

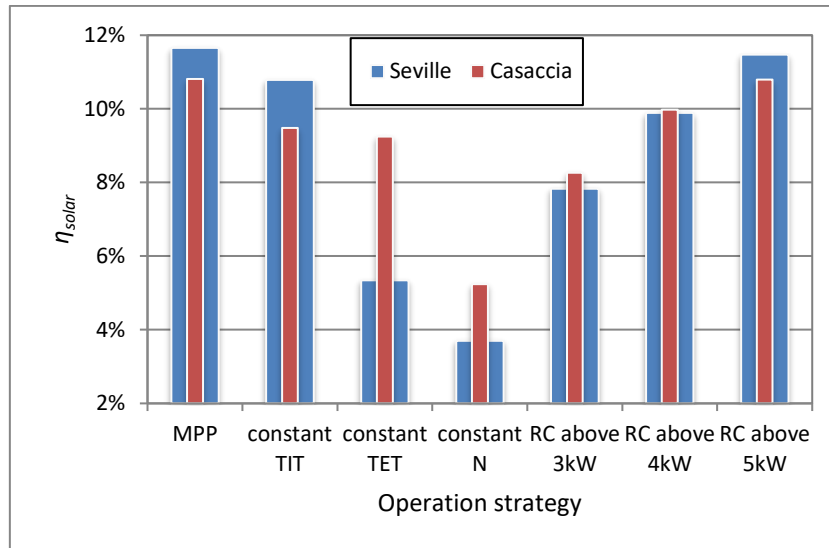


Figure 4.33 overall solar efficiency for different operation strategies

It should be noted that the system performances which are compared here are for the system design with the same component sizes including the dish. It is clearly possible that a smaller dish size for high DNI regions; like Seville, would attenuate the effects of excessive DNI. Therefore, a trade-off between the degree of recuperator bypass and the optical components size may be considered when the system is designed for a particular region.

4.6 Conclusions

Not only the design of a dish-MGT system is important for its performance, but the operation strategy which is used to run this system also has a very important role on the overall generated electricity and its solar efficiency. Different operation strategies were studied in this chapter and their applicability and suitability were compared particularly in terms of annual generated electricity and flexibility against the power demand. It was found that the MPP operation strategy allows maximisation of the generated power when the electric load on the system is flexible. For load-oriented applications when the MGT is required to follow the variations of power demand, the concept of recuperation control has been proposed. It was shown that this novel concept helps the pure solar dish-MGT systems to match variable load conditions while the solar irradiance is changing and at the same time, stay in the safe operation window. From the performance point of view, recuperation control reduces the overall solar efficiency of the system. This is inevitable when the dish-MGT is supposed to generate a different (lower) power than the maximum achievable value with the MPP strategy. However, it is the application of the dish-MGT which determines which strategy must be chosen. Further points are listed here:

- A power regulation control strategy is required to operate the system in MPP strategy.

- Voltage regulation is deemed to be more effective than other power regulation strategies.
- The control system regulates the power during variation of DNI to achieve the maximum generated power.
- Constant speed operation strategy significantly reduces the performance of the system.
- If a constant speed operation is required, it is much more efficient to apply recuperation control than using power regulation.
- Recuperation control can be successfully applied to save the solar receiver from overheating when the system is exposed to excessive solar irradiance.
- When recuperation control is applied only above the nominal DNI value, the difference in system performance with the performance in MPP operation is negligible.
- When the recuperation control is applied from lower DNI values, the reduction in overall solar efficiency is highly dependent on the geographical point and annual solar income.
- If most of solar irradiance is received in low DNI values, then the difference in generated power between MPP strategy with constant TIT or TET is less significant.
- Because of less degradation of solar efficiency in regions with lower solar income, the pure solar dish-MGT systems can be used in load-oriented application more successfully than in areas with higher annual DNI.
- In high DNI areas it is preferable to use the solar dish-MGT units in connection with a flexible load such as a large power grid to achieve maximum efficiency rather than load-oriented applications and recuperation control.

5 Techno-economic optimisation of dish-MGT systems

5.1 Introduction

The effects of the control and operation strategies on the performance of pure solar dish-MGT systems were analysed in the previous chapter. Obviously, the system performance is also affected by the system design point parameters. It was demonstrated in chapter 3 how the design point parameters of the system can be used to generate the component performance maps which ultimately determine the system performance. These parameters also affect the economic figures of the system including the initial investment cost and the cost of generated electricity. Choosing design point parameters based on a low level technology and less advanced materials reduces the costs of the components, but it also results in lower system performance. On the other hand, a more expensive engine (for example with higher allowable TIT) would achieve better efficiencies which in turn, would require lower solar heat from the parabolic dish to the receiver. This means a smaller dish and probably a lower total cost of the system. Therefore, the design problem when the system constraints like maximum allowable TIT are taken into account in relation with the economic figures (economic performance), requires a thermo-economic optimisation. The optimisation of pure solar dish-MGT systems is done in this chapter with both technical and economic objectives included. An overview of the problem is given in the beginning followed by a detailed analysis of the optimisation problem to define its principal elements, solution methods and algorithms and the framework established to attempt the problem. To calculate the economic indicators, an economic model which is specifically developed for small-scale dish-MGT systems within the OMSoP consortium has been introduced and used with little modification. The thermo-economic optimisation of the dish-MGT system is attempted for two individual applications. In the first application, a system with a fixed rated output power is considered and in the second application the optimised design, within the overall feasible range of dish-MGT sizes, has been considered. The results are discussed in this section, followed by general conclusions.

5.2 Analysis of the optimisation problem

The optimisation problem generally involves finding values for the design parameters of the system which result in its optimal performance from the economic and technical points of view. Each optimisation problem consists of three main sets of parameters which are the design (or so-called decision) variables, the objective functions and constraints. The optimisation procedure is completed with imposed limits for the decision variables which is called the decision space. While executing the optimisation procedure, the involved mathematical algorithms may generate results which are beyond certain acceptable limits. These results are excluded from the ultimate output by the implementation of the appropriate constraints pertaining to the allowable limits of the system design such as the rotational speed and maximum permissible temperatures in the system.

5.2.1 System design variables

This section identifies the decision variables and system constraints which must be considered when attempting the optimisation. As shown in chapter 3, the main parameters which determine the overall design of the dish-MGT system can be categorised as the component design point performance data, system constraints and the nominal values for the ambient conditions which must be used for the calculation of the design point performance. The component performance data are the efficiencies of the turbine, compressor and recuperator and the efficiencies of the solar receiver and the dish. The effects of these efficiencies on the overall performance of the system are monotonic functions and only affect the optimisation results if they appear to influence in the economic performance of the system. The main constraints, as already introduced in chapter 3, are the maximum allowable TIT and TET, the rotational speed and the compressor's surge margin. The latter does not have any direct effect on the economic indicators, but limits the compressor performance which results in lower overall system performance. In addition to the surge margin, there are two technical parameters which are mainly related to the design of the compressor and turbine in the MGT. In the rest of this section it is shown that these two parameters, although not affecting the cost, have considerable effect on the overall performance of the system and must be included in the decision variables.

In chapter 3 it was shown that for a given case study, when the system constraints, such as TIT and TET and component performance assumptions at the design point, are fixed, the system performance varies with the pressure ratio (see section 3.3). For a particular pressure ratio, the efficiency of the system at the design point reaches its maximum value. Table 5-1 shows that although the maximum efficiency of the dish-MGT system is achieved at a pressure ratio of 3, the annual generated electricity is greater when a higher pressure ratio is chosen for the design

point. The design point efficiency of the MGT is lower by 0.5% at the new design point, but the system will be able to generate about 0.25MWh more electricity during a year. The annual performance decreases compared to the initial design point when a lower pressure ratio (2.5) is chosen. Nevertheless, annual generated electricity is not the only parameter to take into account for comparing the different cases. When the pressure ratio at the design point is changed, the required dish area will be different. To make a better comparison of the dish-MGT performance, the electricity generated by the system per unit area of the dish is also shown in the table. Although the higher pressure ratio results in better annual performance, technical limitations pertaining to the size and rotational speed of the MGT must be taken into account. Higher pressure ratios result in smaller engine components (lower mass flow rate) and higher rotational speeds (see Figure 3.7 and section 3.3). Consequently, viscous losses and rotor dynamics concerns will be more significant.

Table 5-1 dish-MGT performance results for sample design points with different pressure ratios. Initial design point is shaded.

Pressure ratio (π)	η_{DP} (%)	E_{an} (MWh)	Change in E_{an} (%)	A_{dish} (m ²)	E_{an}/A_{dish} (kWh/m ²)
2.5	20.5	8.761	-4.2	37.45	234
3	20.7	9.148	0.0	37.11	246
3.5	20.2	9.394	+2.7	37.91	248

Another important parameter, which affects the annual system performance, is the position of the design point of the system on the compressor's performance map. With the map scaling method, which was explained in section 3.4.1, once the design point data for the compressor are known, the compressor map can be generated. The basic principle which is included in the scaling technique is that the design point, which is determined by its corresponding mass flow rate and pressure ratio, is chosen on the maximum efficiency line of the compressor map. This line represents the points with maximum efficiency for each compressor speed. Figure 5.1 shows the maximum efficiency line on a sample compressor map. The question would be where to choose the system design point along this line. The annual performance of the system is largely affected by the choice of the design point, which does not necessarily correspond to the highest compressor efficiency, as will be discussed later. When generating the compressor map in the scaling procedure, the position of the design point on the maximum efficiency line can be defined by the ratio of its corresponding rotational speed to the rotational speed of the point with the highest efficiency value on the compressor map. This ratio is defined here by equation 5.1.

$$\sigma = \frac{N_{dp}}{N_x} \quad 5.1$$

Where N_{dp} is the rotational speed of the design point and N_X is the rotational speed of maximum efficiency point (**X**) on the map (see Figure 5.1).

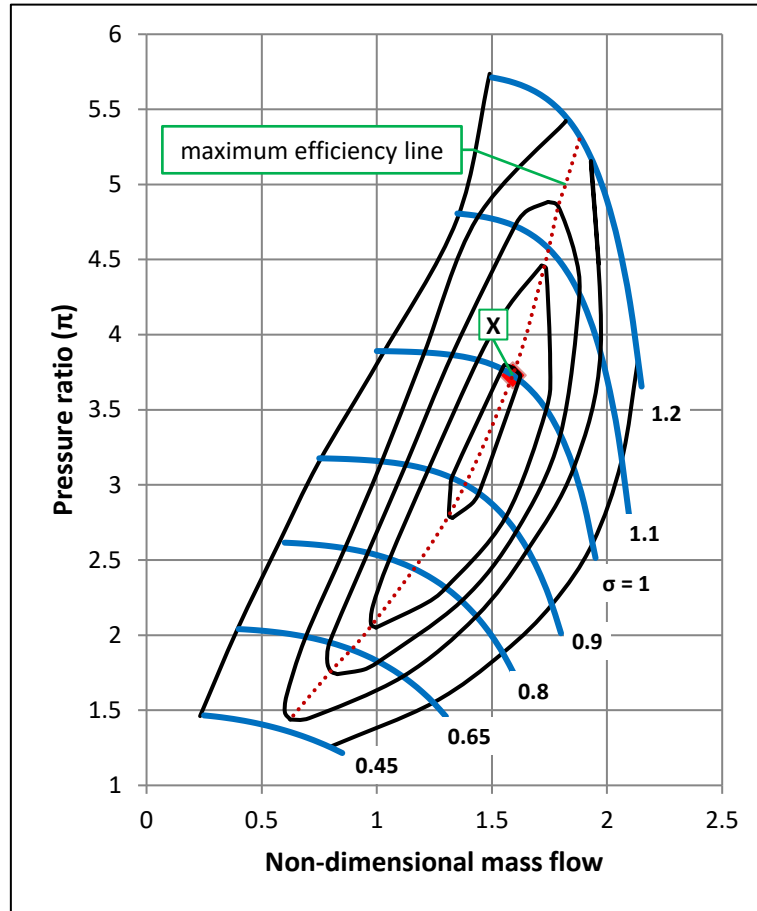


Figure 5.1 position of the system design point on a sample compressor map generated by scaling.
 Maximum efficiency point (**X**) appears in the middle of the line.

The effect of the position of the design point on the maximum efficiency line with respect to point (**X**) is shown in Table 5-2. By moving the system design point from the maximum compressor efficiency point (**X**), the cycle efficiency at the design point decreases because of the reduction in the compressor efficiency. Reduction of the design point efficiency directly affects the dish size which is also shown in Table 5-2. However, it can be seen that the annual generated electricity is significantly increased as σ increases. In fact, the generated electricity increases when the design point of the system moves to the higher speed lines. This can be justified by the fact that the majority of power generation by the dish-MGT system takes place when the DNI, and hence the rotational speed, is lower than the design point value. With the system design point located at higher speed lines, most of the engine operation takes place in the lower speeds where the compressor efficiency is very close to its maximum value. It is also shown that the generated electricity per unit area of the dish decreases because of the larger dish required to generate the

nominal power (5kWe) at the design point. It may be considered to be a set back in terms of system design, however, a proper decision can be made when the economic indicators of the system design and performance are also taken into account. It is important to note that σ only determines the ratio of the rotational speeds of the design point and point **X**. The value of the rotational speed is calculated by the procedure which was explained in section 3.3.3 and depends on the specific speed and thermodynamic parameters at the design point.

Table 5-2 dish-MGT performance results when the position of the design point changes on the compressor map

Position (σ)	η_{DP} (%)	E_{an} (MWh)	Change in E_{an} (%)	A_{dish} (m ²)	E_{an}/A_{dish} (kWh/m ²)
0.9	20.67	8.517	-6.7	37.22	229
1	20.7	9.148	0.0	37.11	246
1.1	14.38	9.795	+7.1	41.03	239
1.2	18.63	11.502	+25.7	53.25	216

Similar consideration of the position of the design point with respect to the turbine performance map may be applied to the turbine. However, when non-dimensional flow is considered versus non-dimensional speed, turbines do not exhibit significant variations (Saravanamuttoo, et al., 2009).

5.2.2 Economic and performance indicators of the system

To quantify the technical and economic performance of the dish-MGT system, it is necessary to use a number of properly defined parameters as the economic and technical performance indicators. For any set of new decision variables, the performance of the system can be evaluated by the thermodynamic performance indicators. The economic performance of the system will also be represented by the calculation of the economic indicators for any particular system design. These thermo-economic indicators will be used to define the objective functions in the optimisation problem.

Thermodynamic performance indicators

The main performance indicator for the dish-MGT system is the annual generated electricity by the system, E_{an} , which has already been used for the comparison of the dish-MGT system performance. This parameter was used to evaluate the effect of applying different control strategies in chapter 4, and when different pressure ratios were considered for the design point earlier in this chapter. Solar to electric efficiency is also a suitable performance indicator of the system which shows the effectiveness of the system for the conversion of the available solar radiation to electricity. However, this parameter is only important when the decision space

includes different geographical locations. Otherwise, the solar efficiency is completely proportional to E_{an} . The annual generated electricity per unit area of the dish is also similar to the solar to electric efficiency except for the fact that it is not related to the annual solar income of the installation site.

Economic performance indicators

The total cost of investment which is required to build a solar dish-MGT system, C_{inv} , is obviously the first economic performance indicator to be considered. It consists of the total purchase cost of the equipment plus the additional costs required for the commissioning and installation of the system and is expressed in Euros (€) in the present work. An economic model which includes related cost functions is required to calculate the final value of C_{inv} for any system design. Details of such a model are given in section 5.3. To provide a better means of comparison for the investment costs of dish-MGT systems with different power ratings, the specific cost of investment, c_{inv} (€/kWe) is often used instead of the total cost of investment and is calculated by dividing the total investment cost by the nominal power rating of the system as shown by equation 5.2.

$$c_{inv} = \frac{C_{inv}}{PWe} \quad 5.2$$

Another important economic indicator is the levelised cost of electricity (LCOE). It is the minimum sale price of the generated electricity which allows the system to recover the total cost of its production during the lifetime of the dish-MGT system. LCOE is calculated on an annual basis considering the total annualised costs and generated electricity and is commonly expressed in either cent€/kWh or €/MWh; the latter is used here. The total annualised costs include the cost of operation and maintenance plus an annualised equivalent of the total cost of investment.

$$LCOE = \frac{\alpha C_{inv} + C_{op} + C_{maint}}{E_{an}} \quad 5.3$$

In equation 5.3 C_{op} and C_{maint} are the operation and maintenance costs respectively and α is capital recovery factor which is used in order to convert the capital costs (C_{inv}) to an equivalent annual cost paid during the system lifetime. The capital recovery factor is calculated based on the number of years of operation, t and the real interest rate, i as shown in equation 5.4 (Madureira, 2014).

$$\alpha = \frac{i(1+i)^t}{(1+i)^t - 1} \quad 5.4$$

The real interest rate is the difference between the nominal interest rate which is officially announced by each country and the inflation rate for a particular year. The real interest rate for each country is calculated and reported by the World Bank organisation (World Bank, 2016).

5.2.3 Multi-objective optimisation algorithm

In the context of techno-economic optimisation of the solar powered dish-MGT systems, normally two objectives must be considered. The system must achieve high generated electricity while a very low cost of the investment is also an important objective to persuade the investors and consumers. As such, the optimisation problem for solar powered dish-MGT systems is often a multi-objective optimisation problem which requires the implementation of an appropriate mathematical technique. To perform a multi-objective optimisation, a common technique is to create a single function from multiple objective functions by the combination of these functions and weight factors as is shown in equation 5.5.

$$F[\mathbf{X}] = \varphi_1 f_1(\mathbf{X}) + \varphi_2 f_2(\mathbf{X}) + \dots + \varphi_n f_n(\mathbf{X}) \quad 5.5$$

Where $f(\mathbf{X})$ represents individual functions each of which multiplied by a weight factor, φ . However, such combination techniques suffer from the problem that they depend on how the weight factors are defined, which directly affect the value of the combined objective function and optimisation result. A more appropriate method to deal with multiple objective functions is to use the Pareto optimality concept.

The concept of Pareto optimality is shown in Figure 5.2. When performing multi-objective optimisation, it is possible to do an equally weighted study by using the concept of Pareto optimality. In this case, no weighting factors are required. Results are not presented as a single optimum point, but a number of answers which form the optimal front will represent the solution.

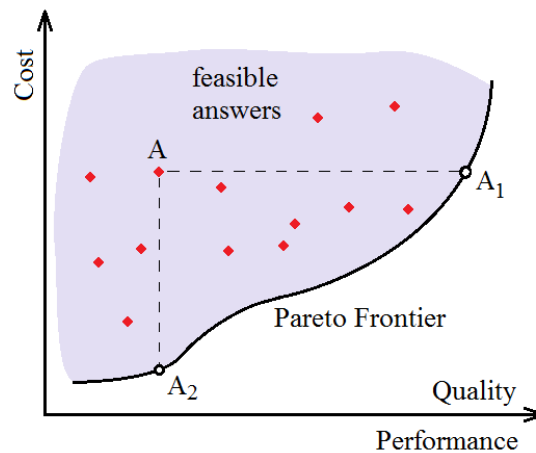


Figure 5.2 Pareto optimality

Every single point on the optimal front corresponds to set of particular decision variables $[\mathbf{X}]$, in which it is impossible to find better value for at least one of the objectives while other objectives don't change. A trade off among the results is required to select one or a few particular points as the best decision.

Therefore, the results are not presented as a single optimum point, but a number of solutions which form the Pareto frontier (optimal front). Every single point on the optimal front corresponds to set of particular decision variables, $[\mathbf{X}]$, in which it is impossible to find better value for at least one of the objective functions while other objective functions don't change.

To choose an appropriate multi-objective optimisation algorithm, studies made by Pelster (Pelster, 1998), Leyland (Leyland, 2002) and Spelling (Spelling, 2013) have been taken into account which emphasise that for energy systems like solar powered gas turbine cycles the optimisation problem are non-linear and include several local minima and discontinuity. As such, evolutionary algorithms (EAs) are considered as suitable tools for this kind of problem because of their robustness and have the capability to find the ultimate global minimum. Inspired by biological evolution, an EA applies mutation and reproduction procedures on an initially chosen population of the design points (first generation) to ultimately find a number of optimal design points (last generation). The initial population is chosen from candidate solutions which are simply within the feasible region where any set of the decision variables satisfy the constraints. In this work, a genetic algorithm (GA) has been used.

5.2.4 Optimisation framework

The general representation of the workflow which is designed in the current thesis for the optimisation consists of two main modules: OPTIMISER which uses an algorithm to generate or modify the values of the decision variables $[\mathbf{X}]$ and MODEL which calculates the objective functions $\mathbf{F}[\mathbf{X}]$ for any set of the given decision variables. To create the first generation of decision variables, OPTIMISER uses a uniform distribution algorithm which chooses the initial $[\mathbf{X}]$ from all over the decision space which is determined by the available technology. Application of this algorithm reduces the risk of missing an area within the decision space which contains the global minimum. For the next generations, the OPTIMISER module analyses the values of the objective functions which are calculated by the MODEL and modifies the values of the decision variables. Figure 5.3 shows the structure of the optimisation procedure and arrangement of the OPTIMISER module and MODEL. The system performance is checked against the predefined constraints before the results are fed to the OPTIMISER. When the performance of the system is beyond the

safety limits (system constraints), an error signal is sent to the OPTIMISER to consider and save this hole in the decision space and generate a new set of $[X]$ values.

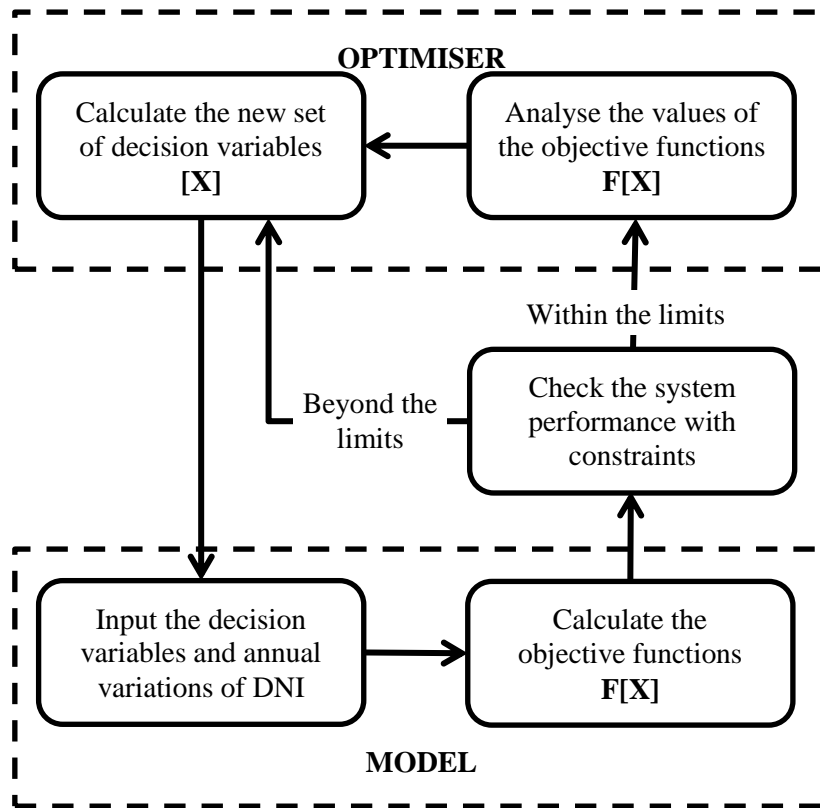


Figure 5.3 diagram of the optimisation framework

An optimisation module from MATLAB software is used for the OPTIMISER block. MATLAB provides two main toolboxes for optimisation which are the “Optimisation Toolbox” and the “Global Optimisation Toolbox” (MATLAB GO toolbox, 2015). The latter includes optimisation algorithms to find the global minimum of the objective function when the optimisation problem may include several local minima at the same time. A multi-objective optimisation module which employs a genetic algorithm is also included in the toolbox to find the global minima of the fitness (objective) functions. Clearly, some objectives such as the generated electricity are required to be a maximum for optimal performance. This is accomplished easily by setting the negative value of such functions as the ultimate objective function in the minimisation procedure. To avoid weight factors the multi-objective optimisation, Pareto optimality option is used.

The optimisation module must be able to communicate with MODEL. This is accomplished by using MATLAB as the main platform. Each time, the genetic algorithm in the optimisation module makes a new generation which includes N sets of decision variables. For each set of the decision variables, the performance code is executed within the MATLAB environment. The economic model is then called in the same way in MATLAB. Thermodynamic and economic

performance data are then used by a MATLAB code to calculate the objective functions. When the corresponding objective functions for the whole generation are calculated, the results are returned to the optimisation module to analyse and create the new generation.

The optimisation algorithm continues until the Pareto solutions satisfy the termination criteria which confirm that the optimisation procedure has converged and the results are close enough to the ultimate solution. The termination criteria are defined based on the movement of the Pareto frontier over a given number of generations. These criteria are the change in the position of the Pareto front members between the last two iterations and also the average spread of the points on the Pareto front over the last generations. The spread of the points on the Pareto frontier is determined as the standard deviations of the objective functions on this line with respect to their mean.

5.3 Economic model

The economic model provides the cost functions which are required to ultimately calculate the investment cost and other economic indicators which were introduced in section 5.2.2. The main component of the investment cost is normally the purchase cost of the system equipment which includes the cost of the micro gas turbine, solar receiver and solar concentrator (dish). It is important to distinguish between the manufacturing cost and the purchase cost of the equipment. Although the former is the basis for the calculation of equipment cost, economic models require the purchase cost of the system to evaluate the ultimate value of the investment cost and also the cost of the generated electricity. The purchase cost is related to the manufacturing cost by a profit margin.

As mentioned in chapter 2, the main challenge to provide a suitable economic model for the dish-MGT systems is that existing data on the cost of small scale micro gas turbines and solar components are very limited. The economic models which were introduced in the literature review have been developed based on data from much larger engines. Therefore, the application of such models for small micro gas turbines cannot be properly justified. To accomplish one of the main tasks which was defined within the OMSoP project, a team of three members of the consortium, University of Seville, University Roma three (RO3) and Compower worked on the cost analysis of the system and provided a model which is sensitive to not only the design parameters of the system but also the annual production rate. The model has been developed based on data which are available for micro gas turbines in the power range from 5 to 50kWe and also on actual data provided by the consortium members, including City, who was responsible for the design and build of the MGT unit, and KTH who provided the solar receiver. The proposed model

includes cost functions for the individual components of the system which are suggested for a specific quantity of annual production.

The total cost of investment is the sum of the major components purchase cost C_{eq} , the costs associated with the auxiliary components including the electric boxes and switches, C_{aux} (see section 5.3.4), and the costs of system installation C_{inst} as shown by equation 5.6. The total purchase cost of the components is divided into the cost of the MGT as a complete unit, the solar receiver and the dish (equation 5.7).

$$C_{inv} = C_{eq} + C_{aux} + C_{inst} \quad 5.6$$

$$C_{eq} = C_{MGT} + C_{recv} + C_{dish} \quad 5.7$$

The purchase cost of the components is calculated from their manufacturing costs by merely using a profit margin which is estimated to be about 15% by the OMSoP partners based on common industrial practice. It is important to note that the profit margin which is defined here, does not cover overhead and unpredicted costs. These costs are assumed to be covered by the commissioning and installation costs, otherwise, a much larger profit margin should be used in the economic model. The relation between the purchase cost, C_{eq} , the manufacturing cost $C_{eq,m}$, and profit margin PM is shown by equation 5.8.

$$C_{eq} = \frac{C_{eq,m}}{1 - PM} \quad 5.8$$

5.3.1 Cost functions for the MGT assembly

The OMSoP model provides the manufacturing cost of the equipment. For the MGT, the manufacturing cost function covers the rotor assembly, recuperator and electrical components and is given by equations 5.9 to 5.11 (Sánchez, 2015).

$$C_{MGT,m} = c_{MGT,m} \cdot f_{MGT} \cdot \dot{m} \quad 5.9$$

$$c_{MGT,m} = a_{MGT,\dot{m}} \dot{m}^2 + b_{MGT,\dot{m}} \dot{m} + c_{MGT,\dot{m}} \quad 5.10$$

$$f_{MGT} = a_{MGT} L^{b_{MGT}} + c_{MGT} \quad 5.11$$

In the above equations $C_{MGT,m}$ is the total manufacturing cost of the MGT system, $c_{MGT,m}$ is the cost per unit mass flow rate (in g/s) and f_{MGT} is the correction factor when the production rate of the units, L, varies. Coefficients $a_{MGT,\dot{m}}$ to $c_{MGT,\dot{m}}$ depend on the TIT and effectiveness of the recuperator. These parameters are considered as the main design parameters of the micro gas turbine which not only affect its performance, but are also very influential on its total cost. There

are other design parameters like pressure ratio and the component efficiencies which have an important role on the ultimate performance of the MGT, but once a system is designed and efforts to achieve high efficiency components are completed, the manufacturing cost is not affected significantly by these parameters. The cost model for large engines includes terms for the pressure ratio because higher pressure ratio in such machines is achieved by increasing the number of turbine and compressor stages which results in higher cost. For a recuperated MGT engine, such architectures are not used and the cost is not affected by the pressure ratio. The coefficients a_{MGT} to c_{MGT} in equation 5.11 are used for the correction of the production rate factor. When the production rate is 1000 devices per year, f_{MGT} is equal to unity. Table 5-3 shows the numerical values of the coefficients used in the above equations followed by Table 5-4 which includes economic data for the MGT assembly.

Table 5-3 coefficients of the economic model for the micro gas turbine

TIT (°C)	Recuperator effectiveness	a	b	c
800	0.85	1.439×10^{-4}	-0.10239	48.278
800	0.90	1.483×10^{-4}	-0.10552	49.755
900	0.85	1.630×10^{-4}	-0.11594	54.664
900	0.90	1.682×10^{-4}	-0.11969	56.432
Coefficients for f_{MGT}		6.116	-0.2911	0.1861

Table 5-4 specific manufacturing cost of the MGT (no combustor) for two design points (Sánchez, 2015)

TIT (°C)	ε (%)	Specific cost (€/kWe)
800	85	530
900	85	430

The cost values are presented in specific form and therefore are independent of the rated power of the system. The specific cost is reduced for the higher TIT because a smaller engine will be enough to achieve the same power rating with the elevated turbine inlet temperature.

Although this model is suitable for small-scale MGTs, it doesn't address the effects of the key parameter, the turbine exit temperature, on the cost of the recuperator. The TET plays an important role on the annual performance of the dish-MGT system and enters in the calculations as a constraint. For a high turbine inlet temperature to be very effective in the improvement of annual generated electricity, an appropriate material with high temperature resistance should be used for the construction of the recuperator. Otherwise, the use of improved turbine material and its corresponding higher cost will be wasted. Using the methodology which is suggested and

applied in the current thesis, the effect of the chosen TET is properly considered in the performance calculation and is required to be also considered in the economic performance of the system. Therefore, it is required to break down the cost of the total MGT assembly to the main engine and the recuperator. Then, it will be possible to include the effect of the maximum allowable temperature of the recuperator in the cost calculations.

According to McDonald and Rodgers, cost of the recuperator is about 30% of the total cost of small micro gas turbines (McDonald & Rodgers, 2008). Taking this figure into account, it is possible to estimate the cost of the recuperator for an MGT with known design and cost data. From the given data for the base case system with 85% effectiveness, a TIT of 800°C and a stainless steel recuperator which allows for a maximum TET of 650°C, the manufacturing cost of the MGT is about 530 €/kWe and the corresponding cost of the recuperator would be 160 €/kWe. The cost of the recuperator is affected by the total cost of the material used in its construction which in turn is a function of its mass flow rate, effectiveness and its maximum allowable temperature (TET). The first two parameters determine the size of the recuperator while the material used in the recuperator depends on the chosen TET limit. According to Rodgers, the cost of the recuperator can be calculated using the following equation (Rodgers, 2000).

$$C_{recp,m} = k_{recp} \dot{m} \frac{\varepsilon}{1 - \varepsilon} \quad 5.12$$

To calculate the constant k_{recp} , the cost of the stainless steel recuperator and the corresponding design data for the base case is known and may be used as summarised in Table 5-5.

Table 5-5 cost of stainless steel recuperator and the corresponding multiplier

Specific cost (€/kWe)	160
Rated power (kWe)	6
C_{RECP} (€)	960
\dot{m} (kg/s)	0.088
ε	0.85
k_{recp}	1925

For a recuperator made from a different material, a multiplier is suggested as shown in Table 5-6 (McDonald, 2003).

Table 5-6 maximum working temperature of the recuperator for different materials and the corresponding multiplier in respect to stainless steel (S/S)

Material type	S/S	S/S super alloy	Inconel	Haynes 230	Haynes 214
Max temperature (°C)	675	750	800	850	900
Ratio to S/S alloy (R_{recp})	1	1.5	5	7	9

The final form of the recuperator cost function will be given by equation 5.13.

$$C_{recp,m} = 1925 R_{recp} \dot{m} \frac{\varepsilon}{1 - \varepsilon} \quad 5.13$$

With the cost of recuperator determined by equation 5.13, its share in the total cost of the MGT is subtracted from the equations 5.9 to 5.11. To extend the functionality of these equations to the variation of TIT, a linear regression is applied over the coefficients of equation 5.10 between TIT values of 800°C and 900°C with a fixed recuperator effectiveness. The result is a modified cost equation with the effect of TIT (K) directly included in the coefficients of the cost function as shown in equations 5.15 to 5.16.

$$a_{MGT,\dot{m}} = 1.337 \times 10^{-7} TIT - 4.273 \times 10^{-5} \quad 5.14$$

$$b_{MGT,\dot{m}} = -9.485 \times 10^{-5} TIT + 3.0101 \times 10^{-2} \quad 5.15$$

$$c_{MGT,\dot{m}} = 4.4702 \times 10^{-2} TIT - 14.1706 \quad 5.16$$

Using equations 5.13 to 5.16 in combination with equations 5.9 and 5.10 provide the cost model for the recuperator and the MGT.

5.3.2 Cost function of the receiver

The cost function for the solar receiver in the OMSoP economic model takes the effects of the receiver's size and working temperature on its manufacturing cost in a unique set of functions similar to equations 5.9 and 5.10 (Sánchez, 2015).

$$C_{recv,m} = c_{recv,m} \cdot f_{recv} \cdot q_{recv} \quad 5.17$$

$$c_{recv,m} = a_{recv,q} \cdot q_{recv}^2 + b_{recv,q} \cdot q_{recv} + c_{recv,q} \quad 5.18$$

$$f_{recv} = a_{recv} L^{b_{recv}} + c_{recv} \quad 5.19$$

In the above functions, $C_{recv,m}$ is the total manufacturing cost of the receiver in (€) and $c_{recv,m}$ is the specific cost of manufacturing per thermal heat input to the receiver (€/kWth). As introduced in chapter 3, q_{recv} is the thermal heat from solar irradiance received at the aperture of the receiver (kWth). The coefficients of the function are mainly derived from the data provided by the consortium members, the Royal institute of technology in Stockholm (KTH) and Innova, a company which used to commercialise small scale dish-Stirling systems including directly illuminated solar receivers. The data from KTH is based on the prototypes of cavity receivers manufactured for the OMSoP project. The model also includes a correction factor to account for

a production volume similar to the MGT cost model. This correction factor is based on previous studies investigating pressurised solar receivers which were completed by two individual research teams (Gallup & Kesseli, 1994) and (Pioneer engineering Co., 1980).

Similar to the cost functions for the MGT, the coefficients $a_{recv,q}$ to $c_{recv,q}$ account for the effects of the working temperature of the receiver. Because the working temperature of the receiver is close to the turbine inlet temperature, it also appears in the coefficients of the cost function for the receiver as shown in equations 5.20 to 5.22.

$$a_{recv,q} = 2.11 \times 10^{-6}TIT - 1.133 \times 10^{-3} \quad 5.20$$

$$b_{recv,q} = -6.78 \times 10^{-4}TIT + 3.9489 \times 10^{-1} \quad 5.21$$

$$c_{recv,q} = 8.146 \times 10^{-2}TIT - 50.1166 \quad 5.22$$

The coefficients in the equation 5.19 to calculate the correction factor for the rate of annual production are shown in the following table.

Table 5-7 coefficients of the economic model for equation 5.19

	a_{recv}	b_{recv}	c_{recv}
f_{RECV}	14.694	-0.4231	0.2292

5.3.3 Cost of the dish

Principally, the cost of the dish is a function of its aperture size. To suggest a cost function for the dish, data from an OMSoP consortium member, Innova, has been taken for their own manufactured parabolic dish systems and extended for a wider range of aperture areas using existing data from previous work (Pioneer engineering Co, 1981). The resultant data are shown in Table 5-8.

Table 5-8 manufacturing cost of the solar dish as for different aperture sizes (Sánchez, 2015)

Area (m ²)	Material cost (€)	Production cost (€)	Total cost (€)	Specific cost (€/m ²)
50	11433	2174	13608	272
90	19404	3914	23319	259
130	29079	5654	34733	267
170	41625	7394	49019	288
210	58381	9134	67516	322

It can be seen that cost of the dish per unit area (specific cost) decreases for small sizes. However, unlike other components, the specific cost doesn't show a monotonic trend and increases after a

particular aperture size. There are a number of reasons which can be considered for the justification of the increase in the specific cost for large dishes.

1. Higher surface quality is essential for a very large dish to avoid excessive spillage and achieve the same reflective efficiency as a smaller dish to keep the proportionality between the MGT system and dish size.
2. Mounting of the facets and calibration of the dish requires a higher level of technology for larger focal lengths and also increases the labour cost.
3. The cost of the foundation and the supporting structure rapidly increases for large aperture sizes because of the nonlinear effect of wind load on the dish.

The manufacturing cost is formulated similar to the functions for the MGT assembly and the solar receiver, and is given by equations 5.23 and 5.24. To account for the effect of production volume on the manufacturing cost of the dish, Innova provided data for different annual production rates ranging between 50 and 10,000 units per year. These data are used in order to suggest a correction factor (equation 5.25) which takes the effect of the production volume on the manufacturing cost into account.

$$C_{dish,m} = c_{dish,m} \cdot f_{dish} \cdot A_{dish} \quad 5.23$$

$$c_{dish,m} = a_{dish,A} \cdot A_{dish}^2 + b_{dish,A} \cdot A_{dish} + c_{dish,A} \quad 5.24$$

$$f_{dish} = a_{dish} L^{b_{dish}} + c_{dish} \quad 5.25$$

In the above equations, $C_{dish,m}$ and $c_{dish,m}$ are the total (€) and specific (€/m²) costs of the dish respectively. The coefficients that are used in equations to are given in Table 5-9.

Table 5-9 manufacturing cost of the solar dish as for different aperture sizes (Sánchez, 2015)

	Cost function coefficients		
	a	b	c
$c_{dish,m}$	4.760x10 ⁻³	-0.9140	304.54
f_{dish}	3.610	-0.3095	0.5308

5.3.4 Additional costs of the plant

In addition to the main components of the dish-MGT system, there are other items which must be taken into account including the cabling, fire extinguishing system and electrical switches and boxes which are mounted either on the ground or on the dish. The total cost of these items is termed as the auxiliary equipment cost in the OMSoP economic model and is calculated using equations 5.26 and 5.28.

$$C_{aux,m} = c_{aux,m} \cdot f_{aux} \cdot A_{dish} \quad 5.26$$

$$c_{aux,m} = 455.7A_{Dish}^{-1.022} + 0.5617 \quad 5.27$$

$$f_{aux} = 19.75L^{-0.5439} + 0.3691 \quad 5.28$$

Other expenses to raise a solar dish-MGT plant include the costs of commissioning and civil work for the installation of the system as indicated in equation 5.6. Commissioning costs cover the assembly of the system components (mainly on the ground) and auxiliary equipment, connection to the grid and testing and validation operations before the start-up of the system. Civil work is required to prepare the foundation for the installation of the dish. The specific installation cost is calculated per unit area of the dish as it is mainly affected by the area of the dish and the system power rating which is again related to the dish size. Equation 5.29 shows the cost function for the installation costs.

$$C_{inst} = A_{dish}(c_{civil} + c_{comm}) \quad 5.29$$

Where the specific cost of the civil work and commissioning of the system are 28.7€/m² and 57.4€/m² respectively (Gavagnin, et al., 2017).

Having all of the items in the investment cost discussed and formulated, it is possible to calculate the total cost of investment for any particular set of design parameters. The total cost and economic details for the OMSoP base case system with a 5kWe rated output power which was considered in section 3.3.1, are indicated in Table 5-10. The design parameters for this particular case were given in section 3.3.

Table 5-10 cost of the components for the case study system with net power output of 5kWe (design point)

MGT (€)	3012
Recuperator (€)	1169
Receiver (€)	931
Dish (€)	13594
AUX (€)	522
<hr/> C _{eq} (€)	<hr/> 19228
Installation (€)	3624
<hr/> C _{inv} (€)	<hr/> 22852
<hr/> Specific (€/kWe)	<hr/> 4570

Figure 5.4 shows the cost breakdown and the share of each component in the total cost of the system.

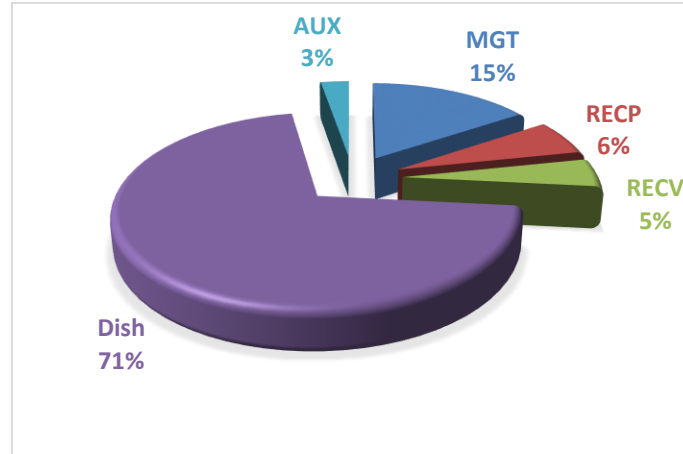


Figure 5.4 shares of the components costs in the total cost of the system designed for case study.

To calculate the levelised cost of electricity (equation 5.3), the operational and maintenance costs which are continuously incurred throughout the lifetime of the system have to be considered. For a pure solar dish-MGT system, the operation costs are not significant because unlike the hybrid solar systems there is no fuel supply; therefore the operational cost cover the cost of the water consumed for the cleaning of the dish. The cost of water for industry in European countries is very different. For Italy, where the OMSoP dish-MGT will be installed, and for Spain it is 0.5€/m³ and 1.1€/m³ respectively (Lallana, 2003). The water consumption per unit area of the dish is about 50litre/m² (DOE, 2001). Therefore, the total cost of the consumed water is calculated using equation 5.31.

$$C_{op} = C_w = 0.05a_w A_{dish} \quad 5.30$$

Where a_w is cost of water per cubic meter. The maintenance cost is calculated as a percentage of the cost of each piece of equipment. As suggested by Spelling, these are set to 2% for the MGT, 3% for the dish, and 4% for the receiver (Spelling, 2013).

$$C_{maint} = 0.02(C_{MGT} + C_{recep}) + 0.03C_{dish} + 0.04C_{recv} \quad 5.31$$

5.4 Optimisation of the dish-MGT systems

Having established the optimisation framework and the economic model, it is possible to define the optimisation problems in accordance with the objectives of the current research. Two different problems are attempted in this work. The first problem focuses on the optimisation of a pure solar dish-MGT system with a fixed rated output power while the main influential design parameters on the system performance are allowed to change. The objective of this problem is to find the design parameters which result in the optimal trade-off between thermodynamic and economic performance. The results facilitate a comparative study between the performance of a pure solar

dish-MGT and other solar powered systems. The second problem performs the optimisation over a wide range of feasible dish sizes. Other parameters including the rated power are allowed to change. The main objective of this problem is to explore the optimal system sizing for pure solar dish-MGT systems.

5.4.1 Fixed rated power

For this study a dish-MGT system with 5kWe rated power similar to the case study introduced in section 3.3.1 and based on the target power of the OMSoP project is considered. The objective functions for the system optimisation are chosen to be the total investment cost of the system, C_{inv} and the annual generated electricity, E_{an} . The cost of the investment is chosen as the economic performance indicator because a low C_{inv} would be the main incentive to choose between dish-MGT and the competitor technologies, dish-Stirling and PV, at the first place. The decision variables for the optimisation of the system are those design parameters which are influential to either the economic or thermodynamic performances of the system and preferably on both of the performance indicators. Among the design parameters, compressor efficiency, pressure ratio, the relative position of the maximum efficiency point, σ and turbine efficiency, which are inherently compressor design parameters, considerably affect the overall system performance. However, they are not influential on some of the economic indicators, particularly the investment cost. These parameters are technical parameters which affect the topology of the compressor and turbine map and their initial design. As shown in section 5.3, the maximum allowable TIT and TET, recuperator effectiveness and the mass flow rate directly affect the cost of the investment and, at the same time, the economic performance of the system.

Optimisation setup

The optimisation is performed for a dish-MGT system with fixed rated output power. The system is assumed to be installed in Casaccia, Italy, where data is available for the annual variations of DNI, ambient temperature and relative humidity with a time resolution of 30 minutes. For the calculation of the system cost, a production volume of 1000 units per year is assumed. The decision variables and objective function as well as the system constraints are shown in Table 5-11.

The multi-objective optimisation problem includes two contradictory objective functions, where their optimal values do not occur at the same point in the decision space. Maximum system performance requires maximum achievable system specifications which results in very high C_{inv} . This indicates the existence of optimal designs and a Pareto optimality approach can be used to find all potential solutions.

Table 5-11 problem setup to find optimal compressor design parameters

Decision variable		π	σ	ε	η_c	η_t	TIT_{max}	TET_{max}
Decision space	Lower limit	2.5	0.8	0.8	0.7	0.75	750°C	650°C
	Upper limit	4.0	1.2	0.9	0.8	0.85	1000°C	800°C
System constraints					$TIT < TIT_{max}$ $TET < TET_{max}$ $N_{dp} < 150krpm$			
Objective functions		E_{an}			C_{inv}			

Justification of the selected variables are given by the following points. Upper and lower limits for the decision space are chosen based on the current state of art technology. Except for the maximum rotational speed, system constraints are defined in a parametric form and change with the decision variables TIT_{max} and TET_{max} . The maximum limit for the rotational speed at the design point has been already discussed in chapter 3. The efficiencies of the major components of the MGT are included in the decision variables which allow for the calculation of the rotational speed and apply the corresponding constraint. Although the mass flow rate appears explicitly in the cost of MGT, it has not been added to the decision variables because it is derived during the calculations. The efficiencies of the optical components are not included because their effect on the objective functions are monotonic functions and therefore the maximum values with the currently available technology are considered.

Optimisation convergence

Genetic algorithm was used in the multi-objective optimisation module in MATLAB, which converges to a Pareto optimal front (MATLAB GO toolbox, 2015). Figure 5.5 shows the evolution of the designs as the genetic algorithm progressed.

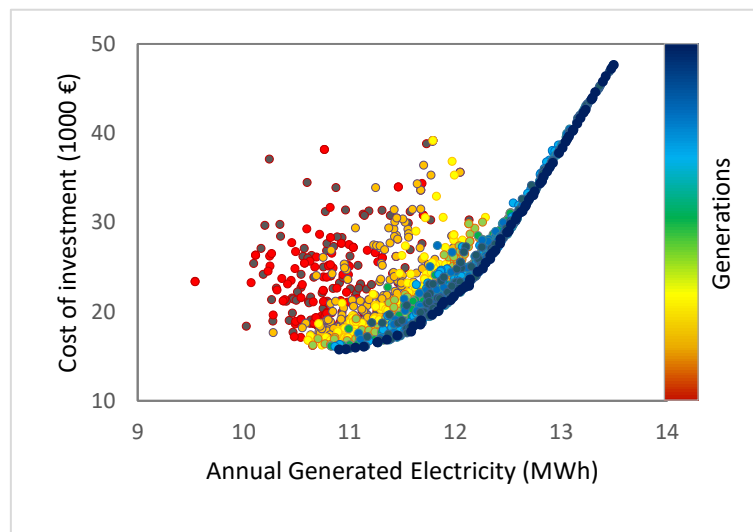


Figure 5.5 evolution of the optimisation results towards Pareto front

The algorithm converged after 75 generations with an initial population size of 200. The results in the last generation clearly form a Pareto front. The population of the Pareto solutions is chosen to be 70 (35% of the total population for each generation). Obviously, Figure 5.5 doesn't show all of the 75 generations to allow the reader distinguish between different colours allocated to progressive generations.

The Pareto front provides a number of optimal systems with specific costs as high as 9400€/kWe and generated electricity of about 13.5MWh per year. This reduces to 11MWh per year for the cheapest designs. A trade-off among the existing solutions requires considering several technical and economic parameters to ultimately choose one of the optimum designs. The levelised cost of electricity is a determining parameter which is the main basis for the comparison between different systems. Figure 5.6 shows the LCOE for the Pareto solutions against the annual generated electricity. The point corresponding to the minimum LCOE is the most attractive design from an economic perspective. This point is shown as MINC (minimum cost) in the graph and its specifications are given by Table 5-12.

Table 5-12 specifications of minimum LCOE point on the Pareto front

π	σ	TIT_{max} (°C)	TET_{max} (°C)	ε	η_c	η_t
2.9	1.04	935	727	87%	79%	84%

Figure 5.6 also shows the position of the initial design point (IDP) which was introduced in section 3.3.1 for the base case study. The thermo-economic performance of the IDP and the MINC designs are highlighted in Table 5-13. Generating almost the same amount of electricity during a year, the optimised MINC system requires a 32% smaller dish compared to IDP design which reduces the capital investment cost by 30%. This substantially affects the cost of electricity and the solar to electric efficiency of the system.

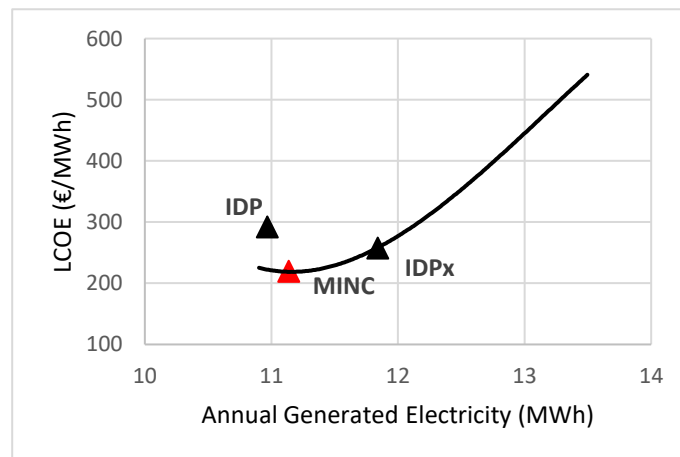


Figure 5.6 LCOE for the Pareto solutions

Another design which may be picked from the Pareto front is the system with equal capital cost of the IDP. This is designated as IDPx in Table 5-13 and this system shows the performance improvement which is achievable at no extra cost compared to the initial design. More electricity is achievable with a smaller dish when this design is used which results in a lower cost of electricity and considerable improvement in the solar efficiency.

Table 5-13 performance data for the selected points on Pareto front

Design	E_{an} (MWh)	A_{Dish} (m ²)	c_{inv} (€/kWe)	LCOE (€/MWh)	η_{solar}
MINC	11.06	29.01	3196	219	23.3%
IDP	10.97	42.06	4570	292	15.9%
IDPx	11.84	34.21	4570	257	21.1%

Figure 5.7 shows how the percentage of the components costs change in respect to the total purchase cost of the system. Compared to Figure 5.4, it can be seen that the share of the dish has been reduced because of the smaller dish required in the optimised system compared to the initial design. Instead, the recuperator share in the total cost has considerably increased because of higher effectiveness and maximum temperature.

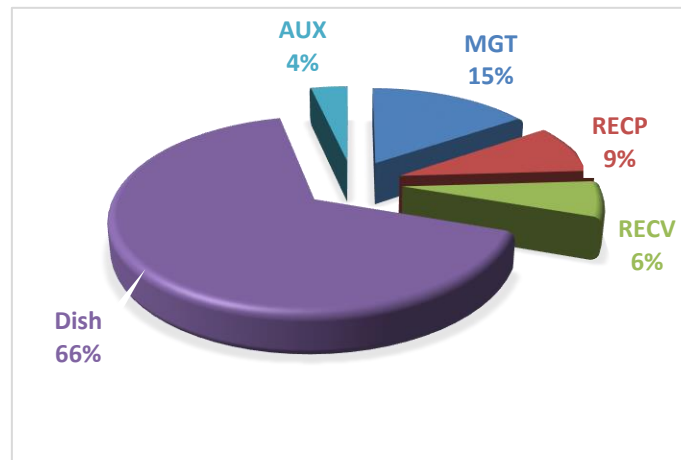


Figure 5.7 shares of the components in the total cost of the optimised system

Technical improvement

Optimised designs, which are focused on here, are also different from initial design in terms of the system specifications. The turbine inlet and exit temperatures in the MINC and IDPx designs are higher than the values assumed for the initial design as shown in Figure 5.8.

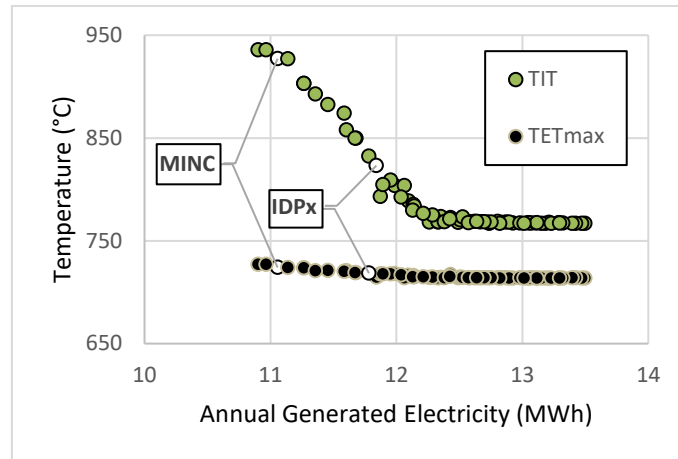


Figure 5.8 Turbine inlet and exit temperatures for Pareto line designs

Therefore, more advanced materials will be required for the manufacturing of the components of MGT. Additionally, the rotational speeds of the optimised designs, MINC and IDPx, appear at the uppermost limit of the problem setup. High rotational speed can introduce rotor dynamic issues in addition to the higher mechanical stress in the turbine wheel which can be addressed using advanced, hence expensive materials with lightweight and high mechanical yield strength at high temperatures. In the OMSoP project, a Titanium Aluminide turbine is used for the first time to deal with the rotor dynamic complexities as well as the high temperature strength. Although the pertaining costs are included in the economic model, such technical improvements require extensive research before they can be applied to the production lines.

The positive effect of a high TIT in the optimum design is that it leads to lower mass flow rate. High efficiency and a low mass flow rate results in a smaller dish and other components like the solar receiver and recuperator as shown in Figure 5.9. An interesting point to notice about the results on the Pareto front is that the designs which result in higher LCOE (see Figure 5.6), require less technical improvements. As it can be seen in Figure 5.8, the maximum allowable TIT and TET are much lower for these designs compared to the points close to MINC. With low TIT, the efficiency of the MGT will be lower whilst the dish size will be larger, as shown in Figure 5.9. Such designs bring about a noticeable advantage in that they are placed well below the current technical limits which makes them suitable for users with limited access to advanced technologies and support. This can be a determining factor when the installation of a dish-MGT system is being made in a less developed region.

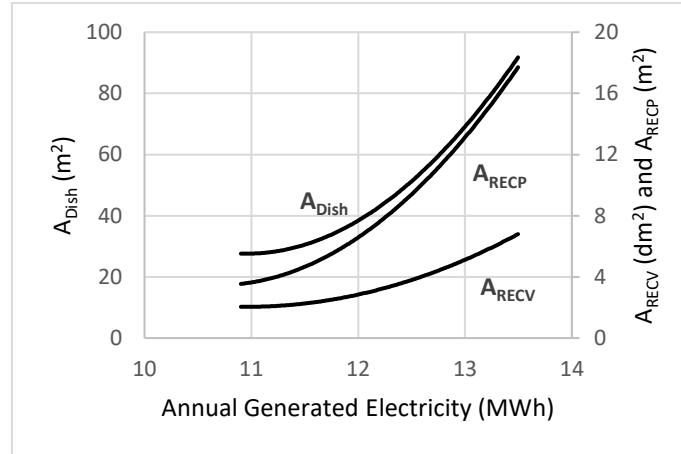


Figure 5.9 size of the components for the optimal design points

Effect of annual DNI income

To study the effect of the annual DNI income, optimisation is also done for Seville with cumulative annual DNI of about 2.25 MWh/m^2 which is higher compared to 1.51 MWh/m^2 for Rome. The optimal front achieved after 40 generations and is shown in Figure 5.10.

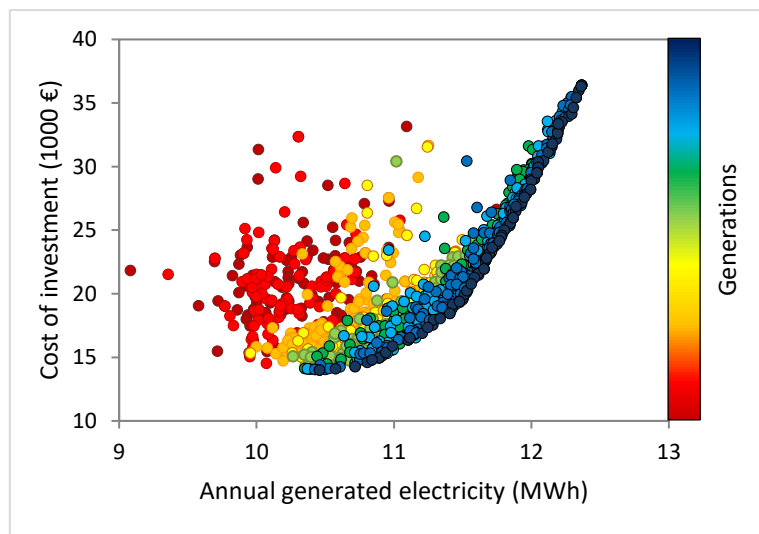


Figure 5.10 Pareto solutions for 5kWe dish-MGT in Seville

The main economic and performance indicators for the optimal designs in two geographical positions are compared in Figure 5.11. While the annual generated electricity is almost the same for both regions because of the similar rated power output, the required dish size is considerably smaller for Seville which results in lower investment cost. Because of the reduction in the cost of the system, the LCOE considerably decreases from 219 €/MWh for Casaccia to 158 €/MWh for Seville.

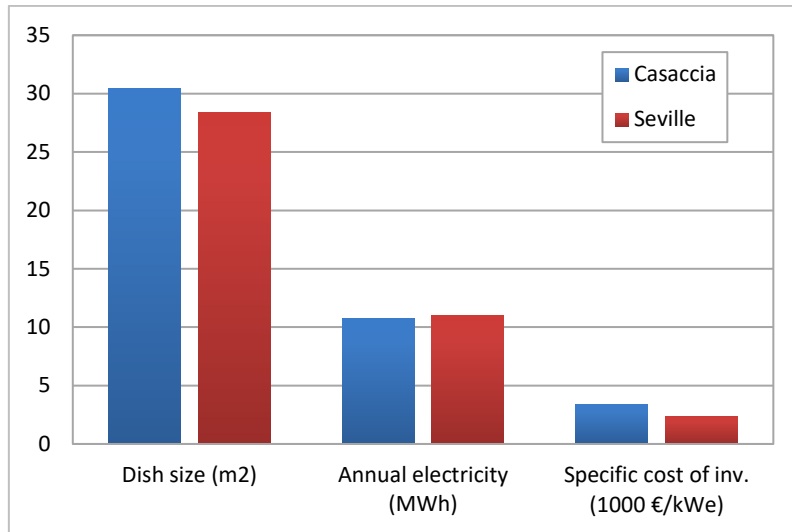


Figure 5.11 comparison of the performance indicators of the optimised designs for Casaccia and Seville

This decreasing trend is shown in Figure 5.12 against the annual solar income and this obviously indicates that the cost of electricity is significantly determined by the geographical location where the system is installed.

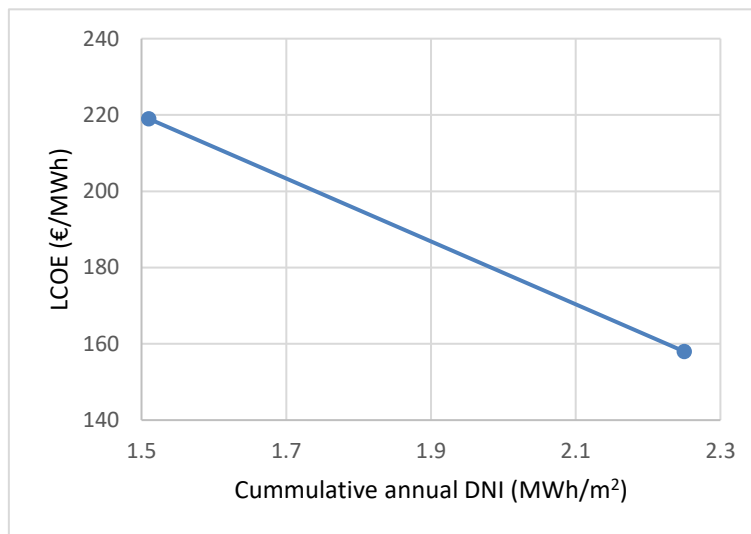


Figure 5.12 variation of LCOE with the total DNI income

Table 5-14 real interest rates for Italy and Spain for three consecutive years (World Bank, 2016)

year	2014	2015	2016
Italy	3.9	3.4	2.7
Spain	6.4	4.0	3.9

The effect of the installation location is important not only because of the strong effect of DNI income, but also because of the effect of local value of the real interest rate which directly enters

in the calculation of LCOE. The real interest rates for Italy and Spain from 2014 to 2016 are shown Table 5-14.

Compared to the achievable cost of electricity in dish-Stirling systems, which is about 270€/MWh as reported by (Osborn, et al., 2003), the economic performance of the dish-MGT systems is deemed to be promising. However, this is still far from the hybrid solar gas turbine based power plants with about 120€/MWh and PV systems that range between 55 and 80€/MWh. Larger production volumes reduce the cost of each unit and result in a lower cost of electricity. As it can be seen from Figure 5.13, the cost of the generated electricity reduces to 92€/MWh for Seville for a production rate of 50,000 units per year. Considering the fact that the given electricity costs for PV and solar thermal technologies mentioned here are for large installations and production rates, the pure solar dish-MGT systems show a good potential for electricity generation in high solar income areas provided that the technology and the market become mature enough to allow for the mass production of dish-MGT units.

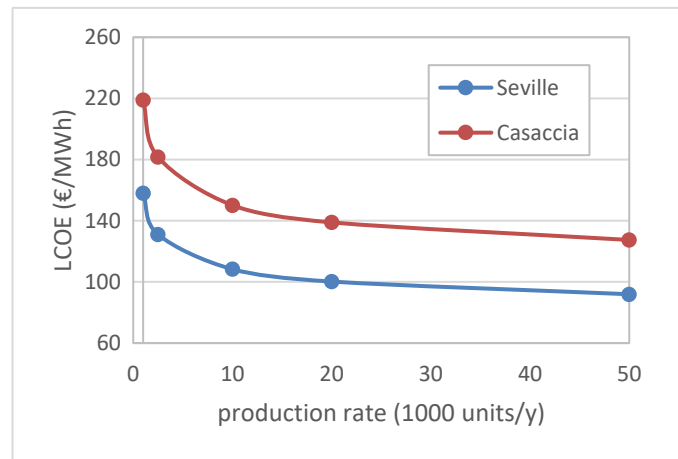


Figure 5.13 cost of electricity for larger production volumes of a 5kWe dish-MGT system

From the MGT design perspective, there is not a big difference between optimal designs except for the TIT. As presented in Table 5-15, the turbine inlet temperature in the optimal design for the micro gas turbine in Seville is about 45°C lower than Casaccia which results in a further reduction of the cost.

Table 5-15 specifications of the optimal design of the MGT for Casaccia and Seville

Region	TIT	TET	π	η_c	η_t	ε
Casaccia	890	720	2.8	0.79	0.84	0.87
Rome	935	727	2.8	0.8	0.84	0.87

5.4.2 Variable rated power

In the last section optimisation of dish-MGT system was completed for a given rated power output. However, the optimised system needed to be produced in quite a large volume to be competitive from an economic point of view. The levelised cost of electricity will also decrease for larger dish-MGT systems, because of the increased annual generated electricity, provided that the specific cost of investment is also decreased. In the light of this point, it is possible to achieve systems sizes (rated power) with better thermo-economic performance. Reviewing the effect of the size on the component cost functions, it is expected that the specific cost decreases as the rated power of the system increases. However, because the specific cost of the dish starts to increase after a particular size, the specific cost of the dish-MGT system may increase after an initial decreasing trend. As such, there should be an optimal size of the dish-MGT system which provides lower LCOE compared to other designs.

An optimisation problem is therefore defined for the dish-MGT system to find a system design with minimum LCOE over the feasible range of system size. Compared to the last section, the problem setup will have one additional decision variable for the size of the system which is defined as the rated output power.

Optimisation setup

The problem setup is mostly similar to the case that was defined in section 5.4.1. However, a main difference is that the size of the system varies within a range of 5kWe to 30kWe. The latter is considered as the upper limit of the dish-MGT systems which is imposed by the wind loads and structure of the dish. With the variable system size, the cost of the investment is not only a function of system design parameters, but also the system rated power. Therefore, minimisation of C_{inv} causes the optimisation algorithm to tend towards small systems. To address this problem, the optimisation task is done with LCOE as the objective function. Because of the linear relation between LCOE and annual generated electricity (see equation 5.3), there will be no need to perform multi-objective optimisation. The variables of the problem are defined in Table 5-16.

Table 5-16 problem setup to find optimal compressor design parameters

Decision variable		PWe	π	σ	ε	η_c	η_t	TIT _{max}	TET _{max}
Decision space	Lower limit	5kWe	2.5	0.8	0.8	0.7	0.75	750°C	650°C
	Upper limit	30kWe	4.0	1.2	0.9	0.8	0.85	1000°C	800°C
System constraints					$TIT < TIT_{max}$ $TET < TET_{max}$ $N_{DP} < 150krpm$				
Objective functions					LCOE				

Results

The single objective problem returns a single design which is the optimal design to achieve the minimum levelised cost of electricity within the given decision space. The result and the corresponding performance parameters are shown in Table 5-17 with the breakdown of the system cost shown in Figure 5.14. Compared to the 5kWe system, the minimum LCOE has been considerably reduced. Although it is much better than dish-Stirling systems, it is still higher than the hybrid solar gas turbine systems and much higher than the PV systems. The minimum LCOE is achieved by a system with a rated power of about 24kWe which makes it suitable for a wide range of consumers ranging from domestic to commercial buildings such as shopping centres and hospitals.

Table 5-17 performance specifications of the optimal design for Casaccia

PWe (kWe)	LCOE (€/MWh)	Ean (MWh)	Adish (m ²)	Specific cost (€/kWe)
24	170	48.5	113.23	2179.6

It is interesting that the minimum LCOE is achieved at a smaller rated power than 30kWe while normally it is expected that the cost of generated electricity reduces for higher system size (power rating). This can be justified by the fact that the specific cost of the dish shows an increasing trend in the large sizes. Because of its considerable share in the total cost of the system, the cost of the dish can significantly affect the total cost and LCOE as a result.

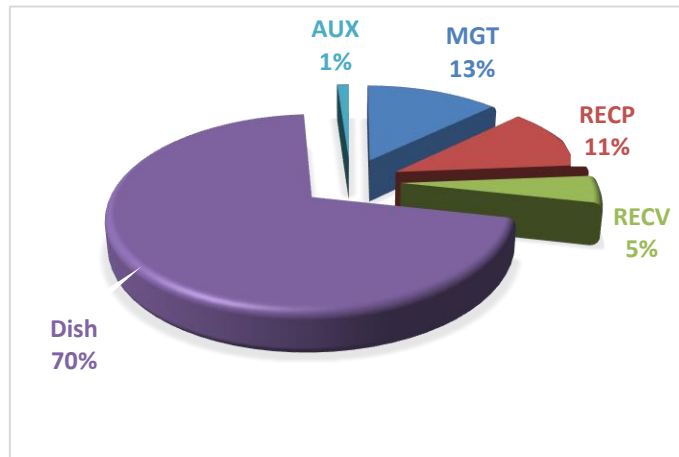


Figure 5.14 components shares in the purchase cost of the optimal design for Casaccia

To get a better picture of the variation of the minimum achievable LCOE with system size, the minimum achievable LCOE for several given rated power values has been calculated. This is done by the definition of individual minimisation problems with the same decision space and variables as the above optimisation problem except for the rated power. The result is shown in Figure 5.15. Each point on Figure 5.15 is an optimised design pertaining to the corresponding

fixed rated power. The graph also shows the total cost of investment for different power ratings. It can be seen that the cost of electricity decreases with the system size until it reaches the minimum value and increases afterwards. However, the variation of the LCOE in the vicinity of the minimum point is not significant. Therefore, other designs with higher or lower rated power than 25kWe may also be considered when choosing a system to match a particular power demand.

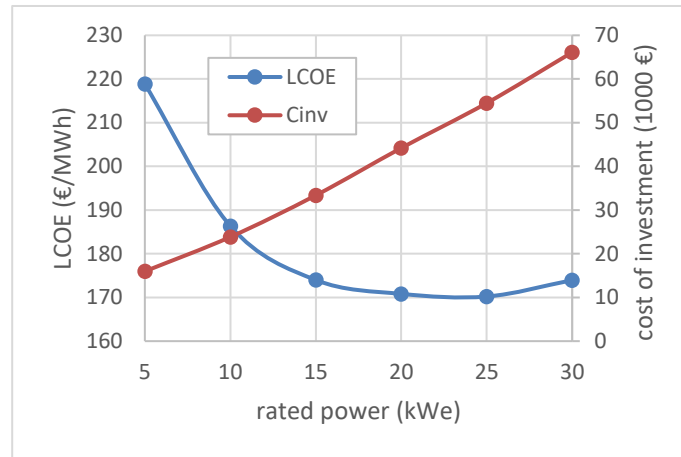


Figure 5.15 economic indicators (LCOE and C_{inv}) for optimised dish-MGT systems with different rated power from 5kWe to 30kWe

Variations of the solar to electric efficiency and size of the dish are also shown for the optimised designs in Figure 5.16. An interesting point here is that the maximum solar efficiency does not take place in the rated power pertaining to the minimum LCOE. Because it is a purely technical term (see equation 3.74) and is not dependent on the economic factors, the solar to electric efficiency doesn't follow the variations of the specific cost or LCOE. Maximum solar efficiency indicates the design which allows for maximum electricity generation per unit area of the dish.

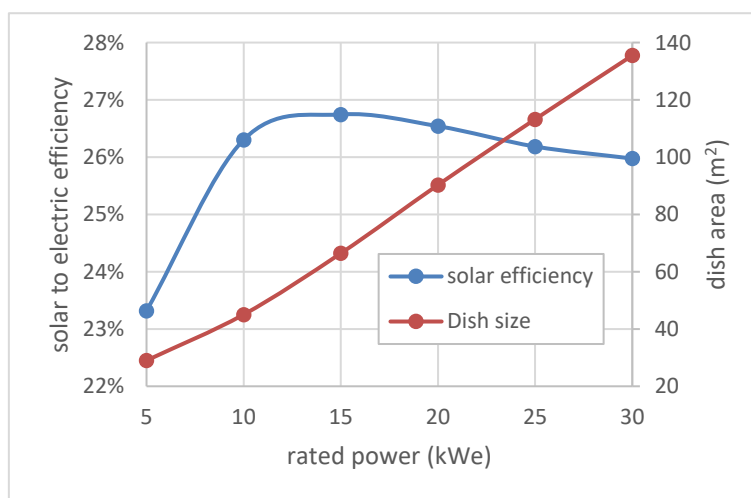


Figure 5.16 solar to electric efficiency and the size of the dish for the optimised designs

Calculations have also been completed for the same scenario when the dish-MGT system is installed in Seville. The minimum levelised cost of electricity for the dish-MGT system is achieved for a system with the rated output power of 22.5kWe and will be as low as 122€/MWh. This is a reasonably low cost compared to the dish-Stirling systems. The investment cost of the dish-MGT systems decreases for higher production volumes which results in even lower LCOE values. The reduction in the cost of generated electricity with the increased rate of annual production is shown in Figure 5.17. To provide a means of comparison, the shaded area shows the average cost of electricity from PV systems which is as low as 55€/MWh (Ren, 2015). The levelised cost of electricity when the optimised dish-MGT system is produced with an annual production rate of 10,000 units per year, reduces to 85€/MWh. These cost figures sound very promising and probably very optimistic. However, it should be noted that the calculated LCOE is given for relatively large annual generated power. An LCOE of 122€/MWh is calculated for the annual production rate of 1000 optimised units with 22.5kWe rated power. This makes a total power of 22.5MWe. According to schwarzbözl et al., the levelised cost of electricity for a hybrid solar installation with 16.1MWe in the US will be about 63€/MWe (Schwarzbözl, et al., 2006). Similarly, the 85€/MWh value is pertaining to a total solar electric power generation as high as 225MWe.

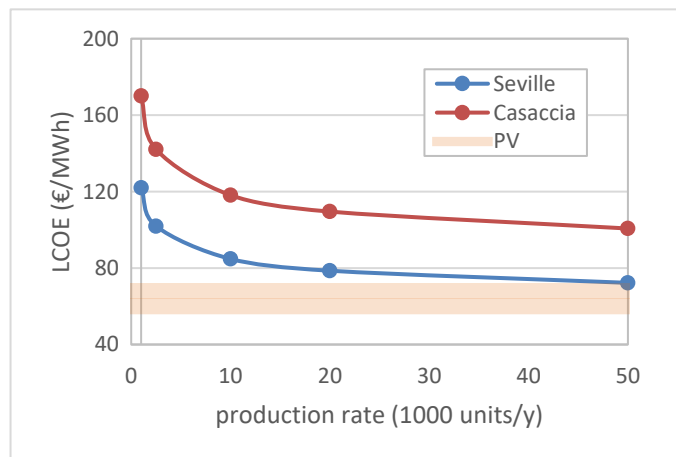


Figure 5.17 variations of LCOE with production volume for the optimised dish-MGT system

5.5 Conclusions

The thermo-economic optimisation of pure solar dish-MGT systems has been conducted under different scenarios. The objective was to investigate whether such systems, if optimised, may provide electricity at a competitive cost compared to dish-Stirling systems. Furthermore, the optimisations also aimed to establish the position of dish-MGT technology relative to other solar electric technologies such as hybrid solar MGTs and photovoltaics from an economic point of view. It was found that dish-MGT systems, with rated powers as low as 5kWe, can generate

electricity with lower costs than dish-Stirling systems. However, the cost of electricity remains higher than the hybrid-solar systems and photovoltaic systems. This difference decreases with the increase in the production volume of the dish-MGT units which could make them attractive for potential consumers. It is also found that the annual DNI income and the ambient conditions of the installation site, as well as the local economic figures such as the real interest rate, are significantly influential for the dish-MGT system to be economic. Further technical conclusions are also listed below.

- There are technical design parameters pertaining to the compressor (pressure ratio, σ) which are not influential on the cost of the system, but have considerable effect on the overall system performance and the cost of the generated electricity as a consequence.
- Other system design parameters which have a substantial effect on the cost of dish-MGT components are TIT_{max} , TET_{max} and the effectiveness of the recuperator.
- A system with high technical specifications, such as the maximum allowable TIT and pressure ratio, needs a more expensive MGT and receiver. The additional costs can be considerable, but will be offset to some extent by the lower cost of the dish
- There are designs on the Pareto optimal front which result in a higher cost of electricity, but require lower specifications and can be a good option when the dish-MGT system is to be installed in less developed regions.
- Although rotational speed does not enter the thermodynamic design of the MGT, its limitation substantially affects the optimisation result. However, this effect becomes less significant for larger sizes.

6 Conclusions and recommendations for further work

6.1 Conclusions

The aim of this work has been to investigate and develop modelling methods which can be used for thermodynamic and economic analysis of solar-only small scale dish-MGT systems in order to find an optimised system design. To achieve this goal, three specific objectives were defined in the introduction chapter which are reproduced here:

- To design and implement a dish-MGT design tool that builds on component performance map generation models with minimum required information and analyse the system performance over the course of variations of solar irradiance more realistically.
- To investigate control strategies for micro gas turbines and develop a control strategy to achieve maximum power generation and avoid technical damage in extreme working conditions
- To design a method to analyse and evaluate optimal values of key parameters in solar powered micro gas turbines which results in optimised techno-economic performance by combining optimisation techniques and realistic performance calculation

To reinforce these objectives, a comprehensive literature review was undertaken in chapter 2 to highlight the required actions and considerations in order to achieve the above objectives. The outcomes of the thesis are concluded here with respect to the objectives and related comments made in the literature review.

6.1.1 Development of the dish-MGT design and analysis tool

It was realised from the literature review that existing research, targeting the identification of the optimal thermo-economic design of a solar powered micro gas turbine, relies on general off-design correlations to avoid more sophisticated system simulations which require component design and performance characteristics to be known. However, for the pure solar dish-MGT systems which are significantly affected by the variations of DNI and operation strategy of the

system, these off-design correlations can produce results that are far from the actual system performance. The first objective of the current thesis was to implement a design tool which can use the same design point data required by the off-design correlations and build a more sophisticated system model for the calculation of system performance over a range of ambient conditions and DNI variations. This objective was achieved in chapter 3 by combining component models, or component performance map generation techniques, with a zero-dimensional system modelling approach in a dish-MGT analysis code. A case study based on the specification of the OMSoP project was used to demonstrate the code. An important achievement which demonstrates the advantage of the developed method over off-design correlations has been demonstrated in chapter 4 as the simulation tool allows the evaluation of the minimum DNI for generating power and also the consumed power for the start-up and shut down of the system. This is a noticeable achievement in terms of applying details of system operation which affect the annual generated electricity that is not achievable by using the off-design correlations.

6.1.2 Control and operation strategies

Control and operation of the dish-MGT systems has been studied in chapter 4 to achieve the second objective of the thesis to find suitable control and operation strategies for the dish-MGT units. Because pure solar dish-MGT systems may not use the fuel flow as a controlling parameter, a power regulation control strategy and more specifically, voltage regulation is designed for the control of system operation.

It was found that the operation strategy has a substantial effect on the performance of the pure solar dish-MGT system. Four operation strategies were modelled and studied using the computational model. These are constant speed, constant TET, constant TIT and proposed maximum permissible power (MPP) strategy. Among the operation strategies which were studied, the proposed MPP strategy proved to be able to achieve the maximum annual electricity generation and solar to electric efficiency provided that the electric load on the system is flexible. For the flexible load conditions, the proposed power regulation control strategy was shown to be a suitable and effective technique which allows the control system to operate the MGT in any of the operation strategies. For load-oriented applications, the recuperation control concept was proposed and analysed. It was shown that this novel concept allows the pure solar dish-MGT systems to match the variations of the electrical load while their input heat from solar receiver is changing. It was also found that the recuperation control inevitably reduces the overall MGT efficiency compared to MPP strategy because of the reduction of the input heat to the receiver. However, it was interesting that the reduction in the overall efficiency of the system for the regions with relatively low solar income is not very significant. This implies that the pure solar

dish-MGT can be used for load-oriented applications more successfully in such regions. Nevertheless, the application of the dish-MGT system determines which strategy must be chosen.

6.1.3 Optimisation of the dish-MGT systems

The outcome of this thesis pertaining to the last, but foremost objective of the project is presented through chapter 5. The ultimate goal of this project was to find system designs for pure solar dish-MGT systems which result in the optimal thermo-economic performance. With the method developed in chapter 3, and coupling the optimisation algorithms to perform multi-objective optimisation, not only are the key design parameters determined for the optimised system, but also the component designs, particularly the performance maps of the compressor and turbine, can be provided by the combined method used in chapter 5. Such an approach has been used in the design procedure of conventional gas turbines. The added value brought by the current thesis is to adapt the method for pure solar dish-MGT systems considering the effects of the operation and control strategy on the overall performance of the system, which of course affects the ultimate results of the system optimisation.

Two different scenarios were considered for the optimisation of the dish-MGT system. The first one is based on the OMSoP project specifications with a given rated output power of 5kWe. The second scenario extends the decision space to a wide range of rated output power from 5 to 30kWe, which is suggested as the maximum system size to be technically and economically viable. The calculations were done for two locations with different level of solar income; Casaccia in Italy and Seville in Spain which receives about 50% more annual solar irradiance than Casaccia. To study the effect of production volume, calculations are also done for different production rates. Generally speaking, the results demonstrate that the levelised cost of electricity reduces as the annual insolation increases. The results also confirm the existence of economies of scale as the cost of electricity, as well as the specific cost of components, reduce for the larger production volumes. An interesting result is that the cost of electricity even for a 5kWe system can be lower than the dish-Stirling systems, but are considerably higher than photovoltaic installations. The cost of generated electricity reaches its minimum value at a rated power of about 23 to 25kWe and then increases for larger sizes. This is justified by the fact that the cost of the dish increases after a particular size because of technical and transport complexities which have a significant effect on the total cost of the system. The minimum values for Casaccia and Seville are 170€/MWh and 122€/MWh respectively for a production volume of 1,000 units per year and are expected to decrease to 101€/MWh and 72€/MWh if the production volume is elevated to 50,000 units per year. With respect to the existing work, this is a step forward in terms of the cost

of generated electricity for pure solar dish-MGT systems which is partly achieved thanks to a recently developed economic model within the OMSoP project.

6.2 Recommendations for further work

Although the objectives of the current thesis have been successfully delivered, several improvements and recommendations for further work can be made.

6.2.1 Improvements to the system design and analysis

The method developed in chapter 3 combines component design and map generation techniques with the system model. An outcome of this method is the performance maps of the compressor and turbine which are generated by the scaling of two base components. The advantage of using this scaling technique is that it is quick and no further data is required in addition to the data required by the thermodynamic model. An important improvement can be accomplished by replacing the scaling technique with more sophisticated map generation algorithms. Having established the optimisation platform in the present thesis, it would be possible to perform the optimisation. Setting the turbine and compressor design data as decision variables provides turbine and compressor designs and their performance maps for maximum system performance.

The focus of the present thesis was on the recuperated micro gas turbine architecture. A more comprehensive study can be made considering more sophisticated cycle configurations incorporating the OMSoP economic model. The thermodynamic model developed in this thesis is flexible to accommodate different system configurations.

6.2.2 Improvements to the control and operation strategies

The analysis of the proposed control strategies for the dish-MGT system has provided a valuable insight on the performance of the system. However, further simulation and analysis could be done to study the start-up and shutdown periods. These events are highly related to the motoring characteristics of the high speed alternator as well as the system warm-up or cool down time. The same concept may be considered when system performance is affected by passing clouds. Clearly, an analysis of such events requires transient simulation of the system. As such, the performance of the control system can be evaluated by a transient model including the response to rapid changes in the ambient conditions, and in particular the DNI.

The recuperation control strategy can be further studied by considering the transient effects. These include the mass imbalance in the recuperator, and the thermal residence time of the recuperator and receiver. Also the performance of the power regulation control strategy could be further

investigated if a more detailed model is developed for the power electronic system and to perform transient analysis of the dish-MGT system.

The effectiveness of the proposed power regulation strategy should be evaluated against the actual results from experimental and field test data. Therefore, the development of a test rig which allows for extensive operational tests of the performance of the control system is highly recommended. The test results would be also beneficial in the verification of the detailed model for the power electronic system as suggested in the above paragraph.

Bibliography

Abbas, M., Boumeddane, B., Said, N. & Chikouche, A., 2011. Dish Stirling technology: A 100 MW solar power plant using hydrogen for Algeria. *International journal of hydrogen energy*, 36(7), pp. 4305-4314.

Agazzani, A. & Massardo, A. F., 1996. *A tool for thermoeconomic analysis and optimization of gas, steam and combined plants*. Birmingham, American Society of Mechanical Engineers.

Aichmayer, L., 2015. *Personal communication*. Stockholm: KTH University, Department of energy technology.

Aichmayer, L., Spelling, J. & Laumert, B., 2015. Thermoeconomic analysis of a solar dish micro gas-turbine combined-cycle power plant. *Energy procedia*, Volume 69, pp. 1089-1099.

Amsdorff, C. & Brewer, M. K., 1999. *Potential Army Application for Micro-Turbine Cogeneration Technology*, Champaign: CONSTRUCTION ENGINEERING RESEARCH LAB (ARMY).

Arroyo, A., McLorn, M., Fabian, M. & Sayma, A., 2016. *Rotor-Dynamics of Different Shaft Configurations for a 6 kW Micro Gas Turbine for Concentrated Solar Power*. Seoul, American Society of Mechanical Engineers.

Avila-Marin, A. L., 2011. Volumetric receivers in solar thermal power plants with central receiver system technology: a review. *Solar energy*, 85(5), pp. 891-910.

Balje, O. E., 1981. *Turbomachines, a guide to design, selection and theory*. New York: John Wiley.

- Barigozzi, G. et al., 2012. Thermal performance prediction of a solar hybrid gas turbine. *Barigozzi G, Bonetti G, Franchini G, Perdichizzi A, Ravelli S. Thermal performance prediction of a solar hybrid gas turbine. Solar Energy. 2012;86(7):2116-2127, 86(7), pp. 2116-2127.*
- Bergman, T. L. & Incropera, F. P., 2011. *Introduction to heat transfer*. 6th ed. New York: John Wiley & Sons.
- Bianchi, M., De Pascale, A. & di Montenegro, G., 2005. *Micro gas turbine repowering with inverted Brayton cycle*. Reno-Tahoe, American Society of Mechanical Engineers, pp. 151-159.
- Borgnakke, C. & Sonntag, R. E., 2009. *Fundamentals of thermodynamics*. 7th ed. University of Michigan: Willey.
- Brändlein, J., Eschmann, P., Hasbargen, L. & Weigand, K., 1999. *Ball and roller bearings: theory, design and application*. 3rd ed. Chichester: John Wiley & Sons.
- Cameron, H. M., Mueller, A. L. & Namkoong, D., 1972. *Preliminary design of a solar heat receiver for a brayton-cycle space power system*, Washington: NASA.
- Çengel, Y. A. & Michael, B. A., 2015. *Thermodynamics: an engineering approach*. 8th ed. s.l.:McGraw-Hill Education.
- Costamagna P, M. L. M. A., 2001. Design and part-load performance of a hybrid system based on a solid oxide fuel cell reactor and a micro gas turbine. *Journal of Power Sources*, 96(2), pp. 352-368.
- Dixon, S. L. & Hall, C., 2010. *Fluid mechanics and thermodynamics of turbomachinery*. 6th ed. Oxford: Butterworth-Heinemann.
- DLR, n.d. *Solar thermal receivers - research for highest requirements*. [Online] Available at: http://www.dlr.de/sf/en/desktopdefault.aspx/tabid-10645/18495_read-43274/ [Accessed 6 April 2016].
- do Nascimento, M. R. et al., 2013. Micro Gas Turbine Engine: a Review. In: E. Benini, ed. *Progress in Gas Turbine Performance*. s.l.:InTech, pp. 109-141.
- DOE, 2001. *Reducing Water Consumption of CSP Electricity Generation*, Washington D.C.: US Department of Energy.
- elektroautomatik, 2015. *Laboratory power supplies*. [Online] Available at: <http://www.elektroautomatik.de/en/Laboratory-power-supplies.html> [Accessed 12 2015].

- El-Sayed, Y. & Tribus, M., 1983. Strategic use of thermoeconomics for system improvement. In: R. A. Gaggioli & M. J. Comstock, eds. *Efficiency and Costing, Second Law Analysis of Processes*. s.l.:American Chemical Society, pp. 215-238.
- Energy Nexus Group, 2008. *Technology Characterization: Microturbines*, Washington DC: Prepared for the Environmental Protection Agency.
- English, R. E., 1986. *Technology for brayton-cycle space powerplants using solar and nuclear energy*, Washington: NASA.
- Fend, T., 2015. *Research Project "MetRec" - New material for volumetric receivers improves performance of solar thermal power plants*. [Online] Available at: http://www.dlr.de/sf/en/desktopdefault.aspx/tabid-10436/12676_read-44618/ [Accessed 6 April 2016].
- Ferrari, M. & Pascenti, M., 2011. Flexible micro gas turbine rig for tests on advanced energy systems. In: E. Benini, ed. *Advances in gas turbine technology*. s.l.:InTech Europe, pp. 89-114.
- Fiedermann, S., Halilovic, J. & Bogacz, T., 2012. *Solar potential of the Sahara Desert with an introduction to solar updraft power plants*. Venice, EEEIC.
- Fisher, U., Sugarmen, C., Ring, A. & Sinai, J., 2004. Gas turbine “solarization”-modifications for solar/fuel hybrid operation. *Journal of solar energy engineering*, 126(3), pp. 872-878.
- Frangopoulos, C. & von Spakovsky, M., 1993. *A Global Environomic Approach for Energy Systems Analysis and Optimization*. Cracow, Proceedings of the International Conference on Energy Systems and Ecology: ENSEC (Vol. 93, pp. 123-132).
- Futral Jr, S. M. & Wasserbauer, C. A., 1970. *Experimental performance evaluation of a 4.59-inch radial-inflow turbine with and without splitter blades*, Cleveland: NASA.
- Galanti, L. & Massardo, A., 2011. Micro gas turbine thermodynamic and economic analysis up to 500kWe size. *Applied energy*, 88(12), pp. 4795-4802.
- Gallup, D. & Kesseli, J., 1994. *A solarized brayton engine based on turbo-charger technology and the DLR receiver*. Monterey, CA, AIAA, pp. 1719-1724.
- Garcia, P., Ferriere, A. & Bezia, J., 2008. Codes for solar flux calculation dedicated to central receiver system applications: a comparative review. *Solar Energy*, 82(3), pp. 189-197.

- Gavagnin, G. et al., 2017. Cost analysis of solar thermal power generators based on parabolic dish and micro gas turbine: Manufacturing, transportation and installation. *Applied Energy*, Volume 194, pp. 108-122.
- Ghavami, M., Alzaili, J. & Sayma, A., 2017. *A Comparative Study of the Control Strategy for Pure Concentrated Solar Power Micro Gas Turbines*. Charlotte, American Society of Mechanical Engineers.
- Gong, Y., Sirakov, B., Epstein, A. & Tan, C., 2004. *Aerothermodynamics of micro-turbomachinery*. Vienna, American Society of Mechanical Engineers.
- GSP, D. t., 2014. *GSP 11 User Manual*. Amsterdam: National Aerospace Laboratory NLR.
- Head, A. & Visser, W., 2012. *Scaling 3-36KW microturbines*. Copenhagen, American Society of Mechanical Engineers, pp. 609-617.
- Hewicker, C., Hogan, M. & Morgen, A., 2011. *Power Perspectives 2030: On the road to a decarbonised power sector*, s.l.: European Climate Foundation (ECF).
- Ho, C. K. & Iverson, B. D., 2014. Review of high-temperature central receiver designs for concentrating solar power. *Renewable and Sustainable Energy Reviews*, Issue 29, pp. 835-846.
- Holeski, D. E. & Futral, S. M., 1967. *Experimental performance evaluation of a 6.02-inch radial-inflow turbine over a range of Reynolds number*, Cleveland: NASA.
- Iki, N. et al., 2007. *Gas Turbine With Ceramic and Metal Components*. Montreal, Canada, American Society of Mechanical Engineers, pp. 901-908.
- Jaffe, L. D., 1989. Test results on parabolic dish concentrators for solar thermal power systems. *Solar Energy*, 42(2), pp. 173-187.
- Jet Propulsion Laboratory, N., 1981. *Solar thermal power systems project, parabolic dish systems development*, s.l.: NASA Lewis Research Center..
- Kalogirou, S., 2014. *Solar energy engineering: processes and systems*. 2nd ed. Amsterdam: Academic Press.
- Klein, S. et al., 2004. *TRNSYS 16–A TRaNsient system simulation program, user manual*, Madison: Solar Energy Laboratory: University of Wisconsin-Madison.
- Knopf, F. C., 2012. *Modeling, Analysis and Optimization of Process and Energy Systems*. 1st ed. s.l.:John Wiley & Sons.

- Kurzke, J., 1995. *Advanced user-friendly gas turbine performance calculations on a personal computer*. Houston, Texas, American Society of Mechanical Engineers.
- Kurzke, J., 1996. *How to get component maps for aircraft gas turbine performance calculations*. Birmingham, American Society of Mechanical Engineers.
- Kurzke, J., 2007. *GasTurb 11: Design and Off-Design Performance of Gas Turbines*, Aachen: s.n.
- Kurzke, J., 2012. *GasTurb 12, user manual*. Germany: s.n.
- Lallana, C., 2003. *Water prices*, Cedex: European Environment Agency.
- Lanchi, M., 2015. *Personal communication*. Casaccia: ENEA (Italian National agency for new technologies, Energy and sustainable economic development).
- Le Roux, W., Bello-Ochende, T. & Meyer, J., 2011. Operating conditions of an open and direct solar thermal brayton cycle with optimised cavity receiver and recuperator. *Energy*, 36(10), pp. 6027-6036.
- Le Roux, W., Bello-Ochende, T. & Meyer, J., 2012. Optimum performance of the small-scale open and direct solar thermal brayton cycle at various environmental conditions and constraints. *Energy*, 46(1), pp. 42-50.
- Lee, J. J., Yoon, J. E. & Kim, T. S. S. J. L., 2007. Performance test and component characteristics evaluation of a micro gas turbine. *Journal of mechanical science and technology*, 21(1), pp. 141-152.
- Lemus, R. G. & Duarte, J. M. M., 2012. *Renewable Energies and CO₂: Cost Analysis, Environmental Impacts and Technological Trends*. 2012 ed. s.l.:Springer Science & Business Media.
- Leyes, R. & Fleming, W., 1999. *The History of North American Small Gas Turbine Aircraft Engines, (Library of Flight Series)*. 1st ed. Washington DC: AIAA.
- Leyland, G. B., 2002. *Multi-Objective Optimisation applied to Industrial Energy Problems*, Lausanne: PhD Thesis, Ecole Polytechnique Fédérale, Lausanne.
- Li, D., Dougal, R., Thirunavukarasu, E. & Ouroua, A., 2013. *Variable speed operation of turbogenerators to improve part-load efficiency*. Arlington, USA, . In 2013 IEEE Electric Ship Technologies Symposium (ESTS) (pp. 353-359). IEEE..

- Lovegrove, K. & Wes, S., 2012. *Concentrating solar power technology: principles, developments and applications*. Cambridge: Elsevier.
- Madureira, N. L., 2014. *Key concepts in energy*. 1st ed. Lisbon: Springer.
- Massini, M., Miller, R. J. & Hodson, H. P., 2011. A new intermittent aspirated probe for the measurement of stagnation quantities in high temperature gases. *Journal of Turbomachinery*, 133(4), p. 041022.
- MATLAB GO toolbox, U. G., 2015. *Global Optimization Toolbox User's Guide, R2015b*, Natick: MathWorks Inc..
- McDonald, C. F., 2003. Recuperator considerations for future higher efficiency microturbines. *Applied Thermal Engineering*, 23(12), pp. 1463-1487.
- McDonald, C. & Rodgers, C., 2008. Small recuperated ceramic microturbine demonstrator concept. *Applied Thermal Engineering*, 28(1), pp. 60-74.
- Mirandola, A. & Macor, A., 1986. *Full load and part load operation of gas turbine-steam turbine combined plant*. s.l., ISEC.
- Monroe, M., Epstein, A. & Kumakura, H. a. I. K., 2005. *Component integration and loss sources in 3–5 kW gas turbines*. Reno-Tahoe, American Society of Mechanical Engineers., pp. 981-988.
- Nakajima, T., 1995. *The development of the 2.6kW micro gas turbine generator*. s.l.:s.n.
- NATO, R., 2002. *Performance prediction and simulation of gas turbine engine operation*, Paris: NATO Research and Technology Organisation.
- NATO, R., 2007. *Performance prediction and simulation of gas turbine engine operation for aircraft, marine, vehicular, and power generation*, s.l.: NATO RTO Applied Vehicle Technology Panel (AVT).
- Neber, M. & Lee, H., 2012. Design of a high temperature cavity receiver for residential scale concentrated solar power. *Energy*, Issue 47, pp. 481-487.
- NSK, 2009. Starting and Running Torques. In: *NSK Technical report No. E728g*. Tokyo: NSK Ltd., pp. 162-171.
- OMSoP, 2013. *OMSoP project website*. [Online] Available at: <https://omsop.serverdata.net> [Accessed 01 09 2016].

- Osborn, B. et al., 2003. Dish-Stirling systems: An overview of development and status. *Journal of Solar Energy Engineering*, 125(2), pp. 135-151 .
- Otto, E. W. & Taylor, B. L., 1950. *Dynamics of a turbo-jet engine as a quasi-static system*, Kitty Hawk: National Advisory Committee for Aeronautics.
- Panne, T., Widenhorn, A., Aigner, M. & Masgrau, M., 2009. *Operation flexibility and efficiency enhancement for a personal 7 kW gas turbine system*. Orlando, USA, American Society of Mechanical Engineers.
- Panne, T. et al., 2007. *Thermodynamic process analyses of SOFC/GT hybrid cycles*. St. Louis, USA, AIAA, pp. 25-27.
- Park, S. H., Lee, Y. D. & Ahn, K. Y., 2014. Performance analysis of an SOFC/HCCI engine hybrid system: System simulation and thermo-economic comparison. *International Journal of Hydrogen Energy* 39, no. 4 (2014): 1799-1810., 39(4), pp. 1799-1810.
- Pelster, S., 1998. *Environomic Modeling and Optimization of Advanced Combined Cycle Power Plants*, Lausanne: PhD Thesis, Ecole Polytechnique Fédérale, Lausanne.
- Pioneer engineering Co., 1980. *Cost analysis of an air Brayton receiver for a solar thermal electric power system in selected annual production volumes*, Warren: Pioneer engineering & Manufacturing Company for the Jet Propulsion Laboratory.
- Pioneer engineering Co, 1981. *Manufacturing cost analysis of a parabolic dish concentrator (General Electric design) for solar thermal electric power systems in selected production volumes*, Warren: Pioneer engineering & Manufacturing Company for the Jet Propulsion Laboratory.
- Poullikkas, A., 2005. An overview of current and future sustainable gas turbine technologies. *Renewable and Sustainable Energy Reviews*, 9(5), pp. 409-443.
- Press, W. H., Teukolsky, S. A., Vetterling, W. T. & Flannery, B. P., 2002. *Numerical recipes in Fortran 90: the art of parallel scientific computing*. 2nd ed. New York: Cambridge University Press.
- Price, H. W., 1997. *Conversion of solar two to a kokhala hybrid power tower*. Washington, D.C., American Society of Mechanical Engineers.
- Rashid, M. H., 2014. *Power electronics : devices, circuits, and applications*. 4th ed. Harlow: Pearson.

- Rautenberg, M. & Kammer, N., 1984. *On the thermodynamics of non-adiabatic compression and expansion processes in turbomachines*. Cairo, 5th International Conference for Mechanical Power Engineering.
- Ren, P. S., 2015. *Renewables 2015 global status report*, Paris: REN21 Secretariat.
- Richerson, D. W., 2006. *Historical review of addressing the challenges of use of ceramic components in gas turbine engines*. Barcelona, Spain, American Society of Mechanical Engineers.
- Richter, C. & Teske, S. a. N. J., 2009. *Concentrating solar power global outlook 09*, s.l.: Greenpeace International/European Solar Thermal Electricity Association (ESTELA)/IEA SolarPACES.
- Rodgers, C., 2000. *25-5 kWe microturbine design aspects*. Munich, American Society of Mechanical Engineers.
- Rodgers, C., 2003. *Some effects of size on the performances of small gas turbines*. Atlanta, USA, American Society of Mechanical Engineers., pp. 17-26.
- Rodgers, C., 2011. *Low Cost Microturbines via the Turbocharger Route*. s.l., American Society of Mechanical Engineers, pp. 703-712.
- Rodgers, C., 2013. *Microturbine Rotational Speed Selection*. San Antonio, American Society of Mechanical Engineers.
- Rosfjord, T., Tredway, W., Chen, A. & Mulugeta, J. , 2008. *Advanced microturbine systems*, s.l.: United Technologies Corporation..
- Sadeghi, E., Khaledi, H. & Ghofrani, M., 2006. *Thermodynamic Analysis of Different Configurations for Microturbine Cycles in Simple and Cogeneration Systems*. Barcelona, American Society of Mechanical Engineers.
- Sánchez, D., 2015. *D3.1 Report on system cost analysis, OMSoP project*, Brussels: European Turbine Network.
- Sanghi, V., Lakshmanan, B. & Sundararajan, V., 2000. Survey of advancements in jet-engine thermodynamic simulation. *Journal of Propulsion and Power*, 16(5), pp. 797-807.
- Saravanamuttoo, H., Rogers, C., Cohen, H. & Straznicky, P., 2009. *Gas turbine theory*. 6th ed. Essex, England: Pearson Education Ltd.

Schiel, W. & Keck, T., 2012. Parabolic dish concentrating solar power (CSP) systems. In: K. Lovegrove & W. Stein, eds. *Concentrating solar power technology*. Cambridge: Woodhead Publishing Ltd., pp. 284-322.

SCHOTT, A., 2016. *Parabolic trough technology*. [Online] Available at: <http://www.schott.com/csp/english/parabolic-through-technology.html> [Accessed 17 March 2016].

Schwarzbözl, P., 2006. *STEC: A TRNSYS Model Library for Solar Thermal Electric Components, Reference Manual, Release, 3*. s.l.:s.n.

Schwarzbözl, P. et al., 2006. Solar gas turbine systems: Design, cost and perspectives. *Solar Energy*, 80(10), pp. 1231-1240.

Shah, R. & Sekulic, D., 2003. *Fundamentals of heat exchanger design*. 1st ed. New Jersey: John Wiley & Sons.

Siegel, N. P., Ho, C. K., Khalsa, S. S. & Kolb, G. J., 2010. Development and Evaluation of a Prototype Solid Particle Receiver: On-Sun Testing and Model Validation. *ASME Journal of solar energy engineering*, 132(2), pp. 1-8.

Sinai, J., Sugarmen, C. & Fisher, U., 2005. *Adaptation and modification of gas turbines for solar energy applications*. Reno, American Society of Mechanical Engineers, pp. 87-94.

SKF, 2015. *The SKF model for calculating the frictional moment*. [Online] Available at: <http://www.skf.com/uk/products/bearings-units-housings/ball-bearings/principles/friction/skf-model/index.html> [Accessed 3 April 2015].

SoDa, 2016. *SoDa: Solar Energy Services for Professionals*. [Online] Available at: <http://www.soda-is.com/eng/index.html> [Accessed 3 May 2016].

SolarGIS, 2011. *SolarGIS: online data and tools for solar energy projects*. [Online] Available at: <http://solargis.info/> [Accessed 3 May 2016].

SolarGIS, 2016. *SolarGIS: online data and tools for solar energy projects*. [Online] Available at: <http://solargis.info/> [Accessed 3 May 2016].

- SOLGATE, 2005. *SOLGATE-Solar hybrid gas turbine electric power system. Final Publishable Report*, Brussels: European Commission.
- Spelling, J., 2013. *Hybrid Solar Gas-Turbine Power Plants: A Thermo-economic Analysis*, Stockholm: PhD Thesis, Royal Institute of Technology (KTH).
- Spelling, J., Favrat, D., Martin, A. & Augsburg, G., 2012. Thermo-economic optimization of a combined-cycle solar tower power plant. *Energy*, 41(1), pp. 113-120.
- Spelling, J., Laumert, B. & Fransson, T., 2004. A comparative thermo-economic study of hybrid solar gas-turbine power plants. *Journal of engineering for gas turbines and power*, 136(1), pp. 1801-1810.
- Spelling, J., Laumert, B. & Fransson, T., 2012. Optimal Gas-Turbine Design for Hybrid Solar Power Plant Operation. *Journal of Engineering for Gas Turbines and Power*, 134(9), pp. 2301-2309.
- Steinhagen, H. M. & Trieb, F., 2004. Concentrating solar power: A review of the technology. *Ingenia, Quarterly of the Royal Academy of Engineering*, February-March, pp. 43-50.
- Tabor, H. & Bronicki, L., 1963. Small turbine for solar energy power package. *Solar Energy*, 7(2), p. 82.
- Traverso, A., 2004. *TRANSEO: A new simulation tool for transient analysis of innovative energy systems*, Genoa: TPG-DiMSET, University of Genoa.
- Traverso, A., Massardo, A. F. & Scarpellini, R., 2006. Externally fired micro-gas turbine: modelling and experimental performance. *Applied Thermal Engineering*, 26(16), pp. 1935-1941.
- Twidell, J. & Weir, T., 2015. *Renewable energy resources*. 3rd ed. New York: Routledge.
- Utriainen, E. & Sundén, B., 2002. Evaluation of the cross corrugated and some other candidate heat transfer surfaces for microturbine recuperators. *Journal of Engineering for Gas Turbines and Power*, 124(3), pp. 550-560.
- Van den Braembussche, R. A., 2005. Micro gas turbines-A short survey of design problems. In: V. d. Braembussche, ed. *Micro gas turbines (AVT/VKI lecture series held at the von kármán institute)*. Belgium: NATO, pp. 1-18.
- Vick, M., Heyes, A. & Pullen, K., 2010. Design overview of a three kilowatt recuperated ceramic turboshaft engine. *Journal of Engineering for Gas Turbines and Power*, 132(9), pp. 2301-2309.

- Vidal, A., Bruno, J. C., Best, R. & Coronas, A., 2007. Performance characteristics and modelling of a micro gas turbine for their integration with thermally activated cooling technologies. *Int. J. Energy Research*, Issue 31, p. 119–134.
- Visser, W. & Broomhead, M., 2000. *GSP, a generic object-oriented gas turbine simulation environment*. Munich, Germany, American Society of Mechanical Engineers.
- Visser, W. P. J. & Dountchev, I. D., 2015. *Modeling Thermal Effects on Performance of Small Gas Turbines*. Montréal, American Society of Mechanical Engineers.
- Visser, W., Shakariyants, S., De Later, M. & Ayed, A. a. K. K., 2012. *Performance optimization of a 3kw microturbine for chp applications*. Copenhagen, American Society of Mechanical Engineers, pp. 619-628.
- Visser, W., Shakariyants, S. & Oostveen, M., 2011. Development of a 3 kW microturbine for CHP applications. *Journal of Engineering for Gas Turbines & Power*, 133(4), pp. 2301-2308.
- Walsh, P. & Fletcher, P., 2004. *Gas turbine performance. Second ed.* , UK: Blackwell Science; 2004. 2nd ed. Oxford, UK: Blackwell Science.
- Whitfield, A. & Baines, N. C., 1990. *Design of radial turbomachines*. 1st ed. Essex: Longman.
- Wilson, A. J. W. et al., 2012. *A robust radial traverse temperature probe for application to a gas turbine HP/IP stage*. Copenhagen, American Society of Mechanical Engineers, pp. 63-71.
- Wilson, D. G. & Jansen, W., 1966. *Aerodynamic and thermodynamic design of cryogenic radial-inflow expanders*. New York, American Society of Mechanical Engineers.
- Woodford, C. & Phillips, C., 2012. *Numerical methods with worked examples: MATLAB edition*. 2nd ed. Newcastle: Springer.
- World Bank, O., 2016. *Real interest rate for all countries and economies from 2007 to 2016*. [Online]
 Available at: <http://data.worldbank.org/indicator/FR.INR.RINR>
 [Accessed 15 12 2016].
- Wu, S.-Y., Xiao, L., Cao, Y. & Li, Y.-R., 2010. A parabolic dish/AMTEC solar thermal power system and its performance evaluation. *Applied Energy*, 87(2), pp. 452-462.

APPENDICES

Appendix A Scaling the performance maps

A performance map can be generated by CFD techniques for a given geometry. More realistic maps can be generated by testing the machine on a suitable test rig. Neither of these options are feasible at the early stage of the engine design since its design point has not been fixed yet and therefore, detailed designs of the components are not available. The method that is applied in this thesis is to generate the maps from the basic information provided by the cycle design point calculations similar to the data sets shown by Table 3-2. This is done in the current thesis by scaling an existing performance map to match the design point of the system.

A.1 Using similitude theory

A simple approach in scaling the existing performance maps to a new design point is to use the similitude theory for the compressible flow turbomachinery as explained in section 3.4.1. Assuming that the size of the original machine, D_1 is known, scaling of the machine will be done by using the equality of non-dimensional groups introduced in equation 3.40. For the non-dimensional mass flow and Mach number, it can be seen that for any two similar machines:

$$\frac{N_1 D_1}{\sqrt{\gamma_1 R_1 T_1}} = \frac{N_2 D_2}{\sqrt{\gamma_2 R_2 T_2}} \quad A.1$$

$$\frac{\dot{m}_1 \sqrt{\gamma_1 R_1 T_1}}{p_1 D_1^2} = \frac{\dot{m}_2 \sqrt{\gamma_2 R_2 T_2}}{p_2 D_2^2} \quad A.2$$

For similar fluid properties and inlet temperature, the above equations reduce to:

$$\frac{\dot{m}_1}{\dot{m}_2} = \left(\frac{D_1}{D_2}\right)^2 \quad A.3$$

$$\frac{N_1}{N_2} = \frac{D_2}{D_1} \quad A.4$$

Indices 1 and 2 represent the original and scaled machines. Pressure ratio will be the same because of the similitude (see equation 3.40). However, it is not true for efficiency due to increased viscous losses in low Reynolds. To account for these losses in the compressor when it is scaled down to smaller sizes, the following equation can be used (Holeski & Futral, 1967) and (Futal Jr & Wasserbauer, 1970).

$$\frac{1 - \eta}{1 - \eta_{ref}} = K + (1 - K) \left(\frac{Re}{Re_{ref}} \right)^{-n} \quad A.5$$

$$Re = \frac{2\dot{m}}{\mu D} \quad A.6$$

Where η_{ref} is the efficiency of the original compressor. Considering the relation of mass flow rate with diameter:

$$\frac{1 - \eta}{1 - \eta_{ref}} = K + (1 - K) \left(\frac{D_{ref}}{D} \right)^n \quad A.7$$

Different values for “n” are suggested for turbine, n_t , and compressor, n_c (Head & Visser, 2012). Typical values of ‘K’ are also between 0.3-0.4 (Whitfield & Baines, 1990). Here, the following values will be used:

$$K = 0.4, \quad n_c = 0.15, \quad n_t = 0.31 \quad A.8$$

A scaling procedure is developed in this work which starts with finding a point on the maximum efficiency line of the original map where the pressure ratio is equal to the design point pressure ratio. The corresponding mass flow rate (\dot{m}_1) will then be used to calculate the diameter ratio so that the mass flow rate of scaled map equals the desired value for the design point (\dot{m}_2). Using diameter ratio, the rotational speed will be calculated. A sample turbocharger compressor map and its scaled result are presented in Figure A.1.

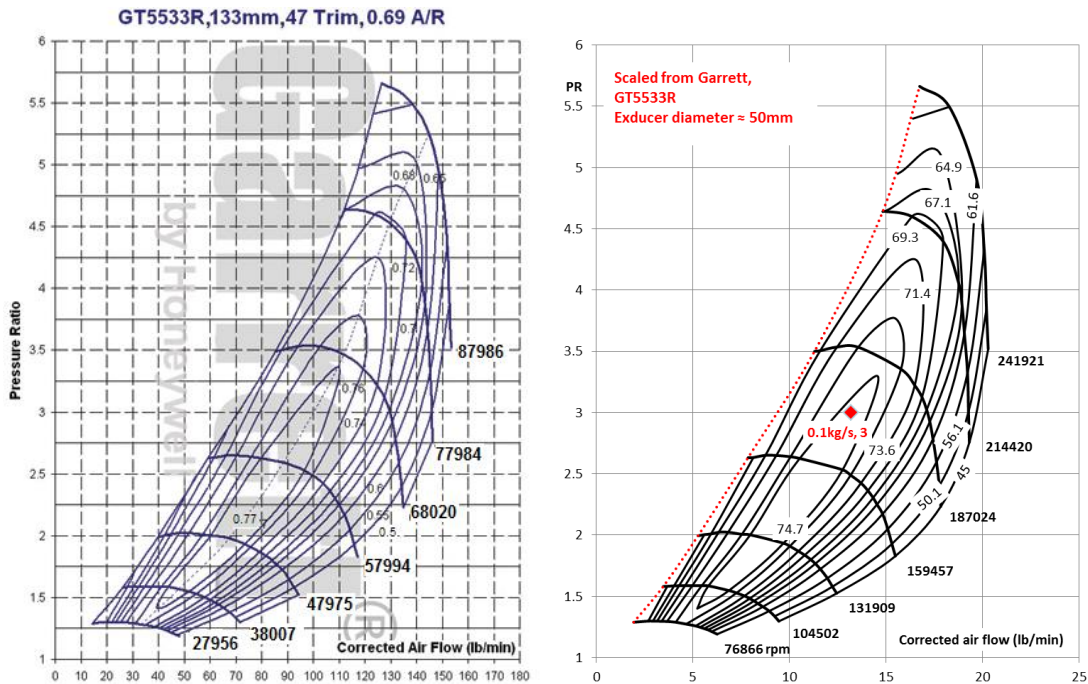


Figure A.1 Compressor maps: original (left) and scaled (right)

This method of scaling has the main advantage that the scaling factor can be directly used to generate the geometry of the new machine. This reduces the effort needed to design the compressor or turbine after finalising the design point calculations. However, it has two disadvantages. To start the scaling of the map, it is required to find a compressor that its pressure ratio at the design point is already equal to the target pressure ratio. The other problem is that the rotational speed of the scaled map at the design point will not be necessarily be equal to the target speed because it is a secondary result of the similitude equations. Change of the speed in the scaled map can be seen in Figure A.1. Over eighty compressors from two major turbocharger firms (Garrett and BorgWarner) were examined and none of them could be scaled to match their original design point to the values given in Table 3-2.

A.2 Constant speed scaling

For a complete match to the design point parameters in the scaling process, a method based on the rotational speed is explained here (Kurzke, 2007). This method uses a reference point on the original map and transfers it to the desired point. Based upon the design point data, a compressor or turbine map should be chosen first. For the non-dimensional speed equal to that of the design point, the maximum efficiency point on the original map will be the reference point. Selection of the map depends on how close is its reference point to its maximum efficiency point.

To address the effects of viscous losses in this method, Kurzke has used Reynolds number index (RNI). RNI is defined as the ratio of the Reynolds numbers calculated at the actual conditions that

the scaled map is going to be used and the reference conditions for which the original map is generated with the same non-dimensional speed (Mach number).

$$RNI = \left(\frac{p}{p_{ref}} \right) \left(\frac{\mu_{ref}}{\mu} \right) \sqrt{\frac{R_{ref} T_{ref}}{RT}} \quad A.9$$

Values with 'ref' subscript are referring to reference conditions of the map. Most compressor performance maps are given with the ISA standard conditions as the reference. When the scaled map is going to be used for conditions different from its original reference conditions, RNI correction must be taken into account. In case of using ideal gas assumption, gas constant will not change and can be eliminated from the equation A.9. Having the RNI calculated, the efficiency and mass flow rate can be corrected using Figure A.2 (Kurzke, 2012) which gives efficiency and flow correction factors ($f_{\eta,RNI}$ and $f_{mass,RNI}$).

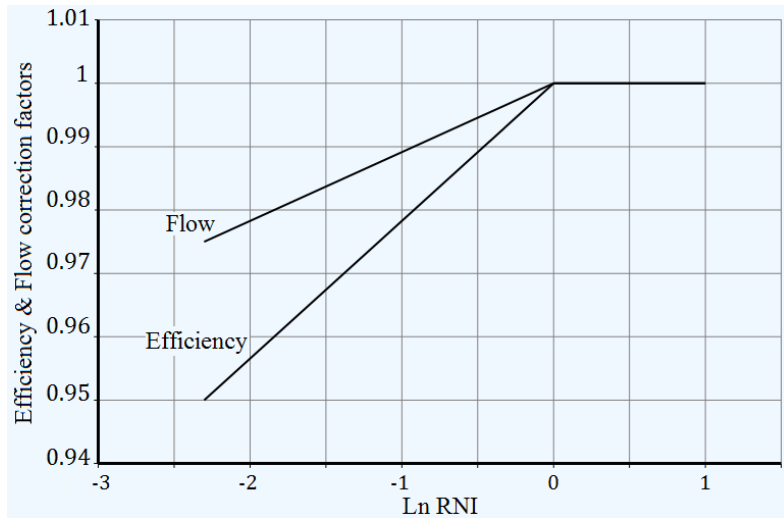


Figure A.2 efficiency and flow factors for RNI

Equations A.10 and A.11 apply the correction factors for the efficiency and mass flow rate to include Reynolds number effects for data read from the original map.

$$\eta_{dp,map} = \eta_{R,map} f_{\eta,RNI} \quad A.10$$

$$\left(\dot{m} \sqrt{T/p} \right)_{dp,map} = \left(\dot{m} \sqrt{T/p} \right)_{R,map} f_{mass,RNI} \quad A.11$$

Subscripts “R,map” and “dp,map” refer to reference point and corresponding corrected values on the original map. The map scaling factors can now be calculated using the design point values.

$$f_{mass} = \frac{\left(\dot{m} \sqrt{T/p} \right)_{dp,map}}{\left(\dot{m} \sqrt{T/p} \right)_{R,map} f_{mass,RNI}} \quad A.12$$

$$f_{eff} = \frac{\eta_{dp}}{\eta_{R,map} f_{\eta,RNI}} \quad A.13$$

$$f_{\pi} = \frac{\pi_{dp} - 1}{\pi_{R,map} - 1} \quad A.14$$

$$f_{speed} = 1 \quad A.15$$

These factors will be applied to all points of the original map so that the new map will be in line with the cycle design point. This procedure is applicable to both turbine and compressor.

Appendix B Electrical power calculations

This appendix presents a model for the electrical system from the output of the high speed alternator to the point of the connection to the grid. The model is based on static simulation of the electrical system with no consideration on the transient effects. The simulation is performed for the generation mode when the system is generating and feeding electricity to the grid. Figure 1 shows the schematic of such system. The model was developed as joint effort of OMSoP partners and in particular City, University of London and ENEA (OMSoP, 2013).

In the architecture of Figure B.1, HSA is a two-pole Permanent Magnet Synchronous Machine (PMSM) that is connected to the electrical grid (3 phase, 400 V – 50 Hz) by means of an Electronic Power Conversion System (EPCS). Such EPCS is composed by a cascade of rectifier (REC) and an active grid connected Inverter (INV). The active inverter has the capability of regulating the fed power to grid.

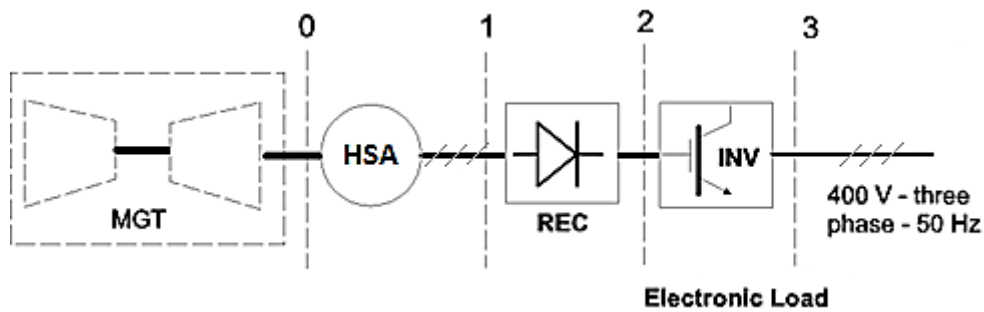


Figure B.1 system arrangement schematic in power generation mode

B.1 High speed alternator

The PMSM is characterised by three main parameters: the inductance (L), the winding resistance (R_{HSA}), and the no-load voltage constant (K_V). The no-load voltage constant is the ratio of the rated magnet voltage and the rated speed in no-load condition ($I = 0$).

The equation B.1 is the energy balance for the high speed alternator and shows that the output voltage of the HSA, V_1 is equal to the no load voltage V_0 minus the voltage losses because of the winding resistance, R_{HSA} and the reactance (inductive) losses, X_{HSA} in the stator when electric current I passes through HSA. The equation is presented in phasor (vector) form and the values of voltage and current are the RMS (Root Mean Square) values. In the equation the inductive losses are separated from other terms by multiplying it with the imaginary number j to emphasis that there is 90° phase difference between the resistance and inductive losses. The no load voltage and reactance losses are proportional to the rotational speed while the resistance of the winding is

assumed constant since it is only a function of the temperature which doesn't considerably change during the operation.

$$\vec{V}_1 = \vec{V}_0 - R_{HSA}\vec{I} - jX_{HSA}\vec{I} \quad B.1$$

The equivalent single phase circuit of the HSA can be represented as shown in Figure B.2. In this circuit the main two elements are the resistor and the inductor. The magnet voltage V_0 is proportional to the rotational speed magnetic field which is the same as the mechanical rotational speed of the rotor as the rotor of the generator is a two-pole magnet.

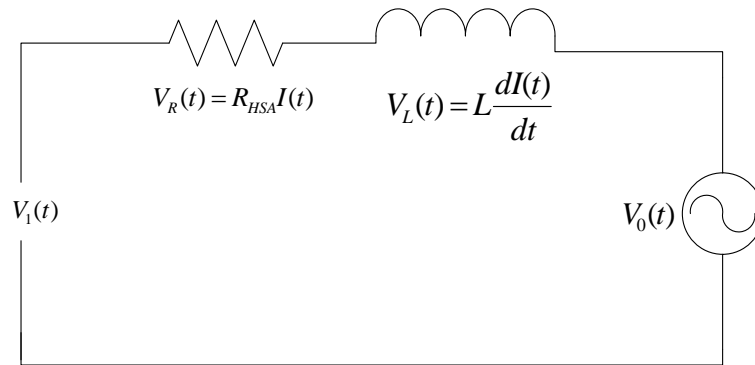


Figure B.2 single phase equivalent circuit of the HSA

For the purpose of this analysis all voltages and the current are assumed as oscillating functions in form of $A \sin(\omega t + \theta)$, where A is the pick value, ω the angular velocity, t is time and θ is the phase angle. The RMS value then is $A/\sqrt{2}$. As all functions have the same angular velocity, only the RMS value and the phase are considered to analysis the HSA circuit.

The RMS value of no-load voltage (phase to phase) is related to the angular velocity as equation B.2

$$V_0 = K_V N \quad B.2$$

Where N is the rotational speed in rpm or krpm. There is a 90° phase difference between V_R and V_L because the first is proportional to the current while the second is proportional to the derivative of the current. As the inductive voltage is proportional to the current therefore the reactance of the inductor is $X_{HSA} = L\omega$. The inductance of the HSA is a constant related to the internal design of the stator. In the following calculations all voltages here will be presented in form of RMS value of phase to phase voltage. By analysing the RL circuit of Figure B.2 one can show that:

$$V_0 = V_1 + I \sqrt{R_{HSA}^2 + (L\omega)^2} \quad B.3$$

The power at point 0 refers to the mechanical power available by the MGT. The relation between the power at point 0 and point 1 modelled as shown in equations B.4 and B.5. The losses in equation B.5 count for losses such as windage loss due to the gap between the magnet and the stator. The constant of this equation is provided by the manufacture of the generator.

$$PW_0 = PW_1 + 3R_{HSA}I^2 + PW_l \quad B.4$$

$$PW_l = k_{HSA}N \quad B.5$$

With good approximation it can be assumed that the power factor for the HSA is equal to unit as in typical PMSM in this range $R_{HSA} \ll X_{HSA}$.

B.2 Rectifier

The rectifier (REC) converts the alternating current generated by the HSA to DC current by means of diodes. The reciter is a passive rectifier which means it doesn't regulate the voltage or the current; it simply converts whatever it is generated in the HSA to DC current. The losses in the rectifier are due to resistance and it is characterised by R_{REC} . The voltage change though the rectifier is modelled by taking in account the ripple effects and the resistance losses over the rectifier as shown in equation B.6.

$$V_2 = 1.35 V_1 - \sqrt{3}R_{REC}I \quad B.6$$

B.3 Invertor

This is an active invertor (INV) which converts the Dc current to 50 Hz AC current which then can be fed to the grid. The invertor feeds the electricity in a constant voltage of the grid irrelevant of the voltage in the HSA. The nominal voltage of the grid in this case was 400 V (phase to phase). Furthermore, the invertor has the capability of regulating the power extracted from the HSA. The invertor is mainly characterised by its efficiency which is typically higher than 95%. The active invertor used in OMSoP project has a pick efficiency of 97% which is assumed to remain constant for a wide range of power input.

$$PW_e = \eta_{inv}PW_2 \quad B.7$$

B.4 Performance of the Electrical System

For purpose of cycle analysis the performance of the electrical system can be modelled by its total efficiency (η_e) and the power can fed to the grid from the HSA (PW_e) at any given speed and current. For any given speed and current (I) the following steps are taken to find the total efficiency of the electrical system and the fed electrical power:

1. The no-load voltage is calculated by $V_0 = K_V N$
2. The angular velocity, $\omega = \pi N/30$
3. Using equation B.2, the value of V_1 is calculated.
4. The electrical power at point 1 is calculated as $PW_1 = \sqrt{3} V_1 I_1$
5. The mechanical shaft power, PW_0 , is then determined by equations B.3 and B.4.
6. The DC voltage, V_2 , after the rectifier is calculated by B.5.
7. The DC power after the rectifier then is calculated as $PW_2 = V_2 I$
8. The power fed to the grid is $PW_e = \eta_{inv} PW_2$
9. The total electrical efficiency is then $\eta_e = \frac{PW_e}{PWSD}$

For a 5kW HSA of OMSoP project the parameters are as shown in Table B-1.

Table B-1 design and performance parameters of the high speed alternator

Parameter	Value	Unit
Nominal rotational speed	130,000	rpm
Nominal frequency	2167	Hz
Nominal angular velocity	13614	rad/s
Nominal phase to phase no-load voltage	295	V
K_V	2.16	V/krpm
Inductance (L)	0.316	mH
Rated current	13	Amp
R_{HSA}	0.159	Ω
k_{HSA}	2.28	W/krpm
R_{REC}	0.237	Ω
η_{inv}	0.97	-

The contribution of each of the electrical sections shown in Figure B.1 can be calculated during the execution of the above procedure and are given by Figure B.3 to B.6.

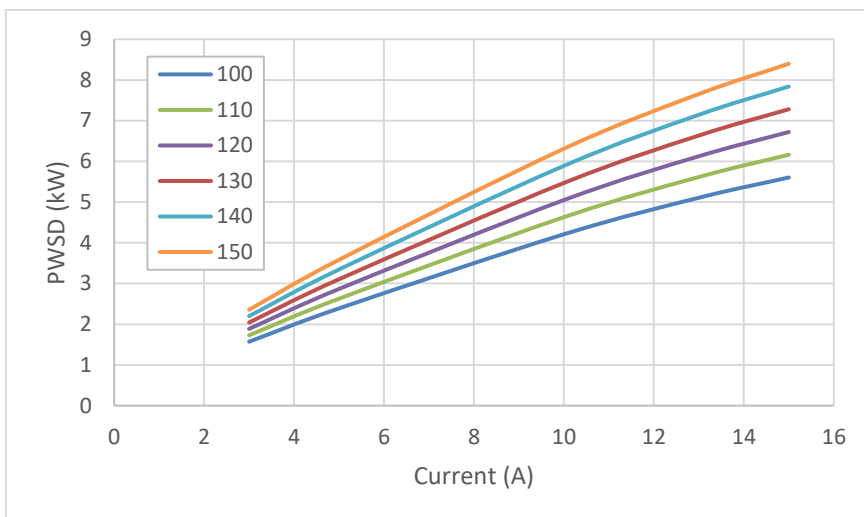


Figure B.3 input power to the HSA represented against the generated electric current at different speeds

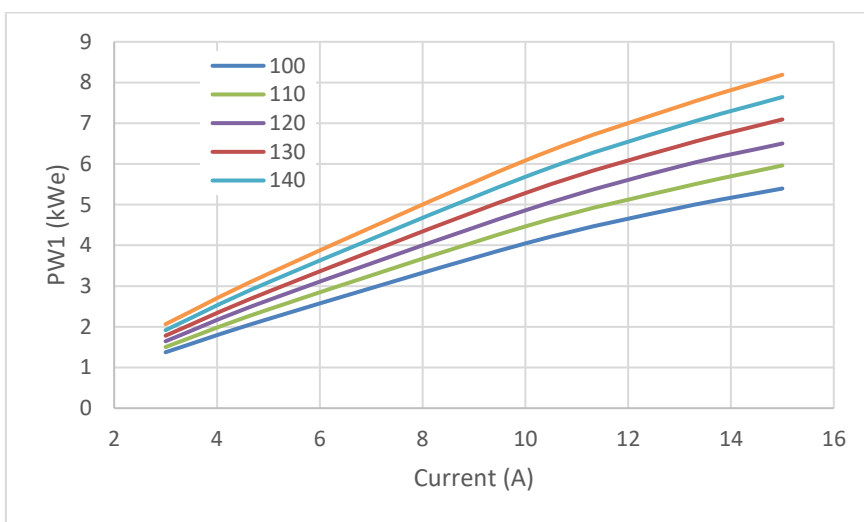


Figure B.4 variation of electric power output from the HSA with speed and electric current

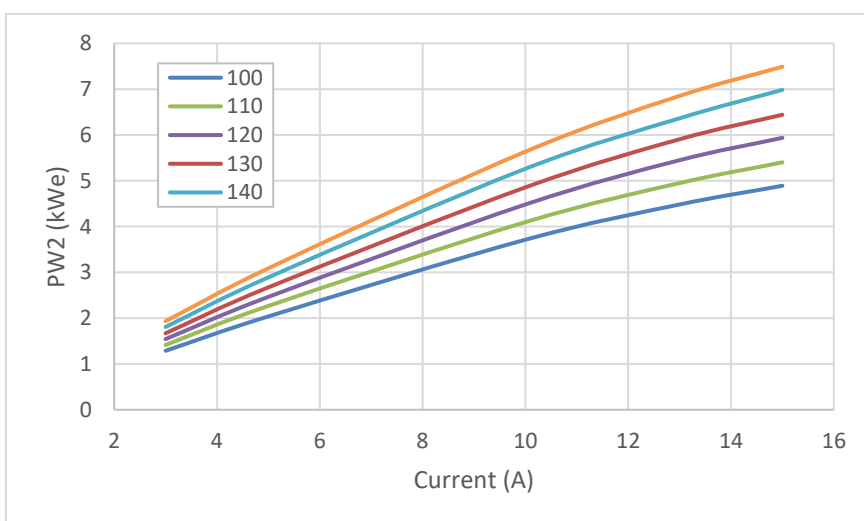


Figure B.5 variation of the electric power output from the rectifier

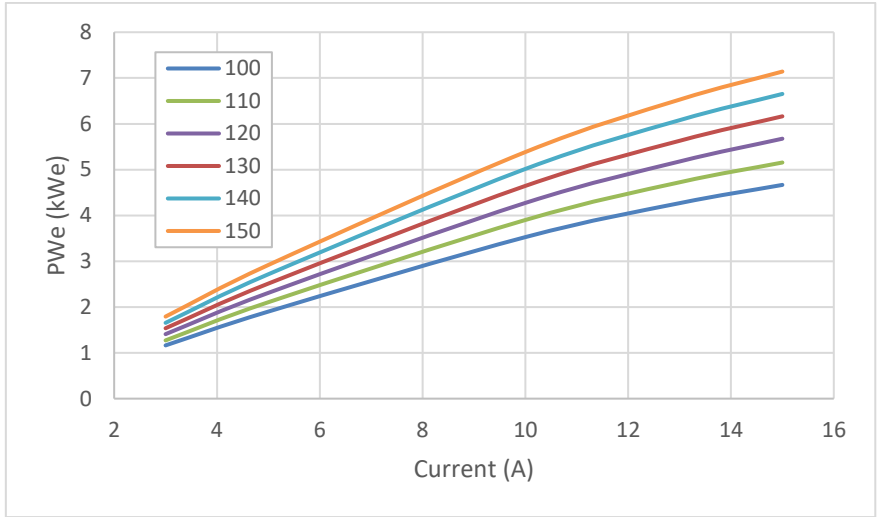


Figure B.6 net output electric power which is fed to the grid